EXPERIMENTAL STUDIES OF SQUAT GRAVITY CAISSONS AND MONOPILES FOR OFFSHORE APPLICATIONS

A Dissertation

by

RYAN DEKE BEEMER

Submitted to the Office of Graduate and Professional Studies
Texas A&M University
in partial fulfillment of the requirement for the degree of

DOCTOR OF PHILOSOPHY

Chair of Committee,	Charles P. Aubeny
Committee Members,	Giovanna Biscontin
	James Kaihatu
	David Brooks
Head of Department,	Robin Autenrieth

May 2016

Major Subject: Civil Engineering

ABSTRACT

This dissertation presents initial results from geotechnical centrifuge experiments on squat gravity caissons and monopiles under cyclic eccentric loading in soft clay under undrained conditions. These experiments were conducted in the 1-g laboratory at Texas A&M University and the 150g-ton centrifuge at Rensselaer Polytechnic Institute. All tested caissons had a length to diameter aspect ratios of two with four tested in the 1-g laboratory and four caissons tested in the centrifuge. Though this aspect ratio is a bit atypical, it could be a reasonable option for offshore renewable hydrokinetic systems or a component in tripod or tetrapod wind tower foundation systems. 1-g experimental results focus of the effect of caisson interior venting on capacity. Centrifuge experimental results focus on behavior arising from an unrestricted vertical coordinate, allowing self-weight to contribute to combined loading, the impact of depth of rotation on caisson resistance, and the global stiffness and damping ratio of the caissons.

With the advent of high accuracy sensors and increased interest in geotechnical centrifuge testing simulating loading within serviceability limits a stronger understanding the strength and orientation of centrifuge gravity relative to the scale model is necessary. This dissertation presents a methodology for determining the 2-Dimensional centrifuge gravity within a model independent of centrifuge type or geometry. This can be used to recompose the gravity field from the direct measurement of single gravity vector, given angular velocity. Finally, the methodology is compared to the mechanics of drum and beam centrifuges to provide physical meaning to coordinate rotation variables.

Microelectromechanical systems (MEMS) accelerometers are becoming more prevalent in geotechnical engineering and geotechnical centrifuge modeling. In geotechnical centrifuge experiments these sensors have shown much promise, but still exhibit some limitations. This dissertation proposes a new methodology for the use of single-axis

low g, high accuracy, MEMS accelerometers to measure orientation of on object in a geotechnical centrifuge. The inclusion of the measured component of cross-axis in orientation calculations significantly improves measurements of absolute orientation, a 3.8º improvement in this study, and reduces errors in orientation measurement by allowing high accuracy low-g accelerometers to be used in the centrifuge.

ACKNOWLEDGMENTS

I would like to foremost thank my committee chair and adviser, Dr. Charles Aubeny. Thank you for your guidance through both my Master of Science and my Doctor of Philosophy degrees. Additionally, I would like to that the Principal Investigator of the research project I participated in (and for all intents and purposes the co-chair of my degree committee) Dr. Giovanna Biscontin. Thank you for all your support and for our wandering discussions.

I would like to thank Dr. James Kaihatu for all of his help and advise throughout my PhD. Thank you for mentoring me and getting me through the bramble that is academic culture, relatively unscathed. I would also like to thank the final member of my degree committee Dr. David Brooks. Thank you for keeping an eye on me and making sure I stayed on target.

I would like to thank the Madhuri Mural and Francisco Grajales for all there help and input on the project. Maddy, I am sorry for keeping you in the lab until midnight discussing the intricacies of total pore pressure and thank you for everything else. Francisco, thank you for everything especially for being a sounding board for my ideas and complaints.

I would like to thank the undergraduate researchers at Texas A&M University that help with my research. Thank you, Tom Anderson, Nicholas Boardman, Daniel Crockett, Oscar Rodriguez, and Elliese Shaughnessy.

I would like the acknowledge the support of the National Science Foundation. This work was funded by the project “Capacity and Performance of Foundations for Offshore Wind Turbines,” award number: 1041604.

I would like the thank the former and current staff of the Center for Earthquake Engineering Simulations at Rensselear Polytechnic Institute. Thank you,

Dr. Anthony Tessari, Dr. Inthuorn Sasanakul, John Lawer, Panagoita Kokkali, Michael Bretti, Jason Thomas, Tanya Vilchek-Vilcu, and Dr. Tarek Abdoun.

I would like to thank Rodney Inmon and the Department of Aerospace Engineering at Texas A&M University for access to the department's 3D printer and for help using it. Thank you.

I would like to thank the staff in the Zachry Department of Civil Engineering at Texas A&M University for all of their help. Thank you.

I would like to thank all of my friends in College Station for their support throughout the last five years. You guys (you'll, for the Texans) were the reason I was able to endure this journey. Thank you, and good luck on all of your adventures and enterprises. Additionally, a special thanks to John Goertz for helping me wrap up my paper work from abroad.

Lastly, I would like to thank my parents for their support throughout my academic meandering. Thank you, I could not have completed this without your emphasis on the importance of education and introducing me to science fiction (including “Star Trek”) from a young age. And thank you to my siblings, grandparents, cousins, aunt, and uncle for letting me jabber on and on about geotechnical engineering when we could have discussed more interesting things.

NOMENCLATURE

V	Normalized velocity
v	Velocity
c_v	Coefficient of consolidation
σ_v	Total vertical stress in the soil
h	Soil depth
ρ	Soil total density
g	A nonspecific gravity
Ø	Caisson diameter
#	Number
ω	Angular velocity of geotechnical centrifuge
$\tilde{g}_e$	Earth's gravity
R	Rotational reference frame within a geotechnical centrifuge
$\hat{i}_r$	Horizontal unit vector in the frame R
$\hat{j}_r$	Vertical unit vector in the frame R
r	Centrifuge radial axis
$\tilde{g}_c$	Centrifugal acceleration
$\tilde{g}$	Centrifuge gravity field dependent on radius
$\tilde{g}_o$	A reference gravity vector in the local coordinate system
x	Horizontal coordinate of the local system
z	Vertical coordinate of the local system
g_{co}	Reference gravity component of centrifugal acceleration
α	Angle of reference gravity vector relative to the centrifuge radius, r
β	Angle of the reference gravity to the local coordinate system vertical, z
ξ	The angle of the local coordinate system vertical, z, to the centrifuge radius, r
g_x	The component of centrifuge gravity vector, g, in local horizontal coordinates axis, x
g_z	The component of centrifuge gravity vector, g, in local vertical coordinates axis, z

α_b	Basket angle from the radial axis, r
M	Mass of the basket and model
L_b	Distance between the basket hinge and the concentrated mass
R_b	Distance between the centrifuge axis and the basket hinge
R_e	Distance between the centrifuge axis and the center of gravity
$\Delta\alpha_b$	Difference in angle between the center line of the basket and project line L_b between the basket hinge and the concentrated mass of the basket and model, M
α_{2D}	angle of the basket from horizontal when the center of gravity is not on center-line of the basket
L	Vertical distance along model axis z from the basket hinge to the basket center of gravity
d	Horizontal distance along model axis x from the basket hinge to the basket center of gravity
α'_b	Centrifuge basket angle with an applied moment about its hinge
m_h	Moment applied about centrifuge basket hinge
$\Delta\alpha_m$	Change in angle due to applied moment about basket hinge
r_h	Radius of basket hinge
f	Coefficient of friction in the basket hinge
m_f	Moment due to friction in the basket hinge
$\Delta\alpha_f$	Change in angle from moment induced by friction
Δa_{fs}	Change in angle from moment induced by friction with small angle assumption
x_{sensor}	Horizontal axis of the MEMS accelerometer
z_{sensor}	Vertical axis of the MEMS accelerometer
a_{meas}	Measured acceleration by the MEMS accelerometer
a_n	Centrifuge gravity component normal to the MEMS accelerometer, x_{sensor}
a_t	Horizontal acceleration, a_h, component tangent to the MEMS accelerometer, x_{sensor}

a_h	Acceleration of the MEMS accelerometer along the local horizontal axis, x
a_{cross}	Measured acceleration due to accelerations perpendicular to the sensor measurement direction
a_{temp}	Measured acceleration due to a change in temperature of the sensor
θ_n	Angle of sensor relative to centrifuge gravity
a_{xg}	Component of measure cross-axis acceleration, a_{cross}, due to centrifuge gravity perpendicular to the sensor's measurement direction
a_{xh}	Component of measure cross-axis acceleration, a_{cross}, due to horizontal acceleration perpendicular to the sensor's measurement direction
a_{xc}	Component of measure cross-axis acceleration, a_{cross}, due to Coriolis acceleration
C_x	Correlation factor of measure cross-axis acceleration due to component of acceleration perpendicular to the sensor's horizontal coordinate, x_{sensor}
b_x	Intercept of measure cross-axis acceleration due to component of acceleration perpendicular to the sensor's horizontal coordinate, x_{sensor}
C_y	Correlation factor of measure cross-axis acceleration due to component of acceleration perpendicular to the sensor's vertical coordinate, y_{sensor}
b_y	Intercept of measure cross-axis acceleration due to component of centrifuge gravity perpendicular to the sensor
θ_t	Orientation of the MEMS accelerometer relative to model local coordinates (x,z)
V_{meas}	Meausred voltage by a MEMS accelerometer due to applied acceleration
V_z	Zero g voltage factor of a specific MEMS accelerometer
CF	Calibration factor of MEMS accelerometers
δ_{max}	Maximum deflection of the pile stem
F_h	Horizontal force
I	Second moment of area
E	Elastic modulus
L_s	Length of pile stem, distance between pile cap and center of stem ball

d_s	Displacement of the caisson at the soil surface
d_r	Displacement of pile at the load application point
h_r	Distance between load application point and the soil surface
θ_{r1}	Initial tilt of the pile
θ_{r2}	Tilt of the pile after load application
d_o	Displacement of the pile at the soil surface due to initial tilt
h_d	Depth of rotation of the pile
ε_v	Vertical strain
ε_1	Strain from gage R1, Fig. 5.8
ε_2	Strain from gage R2, Fig. 5.8
ε_3	Strain from gage R3, Fig. 5.8
ε_p	Strain on the strong axis of the stem
$\varepsilon_{p\text{-}avg}$	Strain on the strong axis of the stem averaged from multiple gages
γ	Rotation of stem strain gages about the stem length
F_v	Vertical force
A	Cross-sectional area
M_n	Bending moment
Z	Section modulus
F_R	Linear unit of soil reaction force at the base of the caisson
ε_c	Strain in the caisson shell
b_c	Thickness of the caisson shell
K_r	Steady state normalized rocking stiffness
θ_d	Differential pile tilt
b	Power low parameter, intercepted in log-log scale
m	Power law parameter, slope in log-log-scale
ΔW	Work done in the hysteresis loop
k	Stiffness of the hysteresis loop
u_a	Amplitude of tilt over half the loop
C_s	Specific damping capacity
ζ	The damping ratio

TABLE OF CONTENTS

Page

Page

Page

LIST OF FIGURES

FIGURE Page

FIGURE Page

FIGURE Page

LIST OF TABLES

TABLE Page

1 INTRODUCTION AND BACKGROUND

1.1 Overview

The overall goal of this dissertation was to investigate the behavior of eccentrically loaded squat gravity caissons in soft kaolinite clay under monotonic and cyclic loading. The caissons had a length to diameter (L/D) aspect ratio of two and were to be tested using both 1-g and centrifuge scale modeling. To accomplish this goal research was conducted into using microelectricalmechanical systems (MEMS) accelerometers to make high accuracy measurements of caisson tilt within a centrifuge model. Including the development a methodology for describing the two dimensional gravity field of a geotechnical centrifuge model. Chapters 2 and 3 of this dissertation discuss centrifuge gravity and MEMS accelerometers while Chapters 4-6 cover squat gravity caissons.

All modeling of gravity caissons/monopiles was conducted in soft clay under undrained conditions. Under these conditions any excess pore pressure that develops in the soil is unable to dissipate. This results in soil strength being independent of applied vertical stress and loading conditions. As long as excess pore pressure does not have time to dissipate, the magnitude and frequency of wave and wind loading should be inconsequential. In general, high frequency loads do not impact clay behavior. Undrained conditions are bounded by a minimum normalized velocity, Eq. (1.1), of 30 (Dejong et al. 2012). The experiments presented in this dissertation have a normalized velocity, V, of 625, well above the minimum.

$$V = \frac{v \text{Ø}}{c_v} \tag{1.1}$$

where: V is normalized velocity, v is velocity of caisson, Ø is caisson diameter, and c_v is the coefficient of consolidation

At rates below a normalized velocity of 30, excess pore pressures generated in the clay are able to dissipate and the behavior is considered drained. At very large normalized velocities viscous effects can occur, but can easily be corrected for (Dejong et al. 2012). Therefore, if wind and wave loading velocities are outside the undrained range the results from these experiments should not be used.

As discussed later, terminology for foundations with L/D aspect ratio under 10 are ill-defined. Therefore, as a general rule the foundations in this dissertation are referred to as either a caisson or a gravity caisson, with gravity referring to the foundation carrying a self-weight load, while the terms monopile or pile are used to refer to the entire assembly tested in the scale model. So, the monopile's foundation was a gravity caisson.

1.2 Geotechnical Centrifuge Scale Model Testing

Scale model testing in geotechnical engineering tends to be difficult to do accurately. Being a continuum, many mechanical properties of soil are based on applied vertical stress (specifically vertical effective stress). In the field much of this stress comes from the soil self-weight as seen in the total stress calculation, Eq. (1.2). As a result if an engineer created a $1/30^{th}$ scale model of a 30 m pile in order test a less expensive 1 m pile the model would have only 3.3% of the vertical effective stress as the field prototype. This would result in significantly different behavior in the model compared to the field prototype, especially at working loads and displacements. It should be noted that normalized undrained ultimate capacity is often scale independent in clays and silts; since undrained shear strength is independent of applied stress. However, this is not the case for moduli in clay, especially when they vary significantly with depth, and failure mechanisms involving surface effects.

$$\sigma_v = \rho \cdot g \cdot h \tag{1.2}$$

where: σ_v is total vertical stress, g is a nonspecific gravity, and h is soil depth

One means of matching vertical stress in a small scale model with those in the field is to increase gravity proportionally with the decreasing depth. This can be done by placing the model in a centrifuge where the centripetal acceleration can serve as gravity in place of Earth's gravity.

Geotechnical centrifuge experimentation is quite an old practice. Some of the earliest documented experiments are contributed to Phillip Bucky at Columbia University in New York City in 1931 (Craig 2014; Scott 1977) and to Georgy Pokrovsky at the Moscow Institute of Hydraulic Engineering and Hydrology in the Soviet Union (Pokrovsky and Fyodorov 1936; Vinogradov et al. 2014). Pokrovsky and Il'ya Fyodorov's work was actually presented at the First International Conference on soil Mechanics and Foundation Engineering at Massachusetts Institute of Technology in 1936 (Pokrovsky and Fyodorov 1936). However, much of the current practice in geotechnical centrifuge modeling (especially in the West) can be linked back to Andrew Schofield at the University of Cambridge (Craig 2002; Schofield 1980).

1.2.1 The Geotechnical Centrifuge

The simplest form of a geotechnical centrifuge is a device that, when spun, exerts a centripetal acceleration on a model. A sketch of a simple centrifuge with a model space (x,y,z), spinning at a radius, r, about its axis, Y, at an angular velocity, ω, is provided in Fig. 1.1. This acceleration, for the most part, is designed to be perpendicular to Earth's gravity.

Drum centrifuges are a common device for scale model testing (Madabhushi 2015; Springman et al. 2001; Stewart et al. 1998). They are essentially hollow cylinders spun at high angular velocities with the soil test bed placed around the inner circumference, Fig. 1.2. In most cases they are mounted such that centrifugal acceleration is perpendicular to earth's gravity. They are capable of pulling very high g and have the benefit of having a large modeling area. It is typically possible to mount a model around

the entire circumference of the drum. They do have to major drawbacks. Since the model space is perpendicular to Earth's gravity it is typically necessary to constructed model at high g while the centrifuge is spinning which is difficult procedure. Additionally, drum centrifuge radii are typically small. This results in a large variation is centripetal acceleration in the model and will also result in proportionally high increments of Coriolis Acceleration acting on moving objects.

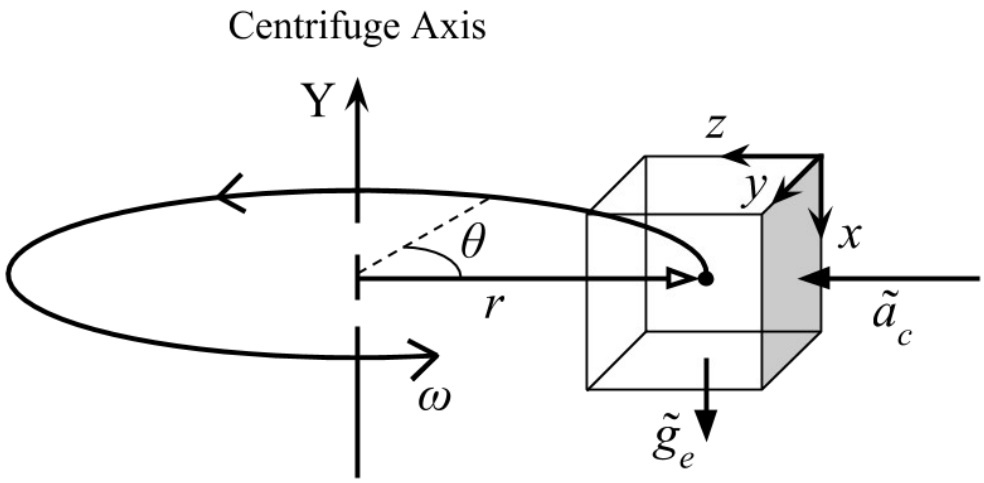

Fig. 1.1. Simplified geotechnical centrifuge

Beam centrifuges are common and can be found throughout the world (Black et al. 2014; Elgamal et al. 1991; Ellis et al. 2006; Kim et al. 2012; Madabhushi 2015; Phillips et al. 1994). An example has been provided in Fig. 1.3. A beam centrifuge consists of a large support beam, a basket, and a counter balance that all spin about an axis, Fig. 1.4. The main benefit of a beam centrifuge is that while the centrifuge is at rest the basket is parallel to the ground, making it easy to construct a model. During spin up the basket will rotate out becoming perpendicular to the ground. There are two types of beam

centrifuges: free-swing baskets and restricted baskets. Centrifuges with free swinging baskets are by far more common. The Turner beam centrifuge at the Schofield Center at the University of Cambridge is the most famous example of a beam centrifuge with a restricted basket (Phillips 1995; Schofield 1980). When the Turner centrifuge spins up its basket comes to rest on a vertical plate keeping it parallel to Earth gravity at centripetal accelerations greater than 10 g.

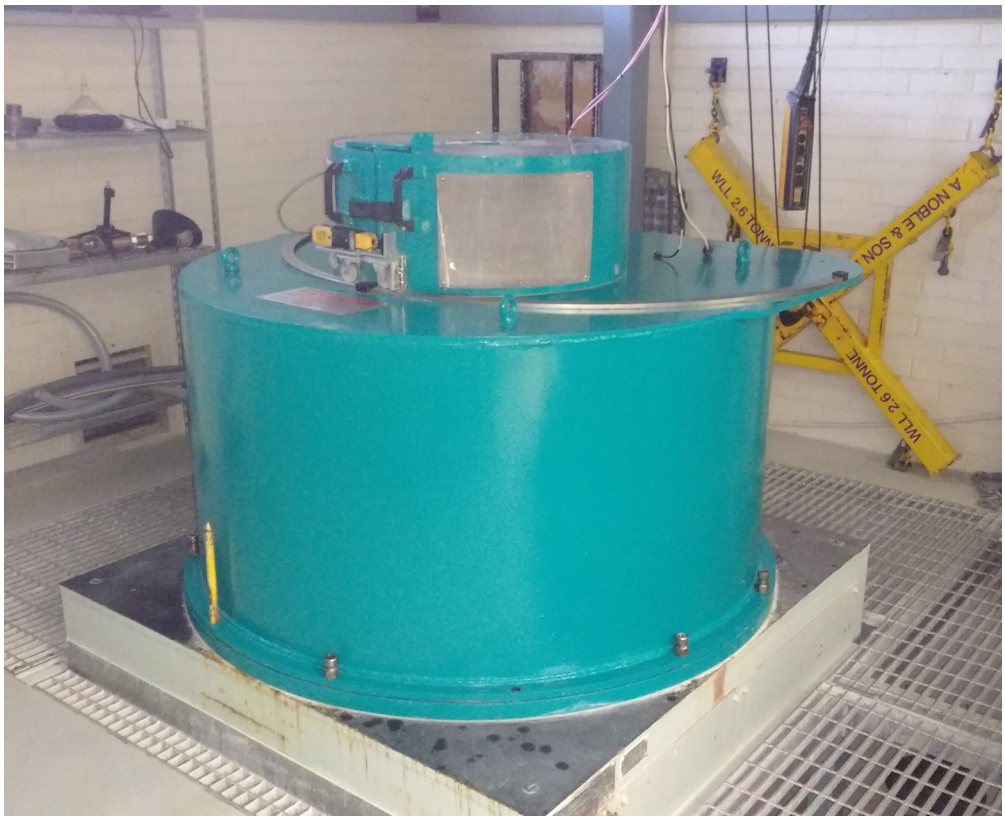

Fig. 1.2. Example drum centrifuge at the Centre for Offshore Foundation Systems at the University of Western Australia

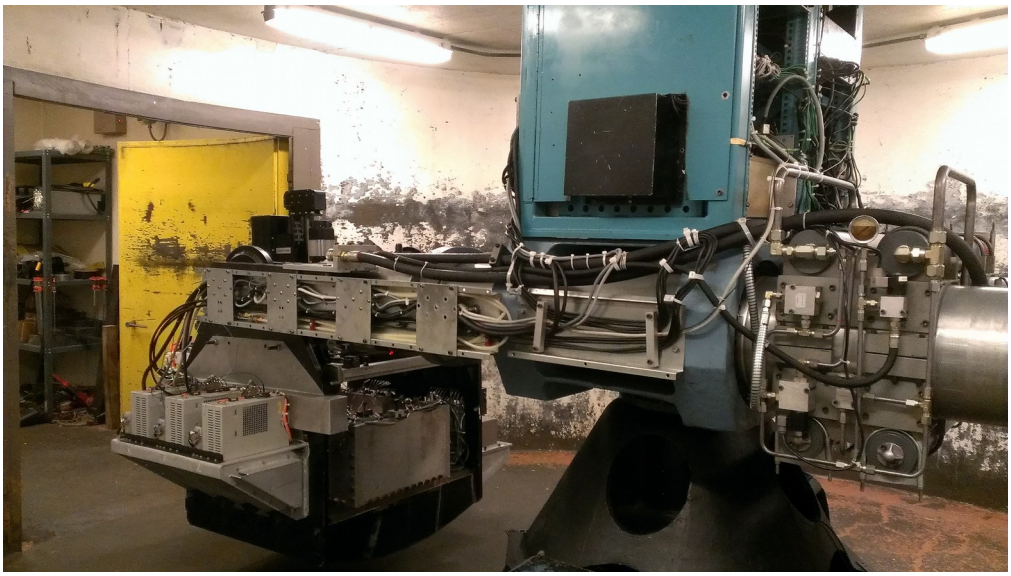

Fig. 1.3. Example of beam centrifuge from the Center for Earthquake Engineering Simulations at Rensselaer Polytechnic Institute

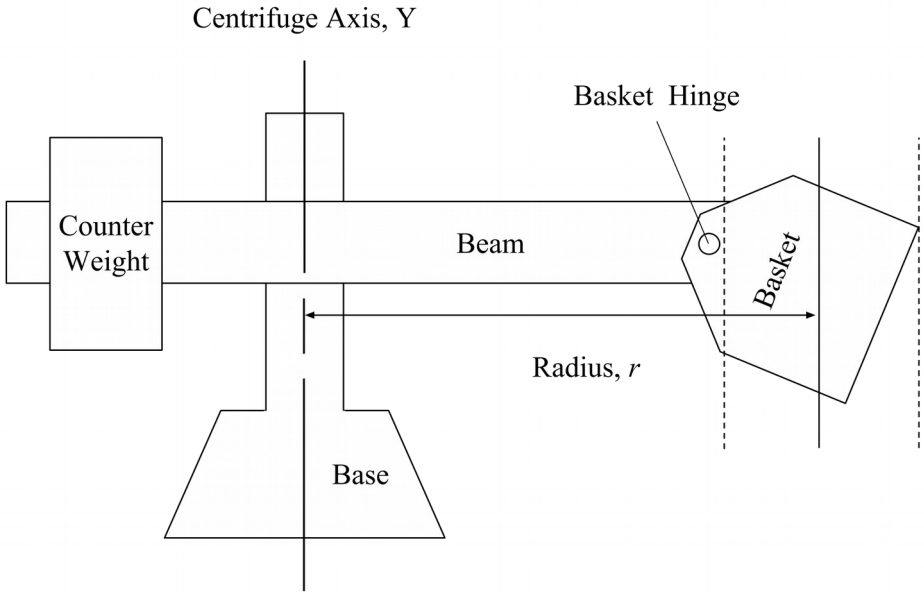

Fig. 1.4. Idealized beam centrifuge with free-swinging basket

In principle, beam centrifuges with free swinging baskets are designed to align centrifuge gravity (the resultant of centripetal acceleration and Earth's gravity) at the nominal radius (distance from the centrifuge axis Y to the mid-depth of the model) with the model's vertical coordinate; in practice this is typically not the case. There are frequently uncertainties in the location of the model's center of gravity and uncertainties in the magnitudes of moment about the basket hinge as discussed in Chapter 2.

1.2.2 Treatment of Centrifuge Gravity

When discussing gravity within a model in a geotechnical centrifuge it is typical to consider it as a one dimensional vector field on the vertical the rotational plane of centrifuge radial distance and the centrifuge axis with the magnitude of the field dependent on centrifuge radius (Madabhushi 2015; Murff 1996; Schofield 1980, 1988; Taylor 1995). This 1D definition can describe a nonlinear effective stress distribution with depth in a small scale model. As this does not occur in the Prototype, Fig. 1.5, it is important to consider when designing and interpreting experiments. Only in limited cases has centrifuge gravity been treated as a two dimensional vector field when on the vertical rotational plane. Phillips (1995) notes the orientation of the centrifuge gravity relative the restricted platform of the Turner centrifuge, while Xuedoon (1988) recommends the use of a potential function Eq. (1.2) (attributed to the Soviet researchers Pokrovsky and Fyodorov) to describe the magnitude and orientation of centrifuge gravity when designing geotechnical centrifuges. Finally, Allmond et al. (2014) briefly discusses the impact of centrifuge basket orientation, from vertical axis Y, has on measurements of tilt within a centrifuge, but the direct relationship between centrifuge gravity and basket angle in not examined.

Centrifuge gravity is more commonly treated as 2D when defining it on the horizontal radial plane (r, θ) (Madabhushi 2015; Park 2014; Taylor 1995). On the radial plane centrifugal acceleration is best defined as constant in polar coordinates and varies across model Cartesian coordinates, with higher variations at smaller radii. It is common practice to modify model geometry to account for this variation if model radial width is

important (Park 2014; Taylor 1995).

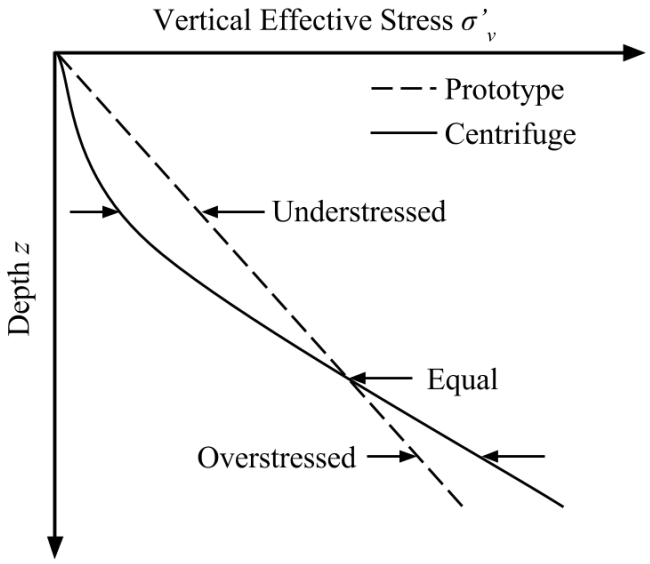

Fig. 1.5. Comparison of prototype and model effective stress (not to scale)

$$Y = \frac{1}{2}\frac{\omega^2}{|g_e|}r^2 + C \tag{1.2}$$

where: Y is the vertical coordinate, r is the horizontal coordinate, ω is angular velocity, g_e is Earth's gravity, and C is an integration constant.

Finally, higher order centrifugal accelerations have been addressed in a vertical rotational reference frame. One of these is Coriolis acceleration, which is be dependent on velocity of an object on the horizontal radial plane and the centrifuge radial coordinate (Madabhushi 2015; Schofield 1980, 1988; Taylor 1995). Another is Euler's acceleration, which is dependent on the angular acceleration of the vertical rotational

plane and the centrifuge radial coordinate. Therefore, it is only relevant during spin up or spin down of the centrifuge (Madabhushi 2015).

Beyond the comments by Phillips (1995) and the potential function provide by Xuedoon (1988), 2D centrifuge gravity in the vertical rotational reference frame of a geotechnical centrifuge is rarely discussed. In part this is due to limited impact of variation in the centrifuge gravity field on geotechnical models. However, with a shift in focus from ultimate load capacity to deformation analysis under working loads and the advent of new sensing technology, a stronger understanding of 2D centrifuge gravity is needed.

1.3 MEMS Accelerometers and Geotechnical Engineering

MEMS accelerometers have become a pervasive part of everyday life. They instruct mobile phones and tablets to rotate when turned sideways, they allow fitness trackers to count steps and award them for taking the stairs, and they activate a cars airbags when the dangerous decelerations of a crash are detected. Their prevalence, in part, is due to the silicon fabrication techniques used to produce them, allowing for low relative costs (Oppenheim et al. 2000; Shaeffer 2013; Spangler and Kemp 1996). Though low costs in themselves make MEMS accelerometers an attractive option for use in geotechnical modeling, it is their ability to measure constant acceleration which makes them ideal for physical modeling. Unlike other types of accelerometers, such as piezoelectric, MEMS accelerometers can measure vectors of constant acceleration and their orientation relative to said vector.

The adaptation of MEMS into civil engineering has been advocated since at least 2000 (Oppenheim et al. 2000). Since then MEMS accelerometers have served two main purposes for geotechnical engineers: dynamic measurements of sensor motion and quasi-static measurements of sensor orientation relative to gravity. It should be noted that, at its current state, the possibility of dead reckoning (double integration of acceleration) measurements of long time periods is limited (Tanaka 2007); however, it is considered a major goal for the technology (Shaeffer 2013). MEMS accelerometers have been used

both in the field and the laboratory by geotechnical engineers. In brief, examples include: measuring wave propagation with custom packaged MEMS accelerometer circuits (Bhattacharya et al. 2012; Hoffman et al. 2006), the shape-acceleration array for measuring soil mass deformation (Bennett et al. 2009), use in liquefaction field tests (Saftner et al. 2008), use in penetrometers to measure surface properties of offshore sediments (Stark et al. 2009), and penetration profiles of dynamically penetrated plate anchors (Blake and O'Loughlin 2015).

An area of geotechnical testing that has recently begun using MEMS accelerometers is geotechnical centrifuge modeling. Examples include: evaluation of MEMS accelerometers in dynamic centrifuge testing (Stringer et al. 2010), seismic evaluation of pile reinforced slopes (Al-Defae and Knappett 2014), evaluation to measure model radial distance from the centrifuge axis and dead recognizing of a dynamically penetrated anchor inline to centrifuge gravity (O'Loughlin et al. 2014), measurements of monopile rotation using high-g accelerometers (Lau 2015), and large angle anchor orientation in sand with a sinusoidal relationship (Chow et al. 2015).

Though these initial uses have been quite successful, there is still room for improvement. Stringer et al. (2010) noted that spurious accelerations were measured during spin up of the centrifuge, though the measurement direction of the sensor was perpendicular to the centrifuge gravity. Additionally, residual velocities (integration of acceleration) were measured after completion of the experiment when the sensors were static. Up to this point, accuracy of orientation measurements with MEMS accelerometers has been relatively low. Chow et al. (2015) reports orientation in ranges of 2º-5º. Lau (2015) found it necessary to amplify the signal from 35 g MEMS accelerometer by a gain of 10 to utilize them and even then there were cases where sensor accuracy was reported as being too low. Low accuracy will limit the use of MEMS accelerometers to measure orientation in the centrifuge, especially for cases like monopile rotation where serviceability tilts are limited to 0.5º (DNV 2007) and lateral spreading on slopes as shallow at 0.6º (Taboada-Urtuzuástegui and Dobry 1998). For continued and successful use of MEMS accelerometers within a geotechnical centrifuge a full and systematic

methodology is needed.

To date, measurements of orientation in the centrifuge (Chow et al. 2015; Lau 2015) have utilized a simple sinusoidal relationships to relate measured acceleration to orientation relative to centrifuge gravity. This processes has been outlined by Allmond et al. (2014). The results presented show good correlation to measurements of rotation by two linear displacement transducers, but little discussion of initial or absolute orientation is provided. The method presented specifically excludes measured cross-axis acceleration, which has been previously suggested to impact measurements of absolute orientation at centrifuge gravity magnitudes as low as 10 g (Beemer et al. 2015). This dissertation will further expand on this concept and show that measured cross-axis accelerations are significant. This theory can also provide an alternative solution for the spurious accelerations measured during spin up by Stringer et al. (2010). The inclusion of cross-axis acceleration into quasi-static orientation theory also allows for the use of high accuracy low-g MEMS accelerometers improving measurement quality.

This dissertation examines the use of MEMS accelerometers to measure orientation within a geotechnical centrifuge and presents a methodology for measuring sensor orientation relative to centrifuge gravity to a high accuracy. This investigation is supported by results from high-g cross-axis experiments on single-axis low g accelerometer. It was found that cross-axis acceleration has a significant impact on orientation measurements and that the use of this new technology in the high-g environment of the centrifuge is more complex than in 1 g.

1.4 Offshore Renewable Energy

The United States and other countries around the world are looking to renewable energy sources to diversify and secure their energy infrastructure. In particular, offshore wind farms are being developed around the globe. Aside from high start up costs and the harsh ocean environment these wind farms hold many advantages. Some of these include: more energetic and consistent winds, proximity to large metropolitan areas, and

capabilities of building larger turbines. Overall, offshore wind energy has the capabilities to provide a significant amount of energy to the grid and many counties are recognizing its potential.

As of 2012 European countries produced the most energy from offshore wind farms with 49 farms producing 3,294 MW (Sun et al. 2012). The National Renewable Energy Laboratory (NREL) in its 2010 report *Large-Scale Offshore Wind Power in the United* (Musial and Ram 2010) states that Europe is expected to increase this production to 40 GW by 2020. As of 2011 China has a single farm constructed producing 102 MW with an additional two farms approved and nine in the planning phase, (Sun et al. 2012). China's goal is to be producing 30 GW of offshore wind energy by 2020, (Sun et al. 2012). Currently the United States has no offshore wind farms with the exception of a few prototype towers. The first farm expected to come online is Cape Wind in Massachusetts which will produce 468 MW (Musial and Ram 2010); however, it has ran into a number of legal hurdles. As of 2010, 13 offshore wind farms have been proposed. The majority of continental coastal states have proposed projects. The Department of Energy expects the US to be producing 54 GW or 20% of its total energy from offshore farms by 2030. The NREL report (Musial and Ram 2010) states this is feasible if development is allowed in federal waters.

As reported by (Musial and Ram 2010) the US could feasible produce 54 GW of offshore wind power by 2030. The US is primed to utilize offshore wind power because its population and therefore energy consumption is concentrated on the coast. The 28 coastal continental states account for 75% of the US' power production (Musial and Ram 2010). Additionally, the majority of the shelf around the country is large enough to allow for construction of farms out of sight of general population; helping to mitigate litigation and reports of other problems such as Wind Turbine Syndrome (Kloor 2013). However, to be successful in its endeavor the US has to learned from the mistakes made in Europe and fund research into the study of foundations for offshore wind turbines.

Musial and Ram (2010) reported that wind farms in Europe installed prior to 2005 had

"higher than expected failure rates" which led to no new projects being constructed until 2008. Many of these problems can be associated with the foundation, where accepted tolerances are on the order of 20 mm (Musial and Ram 2010). Additionally, foundation costs are reported to be 20-40 % of the entire tower cost compared with 14% onshore (Snyder and Kaiser 2009). This is may be due to the fact that foundations for offshore wind towers are being designed based on those used by the offshore petroleum industry instead of using designs optimized for loading unique to wind towers.

Traditionally, offshore foundations have been associated with gravity structures or anchors for the petroleum industry. These piles for petroleum gravity structures need to resist large vertical loads with limited lateral and moment loading. While caissons used for anchoring are designed to carry pure horizontal loads from an anchor chain attached to their sides. However, wind towers are purposely designed to be subjected to moment loads from the wind in order to maximize power generation. Therefore, it is necessary to develop an understanding of the behavior of these foundations under large moment/rotational/rocking loads.

1.5 Caissons and Monopiles

The expansion of offshore renewable energy and subsea systems for the petroleum industry has resulted in engineers utilizing nontraditional foundation in order optimize their designs. Specifically, these foundations need to carry moment and vertical loads in soft soils, where mat and pile foundations are typically ineffective. This has resulted in the emergence of a variety of caisson type foundations and a fluidity between shallow foundations and open ended flexible piles. A caisson type foundation is simply a hollow tube that has a soil plug when installed. These transitional type foundations go by many names including skirted foundations, buckets, monopiles, and caissons. No formal classification of terminology has been made in attempt to unify their design, but anecdotally, naming conventions tend towards those presented in Fig. 1.7. The only defined limit on caisson type foundations is that flexible piles are defines as having L/D aspect ratio greater than 10 with all foundation of smaller aspect ratio being considered

rigid (Poulos and Davis 1991; Randolph 1981). This all does raise an interesting question, what is the difference between a shallow skirted foundation and a rigid squat caisson?

The history of research on squat piles can be demonstrated by referencing *Elastic Solutions for Soil and Rock Mechanics* (Poulos and Davis 1991). This seminal work collects elasticity equations and their solutions, with accompanying graphs and tables, for the majority of relevant cases in soil and rock mechanics. Originally published in 1974, reprinted in 1991 due to popularity, and in 2006 the book provided online in full by Dr. Poulos. The book provides elastic solutions for laterally load piles for aspect ratios between 10 and 100; well above the 1 to 6 range of transitional foundations. Traditionally, squat pile has not been relevant.

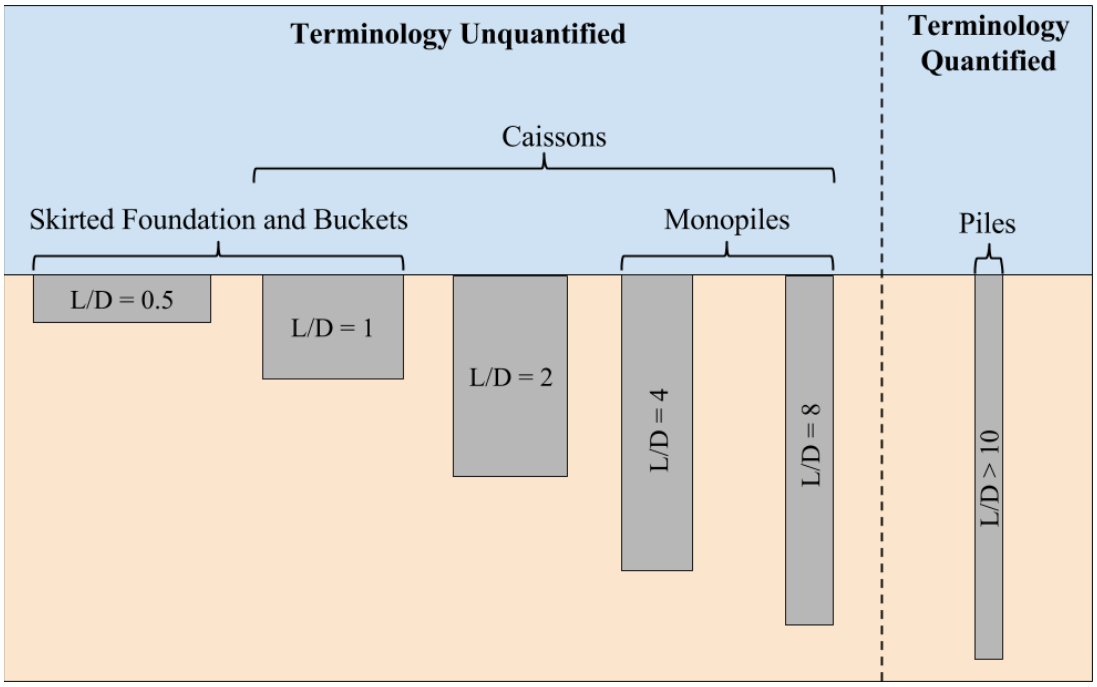

Fig. 1.6. Anecdotal assessment of offshore transitional foundation terminology (not to scale)

The reason for the lack of interest is that there are few onshore cases in which a squat pile would be the most economical design. The main exception being foundations for transmission lines towers; where right-of-way limitations make the use of shallow foundations impossible. To that end, (Mayne et al. 1995) provides an extensive review of laterally loaded pile tests in cohesive soils, up to that date. The paper also provided experimental results for scale drill shaft piles with L/D from 3 to 8. It should be noted that drill shafts are solid with no soil plugs.

Significant research on the lateral loading of piles goes back to Matlock (1970). In this work a number of full scale field tests and small scale laboratory tests were conducted on piles with aspect ratios of 40 and 6, respectively. These tests resulted in methods for calculating the ultimate capacity of a laterally loaded pile and pile displacement with depth through the p–y curve method; which is the current standard for the offshore petroleum industry (Randolph and Gourvenec 2011). The p-y curve method calculates pile displacement by using normalized force displacement curves. They are constructed from laboratory data and can be developed for multiple depths along the pile length. Additionally, the paper includes recommendations for altering the curves for cyclic design.

In recent years, very few large scale or field tests have been conducted. Large scale field tests were conducted on skirts in clay by Houlsby et al. (2005). The skirts had aspect ratios of 0.5 and 0.67. They focused on lateral and moment loading in order to create a five parameter structural model to mimic a skirt foundation. Their model works well for emulating damping, but not stiffness. Additionally, Zhu et al. (2011) ran large scale laboratory tests on skirts with L/Ds of 0.5 in silt. The lateral loading data was used to develop a capacity based design method relying on Rankine active earth pressure theory and to identify failure mechanisms for skirts.

Most research on lateral loading of piles since the 1970s has focused on geotechnical centrifuge testing and analytical modeling. Successful upper-bound plasticity solutions included Randolph and Houlsby (1984), updated in Martin and Randolph (2006), and

Murff and Hamilton (1993), with the latter being most predominately referenced in the literature.

A significant body of experimental research on the lateral loading of piles has been conducted in geotechnical centrifuges. Informative references on the benefit of centrifuge testing can be found in Scott (1983) and Murff (1996). One of the earliest centrifuge tests on the lateral loading piles, L/D of 34.5, is Scott (1977). Included are preliminary results from monotonic and cyclic tests conducted for the American Petroleum Institute, the same organization which funded the experiments in Matlock (1970), in the centrifuge at California Institute of Technology, which is now located at the University of New Hampshire (Ghayoomi and Wadsworth 2014). Another early work of importance Hamilton et al. (1991) which served as a feasibility study for centrifuge testing of model offshore foundations and were used to develop the plasticity model in Murff and Hamilton (1993).

Given the dynamic nature of the offshore environment, an important design aspect of these transitional caisson type foundations will be their behavior under cyclic lateral loading. Traditionally, cyclic lateral capacity of piles can be determined with cyclic p-y curves (Matlock 1970). However, this work was developed for long flexible piles. Additionally, a mean stress method (Andersen and Lauritzsen 1988) can be used to determine cyclic capacity, given the appropriate failure mechanism and laboratory data.

In recent years there has been more development in this area. Jeanjean (2009), Zhang et al. (2011), and Lau (2015) have provided significant results regarding the lateral loading of piles. Jeanjean (2009) included centrifuge tests on model piles with L/D aspect ratio of 22. These experiments indicated that (Matlock 1970) is too conservative for large aspect ratio piles and suggests corrections to the p-y curve method and Murff and Hamilton (1993) ultimate capacity. It should be noted that the tests in Jeanjean (2009) were specific to their distinct cyclic lateral loading conditions of conductors and may not always be applicable to other foundations.

One of the newer geotechnical centrifuge study on the cyclic and monotonic lateral

loading of monopiles is Zhang et al. (2011). The monopiles in the study had aspect ratios 5 and were tested in soft clay. Loading was two-way displacement controlled and the piles were vertically restricted. The ultimate capacity data indicate that predictions from Murff and Hamilton (1993) calibrated with t-bar data appear the most accurate. The paper focuses highly on lateral cyclic stiffness. The paper proposes a method for modeling the degradation of the lateral stiffness due to cycling.

P-y curves for monopiles, in clay, with aspect ratios of approximately 5.2 under combined lateral-moment loading have been investigate by Lau (2015). These centrifuge experiments were conducted under both one-way and two-way cyclic force controlled loading. Results from this dissertation still appear preliminary and a more detailed analysis may be provided in the future.

Another topic of interest involving the lateral loading of piles is the interaction between it and loads from the other degrees of freedom, moment and axial. Early work on combined loading of piles focused on the affects of lateral loading on axial capacity. Anagnostopoulos and Georgiadis (1993) used pile model tests with L/D of 26 to show that lateral load could significantly increase vertical displacement, but vertical load had only a small effect on horizontal displacement.

Later work on combined loading of caissons and skirts has focused on developing capacity interaction curves. These normalized charts and equations describe the foundations ultimate capacity under combined loads. Clukey et al. (2004) examined vertical and horizontal combined loading for an L/D of 5 to 7. Watson et al. (2000) did the same for aspect ratios of 0.4 to 0.5. Acosta-Martinez et al. (2011) did similar work for skirts with aspect ratios 0.3, but the paper focus on uplift (negative vertical load) and moments. Byrne and Houlsby (2004) looked at how constant vertical load impacts moment and lateral capacities of skirts under mainly cyclic conditions in sand.

Lastly, the theories of lateral loaded piles in permafrost could provide useful insight into the cyclic lateral loading of caissons. As outlined in Neukirchner and Nixon (1987) piles under constant horizontal load in permafrost displace laterally a significant amount due

to creep. In the paper they provide creep parameters dependent on temperature and ice content modeling of the rate in change in permafrost-pile lateral stiffness for finite difference calculations.

2 CENTRIFUGE MODEL 2D GRAVITY IN THE VERTICAL ROTATIONAL REFERENCE FRAME

2.1 The Centrifuge Gravity Field

When testing at constant angular velocity, ω, a vertical rotational reference frame, *R,* can be defined on the vertical rotational plane (*r*,Y). Any mass within the reference frame *R* is subjected to a resultant acceleration with components of centrifugal acceleration, g_c, (equal in magnitude and opposite in direction to centripetal acceleration) and Earth's gravity, g_e. Centrifugal acceleration is variable with along the radial axis, *r*, and is defined as:

$$g_c = \omega^2 r \tag{2.1}$$

where: g_c is centrifugal acceleration, ω is rotational velocity, and *r* is distance from the centrifuge axis

The resultant magnitude and direction of these vectors will vary with radial coordinate, r, according to Eq. (2.2) as illustrated in Fig. 2.1.

$$g = g_c \hat{i}_R + g_e \hat{j}_R \tag{2.2}$$

where: *g* is the gravity field dependent on radial coordinate, *r*, $\hat{i}_R$ is the horizontal unit vector in frame *R*, and $\hat{j}_R$ is vertical unit vector in vertical rotational frame R

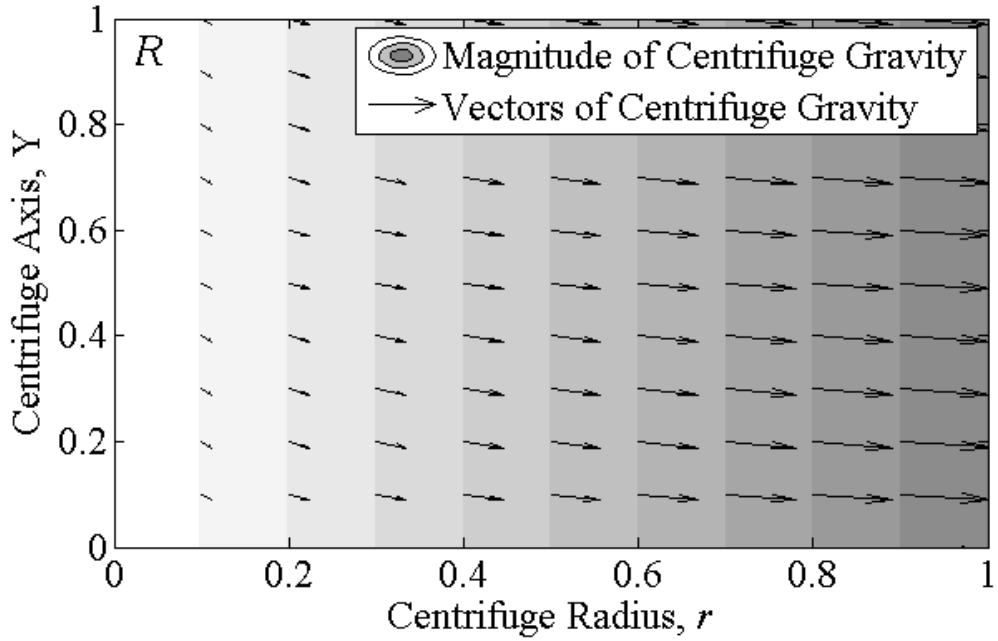

Fig. 2.1. Centrifuge gravity in frame R (Earth's gravity scaled for visual effect)

2.2 Model Local Coordinate System

The model local coordinates are related to the reference gravity vector by an angle, β, and to the reference frame *R* horizontal by an angle, ξ. Given a measured or known centrifuge gravity, $\tilde{g}_o$, vector in *R*, it is possible to describe the magnitude and orientation centrifuge gravity throughout the model local coordinate system. The component of centrifugal acceleration, g_c, in *R* of the known vector $\tilde{g}_o$ can be determined, given Earth's gravity, g_e:

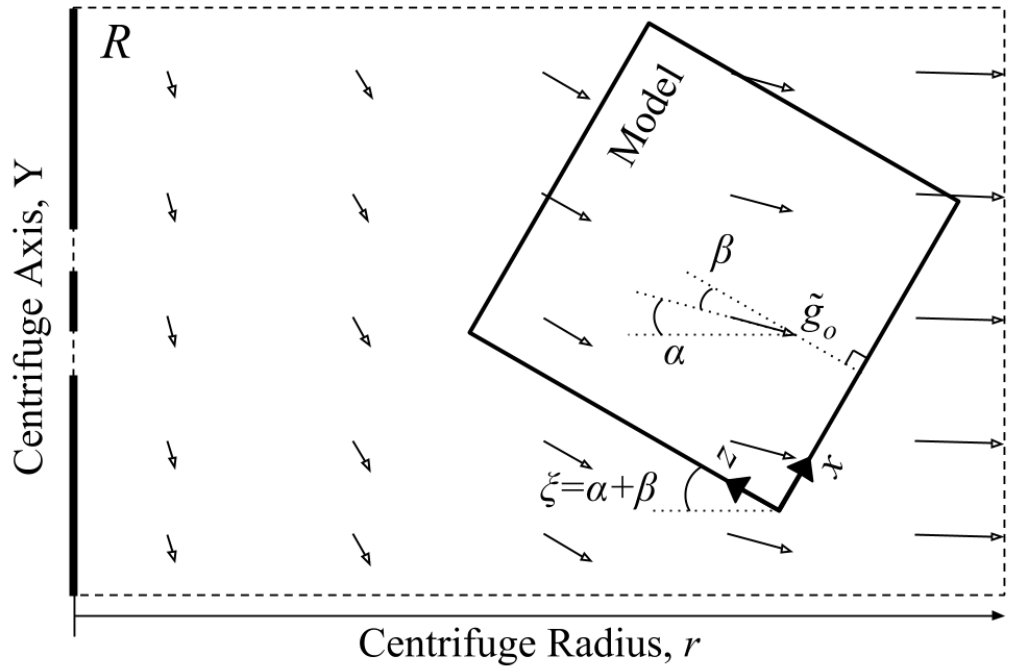

Fig. 2.2. Local coordinate system (x,z) on reference plane R

$$g_{co}=\sqrt{g_o^2+g_e^2} \tag{2.3}$$

where: g_o is the known reference gravity, g_{co} is the component of the reference gravity, g_o due to centrifugal acceleration

The angle of the vector $\tilde{g}_o$ relative to radial axis, *r*, can be determined as:

$$\alpha = \tan\left(\frac{g_e}{g_{co}}\right) \tag{2.4}$$

where: α is the angle between the radial axis, r, and the reference gravity vector, $\tilde{g}_o$

By defining the angle between the local coordinate system and the reference gravity

vector, $\tilde{g}_o$, as β, Fig. 2.2, the orientation of R with respect to the local coordinate system will be:

$$\xi = \alpha + \beta \tag{2.5}$$

Given the relationship between the radial coordinate and local coordinate system (x,z) ξ can be defined as:

$$\frac{\partial r}{\partial x} = \sin(\xi) \tag{2.6}$$

$$\frac{\partial r}{\partial y} = -\cos(\xi) \tag{2.7}$$

where: x is the local horizontal coordinate and y is the local vertical coordinate as in Fig. 2.3

Local coordinates can be related to centrifugal acceleration with the linear relationship:

$$\frac{dg_c}{dr} = \omega^2 \tag{2.8}$$

Resulting in:

$$\frac{\partial g_c}{\partial x} = \omega^2 \sin(\xi) \tag{2.9}$$

$$\frac{\partial g_c}{\partial x} = \omega^2 \cos(\xi) \tag{2.10}$$

With centrifugal acceleration, g_c, defined throughout the local coordinate system (x,z), the components of centrifuge gravity, $\tilde{g}$, can rotated into the local system with the

common transformation matrix:

$$\begin{bmatrix} g_z \\ g_x \end{bmatrix} = \begin{bmatrix} \cos(\xi) & -\sin(\xi) \\ \sin(\xi) & \cos(\xi) \end{bmatrix} \begin{bmatrix} g_c \\ g_e \end{bmatrix} \tag{2.11}$$

where: g_x is the component of centrifuge gravity vector, g, in local horizontal coordinates axis, x, and g_z is the component of centrifuge gravity vector, g, in local vertical coordinates axis, z

Once defined these scalar components can be used to establish the magnitude and orientation of centrifuge gravity within the local coordinate system:

$$g = \sqrt{g_x^2 + g_z^2} \tag{2.12}$$

$$\beta = \arctan\left(\frac{g_x}{g_y}\right) \tag{2.13}$$

where: β is orientation of centrifuge gravity with respect z coordinate axis

With these parameters a complete definition of centrifuge gravity is possible throughout the scale model. This definition is independent of quantities such as centrifuge type or geometry. The only required knowledge is the magnitude and orientation of a single gravity vector within the model and the angular velocity of the centrifuge.

2.3 Centrifuge Mechanics

There are two major types of geotechnical centrifuges: the drum and the beam. The model presented above fits conceptually with both types of centrifuge and the variables β and ξ can easily be related to their mechanics.

2.3.1 Drum Centrifuges

The drum centrifuge is a common device for scale model testing (Madabhushi 2015; Springman et al. 2001; Stewart et al. 1998). They are essentially hollow cylinders spun at high angular velocities with the soil test bed placed around its inner circumference. In most cases they are mounted such that centrifugal acceleration is perpendicular to earth's gravity. If the model coordinate system is aligned with the drum length and radius the angle between the gravity vector, $\tilde{g}_o$, and radius the angle, α, will be equal and opposite to the angle between the gravity vector, $\tilde{g}_o$, and the local coordinate, z, resulting in the angle ξ being zero, Eq. (2.14). This simplifies the gravity throughout the local coordinate system is aligned with frame R, Eq. (2.15) and Eq. (2.16).

$$\xi = 0 \tag{2.14}$$

$$\frac{dr}{dx} = 0 \tag{2.15}$$

$$\frac{dr}{dz} = 1 \tag{2.16}$$

The magnitude and orientation of 2D centrifuge gravity will be:

$$g_{local} = \sqrt{g_c^2 + g_e^2} \tag{2.17}$$

$$|\beta| = |\alpha| = \arctan\left(\frac{g_x}{g_z}\right) \tag{2.18}$$

The above solutions also applicable to a certain beam centrifuges, those with mounting or end plates. Such as the Turner Beam Centrifuge at the University of Cambridge (Schofield 1980). At high-g the basket rests on a vertical mounting plate and the local

coordinate system (x, z) is aligned with the rotational reference frame.

2.3.2 Beam Centrifuges

Beam centrifuges are common and can be found throughout the world (Black et al. 2014; Elgamal et al. 1991; Ellis et al. 2006; Kim et al. 2012; Madabhushi 2015; Phillips et al. 1994). In principal beam centrifuges are designed to align centrifuge gravity, at the nominal radius (distance from the centrifuge axis Y to the mid-depth of the model), with the local vertical coordinates, z, of the centrifuge basket; in practice this is typically not the case due to uncertainties in the location of the model's center of gravity within the basket and moments about the basket hinge. All mechanics that follow a beam type centrifuge with a free-swinging basket,, Fig. 2.3.

The orientation of a free-swinging basket relative to the reference frame R depends on the location of the basket's center of gravity. The basket angle can be determined under a number of assumptions, presented here are Case 1: a single massless rigid member connected to a concentrated mass and Case 2: two massless rigid members, perpendicular to each other, with a concentrated mass at one end. Additionally, the impact of applied moment at the basket hinge for Case 1 will be addressed. Reference to basket angle is limited in the literature; however, Case 1 was used to address moment applied about the basket hinge due to friction (Xuedoon 1988).

In Case 1 the mass, M, of the basket, model, and equipment is represented as a point on the end a rigid tension member with length, L_b, from the basket hinge and an effective radius, R_e, from the centrifuge axis, Y, Fig. 2.4. The orientation of the basket, α_b, can then be determined by a balance of moments from Earth's gravity, g_e, and centrifugal acceleration, g_c, about the basket hinge. The balance of the moments about the basket hinge can be taken as Eqs. (2.19) – (2.21).

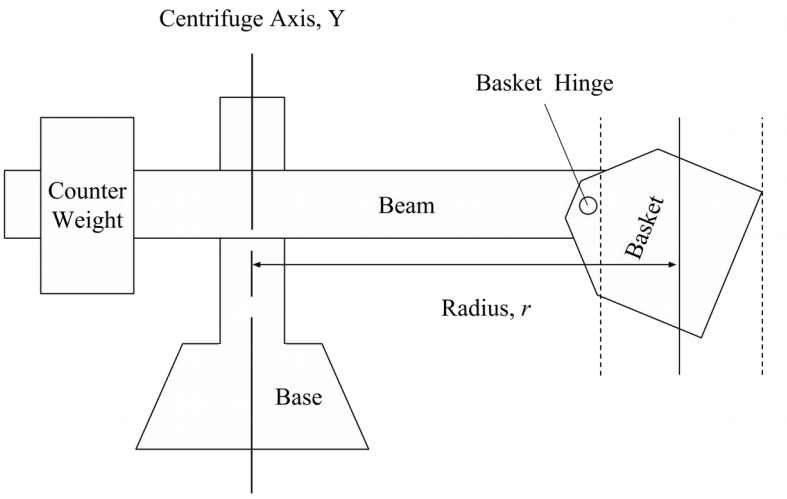

Fig. 2.3. Idealized beam centrifuge with free-swinging basket (reproduced from Fig. 1.4)

$$g_c M \sin(\alpha_b) L_b = g_e M \cos(\alpha_b) L_b \tag{2.19}$$

$$\tan(\alpha_b) = \frac{g_e}{g_c} \tag{2.20}$$

$$\alpha_b = \arctan\left(\frac{g_e}{g_c}\right) \tag{2.21}$$

where: α_b is the angle of the basket, M is the mass of the basket and model, and L_b is the distance between the hinge and the mass

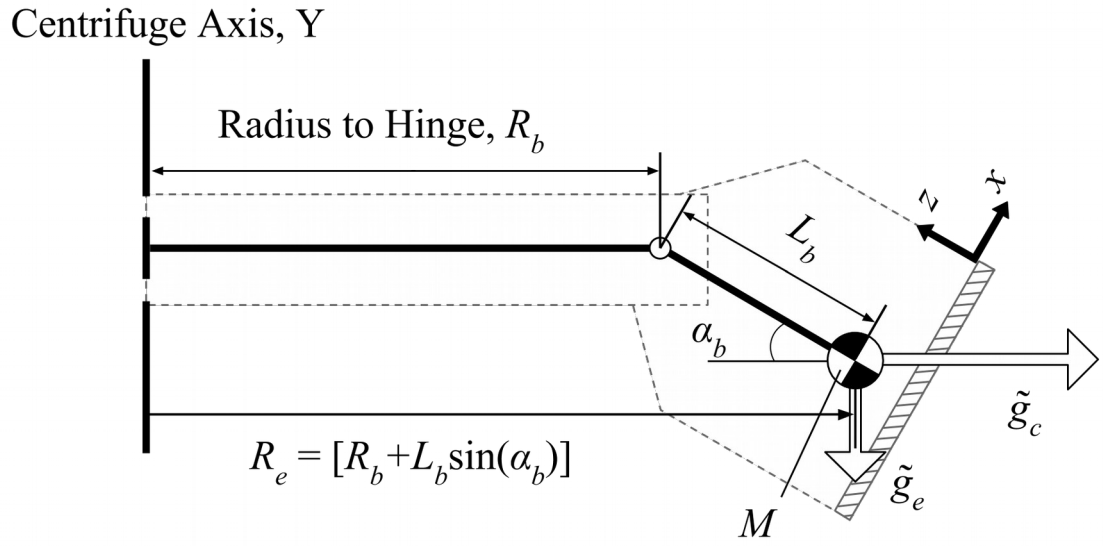

Fig. 2.4. Orientation of centrifuge basket treated as a single rigid member

The above solution is sufficient for the purpose of reconstructing centrifuge gravity from a known centrifugal acceleration, but it is not a complete analytical solution. By solving for centrifugal acceleration, Eq. (2.1), using geometries in Fig. 2.4 it can be seen that iteration on α_b in Eq. (2.22) and Eq. (2.23) is required to predict basket angle, α_b, because centrifugal acceleration, g_c, will be dependent on said angle.

$$g_c = \omega\left(R_b + L_b \sin\left(\alpha_b\right)\right) \tag{2.22}$$

where: R_b is the distance between the centrifuge axis and the basket hinge

For a reference gravity vector, $\tilde{g}_o$, the angle, ξ, between local coordinate system and reference frame R will be equal to α_b, Eq. (2.23), and β, the angle between the gravity

vector, $\tilde{g}_o$, and local vertical coordinate axis, z, will defined by Eq. (2.24). For the special case where the reference gravity vector, $\tilde{g}_o$, is located at the center gravity α will be equal to α_b and thus β will be zero.

$$\xi = \alpha_b \tag{2.23}$$

$$\beta = \alpha - \alpha_b \tag{2.24}$$

As seen in Eq. (2.19) - Eq. (2.21) and as noted by others (Xuedoon 1988) the angle of the basket is independent of basket mass, M; however, Case 1 does not address location of the center of gravity, L_b, within the basket. The distribution of mass along the basket will dictate L_b e.g., a basket containing a tall model will have a shorter L_b than a basket with a compact model. So, it is possible for a centrifuge basket to be oriented at different angles, α_b, while spinning at the same angular velocities, ω, due the distribution of mass, M, in the model. This can be seen in Allmond et al. (2014) where it was demonstrated that actuator movement within the basket changed its angle from vertical in flight.

Developing an analytical form for this case would be difficult and nearly impossible to implement because of uncertainties in the distribution of mass within the basket. Each model will have a different geometry and also requires different configuration of equipment (data acquisition, loading systems, etc.). Instead the impact of the location of centrifuge gravity relative to the local vertical coordinate, z, can be addressed with a quick parametric analysis. This has been done by varying of Eq. (2.21) and Eq. (2.22) for radial distance, presented as percent change in radius, Δr, at various centrifugal accelerations, g_c, in order to simulate the center of gravity moving relative to the local vertical coordinate, z. This result in a change of basket angle, α_b, and therefore change of the angle, ξ, between the local coordinate system and the reference frame R, Fig. 2.5.

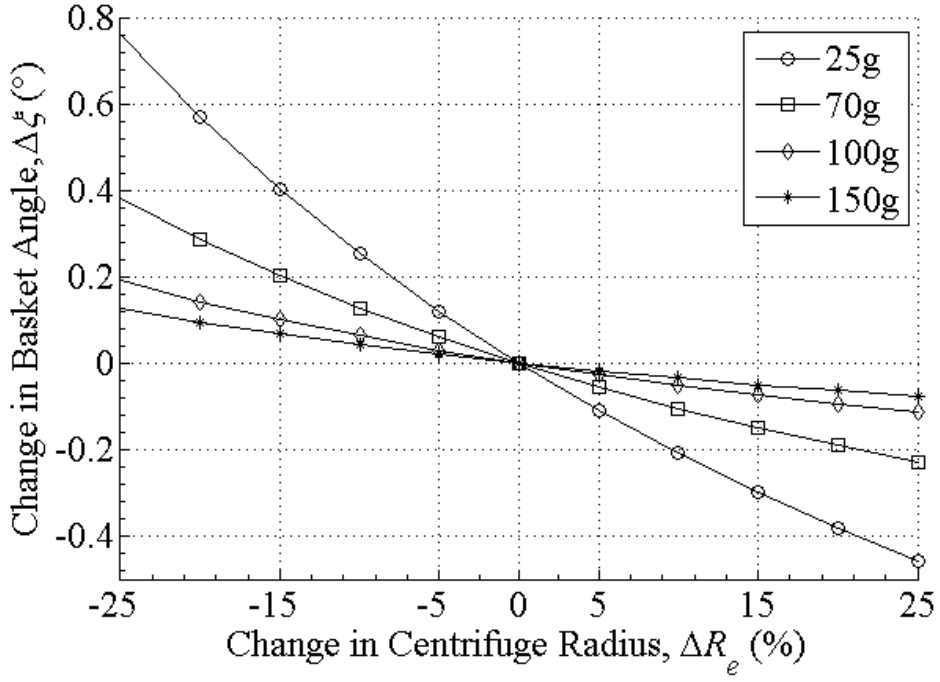

Fig. 2.5. Relative effect of center of gravity on basket angle for varying centrifugal acceleration

By considering the basket as a 2D object its orientation the effect of moving the center of gravity away from the centerline of the basket can be investigated. Assuming the basket consists of rigid massless members perpendicular to each other, with lengths *L* and *d*, connected to a single concentrated mass, M, Fig. 2.6, the projected basket angle, Eq. (2.21), and change in basket angle due to center of mass geometry, Eq. (2.25), can be calculated.

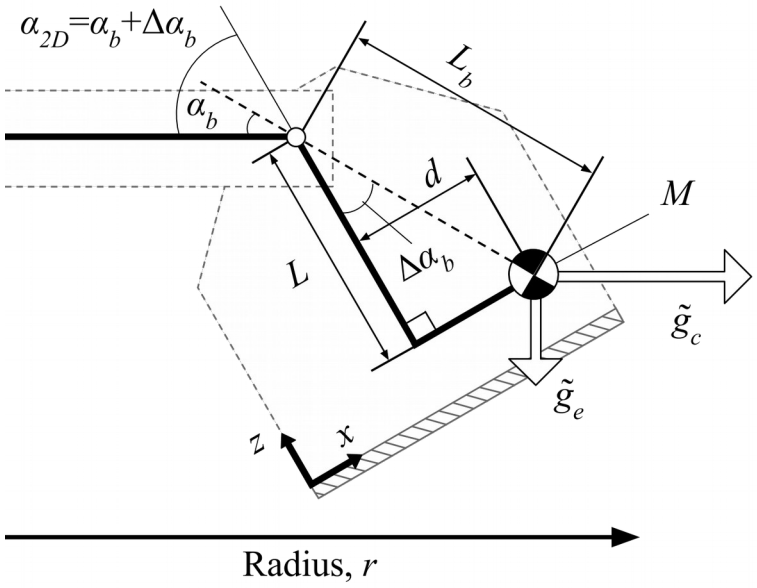

Fig. 2.6. Simplified 2D centrifuge basket (not to scale)

$$\Delta\alpha_b = \arctan\left(\frac{d}{L}\right) \tag{2.25}$$

where: d is the distance between the center of gravity and the center-line of the basket, L is the distance to the center of gravity in the local vertical coordinate axis, z, α_b is the angle from L_b as before, $\Delta\alpha_b$ is the difference in angle between the centerline of the basket and project line L_b

It should be noted that this formulation results in the angle $\Delta\alpha_b$ being independent of centrifugal acceleration. Further the2D basket angle from horizontal can be determined by:

$$\alpha_{2D} = \Delta\alpha_b + \alpha_b \tag{2.26}$$

$$\alpha_{2D} = \arctan\left(\frac{d}{L}\right) + \arctan\left(\frac{g_e}{g_c}\right) \tag{2.27}$$

where: α_{2D} is the angle of the basket form horizontal when the center of gravity is not on center-line of the basket

For a given centrifuge gravity vector, $\tilde{g}_o$, the angle between the local coordinate system and the reference frame R will be equal to α_{2D}, Eq. (2.28). The angle β between the reference gravity vector and the local coordinate system will then be defined by Eq. (2.29).

$$\xi = \alpha_{2D} \tag{2.28}$$

$$\beta = \alpha_b - \alpha + \Delta\alpha_b \tag{2.29}$$

For the special case of the reference gravity vector, $\tilde{g}_o$, being at the basket's center of gravity α_b the angle between the centrifuge gravity vector, $\tilde{g}_o$, and the centrifuge radial axis, r; and β being equal to $\Delta\alpha_b$.

Just as with the 1D model this 2D model does not specify the location of the center of gravity within the basket. The impact of the location of centrifuge gravity relative to the local coordinate system can be addressed by varying lengths of the two rigid members in Eq. (2.25). This results in a change in the 2D basket angle, α_{2D}, and therefore a change in angle ξ, Fig. 2.7.

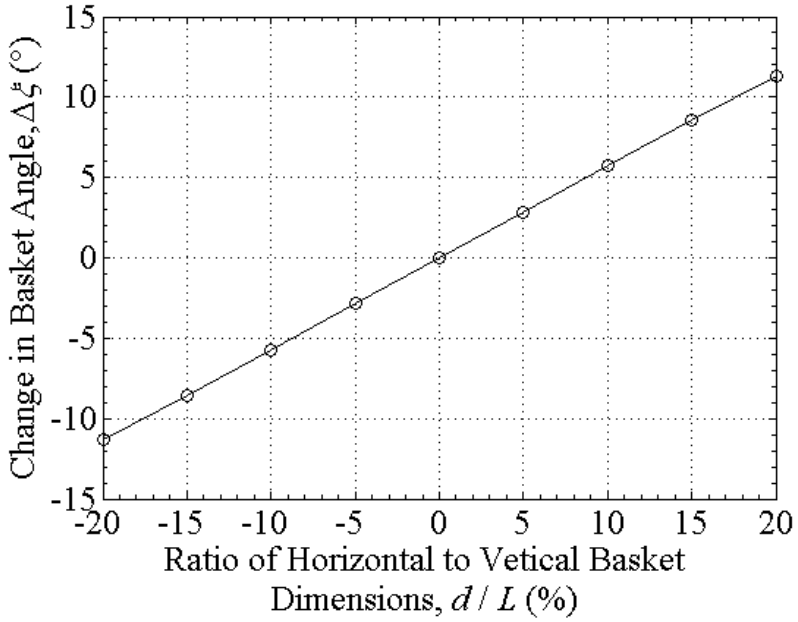

Fig. 2.7. Effect on center of gravity not being aligned with center-line of basket on basket orientation

Basket angle can also be impacted by any applied moment about the basket hinge. Such as that due to friction in the basket hinge and/or resistance from the cabling and/or hosing that transmits various signals, power, and fluids tot he model. A generalized solution for applied moments at the basket hinge has been created and compared to the solution for basket orientation due to friction in the hinge derived by Xuedoon (1988).

A generalized solution for the impact of an applied moment about the basket hinge on its orientation. In this case the centrifuge is assumed to be a single rigid member with a concentrated mass, like Case 1. As in Xuedoon (1988) a change in angle can be derived when comparing two states: no applied moment and an applied moment, Fig. 2.8.

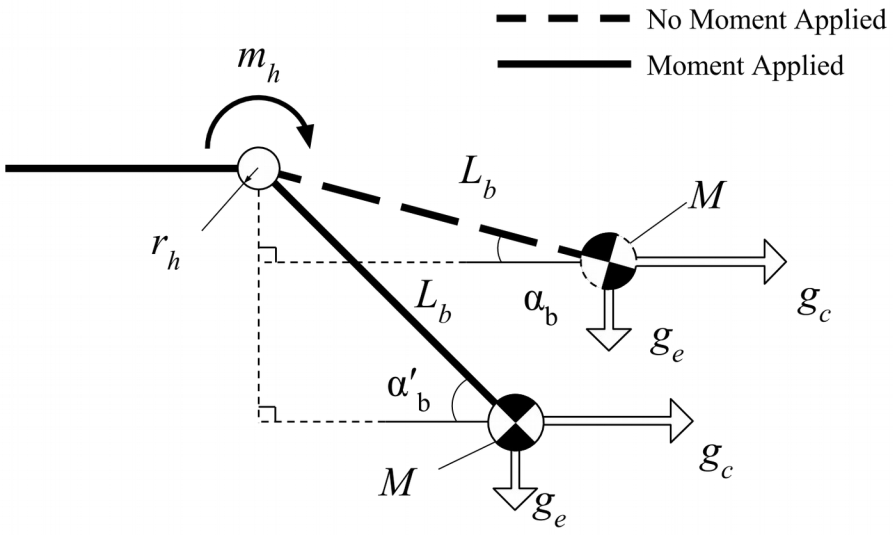

Fig. 2.8. Beam centrifuge with applied moment at basket hinge

The balance the moments between the two state:

$$\sin(\alpha_b) L_b \cdot M \cdot g_c = \sin(\alpha'_b) M \cdot g_c + m_h \tag{2.30}$$

where: α_b is the angle of the basket with no applied moment, α'_b is the angle with an applied moment, m_h is the applied moment about the basket hinge. This can then be simplified using the small angle approximation:

$$\alpha_b \cdot L_b \cdot M \cdot g_c = \alpha'_b \cdot M \cdot g_c + m_h \tag{2.31}$$

This reduces to:

$$\alpha_b - \alpha'_b = \frac{m_h}{L_b \cdot M \cdot g_c} \tag{2.32}$$

$$\Delta\alpha_m = \frac{m_h}{L_b \cdot M \cdot g_c} \tag{2.33}$$

where: $\Delta\alpha_m$ is the difference in angle between the applied moment and the no applied moment state.

For the case where the applied moment is due to friction in the hinge, the induced moment can be defined as in Xuedoon (1988):

$$m_f = r_h \cdot g \cdot f \cdot M \tag{2.34}$$

where: m_f is the moment due to friction in the hinge, r_h is the radius of the hinge, and f is the coefficient of friction in the hinge. With centrifuge gravity being the resultant of centrifugal acceleration, g_c, and Earth's gravity, Eq. (2.1). For large values of centrifugal acceleration it can be assumed equal to centrifuge gravity:

$$m_f = r_h \cdot g_c \cdot f \cdot M \tag{2.35}$$

By setting $m_{h,}$ in Eq. (2.33), equal to moment in the hinge due to friction, Eq. (2.35), the change in angle from moment due to friction will be equal to:

$$\Delta\alpha_{fs} = f \frac{r_h \cdot M \cdot g_c}{L_b \cdot M \cdot g_c} \tag{2.36}$$

$$\Delta\alpha_{fs} = f \frac{r_h}{L_b} \tag{2.37}$$

where: Δa_{fs} is the change in angle from moment induced by friction with small angle assumption.

This solution, Eq. (2.37), can be compared to the Xuedoon (1988) solution for basket

angle with friction in the hinge, Eq. (2.38). The solutions are identical for small basket angles.

$$\Delta\alpha_f = \arcsin\left(f \frac{r_h}{L_b} \right) \tag{2.38}$$

where: $\Delta\alpha_f$ is change in angle, α_b, due to friction in the basket angle by (Xuedoon 1988) and $\Delta\alpha_s$ is change in angle, α_b, due to friction in the basket hinge with the small angle approximation

In terms of the general framework. The angle ξ of the basket relative the to the reference frame R will be equal to the sum of basket angle α_b and change in basket angle, $\Delta\alpha_f$ or $\Delta\alpha_{fs}$, Eq. (2.39). The angle, β, of the reference gravity vector to the local vertical coordinate axis, z, will be Eq. (2.40).

$$\xi = \alpha_b + \Delta\alpha_{fs} \tag{2.39}$$

$$\beta = \alpha_b + \Delta\alpha_{fs} - \alpha \tag{2.40}$$

Variation in tilt of the centrifuge basket can be assessed via a quick parametric study of Eq. (2.37) for the impact of hinge radius and friction coefficient (over typical ball bearing range) and is provided in Fig. 2.9. The range of angles presented should be acceptable for small angle approximation.

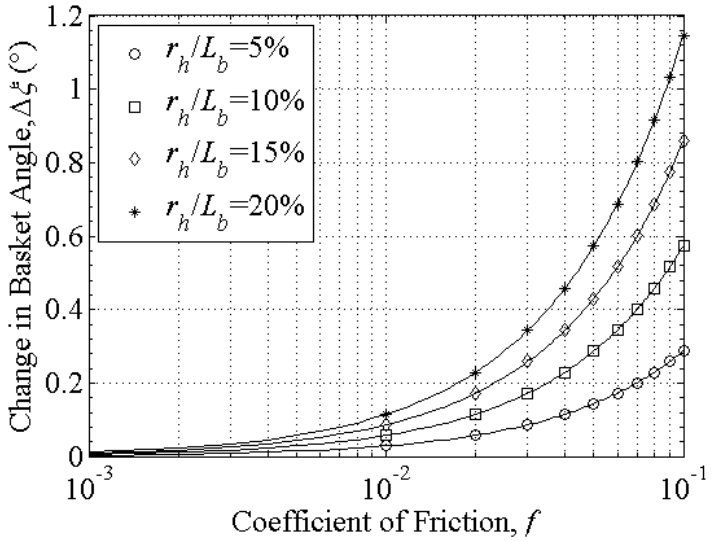

Fig. 2.9. Impact of basket rotation point friction on basket orientation in reference frame

As seen there are multiple source of uncertainty related to the orientation of a beam centrifuge basket; however, they do fit within the proposed methodology for describing 2D centrifuge gravity.

3 USE OF A MEMS ACCELEROMETER TO MEASURE ORIENTATION IN A GEOTECHNICAL CENTRIFUGE

3.1 Acceleration Orientation Theory

3.1.1 Sensor Measurement Geometry

Measurements of orientation by a single-axis MEMS accelerometer are made relative to a resultant acceleration vector, centrifuge gravity. Theoretically, when the sensor is perpendicular to the vector it should read zero g, when it is in line with the vector it should read the magnitude of the vector; however, measurements from a MEMS accelerometer in a centrifuge do not behave this simply. As shown in Fig. 3.1 it is necessary to consider measured quantities of acceleration due to applied centrifuge gravity, $\tilde{g}$, and applied kinematic acceleration, $\tilde{a}_h$, due to the motion of the sensor within the inertial reference frame. These include a_n, the component of centrifuge gravity in the sensor's measurement direction, a_t, the component of $\tilde{a}_h$ in the sensor's measurement direction, a_{cross}, the measured cross-axis due to any acceleration applied perpendicular to the sensor's measurement direction, and a_{temp} measured acceleration due to the sensor's change in temperature. Cross-axis accelerations will have contributions from centrifuge gravity, applied acceleration due to the sensor's motion, and Coriolis acceleration, $\tilde{a}_{cor}$. Coriolis acceleration will be perpendicular to the plane of centrifuge vertical axis and radial axis. It is common for MEMS accelerometers to include estimates of both cross-axis sensitivity and temperature sensitivity in their technical data sheets (MEMSIC n.d.; Silicon Design Inc. 2013). With all of these quantities it is then possible to define single-axis MEMS accelerometer measurements in terms rotation into centrifuge gravity, Eq. (3.2).

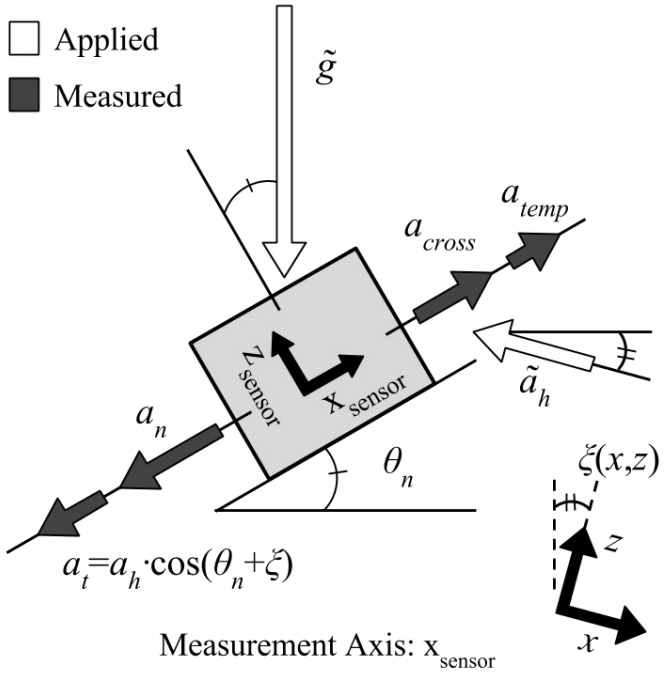

Fig. 3.1. Applied and measured accelerations by a MEMS Accelerometer (not to scale and measurement directions may vary)

$$a_{meas} = a_n + a_t + a_{cross} + a_{temp} \tag{3.2}$$

where: a_{meas} is the total measured value of acceleration by the sensor, a_n is the component of centrifuge gravity in the x_{sensor}-direction, a_t is the component of horizontal acceleration due to the motion of the sensor in the x_{sensor}-direction, a_{cross} is the measured cross-axis acceleration due to the portions of reactive acceleration in the z_{sensor}-direction, and a_{temp} is measured acceleration from temperature change as in Fig. 3.1

Further the components a_n and a_t can be defined in terms of the applied accelerations in the inertial reference frame Eq. (3.3).

$$a_{meas} = g \cdot \sin(\theta_n) + a_h \cos(\theta_n + \xi) + a_{cross} + a_{temp} \tag{3.3}$$

where: g is in the magnitude of centrifuge gravity vector, $\tilde{g}$, θ_n is the angle of sensor orientation relative to centrifuge gravity and a_h is the magnitude of the reactive horizontal acceleration vector, $\tilde{a}_h$, along the local horizontal coordinate axis, *x*.

This is similar to the solution provided in Allmond et al. (2014), but with centrifuge gravity dependent on sensor local coordinates as in Beemer et al. (2015), and temperature effects included. In an update to both previous solutions the cross-axis acceleration is expanded to include contributions from centrifuge gravity, $\tilde{g}$, reactive horizontal acceleration, $\tilde{a}_h$, and Coriolis acceleration, $\tilde{a}_{cor}$.

$$a_{cross} = a_{xg} + a_{xh} + a_{xc} \tag{3.4}$$

where: a_{xg} is the component measured due to centrifuge gravity, $\tilde{g}$, a_{xh} is the component measured due to horizontal acceleration, $\tilde{a}_h$, and a_{xc} is the component due to Coriolis acceleration, $\tilde{a}_{cor}$

The components a_{xg} and a_{xh} are the result of the respective accelerations acting perpendicular to x_{sensor}-$y_{sensor,}$ plane Fig. 3.1, while the Coriolis acceleration, $\tilde{a}_{cor}$. acts perpendicular to the plane x_{sensor}- z_{sensor}. For more on Coriolis acceleration in geotechnical centrifuge see (Randolph et al. 1991; Schofield 1980). As suggested previously in Beemer et al. (2015) cross-axis acceleration can be defined relative to a linear correlation factor and an initial offset:

$$a_{xg} = C_x \cdot g \cdot \cos(\theta_n) + b_x \tag{3.5}$$

$$a_{xh} = C_x \cdot a_h \sin(\theta_n) + b_x \tag{3.6}$$

$$a_{xc} = C_y \cdot a_{cor} + b_y \tag{3.7}$$

where: a_{cor} is the magnitude of Coriolis acceleration, $\tilde{a}_{cor}$, C_x and b_x are the correlation factor and offset, respectively, perpendicular to the x_{sensor}-y_{sensor} and C_y and b_y are the correlation factor and offset, respectively, perpendicular the plane x_{sensor}- z_{sensor}.

Measured acceleration due to variation in sensor temperature will be highly dependent on manufacture and model of MEMS accelerometer. In most cases it will be insignificant (see Discussion); however, since its inclusion does not overly complicate the derivation it will be included.

3.1.2 Quasi-Static Orientation Theory

By assuming a quasi-static condition for a rotating about the model y-axis there will be no relative motion of the sensors resulting in no reactive horizontal acceleration, a_h is equal to zero, and no relative velocity perpendicular to the centrifuge axis to induce Coriolis acceleration, a_c equal to zero. Knowing this, Eq. (3.3) can reduced:

$$a_{meas} = g \cdot \sin(\theta_n) + a_{xg} + a_{temp} \tag{3.8}$$

Sensor orientation relative to centrifuge gravity, $\tilde{g}$ can then be solved for:

$$\theta_n = \arcsin\left(\frac{a_{meas} - a_{xg} - a_{temp}}{g}\right) \tag{3.9}$$

This results in θ_n being dependent on a_{xg} and a_{xg} being dependent on θ_n (Eq. 3.5); so, an

iterative process is required to calculate sensor orientation. This solution is similar to that presented in Beemer et al. (2015) expect it includes measured acceleration from thermal variation, a_{temp}.

3.1.3 Orientation Relative to Basket Local Coordinates

As noted previously the MEMS accelerometer orientation, θ_n, is relative to the centrifuge gravity vector at the location of the sensor. To determine the orientation relative to the local x-coordinate it is necessary to take into account rotation, β, of the local coordinate, (x,z), relative to the gravity vector, $\tilde{g}$. This rotation, β, of the local coordinates, (x,z) could be due to friction or applied moment about the basket hinge and/or movement of the center of gravity off the basket center-line (Beemer et al. 2016). The true orientation of the sensor with respect to the local coordinate system will then be:

$$\theta_t = \theta_n - \beta\left(x, z\right) \tag{3.10}$$

where: θ_t is the orientation relative to the local x-coordinate and β is the angle between the centrifuge gravity vector, $\tilde{g}$, and the local vertical coordinate axis, z, dependent on coordinate location (x,z)

3.2 Validation Testing Program

3.2.1 Accelerometers

The MEMS accelerometer selected to be our representative model the MEMSIC CXL10GP1 single-axis accelerometer (MEMSIC n.d.). with a ± 10 g range, to further be referred to as 10 g Accelerometer. Additionally, a single axis Silicon Design Model 2012 (Silicon Design Inc. 2013) with ± 100g range range of was used to measure applied

acceleration, to further be referred to as 100g Accelerometer. Further technical specifications for the 10g and 100g accelerometers are provided in Table 3.1.

Table 3.1. Accelerometer technical specifications

	10g Accelerometer	100g Accelerometer
Sensitivity (mV/g)	200 ± 5	40
Cross-Axis Sensitivity	± 5 (% of Span)	2 (%) TYP
Noise (mg rms)	35	0.140
Temperature Offset	± 3 g (0º-70º C)	$5x10^{-3}$ g/ºC

3.2.2 Experimental Setup

The experiments were conducted in the 150 g-ton beam type centrifuge at Rensselaer Polytechnic Institute in Troy, NY (Elgamal et al. 1991).

All 10g Accelerometers were mounted to custom test platforms, Fig. 3.2. The platforms were 3D printed in ABS plastic. They were secured to the metal centrifuge floor with small adhesive back rare earth magnets. Additionally, they included markers on the feet to allow visual alignment with the center of the centrifuge basket. Each platform was capable of carrying three 10g Accelerometers; Two parallel to and one four degrees from the basket floor.

A custom Monitoring Platform was also 3D printed to carry the 100g Accelerometer, Fig. 3.3. It was also secured to the metal centrifuge floor with small adhesive back rare earth magnets. The sensor was parallel to the basket floor, at the same height from the basket floor as the 10g Accelerometers, and inline with the plane of reactive centrifugal acceleration and Earth's gravity.

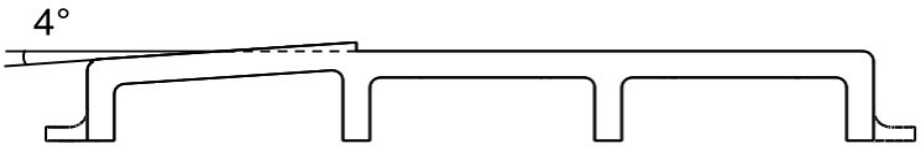

Fig. 3.2. 3D printed MEMS Test Platform for 10g Accelerometers

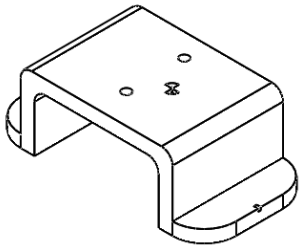

Fig. 3.3. 3D printed MEMS Monitoring Platform for 100g Accelerometer

Three Test Platforms and one Monitoring Platform were mounted in line with center of the centrifuge basket floor. This centered all sensors in the plane of reactive centrifugal acceleration and Earth's gravity and thus on the vertical rotational plane, (*r,* Y). In total, nine 10g Accelerometers (labeled M1-M9) were tested on the centrifuge at once with a single 100g sensor monitoring applied acceleration at the height of the accelerometers. Accelerometer layout is provided in Fig. 3.4 – Fig. 3.5.

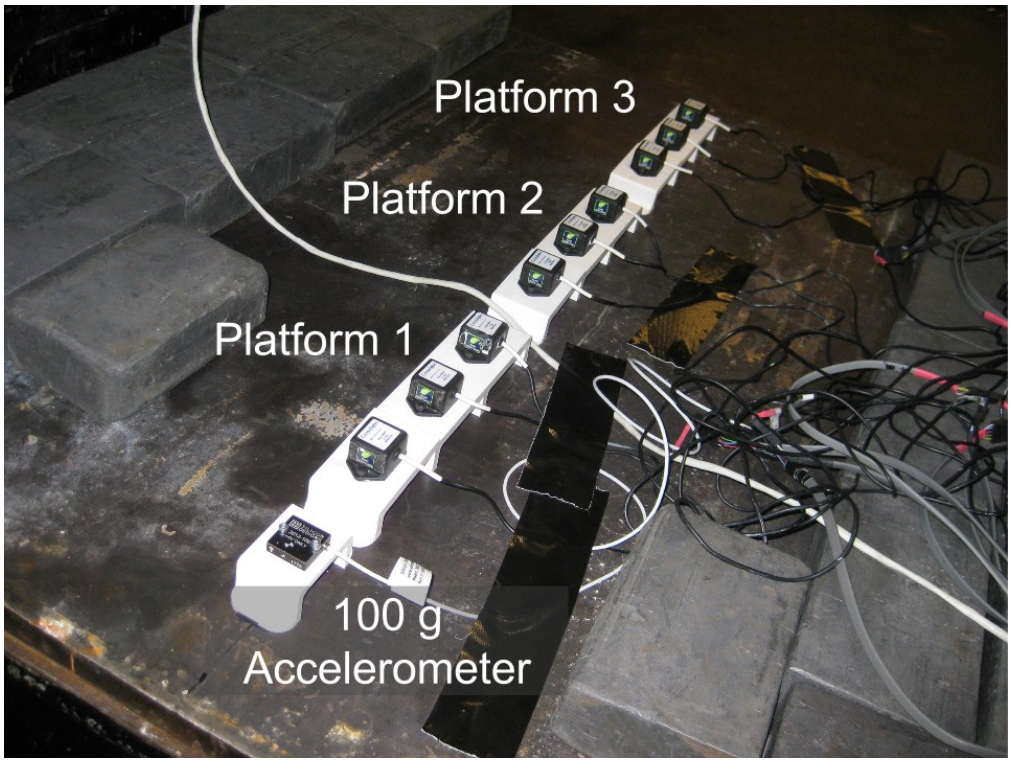

Fig. 3.4. MEMS cross-axis test layout

3.2.3 Experiments

In total, four experiments were conducted. Each involved a single spin of the centrifuge where the gravity, $\tilde{g}$, was held at varying levels to measure its influence on the measured cross-axis acceleration. Target accelerations were selected at regular intervals increasing in frequency at higher g levels. Applied accelerations were measure with the 100g Accelerometer. It was assumed that angle between the centrifuge gravity, $\tilde{g}$, at the sensor and the model local coordinates, β, is sufficiently small that it does not impact measurements of the 100g Accelerometer. The difference between applied and target centrifuge gravity is due to an assumed experiment height set into the centrifuge controls. Since gravity is a function of radius and angular velocity, Eq. (2.1) and Eq. (2.2),a radius must be assumed (or directly measured) in order to select a rotation

velocity, ω. Anecdotally, the assumed radius at the Center for Earthquake Engineering simulations is at the midpoint of the basket. Since the experiments were conducted 2.60 cm from the basket floors, applied accelerations were much higher than target acceleration. Applied acceleration and target accelerations in each experiment are provided in Table 3.2. Between the four experiments the 10g Accelerometers were moved from the zero degree spots on the platform to the four degree. In total each sensor was at four degrees at least once and at zero degrees at least twice, Table 3.3 provides the exact configuration for each experiment.

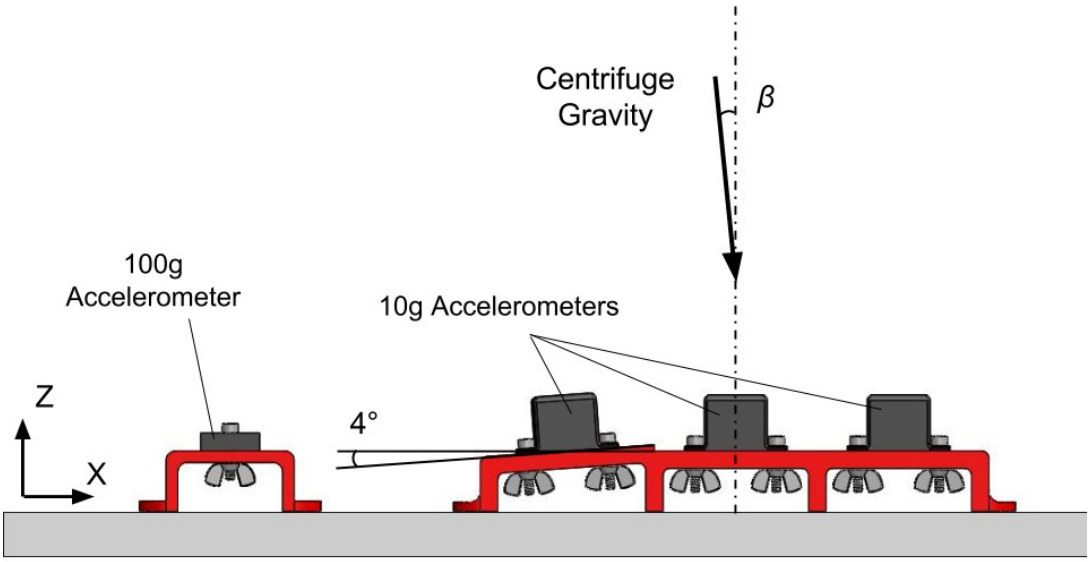

Fig. 3.5. Sketch MEMS cross-axis test layout

Table 3.2. Experiment targeted and applied reactive centrifugal acceleration

Step	Experiment One		Experiment Two		Experiment Three		Experiment Four	
	Reactive Centrifugal Acceleration (g)							
	Target	Applied	Target	Applied	Target	Applied	Target	Applied
1	1	1.00	1	1.00	1	1.04	1	1.06
2	2	2.05	2	2.06	2	2.10	2	2.12
3	10	11.13	20	22.44	10	11.17	10	11.20
4	20	22.46	40	45.09	20	22.50	20	22.52
5	-	-	60	67.77	30	33.82	30	33.85
6	-	-	65	73.46	40	45.16	40	45.18
7	-	-	68	76.87	50	56.5	50	56.52
8	-	-	69	78.01	60	67.85	60	67.87
9	-	-	70	79.16	65	73.54	65	73.56
10	-	-	71	80.29	68	76.95	68	76.98
11	-	-	72	81.44	69	78.09	69	78.11
12	-	-	75	84.86	70	79.24	70	79.26
13	-	-	-	-	71	80.39	71	80.41
14	-	-	-	-	72	81.53	72	81.55
15	-	-	-	-	75	85.94	75	85.96

3.3 Results

3.3.1 Measured Cross-Axis Acceleration

As described earlier, each experiment consisted of a signal spin in which data was collected continuously. Complete experimental data for sensors oriented at zero degrees is provided for Experiment Four in Fig. 3.5. It can be clearly be seen that all sensors react to the cross-axis acceleration, measuring up to 11% of their range in the case of M7. It can also seen that this reaction is not uniform between all sensors and the

magnitude can even be negative, in the case of M8. When measured cross-axis acceleration is plotted vs applied gravity, $\tilde{g}$, a relatively linear relationship can be seen in Experiment Four, Fig. 3.6 – Fig. 3.7, especially at higher gravity.

Table 3.3. Sensor configuration per experiment

Platform	Sensor	Experiment			
		One	Two	Three	Four
		Orientation (degrees)			
One	M1	4	4	0	0
	M3	0	0	4	0
	M5	0	0	0	4
Two	M2	4	4	0	0
	M4	0	0	4	0
	M6	0	0	0	4
Three	M7	4	4	0	0
	M8	0	0	4	0
	M9	0	0	0	4

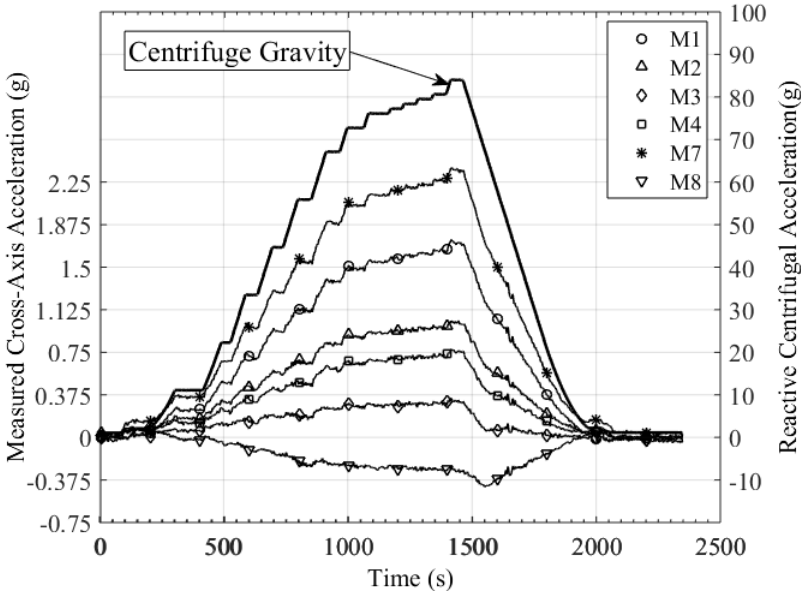

Fig. 3.6. Sensors at zero degree angle in Experiment Four Data

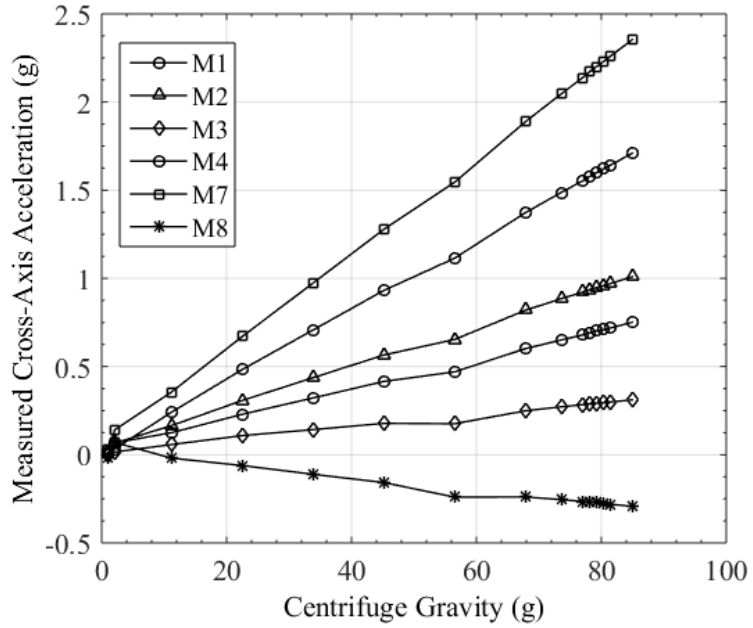

Fig. 3.7. Measured cross-axis acceleration versus centrifuge gravity in Experiment Four

3.3.2 Cross-Axis Acceleration-Centrifuge Gravity Relationship

Measured cross-axis acceleration has been compared for all sensors in Fig. 3.8-3.10; sensors were group by angle during experiments. Experiments One, Three, and Four showed good correlation except in the case of M8. Experiment Two did not correlate well with any other experiment, for all sensors. Given that higher magnitudes of accelerations were measured in Experiment 2 than in the other experiments it is likely that the centrifuge basket tilted relative to Experiments 1, 3, and 4. This would result in a portion of centrifuge gravity, a_t, being measured by the sensors. This can be corrected in the correlation using the measurements when the sensors were held at four degrees. Additionally, at 85 g the measured g drops in Experiment 2. This would result in a portion of centrifuge gravity, $\tilde{g}$, being measured as tangential acceleration, at, by the sensors. Additionally, the drop in measured acceleration, a_{meas}, at 85 g in Experiment 2 is also likely due to basket rotation.

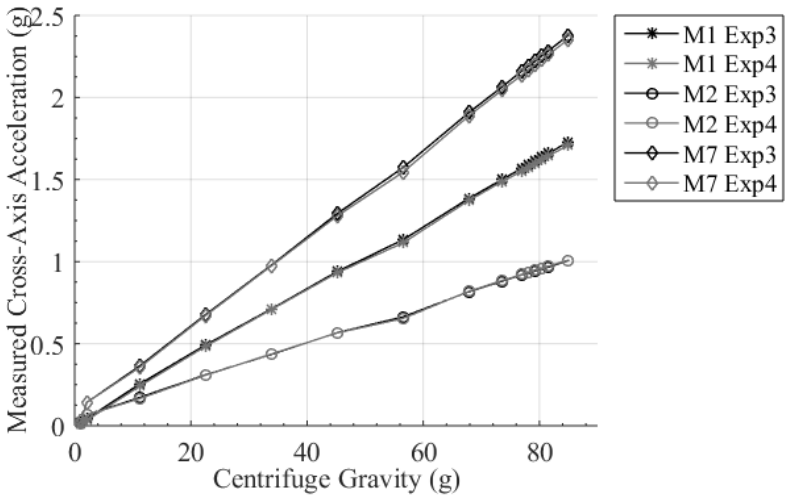

Fig. 3.8. Measured cross-axis acceleration versus centrifuge gravity, M1, M2, and M7

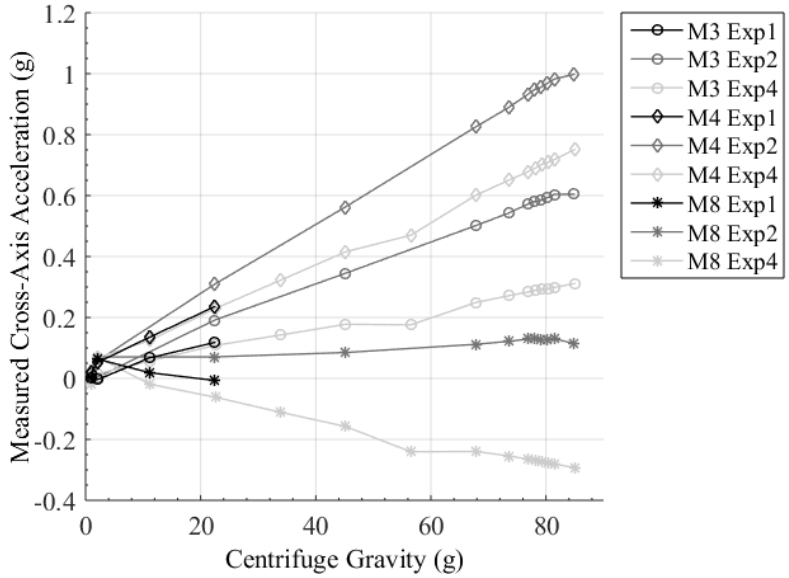

Fig. 3.9. Measured cross-axis acceleration versus centrifuge gravity, M3, M4, and M8

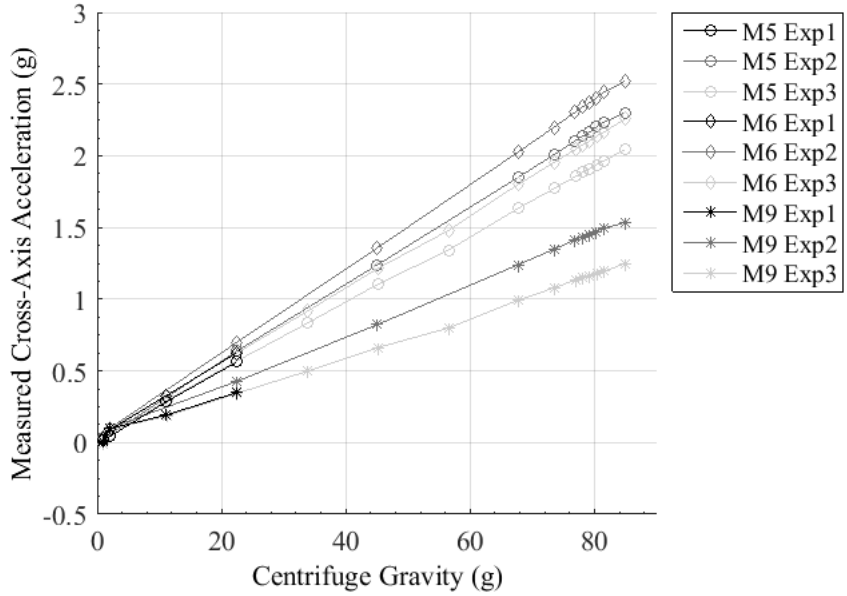

Fig. 3.10. Measured cross-axis acceleration versus centrifuge gravity, M5, M6, and M9

Given the apparent linearity between measure cross-axis acceleration and centrifuge gravity a linear function can be fit to the curves. Curves were fit to data for value 10g and above for Experiments Two, Three, and Four, examples for sensors M1, M2, and M7 in Fig. 3.11. Data below 10g was excluded because of design constraints of the sensors (see Discussion) and concerns of signal to noise ratio. Results for the fitting, Eq. (3.5) with coefficient of determination R^2, of all sensors have been complied in Tables 3.4-3.6. Additionally, results from a targeted high g curve fitting have been included for comparison. The 85.0 g point was excluded from the calibration of Experiment two due to it's apparent nonlinearity. It is likely, that the centrifuge basket rotated slightly at this point, but no definitive answer can be given.

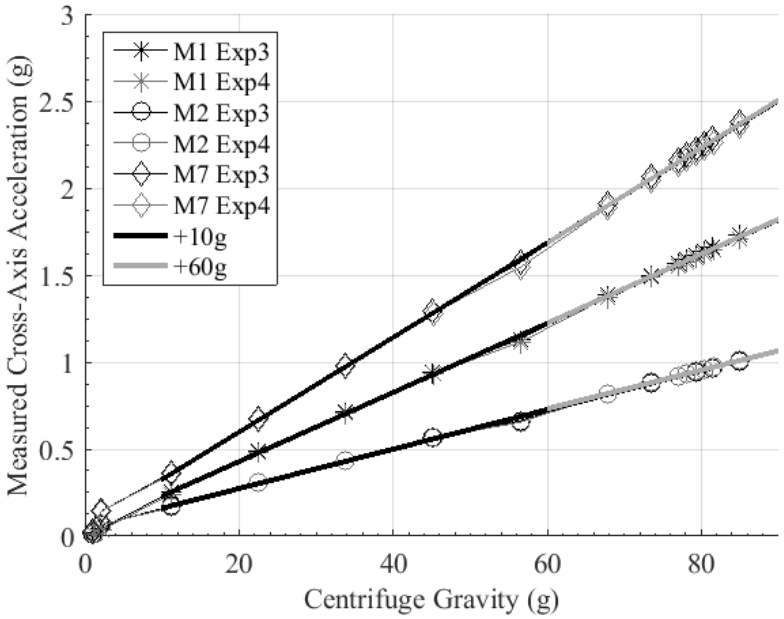

Fig. 3.11. Example of linear curve fitting of M1, M2, and M7

Table 3.4. Linear curve fitting variables from Experiment Two

Sensor	> 20g			> 65g		
	C_x	b_x	R^2	C_x	b_x	R^2
M3	0.0070	0.0320	0.9995	0.0075	-0.0058	0.9963
M4	0.0115	0.0494	0.9999	0.0116	0.0395	0.9984
M5	0.0270	0.0250	0.9999	0.0279	-0.0384	0.9997
M6	0.0295	0.0305	1.0000	0.0302	-0.0184	0.9997
M8	0.0011	0.0424	0.9737	0.0013	0.0250	0.8482
M9	0.0182	0.0121	0.9998	0.0185	-0.0111	0.9991
		Average:	0.9955		Average:	0.9736

Table 3.5. Linear curve fitting variables from Experiment Three

Sensor	> 10g			> 65g		
	C_x	b_x	R^2	C_x	b_x	R^2
M1	0.0199	0.0344	0.9997	0.0201	0.0252	0.9999
M2	0.0113	0.0503	0.9992	0.0110	0.0678	0.9996
M5	0.0237	0.0288	0.9998	0.0239	0.0140	0.9999
M6	0.0262	0.0308	0.9998	0.0265	0.0064	0.9999
M7	0.0273	0.0550	0.9999	0.0275	0.0395	0.9999
M9	0.0145	0.0103	0.9992	0.0147	-0.0042	0.9993
		Average:	0.9996		Average:	0.9998

Table 3.6. Linear curve fitting variables from Experiment Four

Sensor	> 10g			> 65g		
	C_x	b_x	R^2	C_x	b_x	R^2
M1	0.0198	0.0282	0.9995	0.0197	0.0347	0.9999
M2	0.0114	0.0437	0.9986	0.0111	0.0684	0.9997
M3	0.0034	0.0223	0.9817	0.0036	0.0064	0.9965
M4	0.0084	0.0316	0.9971	0.0087	0.0092	0.9993
M7	0.0271	0.0525	0.9997	0.0272	0.0431	0.9999
M8	-0.0036	0.0115	0.9753	-0.0031	-0.0255	0.9910
		Average:	0.9920		Average:	0.9977

It can be seen from the Tables 3.4-3.6 that there is a high variability amongst both the correlation factors C_x and the intercept b_x between all sensors. Results have been divided into Experiment 2 and Experiment 3 and 4 due to the apparent tilt of the centrifuge basket during Experiment 2. In Experiment 2 the mean and standard deviation of correlation factors C_x are 0.0157 and 0.0115 and of intercepts b_x are -0.0015 and 0.0288, respectively (for the high g fitting). It can be seen that results from linear fitting above 10g are better than for 65g-85g, that is the average R^2 is closer to one. In Experiments 3 and 4 the mean and standard deviation of correlation factors C_x are 0.0158 and 0.010 and of intercepts b_x are 0.0237 and 0.0283, respectively (for the high g fitting). It can also be seen that that unlike Experiment 2, linear fitting above 65g is better than for above 10g, that is the average R^2 is closer to one.

The differences between Experiment 2 and Experiments 3 and 4 correlation factors are most likely due to difference in angle, ξ, of the centrifuge basket with respect to centrifuge radial axis, r, and therefore angle, β, of the gravity vector, $\tilde{g}$, with respect to the local vertical coordinate axis, z, between experiments. This can be verified and

corrected for by comparing the cross-axis correlation factors, C_x, because any rotation, β, will result in a change in slope, ΔC_x:

$$\Delta C_x = \frac{\sin(\beta) g_2 - \sin(\beta) g_1}{g_2 - g_1} \tag{3.11}$$

$$\Delta C_x = \sin(\beta) \tag{3.12}$$

where: β is the angle between the gravity vector and the local coordinate vertical, z, g_1 an applied magnitude of centrifuge gravity, and g_2 is a second magnitude of applied centrifuge gravity

The difference between two correlation factors rotated at angles, β_1 and β_2, will then be:

$$C_{x1} = C_x + \Delta C_{x1} \tag{3.13}$$

$$C_{x2} = C_x + \Delta C_{x2} \tag{3.14}$$

$$C_{x2} - C_{x1} = \Delta C_{x2} - \Delta C_{x1} = \sin(\beta_2) - \sin(\beta_1) \tag{3.15}$$

where: β_1 and β_2 is the angle between the gravity, $\tilde{g}$, and the local coordinate vertical, z, and C_{x1} and C_{x2}, are the cross-axis correlation for two spins

With a small angle approximation this can be simplified to:

$$C_{x2} - C_{x1} = \beta_2 - \beta_1 \tag{3.16}$$

The difference in the basket angle between Experiment 2 and Experiments 3 and 4 will be equal to the differences in the cross axis correlation factors, Table 3.7.

Table 3.7. Experiment Two high g cross-axis sensitivity

Sensor	C_x					
	Initial			Corrected		
	Exp 2	Exp 3 and 4	ΔC_x	Exp 2	Exp 3 and 4	Mean
M3	0.0075	0.0036	0.0039	0.0037	0.0036	0.0036
M4	0.0116	0.0087	0.0029	0.0078	0.0087	0.0083
M5	0.0279	0.0239	0.0039	0.0241	0.0239	0.0240
M6	0.0302	0.0265	0.0037	0.0264	0.0265	0.0264
M8	0.0013	-0.0031	0.0044	-0.0025	-0.0031	-0.0028
M9	0.0185	0.0147	0.0038	0.0147	0.0147	0.0147
Mean:			0.0038			

Table 3.7 show that the basket was tilted by a relative angle, $\Delta\beta$, of 0.218 degrees (-0.0038 radians) between Experiments 2 and Experiments 3 and 4. This difference is within the magnitude range, less than 1.0º of possible basket tilt from friction or applied moment about the basket hinge, see Beemer et al. (2016) or Xuedoon (1988). After

correcting the measured signals in Experiment 2 by the normal component, a_n, of centrifuge gravity, $\tilde{g}$, at an angle of 0.218 degrees the cross-axis correlation factors, C_x, between Experiments 2 and Experiments 3 and 4 are nearly identical, Table 3.8.

The final averaged high-g cross-axis correlation factors and intercepts have been compiled in Table 3.8 for use in validating the quasi-static orientation theory. It can also be seen that the correlations show relatively high order of linearity, with M8 being the lowest with an R^2 of 0.9719.

Table 3.8. Averaged high-g correlation factors and intercepts

Sensor	C_x	b_x	R^2
M1	0.0199	0.0299	0.9999
M2	0.0111	0.0681	0.9996
M3	0.0036	0.0003	0.9907
M4	0.0083	0.0244	0.9979
M5	0.0240	-0.0122	0.9998
M6	0.0264	-0.0060	0.9998
M7	0.0274	0.0413	0.9999
M8	-0.0028	-0.0003	0.9719
M9	0.0147	-0.0076	0.9989

3.3.3 Model Validation

As previously noted three 10g accelerometers were held at a four degree angle during each experiment. These sensors serve as a point of comparison for the two analytical models describing MEMS accelerometer orientation when cross-axis acceleration is taken into account and when it is not. The averaged correlation factors and intercepts

over all experiments, Table 3.8, were used to calculate tilt for the updated orientation theory. Results of sensors in Experiment Two: M1, M2, and M7, Experiment Three: M3, M4, and M8, and Experiment Four: M5, M6, and M9 are presented in Table 3.9. In both cases no measured acceleration from thermal effects were considered.

Table 3.9. Cross-axis sensitivity validation, corrected C_x and corrected signal

	Sensor	Cross-Axis	Average Applied Centrifuge Gravity (g)								Mean
			67.86	73.57	76.95	78.10	79.25	80.40	81.54	85.95	
			Measure Angle (º) - Platform = 4º								
Experiment Two	M1		2.57	2.59	2.59	2.59	2.59	2.58	2.59	2.58	2.58
			3.75	3.75	3.749	3.75	3.75	3.75	3.74	3.74	3.75
	M2		3.31	3.32	3.32	3.32	3.32	3.32	3.32	3.32	3.35
			4.03	4.01	4.01	4.00	4.00	4.01	4.00	4.00	4.01
	M7		2.26	2.28	2.28	2.28	2.28	2.29	2.28	2.29	2.28
			3.88	3.88	3.88	3.88	3.88	3.88	3.88	3.88	3.88
Experiment Three	M3		3.57	3.57	3.57	3.58	3.58	3.58	3.58	3.58	3.58
			3.78	3.78	3.78	3.78	3.79	3.78	3.79	3.79	3.780
	M4		3.53	3.53	3.53	3.53	3.53	3.53	3.53	3.53	3.530
			4.02	4.02	4.02	4.02	4.02	4.02	4.02	4.02	4.02
	M8		4.11	4.11	4.12	4.12	4.12	4.12	4.12	4.12	4.12
			3.95	3.95	3.95	3.96	3.96	3.96	3.96	3.96	3.96
Experiment Four	M5		2.33	2.33	2.33	2.33	2.33	2.33	2.33	2.33	2.33
			3.70	3.70	3.70	3.70	3.70	3.70	3.70	3.70	3.70
	M6		2.40	2.40	2.40	2.40	2.40	2.40	2.40	2.40	2.40
			3.91	3.91	3.91	3.91	3.91	3.91	3.91	3.91	3.91
	M9		3.04	3.06	3.06	3.06	3.06	3.07	3.07	3.07	3.06
			3.89	3.89	3.90	3.89	3.89	3.89	3.89	3.90	3.89

The results of the comparison clearly show that the cross-axis sensitivity is not negligible and contributes significantly to the portion of the measured angle. On average the 4º platform is measured as being 3.02º while cross-axis sensitivity is assumed negligible and 3.88º when it is not. Additionally, measurements that are not adjusted for cross-axis sensitivity have a much higher standard deviation than those that include cross-axis sensitivity, 0.66º and 0.11º respectively. The increase variation is due to variability in cross-axis correlation factors (Table 3.8) being incorporated into the angular measurements.

It is tempting to say that the difference between the designed angle of the platform, 4º, and the measured angle of the platform, 3.88º, is the result of the basket tilt, ξ; however, this is actually not the case. It is actually mathematically impossible to measure the angle of centrifuge basket with this experimental setup.

The rotation of the model local coordinate system with respect to centrifuge gravity, β, has no impact on the cross-axis calibration of a one-dimensional sensor if said rotation, β, is the same during calibration and experimentation. For a sensor whose cross-axis calibration is determined in a basket with a local coordinate rotation of, β_1, the cross-axis correlation factor will be altered as in Eq. (3.12). This is assuming the sensor cross-axis intercept, b_x, is zero. The measured acceleration for a sensor at an angle, θ_n, to centrifuge gravity, $\tilde{g}$, in a basket tilted at angle, β_2, will then be Eqs. (3.17)-(3.19), assuming quasi-static conditions and no influence of temperature.

$$a_{meas} = a_n + a_{xg} \tag{3.17}$$

$$a_{meas} = \sin(\theta_n - \beta_2)\cdot g + (C_x + \Delta C_x)\cos(\theta_n - \beta_2)\cdot g \tag{3.18}$$

$$\frac{a_{meas}}{g} = \sin(\theta_n - \beta_2) + (C_x + \Delta C_x)\cos(\theta_n - \beta_2) \tag{3.19}$$

where: a_{meas} is measured acceleration by the single axis MEMS accelerometer, a_n is the component acceleration in the normal direction of the sensor, a_{xg} is the measured acceleration due to the acceleration perpendicular to the sensor x-direction, β_2 is rotation of the local coordinates relative to centrifuge gravity, $\tilde{g}$, during a measurement, C_x is the cross-axis correlation factor of the MEMS accelerometer, ΔC_x is the change in the cross-axis correlation factor due to a rotation of the local coordinates relative to centrifuge gravity, β_1, and g is centrifuge gravity at the sensor location

Then substituting for change in the calibration factor, ΔC_x:

$$\frac{a_{meas}}{g} = \sin(\theta_n - \beta_2) + (C_x + \sin(\beta_1))\cos(\theta_n - \beta_2) \tag{3.20}$$

where: β_1 is rotation of the local coordinates relative to centrifuge gravity during cross-axis calibration

If a small angle assumption is taken, with cosine of small angle equal to one, then this can be simplified to:

$$\frac{a_{meas}}{g} = \theta_n - \beta_2 + C_x + \beta_1 \tag{3.21}$$

If rotation of the local coordinate system with respect to centrifuge gravity is the same

during the sensors calibration, β_1, and when a measurement is made by the sensor, β_2, any rotation of the local coordinate system will cancel out:

$$\frac{a_{meas}}{g} = \theta_n - \beta_1 + C_x + \beta_1 \tag{3.22}$$

$$\frac{a_{meas}}{g} = \theta_n + C_x \tag{3.23}$$

This can be compared to the measured rotation of the sensor with no local coordinate rotation, assuming the cross-axis intercept, b_x, is zero:

$$a_{meas} = \sin(\theta_n) \cdot g + C_x \cos(\theta_n) \cdot g \tag{3.24}$$

$$\frac{a_{meas}}{g} = \sin(\theta_n) + C_x \cos(\theta_n) \tag{3.25}$$

If a small angle assumption is taken, with cosine of small angle equal to one, then Eq. (3.25) can be simplified:

$$\frac{a_{meas}}{g} = \theta_n + C_x \tag{3.26}$$

Comparing Eqs. (3.23) and (3.26) demonstrates that at small angles any rotation of the local model coordinates relative to centrifuge gravity, $\tilde{g}$, will not impact measurements of rotation θ_n.

As demonstrated above if a measurement of angle is taken at the same basket orientation, ξ, at which the sensor was calibrated then the basket tilt cancels out. Which means the measured angle will be accurate, but the true cross-axis correlation factor and the true angle of centrifuge gravity with respect to the local vertical coordinate axis, β, will be unknown.

The measured angle, θ_n, varied between each experiment, even though all platforms were suppose to be identical. The average measured tilt and standard deviation were 3.88º and 0.13º, respectively, in Experiment 2, 3.92º and 0.12º, respectively, in Experiment 3, and 3.83º and 0.12º, respectively, in Experiment 4. These standard deviations are nearly three times larger than those for each Test Platform. In the experiments M3 an M5 were on Platform One, M5 and M6, were on Platform Two, and M8 and M9 were on Platform Three. Platform One had a mean and standard deviation of 3.74º and 0.04º respectively, Platform Two was 3.98º and 0.06º respectively, and measured Platform Three was 3.93º and 0.044º respectively.

3.4 Discussion

3.4.1 Sensor Accuracy

Accuracy of orientation measurements with MEMS accelerometers is dependent on, the data acquisition, DAQ, sensor accuracy, sensor orientation, and magnitude of centrifuge gravity, $\tilde{g}$. In general any sensor will only be as accurate as the measurement capabilities of the DAQ sampling it. This has been specifically discussed for MEMS accelerometers by O'Loughlin et al. (2014). Each type of MEMS accelerometer will have an intrinsic measurement accuracy dependent on output noise and output offset. Sensor angular accuracy will be highly impacted by the initial orientation of the accelerometer. If the sensor's measurement direction is initially in-line with centrifuge gravity a low accuracy sensor with a high-g range will be required, but if the sensor is initially aligned perpendicular to centrifuge gravity a high accuracy sensor with a low-g range may be used. Additionally, the sinusoidal functions relating centrifuge gravity to

orientation are more variable when rotating into centrifuge gravity than away from it. That is, the sine of a small angle is more variable than cosine of small angles. The accuracy of orientation measurements is also highly dependent on centrifuge gravity as seen in Eq. (9). Measurements of tilt from a MEMS accelerometer will increase in the accuracy for increasing magnitudes of model centrifuge gravity, but sensor range decreases for increasing magnitude of centrifuge gravity. For example, if the 10g Accelerometer accuracy is take as three time the noise, Table 3.1**,** then its accuracy would be 0.24º at 25g and 0.080º at 75g while its range would be approximately 23.58º and 7.66º, respectively.

3.4.2 Influence of Temperature on Sensor

As reported in the 3.1 Accelerometer Orientation Theory section and Table 3.1 environmental temperature can influence the reading of MEMS accelerometers. Though this effect should be considered on a case by case basis, in general, it should effects should be minimal. This is because major beam centrifuges are ventilated to prevent excessive temperatures (Black et al. 2014; Elgamal et al. 1991; Ellis et al. 2006; Madabhushi 2015; Randolph et al. 1991; Schofield 1980). Given this knowledge the highest expected temperature variation would occur by taking the sensor from room temperature (25º C) to a centrifuge ventilated with outside air in Perth, Western Australia or Davis, California during record highs of ~46.5 ºC, or a 21.5º C differential. Given the 10g Accelerometer in Table 3.1 this would correspond to measured accelerations of 0.18 g (1.8% of the its range) or a measured angle of approximately 0.1º at 70 g. In this extreme case it would be reasonable to include the effect of temperature. Frigid temperatures should also be considered and can result in very large temperature differentials, but this condition will be rarer (Barrette et al. 1999).

3.4.3 Low g Behavior of MEMS Accelerometers

The behavior of MEMS accelerometers at low g is very nonlinear. This is actually expected given single-axis MEMS accelerometers are designed to be used in Earth's

gravity. A user would expect a MEMS accelerometer to behave in the same manner if the sensor was parallel or perpendicular to Earths gravity. For this to occur measured cross-axis acceleration must be zero at 0 g and zero at 1 g. This could be done by post processing filtering in the chip and it is reasonable to assume it could affect cross-axis measurements between 1 and 4 g as seen in Fig. 3.6.

3.4.4 Experimental Validation of Model

Results from the validation show that the proposed model can be used to measure orientation in the centrifuge environment and that the inclusion of cross-axis sensitivity significantly improves measurement of orientation. However, there were some considerations that should be noted. The difference between measured and designed angle of the four degree shelf was 0.12º in Experiment Two, 0.08º in Experiment Three, and 0.17º in Experiment Four. It is believed that this is the result of construction tolerances in the 3D printing processes of Test Platforms and their deformation in under high-g.

As noted standard deviations over the three platforms were nearly one third of that over the three experiments, indicating measurements were dependent on the platform which the sensors were mounted to. The largest difference between the 4º shelves of any two Test Platforms, was 0.263º (M1 and M2 in Experiment Two). The tolerance in 3D printing processes of the platforms was ±0.127 (Stratasya 2015). Given this, the maximum possible error between the two legs holding the sensor at 4º would be 0.254 mm and the maximum angular error would be 0.21º and would account for the majority of error in the measurements seen between the platforms.

A likely source for the additional variation between experimental platforms and experiments is deformation of the platforms under high g. The 4º section of the calibration platform was created by making one of the platform's leg longer than the other, Fig. 3.2. Under stress from self-weight in high g it would be expected that the long leg would undergo more deformation that a short leg. This would result in a reduction in

the angle of the 4º shelf on the platform. The results from the experimental validation match this behavior. Additionally, it should be noted that the platforms were only secured to the centrifuge baskets with magnets. Therefore it is likely that as the platform deformed its outside leg would translated along the basket floor. This would engage a friction force that would vary every spin. Resulting in a possible source of variation in measured angle of the 4º shelf between experiments.

As previously noted it is not possible to measure the absolute orientation of a centrifuge basket unless the MEMS accelerometers cross-axis correlation was determined in a tilted basket. Therefore, it is also not possible to reconstruct centrifuge gravity throughout the model local coordinates as outlined in Beemer et al. (2016). Though orientation of centrifuge gravity with respect to model local coordinates is unknown in the three experiments, some comments can be made. Variation in centrifuge gravity throughout the model local coordinates is caused by the model's local horizontal coordinate not being parallel to the centrifuge axis. This will result in one side of the centrifuge basket having a larger magnitude of centrifuge gravity than the other. If this variation was significant, one would expect variation in measured tilt across the length of the basket due to the fact that only a single 100 g MEMS accelerometer, located at the bottom of the basket (closest to the origin in Fig. 1), was used to measure applied acceleration. In the experiments Platform One: M1, M3, and M5 was located at the bottom of the basket, Platform Two: M2, M4, and M6 was located in the center of the basket, and Platform Three: M7, M8, and M9 was located at the top of the basket, Fig. 3.4. If the basket was significantly tilted it would expected to see a gradient in measured tilt across the platforms. Instead, the validation results show that the largest measured tilts were with sensors on the center platform, Platform Two, indicating that variation in platform construction resulted in larger variation in measured orientation than the tilt of the centrifuge basket.

3.4.5 Method for Application of Single-Axis MEMS Accelerometers in a Centrifuge

The following provides recommendations for utilizing MEMS accelerometers to measure orientation of an object on the vertical rotational plane, *R*, of centrifuge axis, Y, and centrifuge radial axis, *r*, in a geotechnical centrifuge.

4.4.5.1 Required Information

1. Measurement of acceleration, a_{meas}, from a single-axis MEMS accelerometer (M_{meas}) at an angle, θ_t, from the model local coordinates (x,z).
2. Orientation, β, of the centrifuge gravity vector, $\tilde{g}$, with respect to the local coordinate system (x,z)
3. Magnitude of the centrifuge gravity vector at the sensor, g
4. Measured acceleration due to temperature effects, a_{temp}, if significant.
5. Cross-axis correlation factor, C_x, and intercept, b_x, of the MEMS accelerometer

4.6.5.2 Procedure

1. A measurement of acceleration is made by a single-axis low g MEMS accelerometer, M_{meas}, that is at an angle, θ_t, to the local coordinate, system at a point (x_{meas},z_{meas})
2. Magnitude of centrifuge gravity, $g(x_{meas},z_{meas})$, can be be measured by a high g MEMS accelerometer (M_{high}) parallel to centrifuge gravity at the same radius as $M_{meas.}$ M_{high} must have an acceleration range larger than the target magnitude of centrifuge gravity
3. Orientation, $\beta(x_{meas},z_{meas})$, of centrifuge gravity, $\tilde{g}$ (x_{meas},z_{meas}), relative to the local coordinate system (x,z) can be measured using a low g MEMS accelerometer (M_a) at a known angle, θ_a, to the local x-coordinate and at the same radius as M_{high}. A measurement of orientation, θ_{test}, can be made by following steps 4 and 5 in this procedure. The difference between between the known angle, θ_a, and the

measured angle, θ_{test}, will be equal to $\beta(x_{meas},z_{meas})$. M_a must have a large enough range to measure the sum of the angle, θ_a, and angle of centrifuge gravity with respect to the local coordinate system, $\beta(x_{meas},z_{meas})$.

4. The cross-axis correlation factor, C_x, and intercept, b_x, of M_{meas} must be calibrated for over a range encompassing the target centrifuge gravity, $g(x_{meas},z_{meas})$. As demonstrated above cross-axis calibration of a single-axis MEMS accelerometer, M_{meas} or M_a, must be done with the sensor either perpendicular to centrifuge gravity or at a known angle to centrifuge gravity

5. With $g(x_{meas},z_{meas})$, C_x, and b_x orientation, θ_n, can then be determined by iterating Eq. (3.5) and (3.9). And finally, orientation relative to the local model coordinates can be calculated by subtracting, $\beta(x_{meas},z_{meas})$, Eq. (3.10)

Simplifications:

1. It is possible to measure the magnitude and orientation of centrifuge gravity, $g(x,z)$ at any point within model local coordinates, such as the basket floor, and then reconstruct the acceleration field throughout the basket. However, doing so as close to M_{meas} will reduce potential errors

2. Though it is desirable to keep M_{high} parallel to centrifuge gravity, $g(x,z)$, it may not be necessary for small angle of local coordinate rotation, $\beta(x,z)$, if cosine of the angle, β, can be assumed equal to one

   For example: if rotation of the local coordinate frame, $\beta(x,z)$, is 4º a high g accelerometer would measure 74.81g instead of an applied 75g

3. In case of small rotations of the local coordinate frame, $\beta(x,z)$, variation in of centrifuge gravity along the local x-coordinate will be small and could be excluded. In this case the magnitude and orientation of centrifuge gravity would only be dependent of the local z-coordinate; such that they are: $\beta(z)$, and $g(z)$.

4 DESIGN OF 1-G AND CENTRIFUGE EXPERIMENTS

4.1 Design of 1-g Experiments

This chapter covers the design of the 1-g experiments conducted on squat caissons, length to diameter ratio of two. In total four experiments rotational monotonic failure tests were conducted. Between each test venting or sealing of the caissons and load eccentricity was varied.

4.1.1 Cartesian Robot for Automated Marine Engineering

The Cartesian Automated Robot for Marine Engineering or CARMEn will be used to test the model foundations, Fig. 4.1. It is constructed from two cross mounted 100 Series Lintech carriages and SM23375DT Animatics Smart Motors. It has vertical and horizontal ranges of 150 mm and 300 mm. The 0.6 Newton-meter motors result in vertical and horizontal capacities of 445 N (100 lb) under continuous loading. The carriages contain five mm lead (distance per revolution) ball screws that when combined with the 4,000 count (steps/revolution) motors result in a theoretical minimum step of 1.25 microns. CARMEn's maximum velocity is limited to 3 m/s by the carriage. This information is collected in Table 4.1.

Table 4.1. CARMEn properties

Property	X-Axis	Y-Axis
Travel (mm)	300	1500
Capacity (N)	445	445
Minimum Step (μm)	1.25	1.25
Maximum Velocity (cm/s)	300	300

CARMEn is supported by a metal frame with a built in floor and moveable shelf. The horizontal actuator is affixed directly to the shelf. The shelf can move vertically along two guide bars and a ball screw. By rotating the ball screw the height can be set anywhere between 60 cm and 180 cm off the ground. The built in floor allows soil bed's self weight to stabilize the entire system.

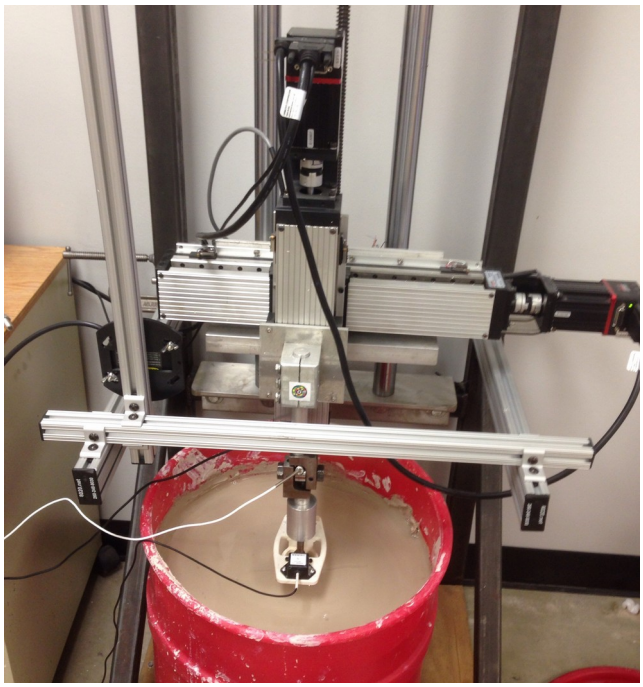

Fig. 4.1. CARMEn robot in the Texas A&M University 1-g laboratory

The robot is operated through a custom control suite. The program was developed in MATLAB using a Windows COM Object include by electric motor manufacturer. The control software (CARMEn_GUI) allows the user to control the robot via script program files or a graphical user interface (GUI) front end, Fig. 4.2. From the front end the user can enter the Cartesian coordinates of a designated location or guide the robot with the

direction pad at a preset velocity or step size. CARMEn_GUI has also been fully integrated with our custom data acquisition (DAQ) software, Basic_DAQ, Fig. 4.3. Basic_DAQ can be called from the front end then used to setup any number of channels, on the National Instruments Compact DAQ system, for data collection. When the robot is set into motion the DAQ is immediately started and CARMEn is placed on a three second delay. This delay ensures the entire experiment is recorded and allows for the data to be easily synced with the robot's motion.

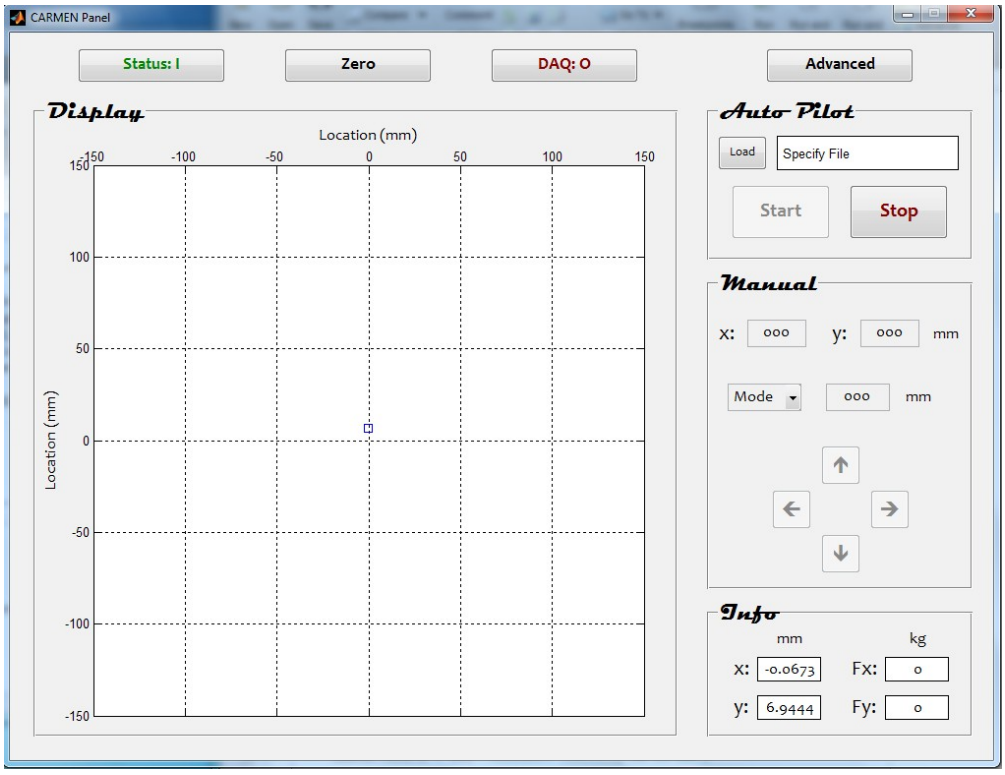

Fig. 4.2. CARMEN_GUI front end

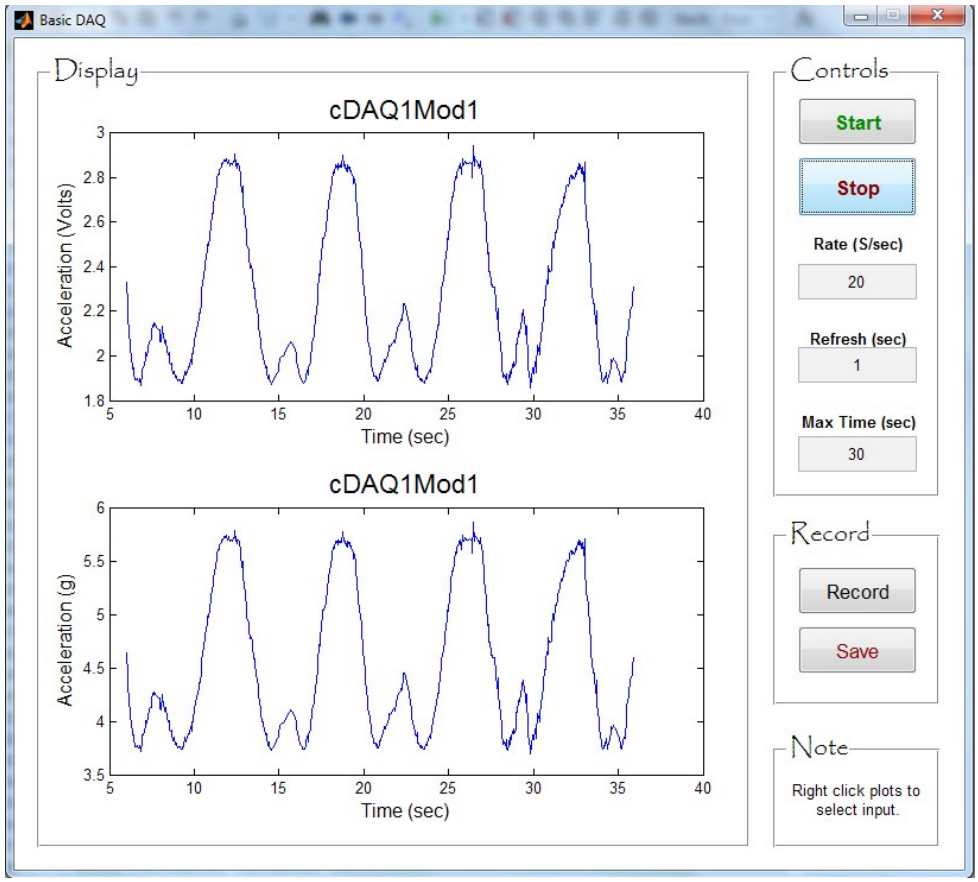

Fig. 4.3. BASIC_DAQ software with example accelerometer data

4.1.2 Sensors

Four transducers were used in the test a vertical load cells, a horizontal load cell, a MEMS Tilt sensor, and a Laser Displacement transducer. Transducer properties are provided in Table 4.2.

Table 4.2. Transducer calibration factors

Name	Sensor	Model	Serial Number	Calibration Factor	Zero Offset	Range
BL02 TAMU	Laser	Banner LG5	NA	0.063 in/V	NA	±5 mm
MT	MEMS Tilt	MEMSIC CXTLA01	1109340159	9.92 (º)/V	2.5219 V	±20°
Vertical	Force	Interface SML	345835	2.08 mV/V	0 mV/V	890 N
Horizontal	Force	Interface WMC-250	350635	1.98 mV/V	0 mV/V	1,112.05 N

4.1.3 Soil Test Bed

The test was conducted in a 57 liter (15 gallon) plastic barrel with a 20.3 cm (8 in) radius. The test bed was constructed from a filler layer of US Silica F-Series sand topped with a layer of EPK kaolinite clay, Fig. 4.4. The sand layer was 22.7 cm deep while the clay layer was 20 cm. This results in a 10 cm clearance to the top of the barrel of which approximately 2.5 cm was filled with water. The clay soil was partially reused between experiments to decrease model construction time. Clay immediate around the caisson and T-bar location was disposed of. The rest of the clay was remixed with new clay mixed at a target water content of 60%. All clay placed by hand.

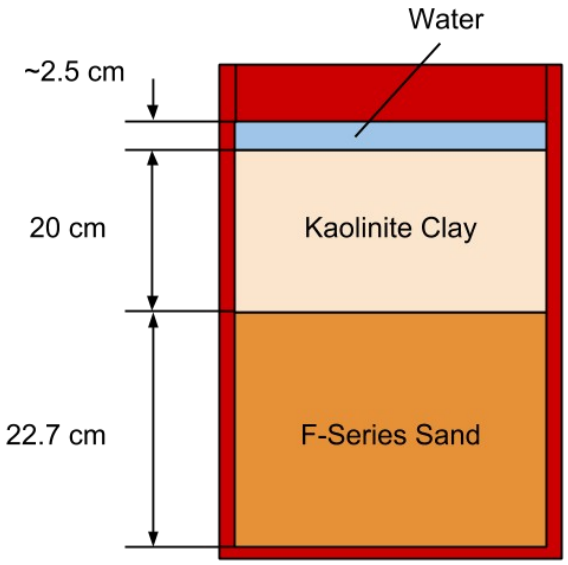

Fig. 4.4. Sketch of soil test bed

A single T-Bar test to a depth of 13 cm with a velocity and acceleration of 2 mm/s and 48.82 mm/s^2 respectively were conducted after each experiment. The T-bar test location varied but were always located, approximately half-way between the pile and the barrel wall. The T-Bar diameter was 1.27 cm (0.5 in) and length was 5.08 cm (2 in). With a velocity of 2 mm/s and diameter of 1.27 mm the T-bar had a normalized velocity ($V = vd/c_v$) of 160, well above the minimum for undrained conditions of 20 (Dejong et al. 2012). The shaft intentionally has a much smaller diameter, 0.953 cm (3/8 in), than the T to prevent the shaft from contacting the soil; however, some clay did adhere to the t-bar test during testing. This indicates that a small amount of shaft resistance was incorporated into the undrained strength measurements. A T-Bar factor of 10.5 was used. Free surface corrections were not applied therefore only results a few diameters below the surface may be accurate. Example of the T-bar testing is provided in Fig. 4.5. Results from all T-bar tests on all four test beds is provided in Fig. 4.6a-4.7b.

Fig. 4.5. Examples of T-bar experiment during 1-g experiments

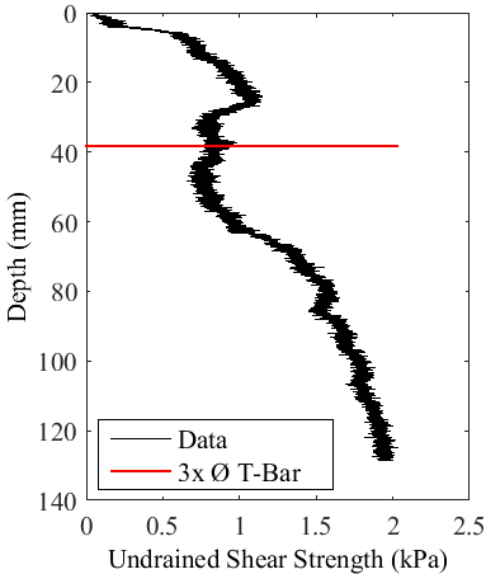

Fig. 4.6a. Test 1 T-bar result

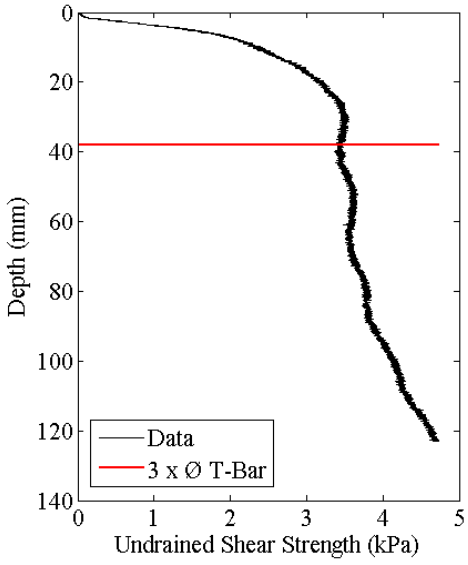

Fig. 4.6b. Test 2 T-bar result

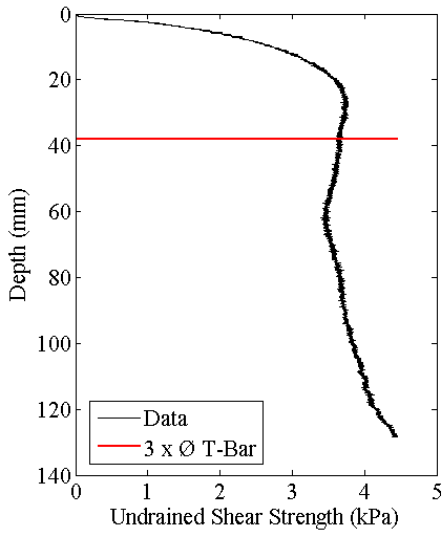

Fig. 4.7a. Test 3 T-bar result

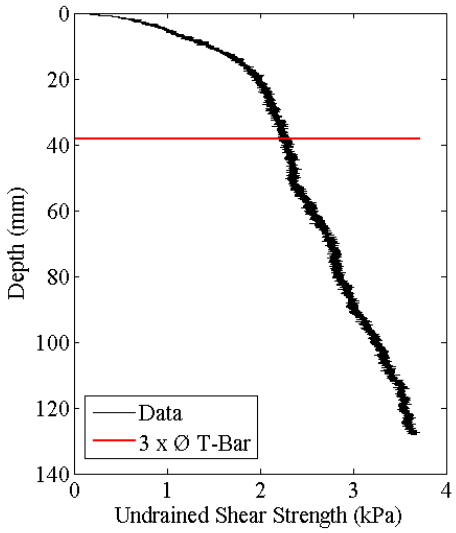

Fig. 4.7b. Test 4 T-bar result

Water contents were taken after each experiment along the depth of the soil test bed. The results for all four tests are summarized in Table 4.3.

Table 4.3. Water content results for 1-g Experiments

Depth (cm)	Test				
	1	2	3	4	
	Water Content (%)			Depth (cm)	Water Content (%)
2	69.3	61.33	61.97	10	62.88
6	67.5	62.76	61.41	12	63.10
13	67.6	62.14	60.83	14	64.21
20	66.9	56.23	58.39	15.24	63.77
				16	63.05
Average	67.8	60.62	60.65	--	63.05

4.1.4 Pile Properties

Two different piles were tested. Pile 1 had a stem which allowed for eccentric loading at 0.9 diameters and Pile allowed for a load eccentricity of 1.2 diameters. A single pile was tested in each experiment they were constructed from three parts the stem, the caisson, and the MEMS platform. The stems were constructed from aluminum and had diameter of 0.953 cm and was topped with a 2.54 cm ball to create a moment-less connection with the robot. The caisson was constructed from aluminum tubing that was turned down on a lathe to reduce wall thickness welded to a 1.27 cm thick pile cap. All caisson properties can be found in Table 4.4. The cap had a vent drilled into the top to allow easy installation. The caisson was coated in a layer of spray on rubber to mimic the pile soil interface/adhesion in the centrifuge tests. The stem was secured to the caisson by threading it through the MEMS platform and fastening it with a nut and a washer. Sketch of Pile 1 and Pile 2 are provided in Fig. 4.8a – 4.8b.

Table 4.4. Caisson properties

Outer Diameter (cm)	4.96 (1.952 in)
Total Length (cm)	11.43 (4.5 in)
Pile Installation Depth (cm)	10.16 cm (4 in)
Thickness (cm)	0.609 mm (0.024 in)
Young's Modulus (cm)	69 GPa

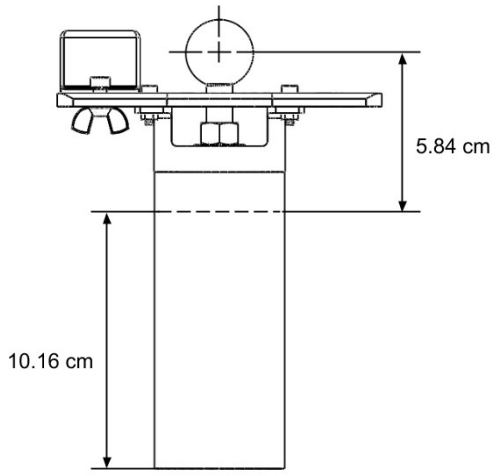

Fig. 4.8a. Pile 1 sketch (not to scale)

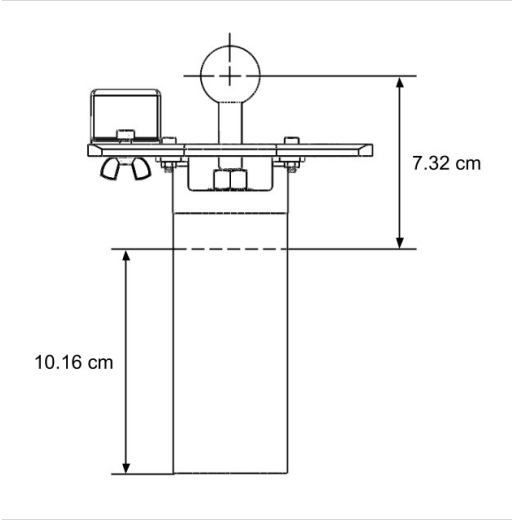

Fig. 4.8b. Pile 2 sketch (not to scale)

4.1.5 Model

A single pile was installed by hand in the center of the test bed. Pile was installed until the entire plug was filled, a depth of 10.16 cm and then the vent in the top caisson was either plugged to sealed it or left open to allow it to vent. The depth between the bottom of the pile and the sand layer was 9.84 cm. An example sketch of the an experiment is provided in Fig. 4.9a and an example picture is provided in Fig. 4.9b. To scale drawings are provided in the APPENDIX B.

4.2 Design of Centrifuge Experiments

In total three sets of centrifuge experiments, divided into Phases One to Three, were conducted in the centrifuge, Table 4.5. Phase One was rendered invalid due to desiccation of the model in flight. Phases Two and Three each consisted of two experiments of three model Piles. Experiment One focused on rotational monotonic capacity and consisted of three parts: a monotonic failure test, a set of cyclic loading

tests, and finally a post cyclic failure test. Experiments Two focused on pile cyclic behavior and consisted of two parts: a set of cyclic tests and post-cyclic rotational monotonic failure capacity tests. This dissertation focuses solely on the cyclic tests in Experiment Two of Phase 2 and Phase 3, the more information specific loading schemes can be found in Chapter 6. Further information on Experiment One, Phase Two and Phase Three, and post-cyclic capacity in Experiment Two and Phase 2 and Phase 3 can be found in Murali (2015).

Fig. 4.9a. Example sketch of 1-g experiment

Fig. 4.9b. Example picture of 1-g experiment post T-bar testing

Table 4.5. Outline of experiments

Phase (#)	Experiment (#)	Monotonic	Cyclic
1	1	Desiccated	Desiccated
	2	Desiccated	Desiccated
2	1	Virgin	Post-Monotonic
	2	Post-Cyclic	Virgin
3	1	Virgin	Post-Monotonic
	2	Post-Cyclic	Virgin

4.2.1 Coordinate Systems

Whenever possible, relative dimensions independent of a coordinate system were used. That way a user defined local coordinate systems can be easily easily be implemented. However, is some cases a relative dimensions could not be easily used. In these cases two coordinate systems were used in the centrifuge experiments: Global and Robot. The Global coordinate system is a Cartesian system were all experiment components are referenced to the bottom corner of the rigid box, Fig. 4.10. Refer to APPENDIX B for drawings more accurately depicting the global coordinate system. This is useful for defining the location of the pore pressure sensors. The Robot coordinate system is that of the Rensselaer Polytechnic Institute (RPI) four degree of freedom (DOF) robot and defines its motion. The RPI four DOF robot was used to measure caisson movement after spin up and settlement. The relationship between the Robot and Global system is different for each centrifuge experiment.

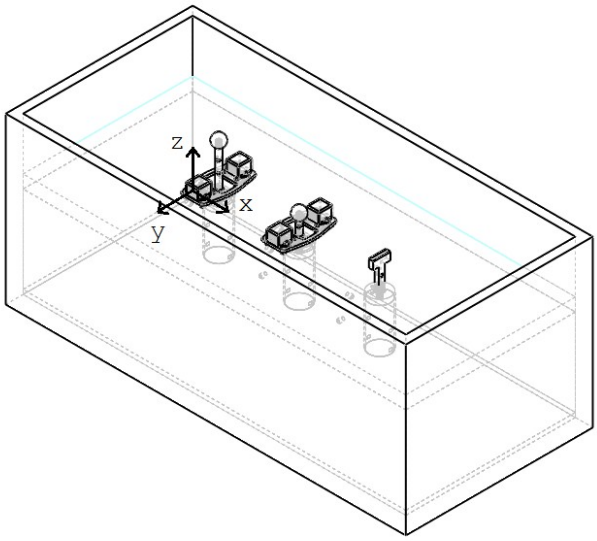

Fig. 4.10. Global coordinate system, located between sand and clay layer

4.2.2 Sensors

4.2.2.1 MEMS Accelerometers

Two types of single-axis MEMS accelerometers were used in these experiments: Silicon Design Model 2012 (Silicon Design Inc. 2013) with ± 100 g range and MEMSIC CXL10GP1 single-axis accelerometer (MEMSIC n.d.). They will to be further referred to by the generic names of the 100 g Accelerometer and the 10 g Accelerometer, respectively. Additional properties for both sensors have been complied in Table 4.6. A single 100 g Accelerometer was used to measure centrifuge gravity at the experiment height in real time and six 10 g Accelerometers were used to measure rotation of the caissons. Calibration factors for all MEMS accelerometers can be found in Table 4.7.

Table 4.6. Accelerometer technical specifications (reproduced from Table 3.1)

	10g Accelerometer	100g Accelerometer
Sensitivity (mV/g)	200 ± 5	40
Cross-Axis Sensitivity	± 5 (% of Span)	2 (%) TYP
Noise (mg rms)	35	0.140
Temperature Offset	± 3 g (0º-70º C)	$5x10^{-3}$ g/ºC

The six 10 g Accelerometers used in this experiment were given labels M1-M6. Calibration factors, zero g voltages, cross-axis correlations factors, and intercepts for each sensor are provided in Table 4.7. Calibration factors and zero g were obtain from a 1-g calibration using the 3D printed angular calibration device in Fig. 4.11. Cross-axis correlation factors and intercepts are discussed in CHAPTER 3. Cross-axis correlations were not assessed for the 100 g Accelerometer, since it was mounted inline with gravity.

Table 4.7. MEMS accelerometers used in centrifuge experiments

Name	Range	Calibration Factor	Zero g	Cross-Axis Factor, Cx	Cross-Axis Intercept, bx
	(g)	(g/V)	(V)	(g/g)	(g)
M1	±10	4.982	2.242	0.020	0.030
M2	±10	5.044	2.279	0.011	0.068
M3	±10	5.068	2.321	0.004	0.000
M4	±10	5.087	2.366	0.008	0.024
M5	±10	4.99	2.214	0.024	-0.012
M6	±10	5.00	2.252	0.026	-0.006
M100	±100	25.112	-0.037	–	–

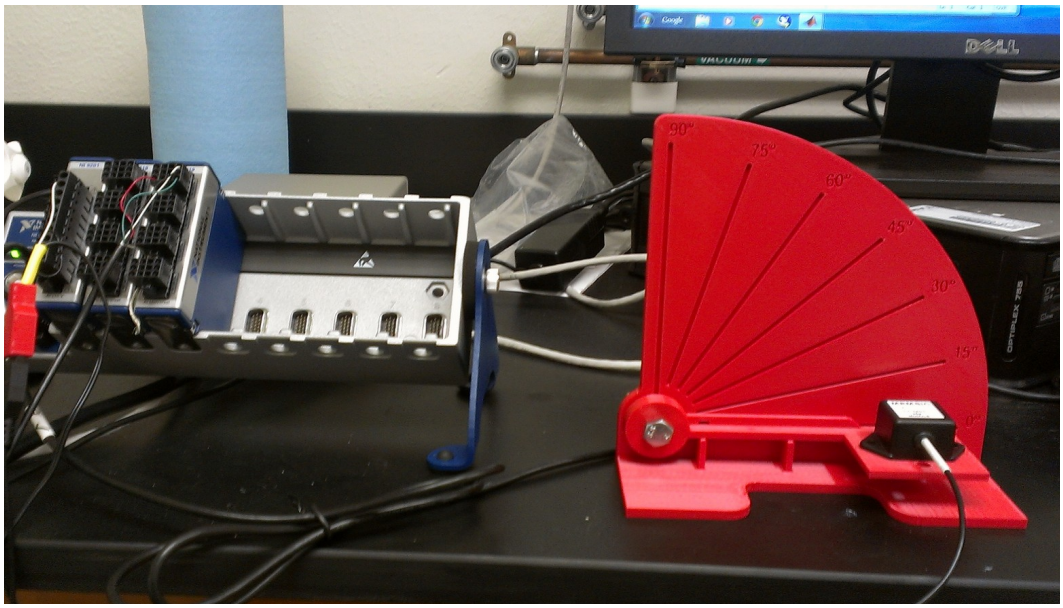

Fig. 4.11. 1-g MEMS calibration device

4.2.2.2 Pore Pressure Sensors

Pore pressure sensors were provided by RPI. The two models used were the GE Druck PDCR 81-3478 and the Keller 2MI-81840. Calibration factors for all pore pressure sensors used in Phase Three Experiment Two can be found in Table 4.8.

4.2.2.3 Linear Variable Displacement Transducers

Linear Variable Displacement Transducer (LVDT) sensors were provided by RPI the model used was the Schaevitz MHR series. Calibration factors for the LVDT sensors for Phase 2 Experiment Two can be found in Table 4.9. while LVDT sensors for Phase 3 Experiment 2 can be found in Table 4.10.

Table 4.8. Pore pressure sensor calibration factors

RPI Number	Experiment Number	Calibration Factor (V/kP)
6177	Phase 2 Experiment 2	0.08059
10580	Phase 2 Experiment 2	0.0225
6173	Phase 2 Experiment 2	0.075122
5706	Phase 2 Experiment 2	0.116386
6174	Phase 2 Experiment 2	0.0799
6175	Phase 2 Experiment 2	0.0776
10584	Phase 2 Experiment 2	0.023479
12185	Phase 2 Experiment 2	0.05279
10579	Phase 2 Experiment 2	0.022659
6200	Phase 3 Experiment 2	0.094835
6199	Phase 3 Experiment 2	0.0763158
10586	Phase 3 Experiment 2	0.022652
11642	Phase 3 Experiment 2	0.050312709
11718	Phase 3 Experiment 2	0.0534849
11646	Phase 3 Experiment 2	0.04742826

Table 4.9. Phase Two Experiment Two LVDT calibration factors

LVDT Number	Experiment	Serial Number	Calibration Factor (mm/V)
LVDTP1	Phase 2 Experiment 2	5263	59.19
LVDTP2	Phase 2 Experiment 2	5265	57.39
LVDTP3	Phase 2 Experiment 2	7228	50.55
LVDT1	Phase 3 Experiment 2	5263	55.32
LVDT2	Phase 3 Experiment 2	5265	57.19
LVDT3	Phase 3 Experiment 2	7228	54.02

Table 4.10. Phase Three Experiment Two LVDT calibration factors

LVDT Number	Serial Number	Calibration Factor (mm/V)
LVDT1	5263	55.32
LVDT2	5265	57.19
LVDT3	7228	54.02

4.2.3 Model Test Bed

The model was constructed in the RPI Large Rigid Box which is 88 cm by 39 cm. It consisted of two layers of soil one of Nevada Sand for drainage and one of kaolinite. The sand layer was 1 cm to 2 cm thick in the bottom of the box. The sand was placed by raining from a height of 10 cm, this should have resulted in a relative density of 35% and a desired dry density of 1.62 g/cm^3. The sand layer was then leveled and saturated. In order to minimize disturbance, water was siphoned slowly onto a sponge placed on the sand surface, Fig. 4.12. The saturated sand was then covered with geotextile, Fig. 4.13a-4.13b to facilitate drainage. The geotextile was also placed along the sides of the box to allow a drainage path to the surface. The geotextile covering the sides was in turn covered with sheets of Teflon to allow even settlement of the kaolinite during consolidation.

Fig. 4.12. Sand saturation processes

Fig. 4.13a. Geotextile placement along box length (not to scale)

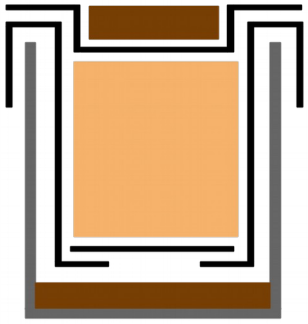

Fig. 4.13b. Geotextile placement along box width (not to scale)

The main component of the model was a kaolinite clay (BASF ASP 600) with Atterburg limits of LL = 61 and PI = 32. The kaolinite soil layer was designed to be at least 20 cm deep after consolidation. Clay was mixed from dry powder to a target water content of 77%, slightly above the liquid limit in a large standing mixer. Water content measurements were taken at multiple depths during construction of the Phase 3 Experiment Two model and are provided in Table 4.11, the point highlighted in red was considered an outlier and not used in the average value calculation. It can be seen from this table that the placement water content was slightly above the target. The average placement was 79.96 % compared to the target of 77 %. Placement water content measurements were not take during Phase Two Experiment Two.

Table 4.11. Phase Three Experiment Two kaolinite soil placement water content

Sample	Water Content (%)	Depth (cm)
A1	78.33	24-32
A2	79.25	24-32
A5	79.29	24-32
A6	79.67	16-24
A8	79.77	16-24
C10	79.72	16-24
A7	79.82	8-16
A10	80.13	8-16
D7	79.66	8-16
A9	82.77	1-8
D8	62.93	1-8
B7	81.17	1-8

The soil was be placed by hand into the rigid box in 3 lifts to a total height of 32 cm. The clay was placed in three lifts solely to accommodate the installation of the pore pressure sensors. The bottom lift was 16 cm, the middle was 6 cm, and the upper lift was 10 cm thick. This was based on calculated settlement during consolidated approximately 8 cm at which point it would be necessary to remove 4 cm to achieve a 20 cm depth. The model construction process can be seen in Fig. 4.14-4.15.

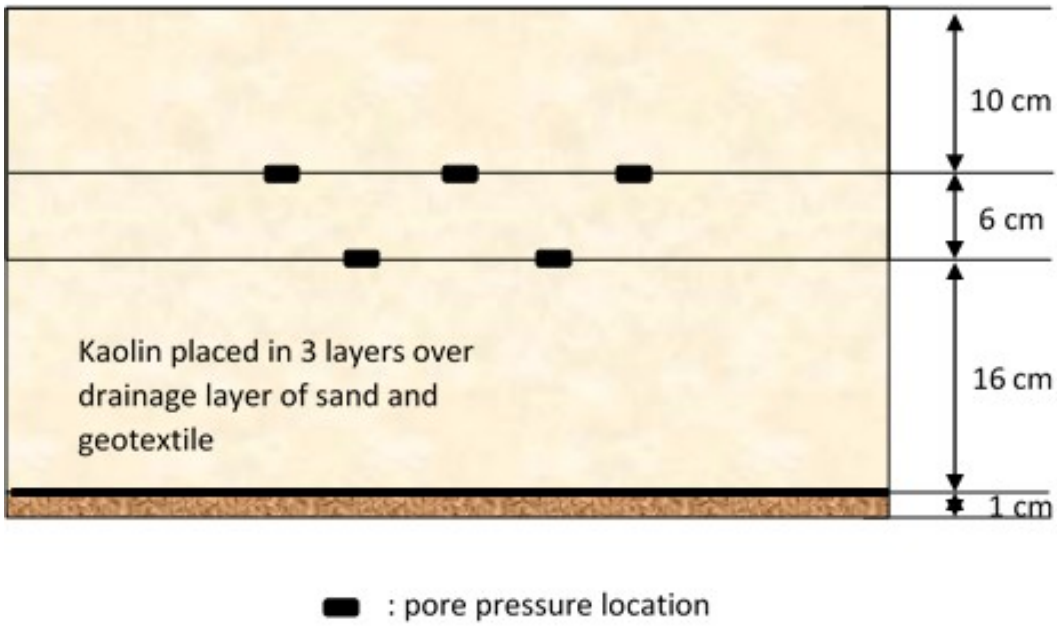

Fig. 4.14. Sketch of kaolinite layers pre-consolidation (not to scale)

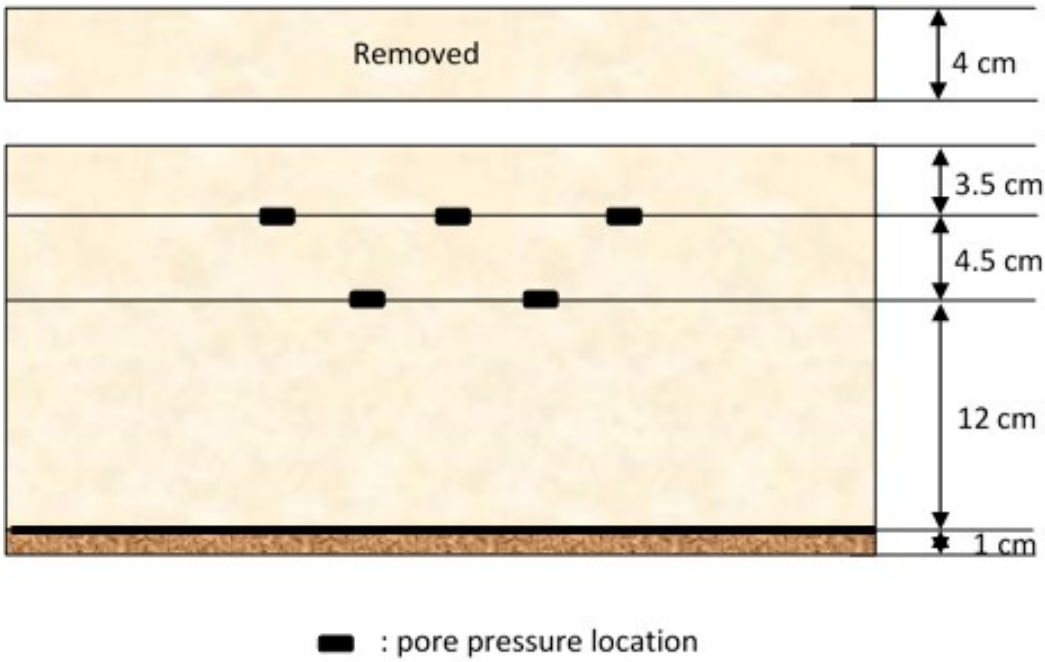

Fig. 4.15. Sketch of kaolinite layers post-consolidation (not to scale)

Pore pressure sensors were installed as shown in Fig. 5.14. A list of pore pressure sensors and there installed locations is provided in Table 4.12-4.13. Sensors at a depth of 10cm were placed 3.81 cm from the monopiles towards the negative x-direction, as shown in the drawings. To scale drawings with relative dimensions are available in the APPENDIX B.

The entire soil mass was then covered with a geotextile layer and overburden sand Fig. 4.16. The geotextile acted as a filter to keep sand from mixing with the clay. The overburden sand layer was 3.00 cm thick filling the large rigid box to the top and providing an over burden pressure 47 kPa.

Table 4.12. Phase Two Experiment Two pore pressure sensor installation locations

Name	RPI Number	Global X (cm)	Global Y (cm)	Depth (cm)
PPNW	6177	74.5	13	16
PPNE	10580	74.5	26	16
PPSE	6173	12.5	26	16
PPSW	5706	12.5	13	16
PPNC	6174	52.75	19.5	16
PPSC	6175	34.25	19.5	16
PP1	10584	31	19.5	10
PP2	12185	49.5	19.5	10
PP3	10579	68	19.5	10

Table 4.13. Phase Three Experiment Two pore pressure sensor installation locations

Name	RPI Number	Global X (cm)	Global Y (cm)	Depth (cm)
PPNC	6178	71.75	19.5	16
PPC	6193	53.25	19.5	16
PPSC	6195	34.75	19.5	16
PP1	6198	31.8	19.5	10
PP2	6197	50.3	19.5	10
PP3	6196	68.8	19.5	10

The clay layer was consolidated in the centrifuge under 100 g of centrifuge gravity. The model had been designed to spin for approximately 586 minutes (9.7 hr). This was to result in an average consolidation of 55%, a target water content of 50%, and an undrained shear strength of 15 kPa at the soil mid-depth, in-flight. These criteria were derived from one-dimensional consolidation calculations and undrained shear strength-water content correlations from Tessari (2012).

During the consolidation process it was necessary to slightly alter the process listed above. Originally the model was to be consolidated for 9.7 hours in order to dissipation of 40 kPa of excess pore pressure. However, due to the long projected work days consolidation was split over two days. For Phase Two Experiment Two the model was consolidated for 5 hours on both days. For Phase Three Experiment Two the model was spun for 8 hours 25 minutes on Day One and for 3 hours on Day Two. Total spin time at 100 g was over 10 hours for both models; longer than originally planned. Consolidation was not stopped until the pore pressure transducer measurements indicated the dissipation of 40 kPa of excess pore pressure. This processes took longer than predicted. It should be noted that small amounts of consolidation should have occurred during the balance spins and the spin up and spin down processes. Meaning more than 40 kPa of excess pore pressure should have been dissipated. The entire consolidation process of the model has been discussed for all centrifuge experiments has been covered in more detail by Murali (2015).

Fig. 4.16. Model overburden

Once the box was removed from the centrifuge the topography was measured to ensure even and consistent settlement occurred, a contour plots of soil depth can be found in Fig. 4.17-4.18**.** Topography determined by measuring the distance from the top of the box to the soil surface.

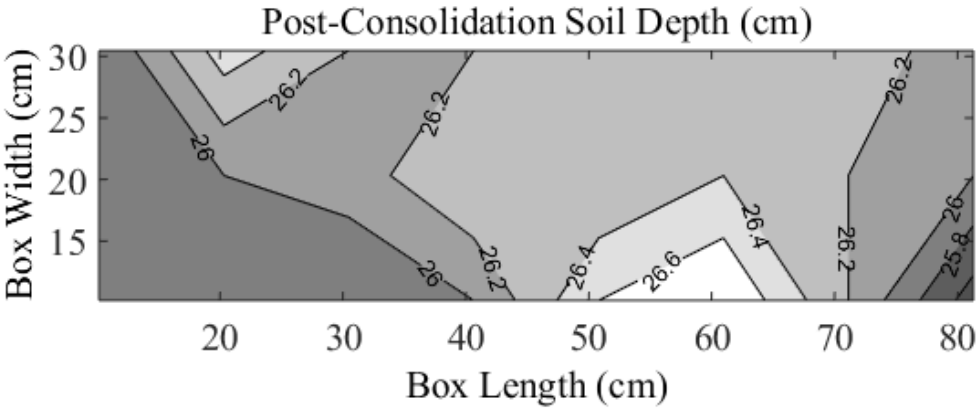

Fig. 4.17. Phase Two Experiment Two post consolidation topography contour plot

After consolidation 3.5 cm was removed during excavation Fig. 4.19. This resulted in a 1-g model height of 23 cm. This is 3 cm taller than the target clay thickness to account for recompression of the soil at 70 g. These are based swell calculations from C_r from Tessari (2012). This made the layer 23 cm thick at 1g and 20 cm at 70g.

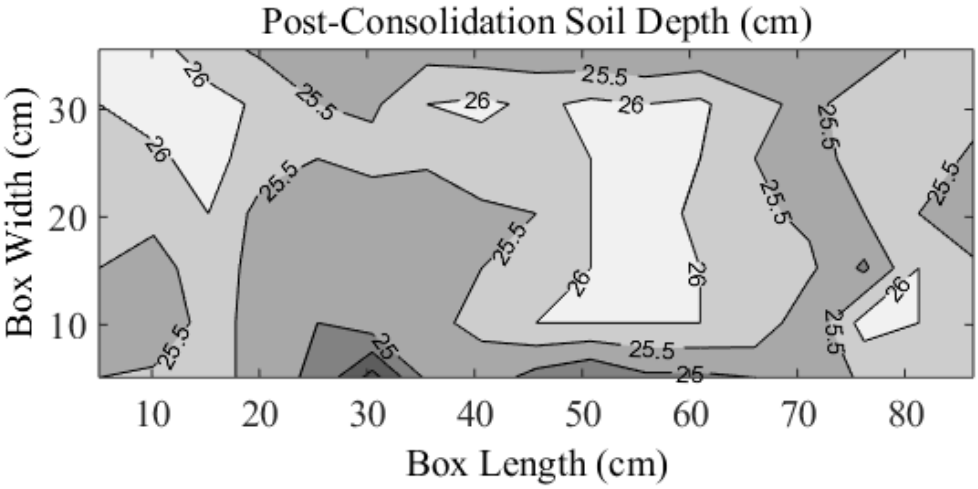

Fig. 4.18. Phase Three Experiment Two post consolidation topography contour plot

Fig. 4.19. Model excavation processes

Post-consolidation water contents were taken from a single 1.90 cm (¾ in) diameter core directly after excavation during Phase Two Experiment Two, provided in Table 4.14. The core was located at global coordinates (3.5 cm, 19.5 cm). During sampling the core was compressed in the sampler by about 4 cm. The depth locations for the water contents were adjusted linearly, given the compressed sample length and soil depth, to account for this compression. The average water content along the core was 61.7% significantly above the target water content of 50%; it is most likely that the coefficient of compression (Cc) used to calculate water content was slightly off. Post-consolidation water contents were not taken during Phase Three Experiment Two.

Table 4.14. Phase Two Experiment Three post-consolidation water contents

Sample	Water Content (%)	Depth (cm)
A1	66.90	0.92
A2	68.01	2.75
A3	68.70	4.58
A4	66.44	6.42
A5	65.56	8.25
A6	63.77	10.08
A7	51.46	11.92
A8	58.96	13.75
A9	56.34	15.58
A10	56.44	17.42
B1	54.64	19.25
B2	53.11	21.08

Model strength was measure: in-flight with a T-bar penetrometer, water content correlations, and SHANSEP analysis as covered in Murali (2015). T-bar tests were conducted adjacent to each pile before and after each set of tests allowing for measurements in time and space. All T-bar measurements have been compiled in Fig. 4.20a-4.20b. All T-bars indicate an average undrained shear strength of approximately 7 kPa over the length of the caissons. For convenience a single undrained shear strength value was used analysis.

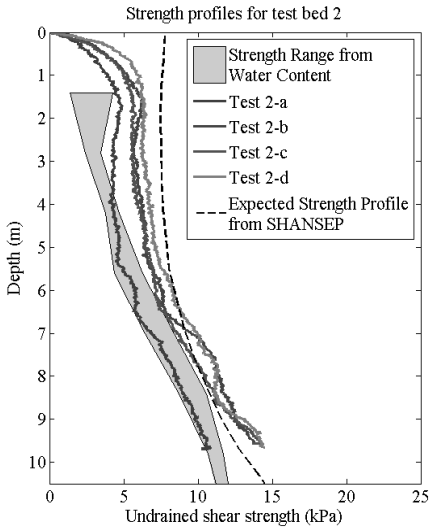

Fig. 4.20a. All Phase Two Experiment Two T-Bar results

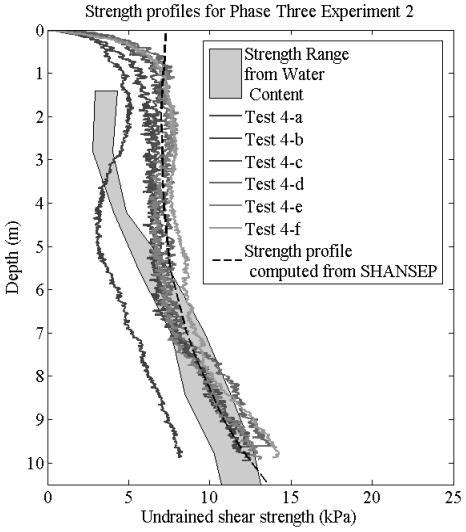

Fig. 4.20b. All Phase Three Experiment Two T-Bar results

Once all testing was completed the model was excavated to determine the final locations of the pore pressure sensors and take final water contents measurements throughout. The final position of the pore pressure sensors is provided in Table 4.15-4.16 with target locations (with added 3 cm) for comparison. It can be seen the sensors migrated quite a

bit, which could happen for any number of reasons. During excavation the soil was removed slowly both to protect the sensors and to get a more accurate measurement of there location, Fig. 4.21.

Table 4.15. Post Phase Two Experiment Two pore pressure sensor locations

Sensor	Global X (cm)		Global Y (cm)		Depth (cm)	
	Post	Initial	Post	Initial	Post	Initial
PPNW	74.5	74.5	11.5	13	9.5	11
PPNE	74	74.5	25	26	9.2	11
PPSE	13.5	12.5	17.5	26	9.2	11
PPSW	12.5	12.5	12.5	13	9	11
PPNC	52	52.75	18	19.5	9.5	11
PPSC	33	34.25	17.5	19.5	9.2	11
PP1	29	31	19.5	19.5	4	6.5
PP2	47.5	49.5	19.5	19.5	4	6.5
PP3	68.5	68	21.5	19.5	4	6.5

Table 4.16. Post Phase Three Experiment Two pore Pressure sensor locations

Sensor	Global X (cm)		Global Y (cm)		Depth (cm)	
	Post	Initial	Post	Initial	Post	Initial
PPNC	71.5	71.75	20	19.5	10	10
PPC	52	53.25	19.5	19.5	9.5	10
PPSC	35.5	34.75	22	19.5	9.5	10
PP1	29	31.8	19.5	19.5	5	5.5
PP2	48	50.3	19.5	19.5	5	5.5
PP3	66.5	68.8	18.5	19.5	5.5	5.5

Fig. 4.21. Pore pressure excavation technique

A total of 71 water contents were taken during the model excavation of the Phase Two Experiment Two model. 46 of these were taken along the plane in which the T-Bar test were conducted. The other 25 were taken at random from the soil mass. A total of 71 water contents were also taken from the Phase Three Experiment Two model. 47 of these were taken along the plane in which the T-Bar test were conducted. The other 24 were taken at random from the soil mass. The T-Bar water contents samples were taken as 1.90 cm (¾ in) diameter cores, Fig. 4.22. The rest of the water content samples were excavated by hand, an example of the process is provided Fig. 4.23a-4.23b. Contour plot of water contents along the plan on which the T-Bar tests were conducted can be found in Fig. 4.24-4.25. A noted previously the 1.90 cm diameter sampler slightly compressed the cores so depth measurements have been linearly corrected for compression.

Fig. 4.22. Water content sampler used at T-bar locations

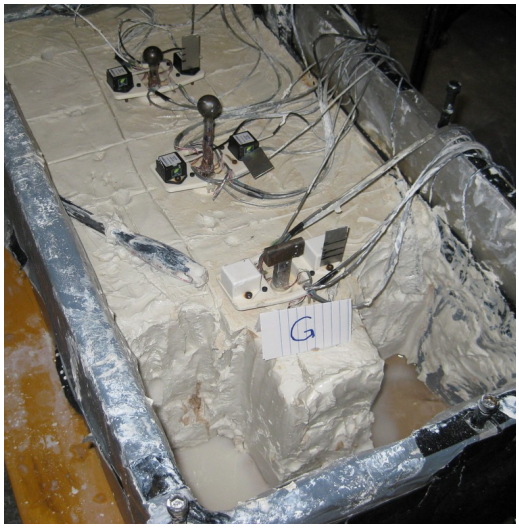

Fig. 4.23a. Excavation sampling from Phase 2 Experiment One

Fig. 4.23b. Hand excavated sample from Phase 2 Experiment One

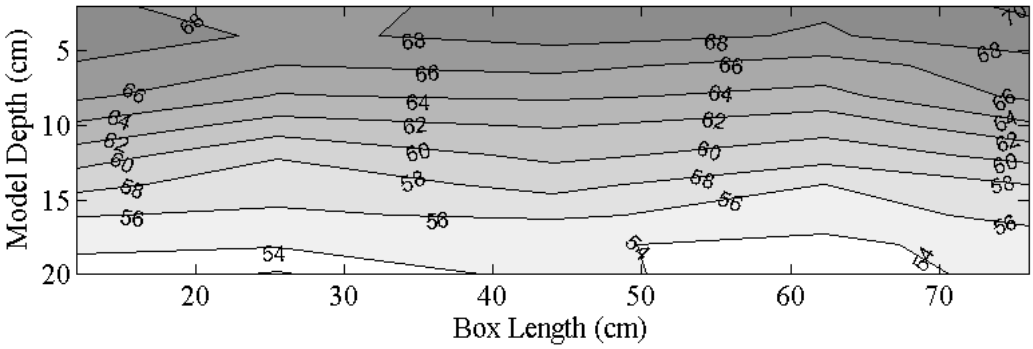

Fig. 4.24. Phase Two Experiment Two water content contours at T-bar locations

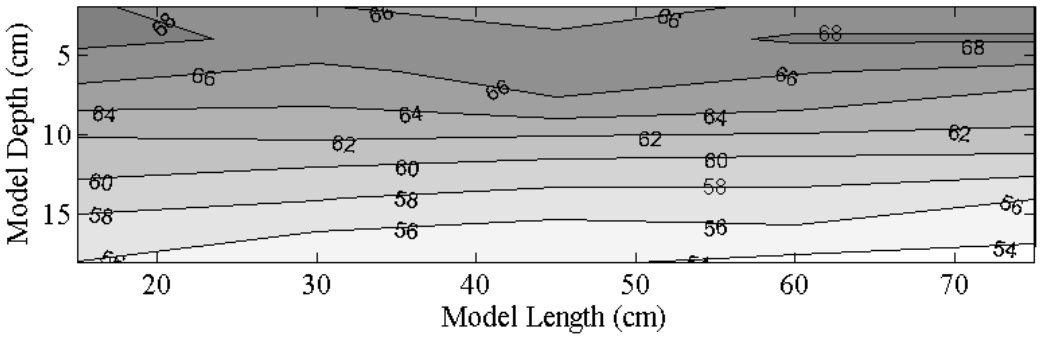

Fig. 4.25. Phase Three Experiment Two water contents along T-bar locations

4.2.4 Model Piles

The piles consisted of an aluminum caisson, an aluminum or steel stem, and an ABS plastic sensors platform. The caissons were created by turning down an aluminum tube to an outside diameter of 4.96 cm and welding on a 1.27 cm thick cap. This configuration resulted in an effective installation depth of 10.16 cm. Further details are provided in Table 4.17 and Figure 2a-b, including prototype dimensions for centrifuge

gravity of 74 g. The caissons had four 350 ohm strain gages attached 1.27 cm (0.5 in) from their bottom. They were evenly spaced along their base

Table 4.17. Caisson properties for centrifuge experiments

	Model	Prototype
Outside Diameter	4.96 cm	3.47 m
Effective Length	10.16 cm	7.52 m
Total Length	11.43 cm	8.46 m
Shell Thickness	6.1 mm	45.14 cm
Vent Diameter	6.35 mm	47 cm
Young's Modulus	69 GPa	69 GPa

The stems were secured through a threaded hole in the cap with a stainless steel nut and nylon washers. The stems were constructed from 9.52 mm (3/8 in) diameter steel or aluminum rod and were topped with a 2.54 cm (1 in) diameter ball, Fig. 4.26a-4.26b. Load was transferred to the ball via a cup adapter on the robot, see ***4.2.6***. Stem lengths were varied between piles in order to change load eccentricity. Three evenly spaced 120 ohm strain gages around the stem circumference were used to measure applied loads. Stems had either one or two levels of gages depending on available space.

During Phase Two Experiment Two the gages and wire were secure by coating them in a rubber coating. This not a completely successful method a number of gages were lost at high g. In Phase Three Experiment Two strain gage wiring was secured by wrapping thread around the wires at the base of the stem and caisson cap; similar to how and eyelet is attached to a fishing rod. The parts were then coated in rubber in order to secure and protect the wiring and gages. This was a much more successful means of securing

the wiring. Only one of the monopiles in Phase three Experiment Two exhibited gage loss at high g.

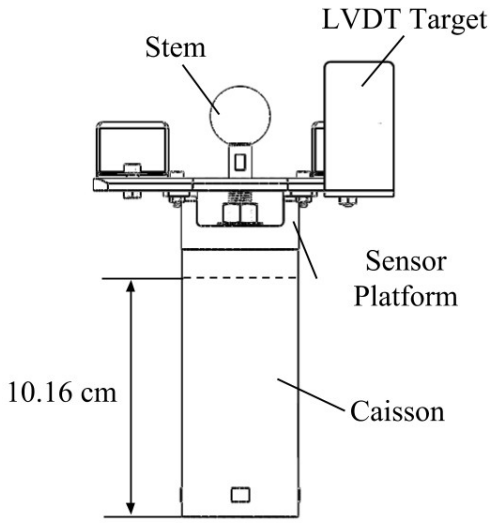

Fig. 4.26a. Monopile sketch (not to scale)

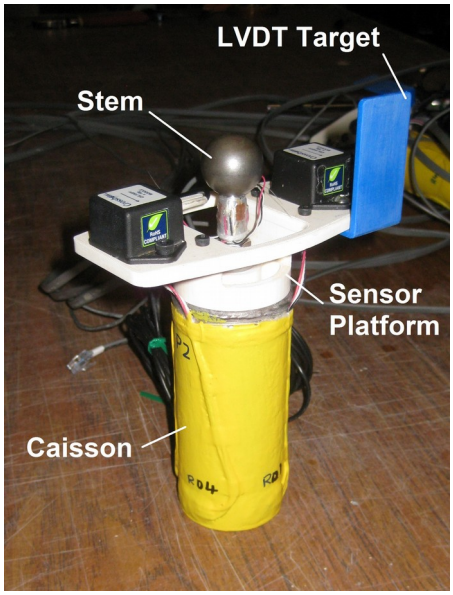

Fig. 4.26b. Example monopile

A sensors platform was designed and 3D printed from ABS plastic to carry two 10 g Accelerometers and a target for the LVDT transducers, Fig. 4.26a-4.26b. In Phase Two Experiment Two the LVDT Targets were made from aluminum sheet metal and super glued to the 10 g Accelerometer. In Phase Three Experiment Two the LVDT targets were 3D printed from ABS plastic and fastened to the sensors platform with the same bolts and nuts used to attach one of the 10 g Accelerometers. The platform was printed in two parts and secured with stainless steel screws. Additionally, the platforms provided additional space for securing any loose wires with cable ties.

To scale drawings of all piles used in Phase Two Experiment Two and Phase Three Experiment Two can be found in APPENDIX B. This also includes sensor configuration and orientation.

4.2.5 Experimental Layout

After excavation of the soil bed the monopiles were installed by hand in 1 g with a guide constructed from foam board. Three piles were installed on the center line of the box 18.5 cm on center, Fig. 4.27-4.28. The piles were installed until the plug was filled, a depth of 10.16 cm (assuming no plug heave) and the vent was then plugged with a cork. LVDT transducers were mounted to the Large Rigid Box with there probes contacting the LVDT targets to measure pile translation. Pore pressure sensors were embedded in the soil bed during the bed construction. The pore pressure sensors were installed at monopile mid-depth, approximately 5 cm, and 3.81 cm away from the piles in the +X direction. A mudmat 3D printed in ABS plastic was installed at the far end of the box in the +X direction. It carried a 100g Accelerometer (Silicone Design Inc. 2013) mounted at the height of the sensors platform on the piles. The 100 g accelerometer allowed for an accurate measurement of centrifuge gravity in the model for use in calculating tilt and scaling to prototype. To scale drawings of both experiments are provided in the APPENDIX B.

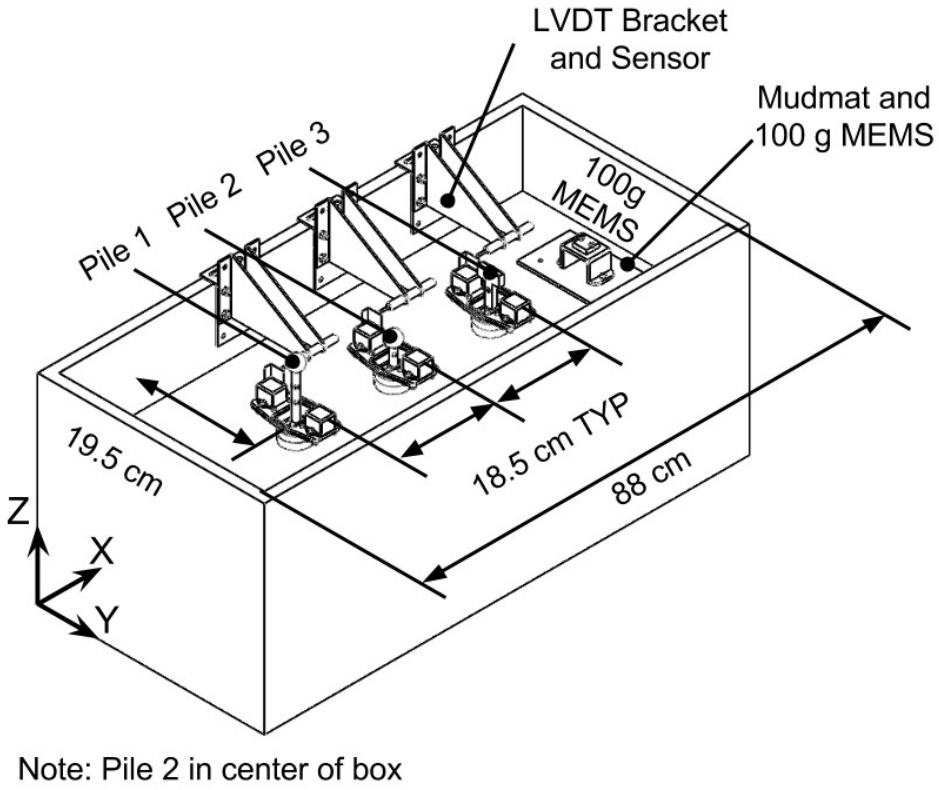

Fig. 4.27. Phase Two Experiment Two layout

4.2.6 Experimental Design

Once the model was placed on the centrifuge and spun up pile testing was complete with the RPI 4 DOF Robot. The target magnitude of centrifuge gravity was 70 g; however, this was based on an assumed radial distance to the model. Since the models present here were shallower than those typically used at RPI the radius to the model larger in typical. In Phase Two Experiment Two the magnitude of centrifuge gravity at the mid-depth of the pile was 75.10 g while it was 73.50 g during Phase Three Experiment Two. Differences in the magnitude of centrifuge gravity between experiments are most likely due to variation in the soil layer thickness.

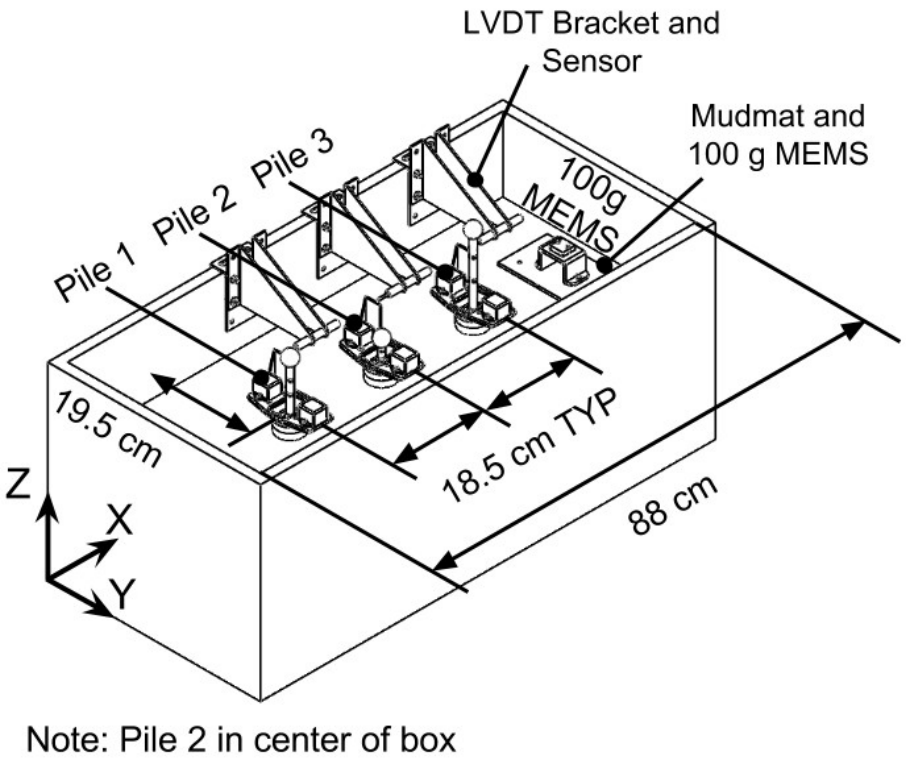

Fig. 4.28. Phase Three Experiment Two layout

All pile loading was applied with the RPI 4 DOF Robot. The robot was able to couple to the pile stems through a cup connector, Fig. 4.29. The cup was 3D printed from a bronze alloy and fastened to the robot with a bolt. The beveled slot was used by Murali (2015) to apply rigid load to piles in Phase Two Experiment One and Phase Three Experiment One. To ease the robot-stem coupling process two cameras were placed in the centrifuge to visually assess the robot's location. Additionally, the signal from the stem strain gages were monitored to identify if the robot was in contact with the pile. Any movements of the robot in proximity to the caissons were kept to no more than 1 mm to ensure the robot did not accidentally disturb them. Any excess pore pressure due to the pile installation at 1 g should have been dissipated by the one plus hour required to spin the centrifuge to 70 g.

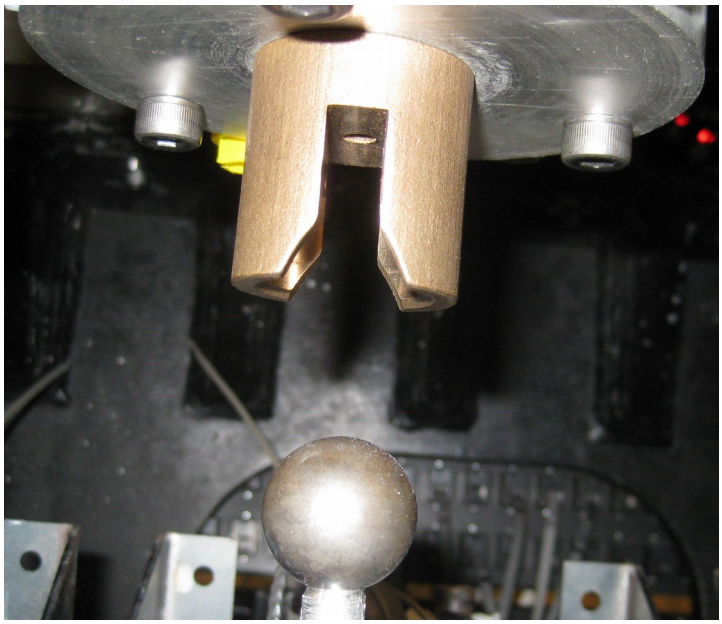

Fig. 4.29. 3D print cup adapter for RPI 4 DOF robot

4.2.7 Experiment Notes

4.2.7.1 Phase Two Experiment Two

There were a number of issues during Phase Two Experiment Two. Many of them revolved around the RPI Four DOF robot. Additionally, there were some issues with the sensors.

The first spin up attempt was aborted when a bolt on the centrifuge beam cut through the robot's power cable at high g and short-circuited the robot. This was a high voltage cable and there was concern that the sensors could be damaged. However, the sensors intact appeared and were working properly. The centrifuge beam is made out of a massive solid piece of metal and was able to handle absorb the excess electricity. After the cable was re-insulated the robot would did not work. Fortunately this was not due to the short-circuit, but was due to the power cable crushing one of the Robot's optical connectors. The RPI staff was able to repair the connector with glue.

After the connection was fixed a large amount of time was spent getting the robot to reinitialize. There was a problem with the planetary gear that controls the Robot's rotation about the it's z-axis. The planetary gear could not be fixed at the time, but the robot was eventually able to initialize. In all it took more than three hours to get the repair the Robot and reinitialize it; so, testing was postponed to the following day.

After running the Pile 1 Pre T-bar test the Robot's tool jaws stopped working. This meant the four DOF was unable to drop or pick up any tools, such as the T-bar or the cup adapter. It was necessary to spin down the centrifuge to correct this problem. It took about three hours to fix and then re-initialize the robot. It turned out that the Robot's hydraulic oil lines were partially clogged and had to be cleared/flushed. Of importance to note is that it was necessary to start and stop the centrifuge during Phase Two Experiment Two. This could effect the stress history of the soil. However, since target centrifuge gravity was constant for each pile test, any affect other than consolidation should be minimal.

After spin down to repair the robot jaws it was apparent that the piles were tilting and rotating about the pile's Z-axis. It appears that this is due to the LVDT springs pushing on the LVDT flags causing creep. Additionally, after the spin down it was noted that Pile 1 had sunk quite a bit during spin up so a larger aluminum LVDT targets were constructed and glued to one of Pile 1's the 10 g Accelerometer. This could not be done to the other piles because of clearance issues between the robot and LVDT target.

During cycling of Pile 1 it was observed that the stem would move significantly without the LVDT flag moving. After spin down to was discover that the stem of Pile 1 had not been properly secured to the caisson and was loose. Therefore, data from this test cannot be used since there is no means to ascertain stem compliance.

A number of strain gauges did not work during the experiment. Specifically, all the strain gauges on the stem of Pile 1 stem did not work and one of the gauges on Pile 3.

4.2.7.2 Phase Two Experiment Three

All the piles were tilted towards the negative X-direction after spin up. This could be due to two possible causes: 1) the LVDT springs applied enough force to the piles to cause creep during spin up 2) centrifuge gravity was not parallel to the model's soil surface and caused the piles to tilt in the negative X-direction.

Pile 1 had significant tilt in the negative X-direction as a result there was concern that the LVTD could go out of range during testing. To minimize the chance of this occurring Pile 1 was realigned to its original pre-spin up location. This disturbed the soil around the soil, but after adjustment the pile was allowed to set for 5 minutes (19 days in prototype time at 74 g) to dissipate any excess pore pressure. Though the distrubance was not ideal it ensured that the tests on Pile 1 could be conducted.

During the final cycling test of Pile One the LVDT probe tips slid off the LVDT target. Fortunately, the washer right below the tip of the probe remained in contact with the target.

Pile Three also had significant tilt in the negative X-direction. To ensure the test could be conducted with minimal problems, it was tested directly after Pile One and before Pile Two. It was also adjusted 5.5 mm in the +X direction to ensure the LVDT would be in range during testing. Again, the pile was allowed to set for 5 minutes (19 days in prototype time at 74 g) to dissipate any excess pore pressure

Pile Two was not tilted as much as the other two. We adjusted it 1 mm in the positive X direction just to verify the LVDT sensor was still in range prior to testing. Again the pile was allowed to sit for a number of minutes to allow any excess pore pressure to dissipate.

Cracking on the negative X side of Pile Two were visible in the soil while cycling, at approximately 2:46pm, Fig. 4.30. Cracks also appeared on the positive X side during the post cyclic monotonic failure test. Loading was in the positive X-direction. The soil was still cover in a layer of water; so, the cracks were not the result of desiccation. The cracks appeared small and there impact on soil resistance to pile motion is unknown.

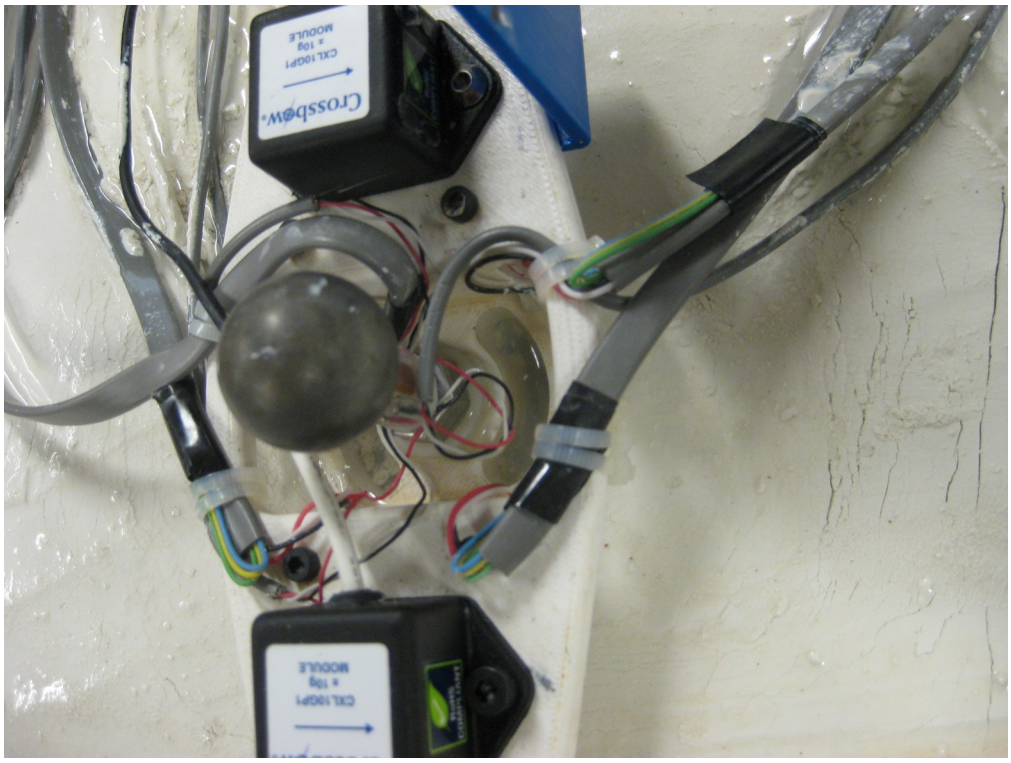

Fig. 4.30. Small cracks around Pile 2 (Eccentricity = 1.25Ø)

There were problems with the pore pressure transducers during the experiment. PP1 was noisy during spin up. Pore pressure measured by PP2 slowly decreased during testing this could be the result of the sensor floating towards the surface. PPNC appeared to be unconnecting and reconnecting during the entire experiment. PPC appeared to be unconnecting and reconnecting during the entire experiment. Finally, PPSC signal appeared a bit erratic during the entire experiment.

5 EXPERIMENTAL DATA INTERPRETATION

5.1 1-g Experiments

This section covers the methods used to interpret the data collected from the 1-g experiments.

5.1.1 Tilt from MEMS Accelerometers

The voltage signal from the MEMS accelerometers was converted to accelerations using the calibration factors and zero g voltages provided in Table 4.6, and Eq. (5.1). The signal quality was high, so no post processing filtering was required. The calibration equation is as follows:

$$a_{meas} = \left(V_{meas} - V_z\right) \cdot CF \tag{5.1}$$

where: a_{meas} is measured acceleration, V_{meas} is measured voltage, and V_z is sensor zero g voltage, and CF is the sensor calibration factor

Tilt was then simply taken from the sinusiodal relationship:

$$\theta_n = \arcsin\left(\frac{a_{meas}}{g_e}\right) \tag{5.2}$$

where: θ_n is the angle of the MEMS accelerometer relative to Earth's gravity and g_e is Earth's gravity

5.1.2 Applied Loads from CARMEn

The data acquisition system utilized in Cartesian Automated Robot for Marine Engineering CARMEn (discussed in CHAPTER 5) outputs bridge signals, like those from load cells and strain gages, as Volt per Volt. The robot's output signal is normalized by internal measurements of excitation voltage. Load from the vertical and horizontal load cells on CARMEn was simply calculated from the sensor range and calibration factor, Table 4.2, as is common with these type of sensors. The signal quality was high, so no post processing filtering was required. Moment at the top of the pile was then calculated from the load eccentricity, distance between the center of the stem ball to the top of the caisson.

5.1.3 Displacement from CARMEn Motion

Unfortunately, all available laboratory sensors did not have enough range to measure displacement over the entire motion of the robot during a monotonic failure test in the 1-g test apparatus. Luckily, CARMEn is extremely accurate (see CHAPTER 5) so it was simple to reconstruct its motion from kinetic parameters such as acceleration, velocity, and displacement. The only issue that arose was selecting the exact moment the robot movement began. CARMEn was programmed to pause for three seconds after activating the data acquisition system before making any motions. The actual duration the robot pauses appears different enough to make the programmed time a suboptimal datum. Instead a GUI which plotted the MEMS accelerometer voltage was used to visually select the time at which CARMEn started moving, Fig. 5.1. In the figure the vertical axis is voltage (V) while the horizontal axis is time (s). It should be noted that the first two seconds of data has been cropped out in the figure.

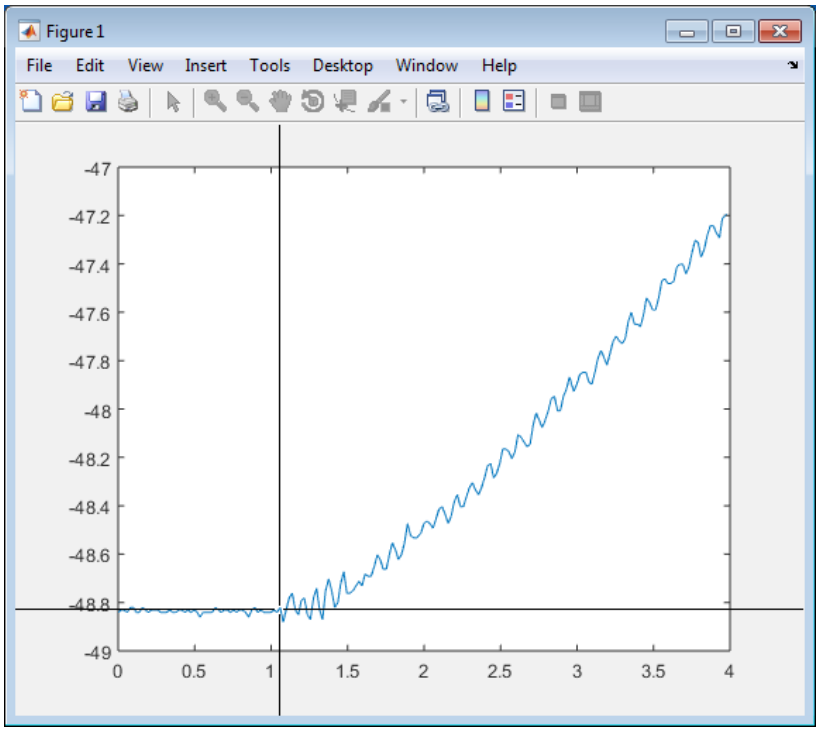

Fig. 5.1. Example of GUI for selecting when the robot started moving

Since the height of the displacement controlled loading varied between piles in each experiment displacement at the soil surface was chosen as a common reference point for comparing pile translation. To calculate displacement at the soil surface it is necessary to assume the stems were rigid, but this was not the case. There should be a slight amount of bending compliance in the stems, Fig. 5.2. Compliance could have been excluded from the data interpretation given its low magnitude (Fig. 5.3a-5.3b), but it was incorporated so the 1-g experimental analysis would be consistent with the centrifuge analysis. By assuming that the stem was a cantilever fixed at the top of the caisson it was possible to calculate stem deflection from applied horizontal force measured from the strain gages, Eq. (5.3). The displacement resulting from a rigid stem was then taken as the computed robot motion minus compliance, Fig. 5.3a-5.3b.

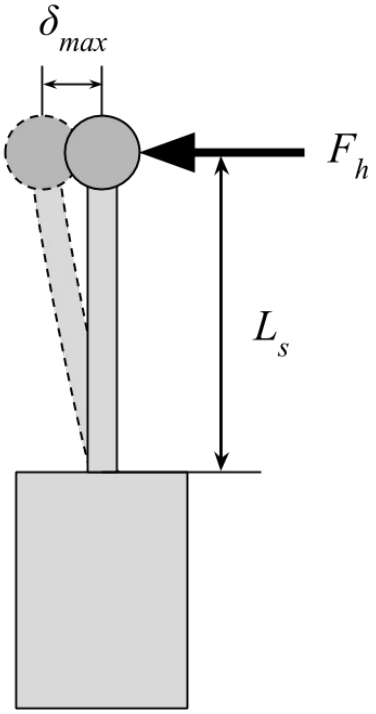

Fig. 5.2. Example sketch of compliance in the pile stems

$$\delta_{\max} = \frac{1}{3}\frac{F_h L_s^3}{EI} \tag{5.3}$$

where: δ_{max} is the max deflection of the stem, I is the second moment of area, F_h is the applied horizontal force, L_s, is the stem length or the distance between the center of the stem ball and the base of the caisson, and E is the elastic modulus

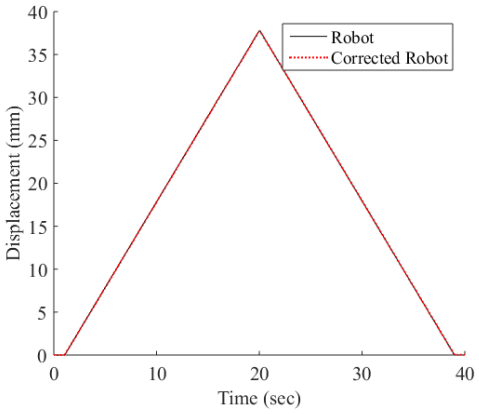

Fig. 5.3a. Example of 1-g robot motion corrected for compliance

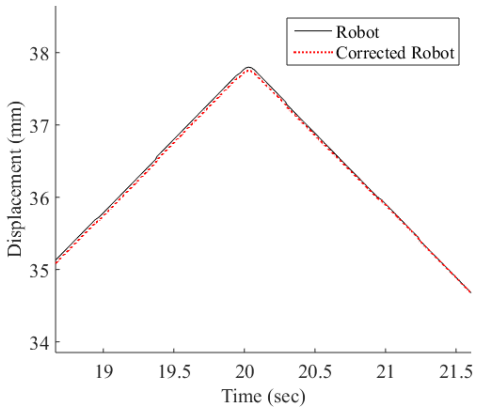

Fig. 5.3b. Example of 1-g robot motion corrected for compliance (zoomed)

5.1.4 Displacement at the Soil Surface

To calculate displacement at the soil surface the piles were assumed to be rigid and that the piles had only two degrees of freedom: rotation and translation. The rigid assumption is reasonable once compliance is corrected for. The assumption of two degrees of freedom is reasonable when the case of an infinitely long pile is considered. In this case any vertical motion can be taken as a horizontal translation, given the piles angle from horizontal, and when the pile is perpendicular to the soil surface no vertical translation is possible. Additionally, the soil was assumed to be a half-space that is it had a surface, but no bottom. Displacement could then be determined given the piles angle from vertical, a single point of translation along its length, and the vertical location of said point, Fig. 5.4.

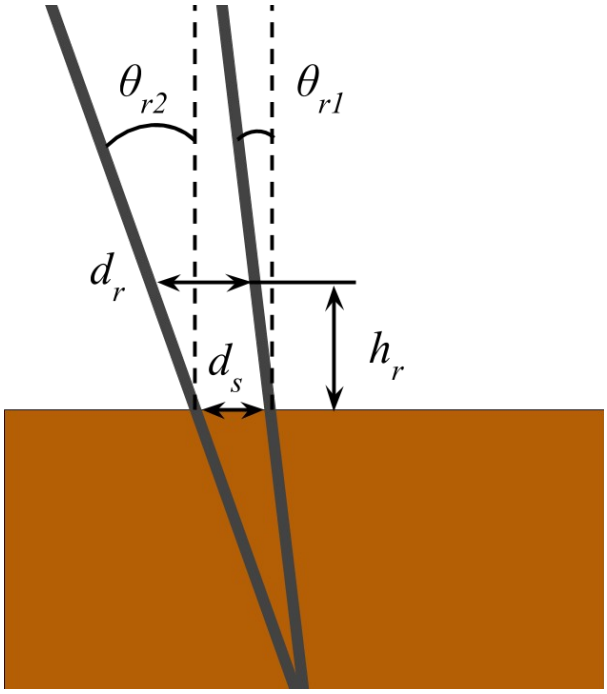

Fig. 5.4. Rigid pile rotation-translation sketch

Given Fig. 5.4 displacement at the soil surface can be calculated as:

$$d_s = d_r + \tan(\theta_{r1}) h_r - \tan(\theta_{r2}) h_r \tag{5.4}$$

$$d_s = d_r + h_r \left(\tan(\theta_{r1}) - \tan(\theta_{r2}) \right) \tag{5.5}$$

where: d_s is displacement at the soil surface, d_r is displacement translation of the robot at the load point, h_r is the height between d_r and the soil surface, θ_{r1} is the initial tilt of the pile, and θ_{r2} is the tilt of the pile after load is applied

The difference in displacement at the soil surface versus that applied at eccentricity by the robot is quite large, Fig. 5.5.

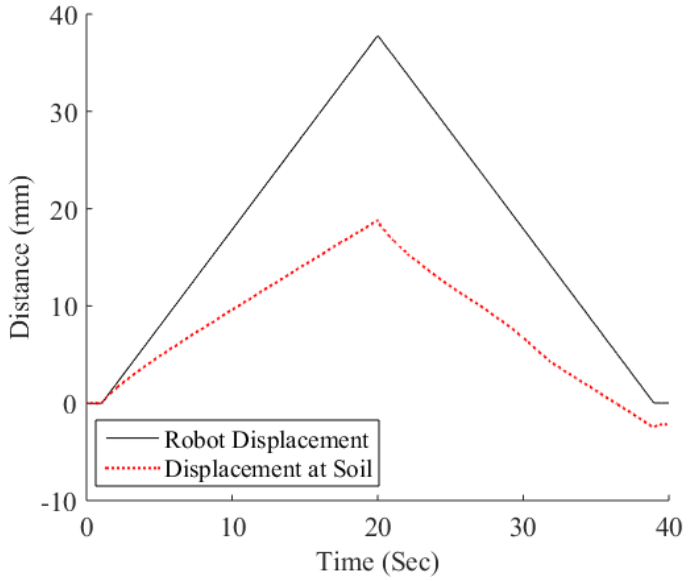

Fig. 5.5. Robot motion versus pile displacement at the soil surface

5.1.5 Depth of Rotation

Pile depth of rotation was calculated assuming they were rigid. The vertical reference line was taken perpendicularly to the soil at the point that the pile initially crossed the soil surface. Since all piles were initially tilted an initial displacement of the pile at the stem ball was calculated as:

$$d_o = \tan(\theta_{r1}) \cdot h_r \tag{5.6}$$

where: d_0 is the initial distance of the pile from the reference vertical line at the load application height

At each subsequent point along the piles depth of rotation was calculated as the distance below the soil surface the infinitely long pile intersects the vertical reference line, Fig 5.6. This was completed with Eq. (5.7).

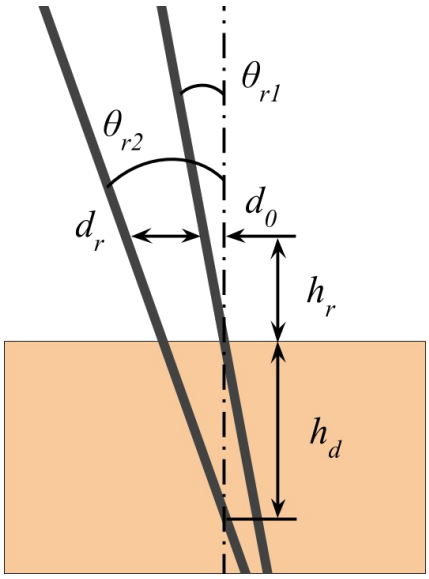

Fig. 5.6. Sketch of depth of rotation calculation

$$h_d = \frac{d_r + d_0}{\tan(\theta_2)} - h_r \tag{5.7}$$

where: h_d is the depth of rotation

5.2 Centrifuge Experiments

5.2.1 Tilt from MEMS Accelerometers

The voltage signal from the MEMS accelerometers was filtered with a moving average filter prior to any interpretation. Voltages were converted to accelerations using the calibration factors and zero g voltages provided in Table 4.6 and Eq. (5.1).

Measured accelerations were used to calculate orientation using the procedure outlined in CHAPTER 4. Unfortunately, a direct measurement of centrifuge basket orientation was not made in flight. Some simple observations and estimates are discussed in CHAPTER 7, but no alterations were made to the data.

The final measurements of orientation from the 10 g Accelerometers were filter using a local regression with a quadratic polynomial over 25 data point. This was done with the MATLAB function 'smooth' and the 'rloess' method ("MATLAB r2013a" 2013). Fig. 5.7 provides an example of the filter.

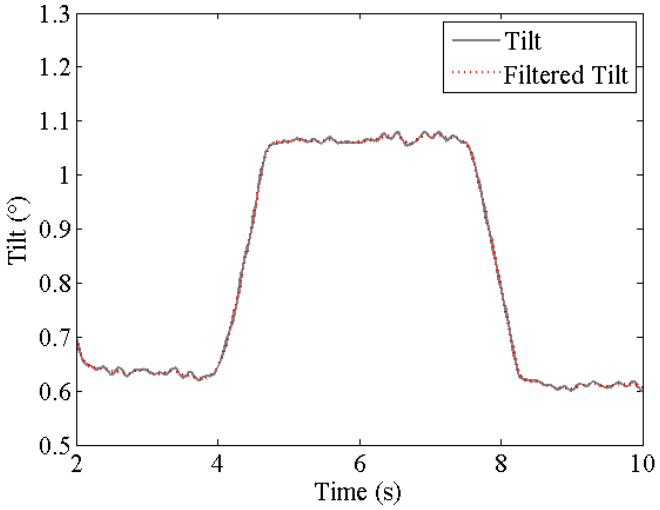

Fig. 5.7. Example of final filtering of orientation from the 10 g Accelerometers

5.2.2 Bending Strains from Stem Strain Gages

Strain gage data from the stem gages was first smoothed with a moving averaged filter and interpreted assuming that the sensors were installed at 120° on center around the stem circumference, Fig. 5.8. If the load direction was aligned with the lead gage, R1, the side gauges, R2 and R3, would measure one half the magnitude strain of R1. With this configuration strain from any applied vertical load can be calculated as Eq. (5.8), (Tuttle 1981).

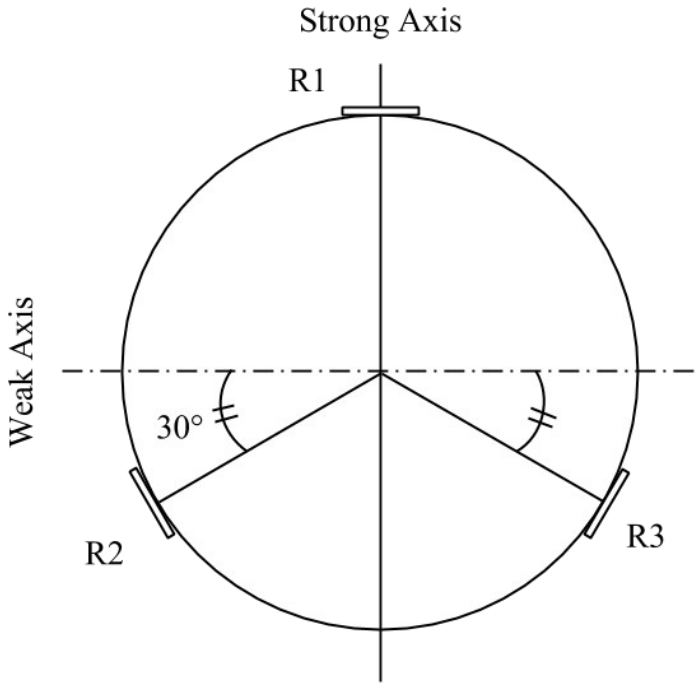

Fig. 5.8. Gage layout on stem cross section

$$\varepsilon_v = \frac{\left(\varepsilon_1 + \varepsilon_2 + \varepsilon_3\right)}{3} \tag{5.8}$$

where: ε_v is the vertical strain, ε_1 is the strain measured from gage R1 on the strong axis, ε_2 is the strain from gage R2, located 30° from the weak axis, and ε_3 is the strain from gage R3, located 30° from the weak axis, orientation R1-R3 as in Fig. 5.8.

Because of apparent rotation of the piles about the model about its length prior and/or during testing, identifiable in the post experiment pictures, Fig. 5.9, it was necessary to determine the loading direction in order to properly interpret strain on the strong axis. Since the lead strain gage was meant to be on the strong axis it was assumed that any rotation was by an angle, γ, away from the axis, Fig. 5.10. This was to correspond with the basic assumption that all rotation was due to the Linear Variable Displacement Transducers (LVDTs) pushing on the piles' blue LVDT targets, Fig 5.9.

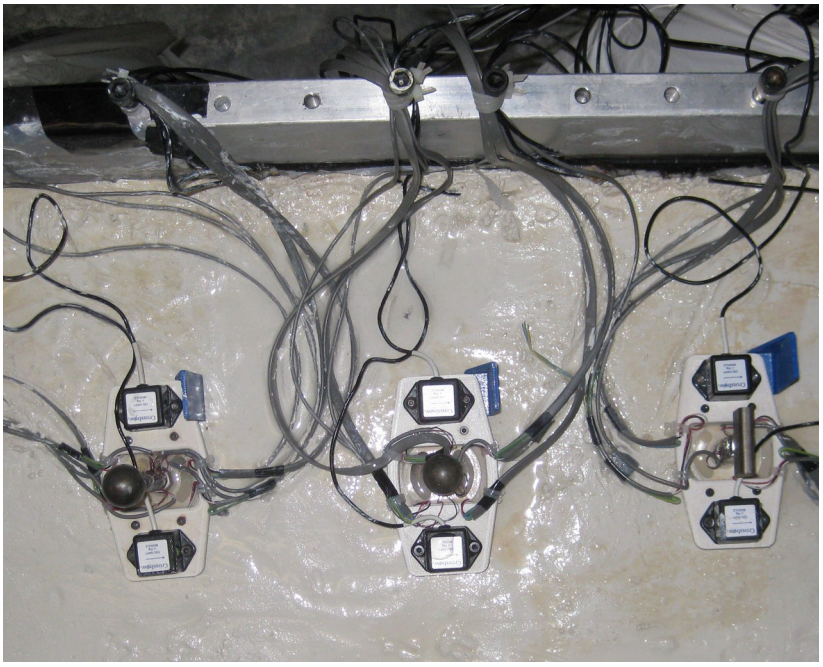

Fig. 5.9. Example rotation of Phase Three, Experiment One, Post-Experiment

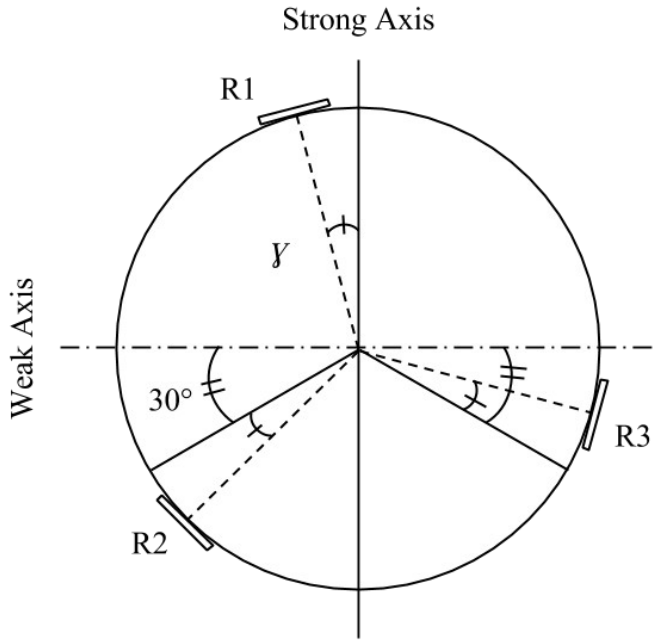

Fig. 5.10. Gage layout on rotated stem cross section

Assuming that the three gages are indeed 120° apart on center. It is possible to solve for the rotation of the pile about its length, γ. The amount of stain measured at the gage will be proportional to its distance from the weak axis (Tuttle 1981). First the strain at each gauge will be:

$$\varepsilon_1 = \varepsilon_p \cos(\gamma) \tag{5.9}$$

$$\varepsilon_2 = \varepsilon_p \sin(30 + \gamma) \tag{5.10}$$

$$\varepsilon_3 = \varepsilon_p \sin(\gamma - 30) \tag{5.11}$$

where: ε_p is the peak strain on the strong axis

Peak bending strain on the strong axis can be solved for all three gages by:

$$\varepsilon_p = \frac{\varepsilon_1}{\cos(\gamma)} \tag{5.12}$$

$$\varepsilon_p = \frac{\varepsilon_2}{\sin(30 + \gamma)} \tag{5.13}$$

$$\varepsilon_p = \frac{\varepsilon_3}{\sin(\gamma - 30)} \tag{5.14}$$

Using any two of Eq. (5.12)-(5.14) it is possible to to solve for peak strain, ε_p: For example substituting Eq. (5.12) into Eq. (5.13) rotation of the stem, γ,can be solved iteratively with:

$$\gamma = \arccos\left(\frac{\varepsilon_1}{\varepsilon_2} \cdot \sin(30 + \gamma)\right) \tag{5.15}$$

Once stem rotation, γ, is calculated it is possible to calculate peak strain on the strong axis corresponding to each gage, R1-R3, with Eq. (5.12)-(5.14) and an average value can then be obtained. This was done for all four piles. Average gage rotation has been

compiled in Table 5.1. Maximum strain during three load cycles was used to calculate rotation during each set of cyclic loading, Fig. 5.11. An average peak strain, $\varepsilon_{p\text{-}avg}$, was then calculated determined, as in Fig. 5.12. In the cases where the stems had two levels of gages this was completed for each level.

Table 5.1. Rotation of stem gages about y-axis

Phase	Pile	Load Eccentricity	Rotation
(#)	(#)	(Ø)	(°)
3	2	1.10	10.30
2	2	1.20	–
3	1	2.25	3.80
3	3	3.05	–

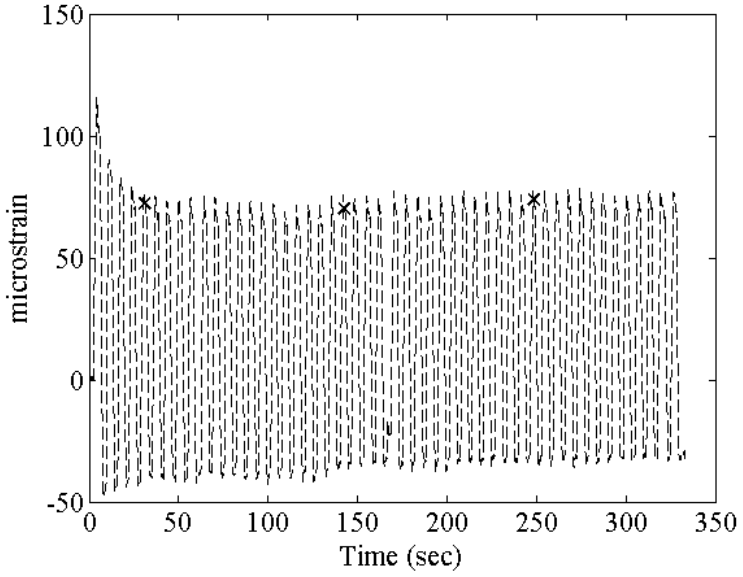

Fig. 5.11. Example of maximum strain selection for rotation calculation

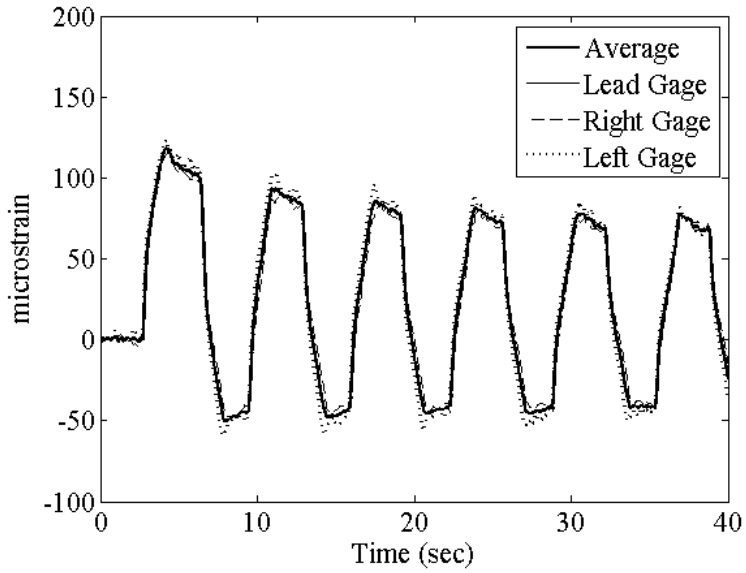

Fig. 5.12. Result of gage rotation to find average peak strain

As noted in Table 5.1 stem rotation is not available for Piles 2 and 4. In the case of Pile 2 gage R3 failed and R2 had measure values of that was ¼ of R1. If the stem had rotated about the model y-axis the measured strain by R2 should have been approximately 0.5 to 1 time the value of R1. There are a number of possible reasons for this discrepancy:

1. Gage R2 is significantly less than 120° from gage R1
2. Gage R2 glue was not properly bonded to the stem
3. Wire on gage R1 was pulling on the gage in phase with cycling
4. A vertical force equal to half of that measured by R1 was applied to the stem in phase with cycling

It was assumed that option 2 was the most likely cause of the discrepancy in measured strain given the failure of gage R3. As such, only strain from gage R1 was used to measure loads. Since only one gage was used, vertical strains could not be calculated.

In the case of Phase Three Pile Three, three of the six gages failed. On the first level, closest to the ball, the lead gage, R1, failed and on the second level the lead and left gages failed, R4 and R6. Peak strains for level one were calculated by doubling the values of R2 and R3 (30° from weak axis) and then averaging them. Orientation was not calculated using these two gages because R3 was greater than R2. The proposed rotation theory makes this impossible; either wire pulling increased the value of R3 or R2 was partially de-bonded from the stem. Since neither option could be confirmed no rotation was assumed. Peak strain from R2 and R3 as well as their averaged is provided in Fig. 5.13. Since only a single gage, R5, on the second level survived it was impossible to calculate rotation. It was assumed that no rotation of the stem occurred and the peak strain was simply taken as twice the value of R5 (30° from weak axis).

Since all three gages were not available on the same level for either Phase Two Pile Two or Phase Three Pile Three vertical strains could not be calculated.

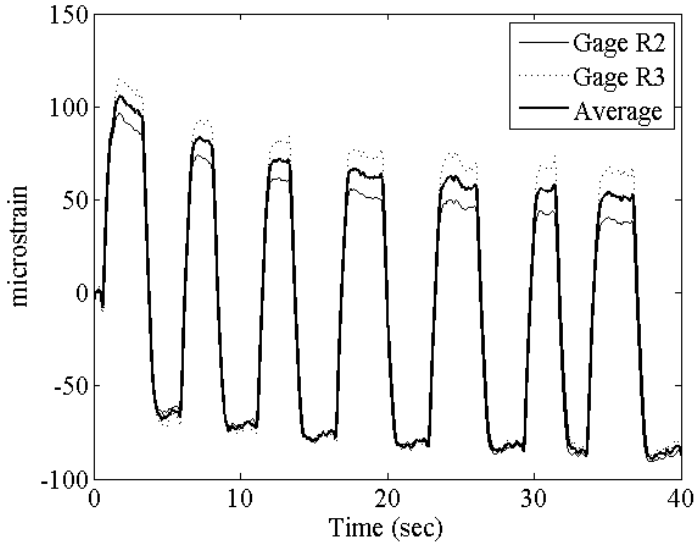

Fig. 5.13. Pile 4 peak strains from gages R2 and R3, Test 1

5.2.3 Vertical Forces, Moments, and Horizontal Forces from Peak Strains

Vertical force was calculated by simply assuming the stem was a column using:

$$F_v = \varepsilon_v \cdot E \cdot A \tag{5.16}$$

where: F_v is the vertical force, A is the cross sectional area of the stem, and ε_v from Eq. (5.8)

Simple cantilever theory was used to calculate moments and horizontal loads from peak strains. It was assumed that the loading was quasi-static; so, the cantilever (stem) was fixed at the pile cap and free at the ball and cup connector. It was assumed the ABS plastic sensors platform did not change the stiffness of the stem.

Moments at each level of the strain gages were calculated using:

$$M_n = \varepsilon_{p-avg} \cdot E \cdot Z \tag{5.17}$$

where: M_n is the moment at the strain gage, Z is the section modulus of the stem, $\varepsilon_{p\text{-}avg}$ is average peak strain on the strong axis at a level of gages

Horizontal force was then calculated at each level of strain gages by dividing by the length of the moment arm, L_s, taken as distance between the top of the caisson and the center of the strain gages. In the case of Pile 3 and Pile 4 the horizontal forces, F_h, calculated from the two levels of gages were averaged.

Finally, with horizontal force the moment at the top of the caisson, M_{top}, was calculated by horizontal force, F_h, multiplied by the moment arm, L_s, distance between top of the caisson and the center of the stem ball.

5.2.4 Displacements from Robot

Unfortunately, real-time displacements of the Rensselaer Polytechnic Institute (RPI) 4 DOF robot were only sampled at a frequency of one hertz. This was not fast enough to accurately measure its motion while cycling at a displacement amplitude of 5 mm and velocity of 2 mm/s. Therefore, it was necessary to theoretically determine the robots time dependent motion from kinetic parameters: acceleration, velocity, and displacement.

An interesting quirk of the RPI 4 DOF robot to note is that it pauses for an indeterminate amount time prior to making a motion. This makes it difficult to reconstruct the robot motion using kinetic parameters. To correct for this a custom MATLAB GUI was created to isolate the duration of each of these pauses. This was done by plotting the output from one of the 10 g Accelerometers and selecting the increments where motion occurred, Fig 5.14. A displacement profile based on acceleration of 50 mm/s^2, a velocity of 2 mm/s, and the test specific displacements was then constructed and placed between the pauses.

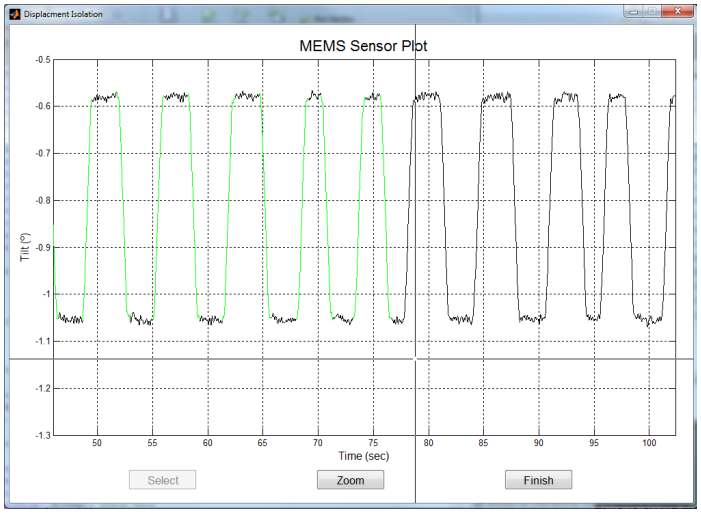

Fig. 5.14. Example of GUI used to determine duration of robot pauses

Since the height of the displacement loading varied between piles displacement at the soils surface was chosen as a common reference point for comparing pile translation. To calculate displacement at the soil surface it is necessary to assume the stem is rigid, but this is not the case. There was significant compliance in the stems especially for Piles 1 and 3 in Phase Three Experiment Two which had longer moment arms, Fig. 5.15. By assuming that the stem was a cantilever fixed at the top of the caisson it was possible to calculate stem deflection/compliance from applied horizontal force measured from the strain gages, as before in Eq. (5.3).

Corrected robot motion was then determined by subtracting out calculated compliance, Fig. 5.15. Finally, a little noise due to the phase differences between the calculated robot motion and the measured loads was present. The phase differences are most likely due to human error in operating the GUI to select the RPI 4 DOF robot's pauses. Start and stop points were selected by eye and could easily be off by a fraction of a second. The noise was corrected by filtering the data using a local regression with a quadratic polynomial over a set window of data points. Window varied from 21 to 65 points. This was done with the MATLAB function 'smooth' and the 'rloess' method (“MATLAB r2013a” 2013).

5.2.5 Displacements from LVDT

The calibration factors for the LVDTs were directly inputted into the RPI centrifuge data acquisition (DAQ) so LVDT outputs from the DAQ were in distance (mm). This output was then filtered slightly with a moving average.

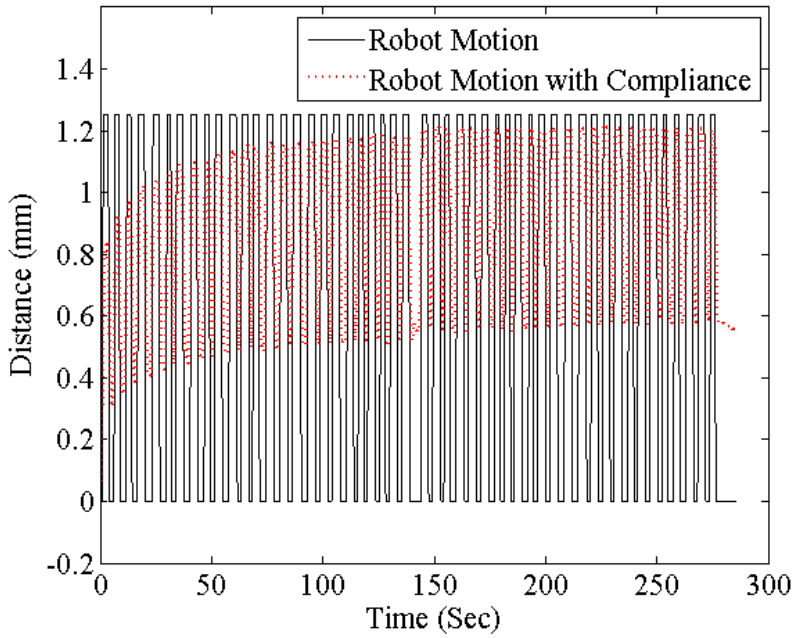

Fig. 5.15. Theoretical robot motion and correct robot motion considering compliance for Pile 4 Test 1

During Test 3 of Pile 1 in Phase Three Experiment Two the end of the LVDT probe separated from the LVDT target due to pile settlement. However, the washer below the LVDT probe tip did catch on the target and data collection continued. This resulted in an artificial abrupt translation in the data that Pile 1 in Phase Three Experiment 2 did not actually undergo. Using Fig. 5.16 as a guideline this was corrected by:

1. Assuming the translation *dy* due to the ball falling off the target is equal to the difference in magnitude between y_1 and y_4
2. Adding *dy* to all points beyond and including Point 3
3. Replacing the data between Point 2 and Point 3 with a linear interpolated set

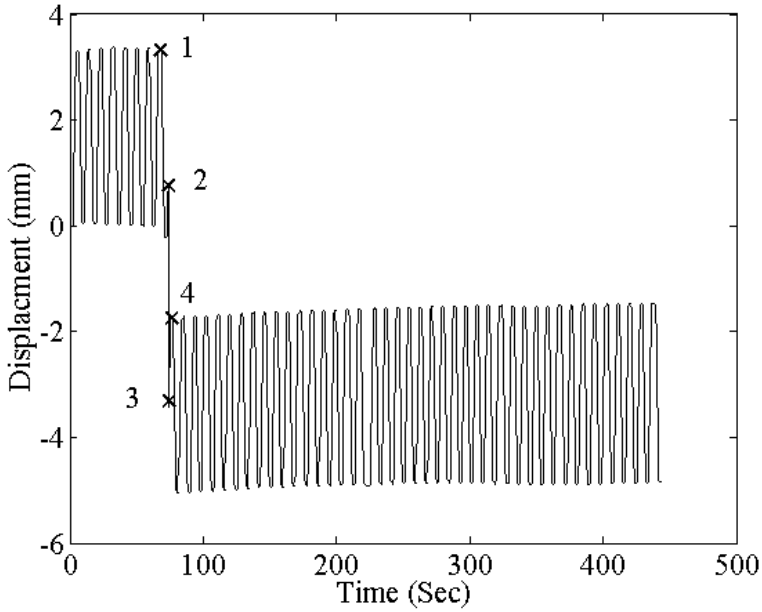

Fig. 5.16. Method to correct displacement data from LVDT slipping off the target in Test 3 of Pile 1 form Phase Three Experiment Two

As seen in Fig. 5.17 this procedure worked well; however, it appears the LVDT started slipping slightly before the return motion. The minimum during that cycle is likely higher than presented in Fig. 5.17. There is not a simple way to fix this erro without altering the entire cycle; so, it was left in the data.

5.2.6 Displacements at the Soil Surface

Displacements at the soil surface can be calculated as present in ***5.1.4***. However, the cyclic loading results from the centrifuge required more post-processing than the 1-g experiments. After calculating displacements at the soil surface from applied robot and LVDT displacement, d_r, slight spikes were present in each half cycle in the results from the LVDT data, Fig. 5.18, and at sporadically in the results from the robot data, Fig. 5.19.

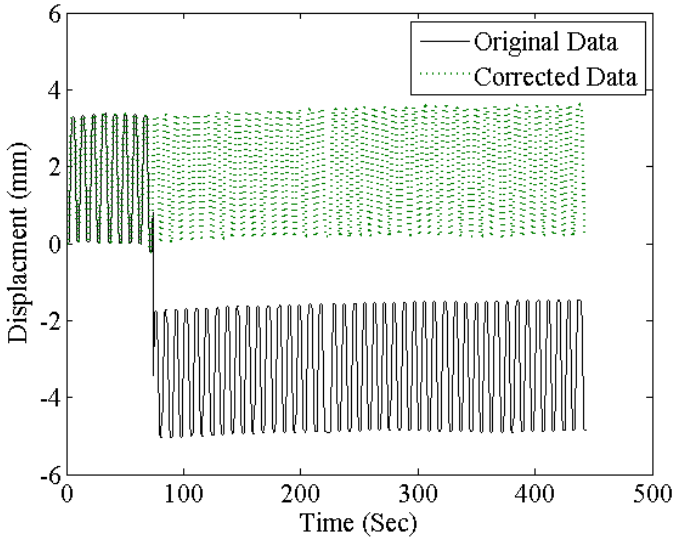

Fig. 5.17. Comparison of original and corrected LVDT measurements for Test 3 of Pile 1

This indicates that the rotation measured from the 10 g Accelerometers was slightly out of phase with the LVDT sensors. The only explanation for the spikes in the data would be if the pile rotated about the LVDT contact point without translating. This does not make sense. The LVDT would not be a strong enough to provide a pivot point for the pile. Additionally, the analog LVDT should have a faster reaction speed than the digital MEMS; meaning it would be more likely for translation to be measured without rotation. A reasonable explanation is that the Telfon tip of the LVDT probe slipped against the LVDT Targets smooth plastic surface as the pile rotated instead of displacing for a fraction of a second. Any spikes or noise in the displacement at the soil surface results derived from the predicted robot motion is likely due to human error in the GUI selection method; similar to before.

To correct any phantom motions due to phase dependencies/slipping, post-processing filtering was used. The data was simply filtered using a local regression with a linear or

quadratic polynomial over a set window of data points. Window varied from 35 to 75 points. This was done with the MATLAB function 'smooth' and the 'rlowess' option for the LVDT data and 'rloess' option for the robot motion ("MATLAB r2013a" 2013). The linear 'rlowess' appeared more successful at removing regular noise than the quadratic 'rloess' filter in this specific case. Examples of filtering on the displacements at the soil surface data from LVDT and robot motion are provided in Fig. 5.18 and Fig. 5.19, respectively.

5.2.7 Depth of Rotation

Depth of rotation was calculated as outlined in ***5.1.5***.

5.2.8 Pore Pressure from Pore Pressure Sensors

Calibration factors for the pore pressure transducers were directly inputted into the DAQ of the RPI CEES centrifuge. Thus measurements with the units of kPa were directly outputted. This output was filter with a moving average filter.

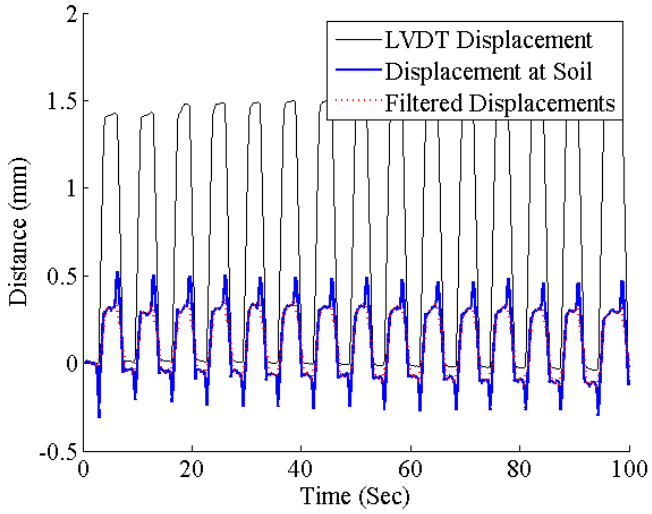

Fig. 5.18. Filtering of soil displacements from LVDT data Pile 1 Test 2

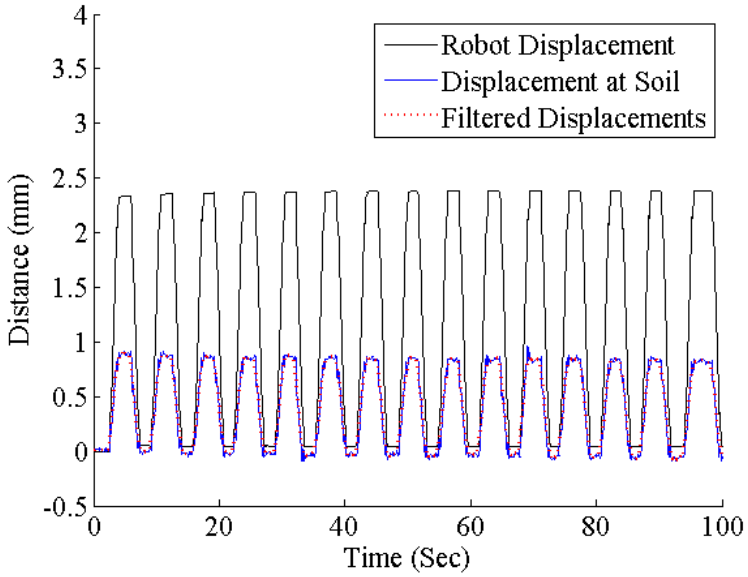

Fig. 5.19. Filtering of soil displacements from robot motion Pile 1 Test 2

5.2.9 Soil Reaction from Caisson Strain Gages

Data from the caisson gages was first smoothed with a moving averaged filter then interpreted assuming that the sensors were installed at 90° on center around the caisson circumference. Only measurements from the side gages, 90° from the load direction, were used. The sides gage signals were averaged and used for calculating reaction force at the base of the caisson for Phase 3 Experiment 2 Pile 1 and Pile 2. Due to gage loss or high signal to noise ratio for Pile 2 in Phase 2 Experiment 2 and Pile 3 in Phase 3 Experiment 2 only a single gage was used.

Measuring and/or determining the reaction loads of the soil against squat piles is difficult to obtain. Not only are strains in the caisson walls miniscule, but finding a simple static interpretation of the problem, in the vein of the cantilever assumption used with the stems, requires many assumptions. For initial analysis and simplicity an infinitely translating tube was chosen for quasi-static analysis. This is no means a great assumption since the caissons have a length to diameter ratio of two; however, in this particular case

it is a good first step.

It was assumed that: the pile is an infinitely long tube and it is being pushed into a half-space of soil, Fig. 5.20. Given this any force applied to the front of the pile must be equally carried in the shell at the two points 90 degrees from the load, Fig. 5.21. With this the reason load the soil places at the base of the caisson can be calculated as in Eq. (5.18).

$$F_R = 2 \cdot b_c \cdot E \cdot \varepsilon_c \tag{5.18}$$

where: F_R is the soil reaction force, b is the thickness of the caisson shell, and ε_c is the average strain measured by the two gages on the side of the caisson

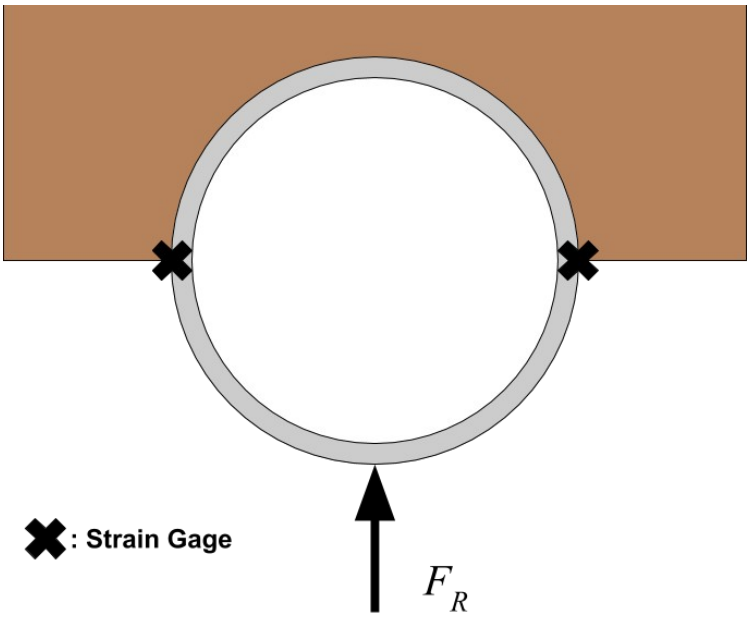

Fig. 5.20. Assumptions used to calculate soil reaction force, F_R, against the caisson

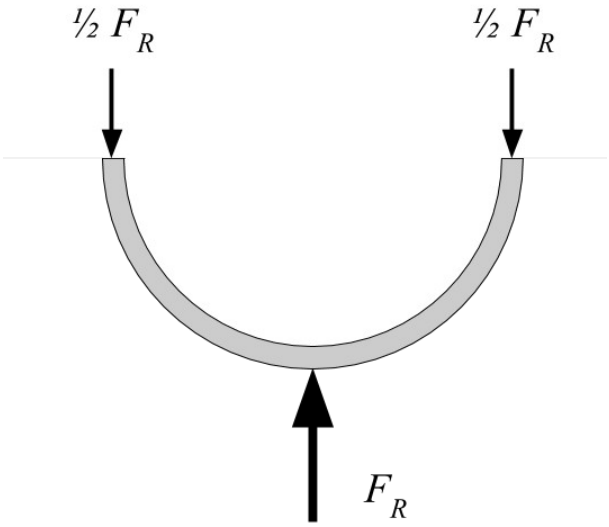

Fig. 5.21. Free body diagram of caisson

5.2.10 Cyclic Stiffness and Damping Ratio

Global stiffness of the caissons was simply taken as the secant stiffness with increasing tilt. Stiffness was taken in terms of angle in units of 360 degrees. Given the issues with the loading scheme it was decided to present in a way which is easier to comprehend for qualitative analysis instead of for use in quantitative analysis.

The pauses in the RPI 4 DOF robot motion also caused significant problems analyzing the global cyclic stiffness of the pile and its cyclic damping ratio. Because of the pauses, minimum and maximum cyclic displacement could not be used to bound the cyclic stiffness. When the minimum or maximum displacement was reached the robot would pause and the pile would creep. This creep significantly increased the cyclic damping ratio, Fig 5.22a-5.22b and had the largest effect on the smallest displacement magnitudes. Bounding values for calculating cyclic stiffness and the cyclic damping ratio came from the GUI described in 5.2.4. Damping ratio calculated for cycles were

little to no creep occurred and these cycles were selected based on qualitative visual inspection in a custom GUI. For example, in Fig. 22a and Fig. 22b cycles 17 and 35 were selected and cycle 22 was not.

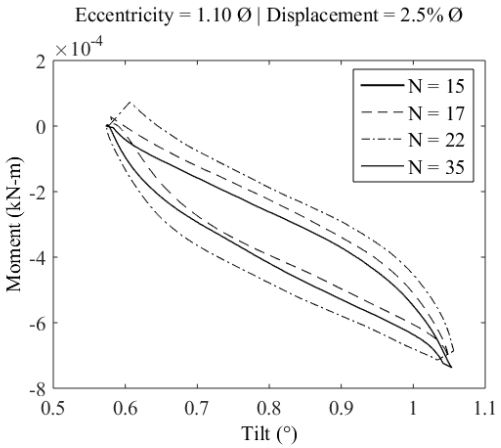

Fig. 5.22a. Impact of creep on hysteresis loops

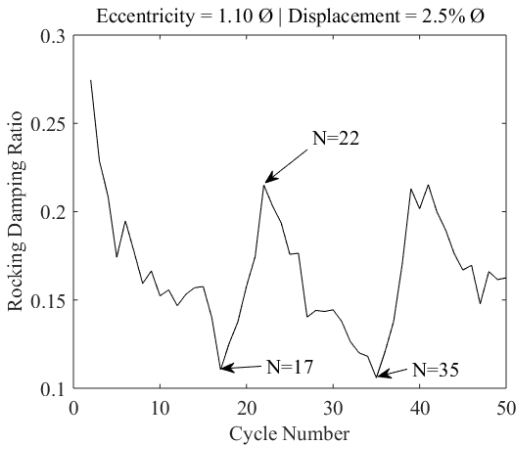

Fig. 5.22b. Impact of creep on damping ratio

Damping ratio was calculated by the means outlined in (Wu 1971). Since loading was one-way stiffness, k, was taken from the point of minimum moment to the point of maximum moment, not from the origin as is common for two-way tests. Additionally, the amplitude of tilt to maximum moment, u_a, was taken and half of the total tilt amplitude for the entire one way motion, not from the origin as is common for two-way tests. The specific damping was taken as in Eq. (5.19).

$$C_s = 2\frac{\Delta W}{k \cdot u_a^2} \tag{5.19}$$

where: C_s is the specific damping capacity, ΔW is the work done in the hysteresis loop, k is the stiffness of the loop, and u_a is the amplitude of tilt over half the loop

With the specific damping capacity the damping ratio can simply be taken as:

$$\zeta = \frac{C_s}{4\pi} \tag{5.20}$$

where: ζ is the damping ratio

6 ONE-G AND CENTRIFUGE EXPERIMENTAL RESULTS

6.1 1-g Modeling Experimental Results

Four scale model gravity caissons were tested with CARMEn (Cartesian Automated Robot for Marine Engineering), a 2D robot, in the 1-g experimental laboratory at Texas A&M University to examine the affect of eccentric loading and caisson venting. The full experimental setup can be found in 4 DESIGN OF 1-G AND CENTRIFUGE EXPERIMENTS, but for clarity; the caissons had a length to diameter aspect ratio of two, model water content varied from 60% to 68%, and further information can be found in the 1-g testing matrix in Table 6.1.

Table 6.1. 1-g testing matrix

Test	Pile	Eccentricity	Venting	Su
#	#	Ø	Sealed/Vented	kPa
1	1	0.9	Sealed	1.44
2	1	0.9	Vented	3.88
3	2	1.2	Sealed	3.76
4	2	1.2	Vented	2.94

6.1.1 General Observations on Caisson Venting

This initial testing reveals the effect of venting on the gravity caisson's capacity, stiffness, and displacement hardening. Monotonic lateral loading curves are provided in Fig. 6.1-6.2. Though only monotonic loading will be discussed the capacity curves do

include unloading. From these results it can be clearly seen that venting the caissons has a large effect on lateral capacity for both load eccentricities and the curves appear to be slightly softer when vented. Finally, they show a displacement hardening behavior at large strains regardless of the caissons venting or load eccentricity.

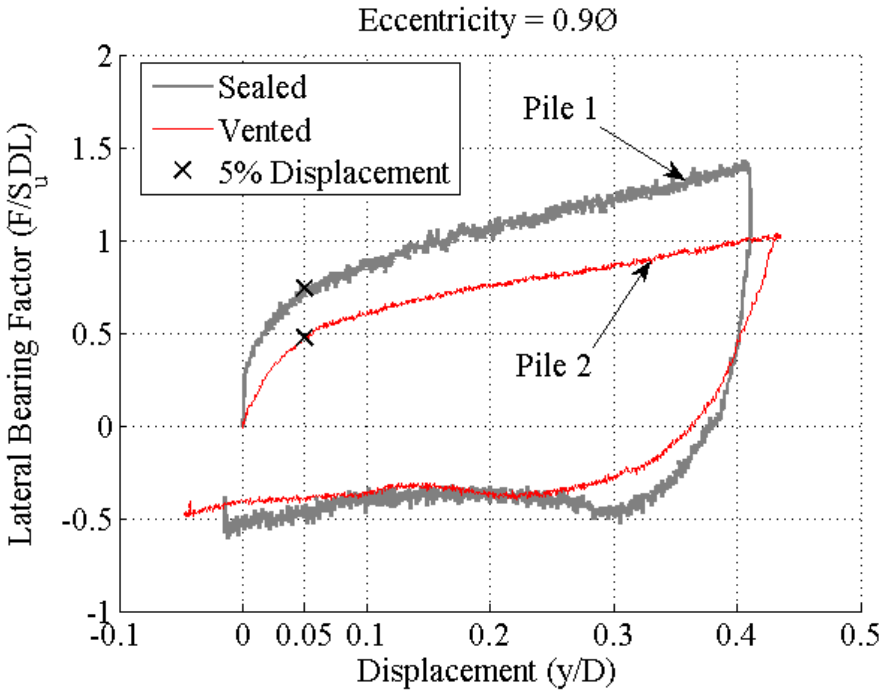

Fig. 6.1. Venting effect on load-displacement behavior, eccentricity of 0.9Ø

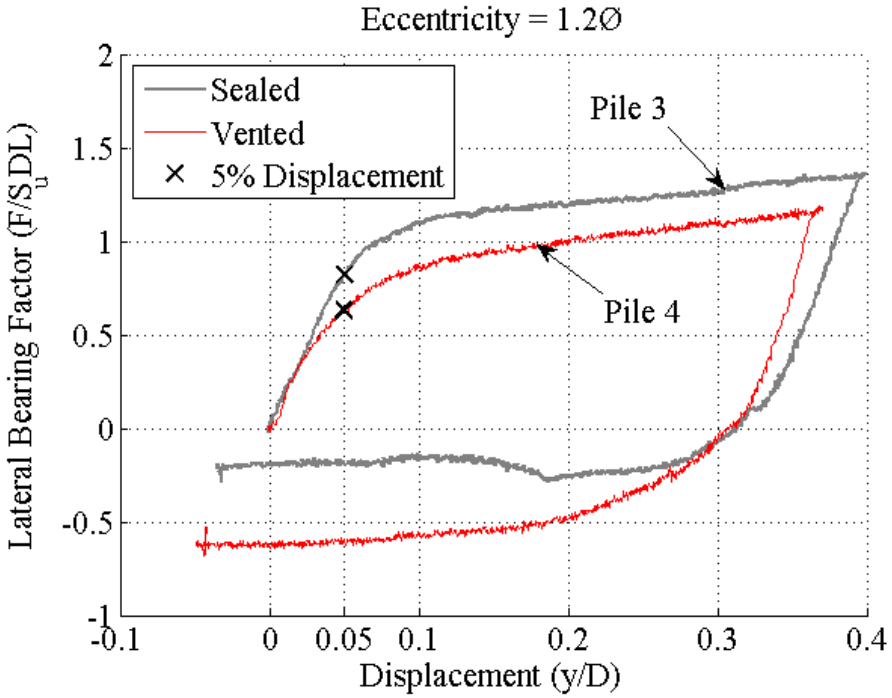

Fig. 6.2. Venting effect on load-displacement behavior, eccentricity of 1.2Ø

Monotonic moment loading curves are provided in Fig. 6.3-6.4. Though only monotonic loading will be discussed the capacity curves do include unloading. From these results it can be clearly seen that venting the caissons has a large effect on moment capacity for both load eccentricities. As with the lateral loading curves moment loading shows rotation hardening behavior at large strains.

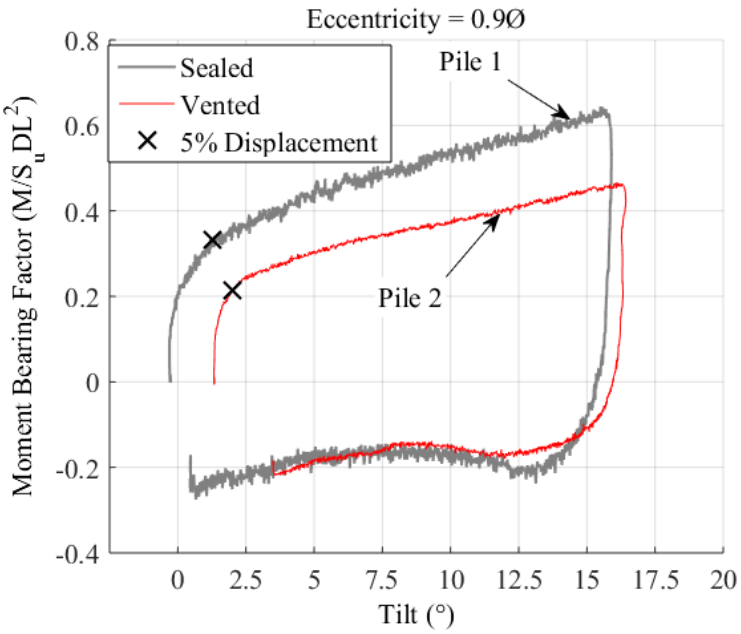

Fig. 6.3. Venting effect on moment-rotation behavior, load eccentricity of 0.9Ø

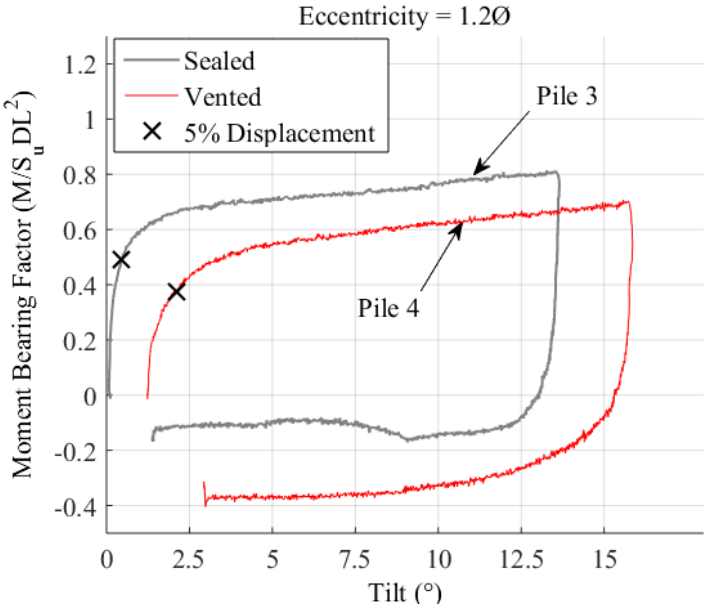

Fig. 6.4. Venting effect on moment-rotation behavior, load eccentricity of 1.2Ø

6.1.2 Effects of Caisson Venting on Capacity

The gravity caissons show a significant drop in normalized lateral and moment capacity when vented. Capacity is defined as magnitude of normalized load at 5% normalized displacement at the soil surface, demarcated with crosses in Fig. 6.1 and Fig. 6.2. This criterion was also used to define moment capacity resulting in tilt at failure being variable, demarcated with crosses in Fig. 6.3 and Fig. 6.4. A service limit definition was used because of the hardening, in all tests a peak load was never reached.

A summary of the effect of caisson venting can be found in Tables 6.2-6.3. Overall venting the caisson resulted in a 35% drop in capacity in both lateral and moment bearing for a load eccentricity of 0.9 diameters. While it resulted in a 23% drop in lateral and moment capacities for a load eccentricity of 1.2 diameters.

Table 6.2. Normalized lateral bearing capacities

Eccentricity	Sealed Bearing Factors	Vented Bearing Factors
	$F/(S_uDL)$	
0.9	0.72	0.47
1.2	0.82	0.63

Table 6.3. Normalized moment bearing capacities

Eccentricity	Sealed Differential Tilt	Sealed Bearing Factors	Vented Differential Tilt	Vented Bearing Factors
	(º)	$M/(S_uDL^2)$	(º)	$M/(S_uDL^2)$
0.9	1.54	0.32	0.63	0.21
1.2	0.34	0.49	0.86	0.38

6.1.3 Effects of Caisson Venting on Depth of Rotation

Venting of the caisson appears to have a dramatic effect on the depth of rotation of a gravity caisson with a length to diameter ratio of two, Fig. 6.5-6.6. Vented caissons start rotating near the height of load application and decrease. At 5% displacement the depth of rotation is approximately at the mid-depth of the caisson, one diameter from the tip. Eventually, they stabilize to 1.5 diameters below the surface, 0.5 diameter from the base.

Sealed caissons behave much differently. Very quickly, their depth of rotation drops below 10 diameters for all tests. Pile 1, in Fig. 6.5, rotates through vertical as it does its depth of rotation increases well above the soil line before dropping. This occurred because the pile was slightly tilted away from the load direction before the test. At 5% displacement the depth of rotation for Pile 1 was approximately 2.25 diameters, right at the base of the caisson, and the depth of rotation for Pile 3 was about 6 diameters, or 4 diameters from the base. As with the vented caissons, depth of rotation appears to stabilize at 1.5 diameters at large rotations.

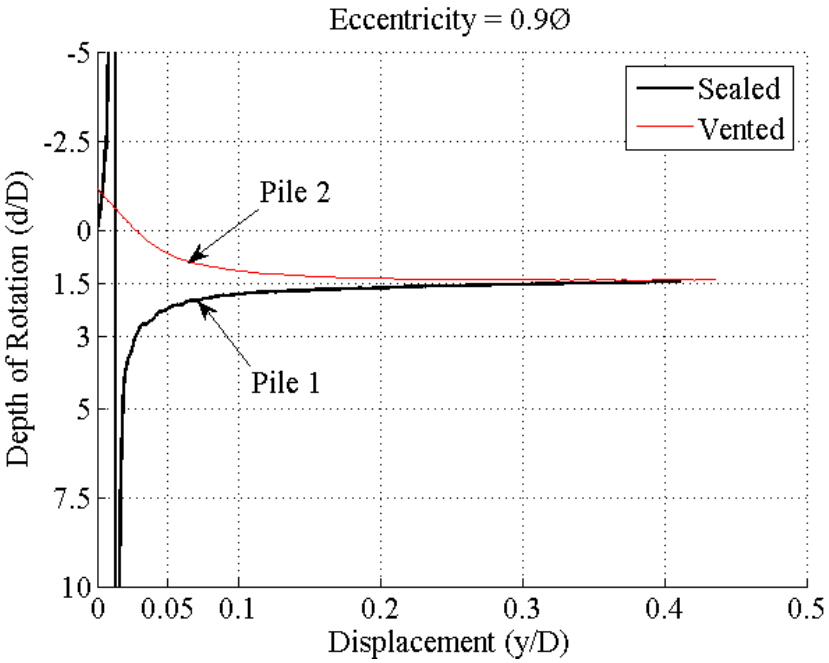

Fig. 6.5. Venting effect on depth of rotation, load eccentricity of 0.9Ø

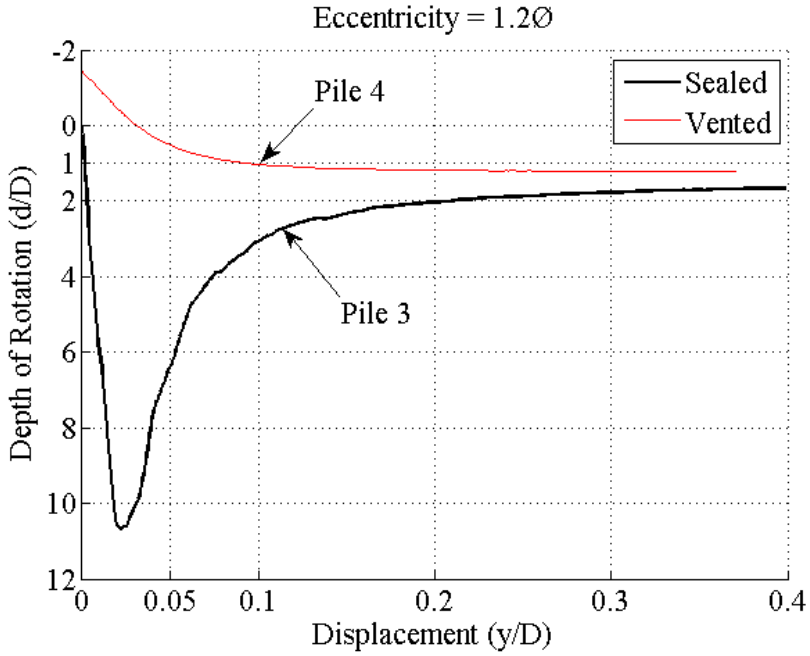

Fig. 6.6. Venting effect on depth of rotation, load eccentricity of 1.2Ø

6.1.4 Effects of Caisson Venting on Stiffness

Stiffness is taken as either force per displacement for lateral stiffness, or moment per rotation for rocking stiffness, below 5% normalized displacement. Lateral stiffnesses are presented in Fig. 6.7 – 6.8 they were not normalized since effective stress in the 1-g model were not typical of those in a field prototype. In general it is difficult to comment on venting's effect on global lateral stiffness given the small sample size. It appears that venting softens the caissons response below 5% normalized displacement for load eccentricity of 1.2 diameters. However, it appears that venting had little to no effect on Piles 1 and Pile 2 with load eccentricity of 0.9 diameters.

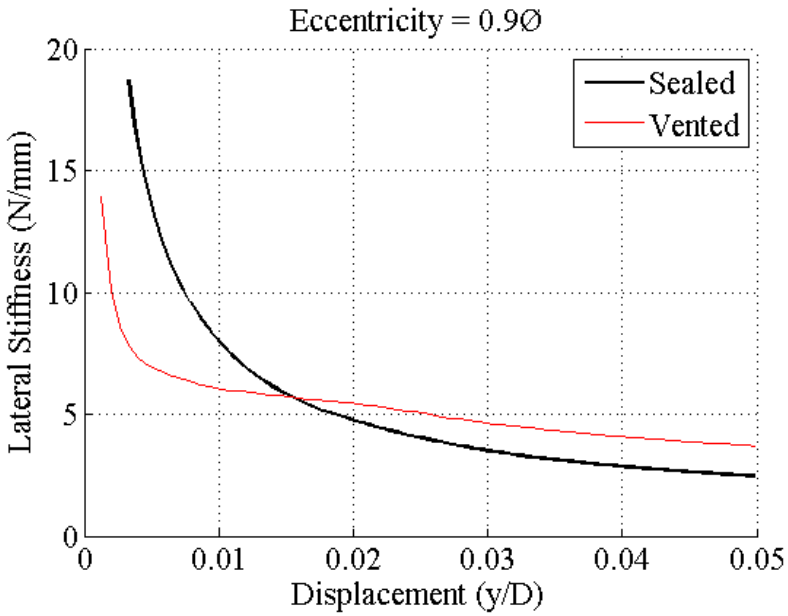

Fig. 6.7. Venting effect on lateral stiffness, load eccentricity of 0.9Ø

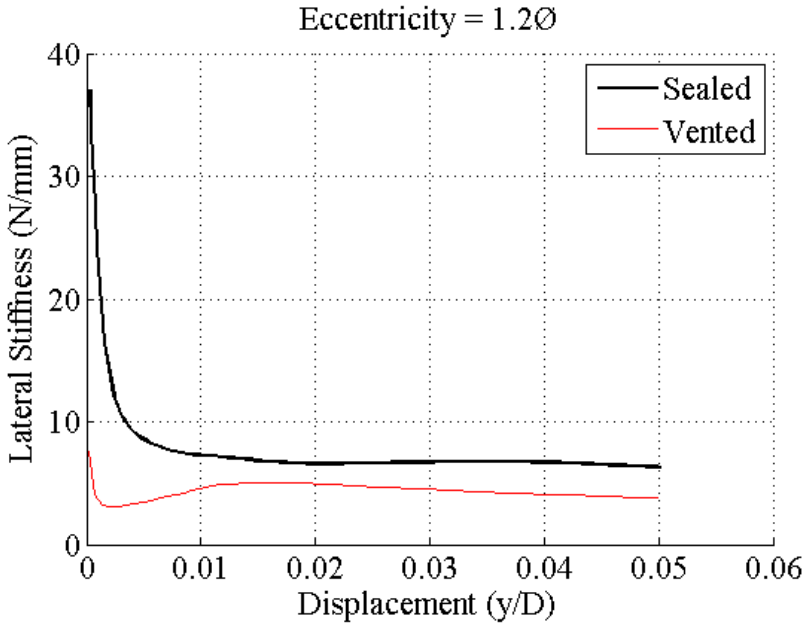

Fig. 6.8. Venting effect on lateral stiffness, load eccentricity of 1.2Ø

Moment or rocking stiffnesses are presented in Fig. 6.9 – 6.10 they were not normalized since effective stress in the 1-g model were not typical of those in a field prototype. In general it is difficult to comment on venting's effect on global rocking stiffness given the small sample size and the fact Fig. 6.9 and Fig. 6.10 indicate different behavior.

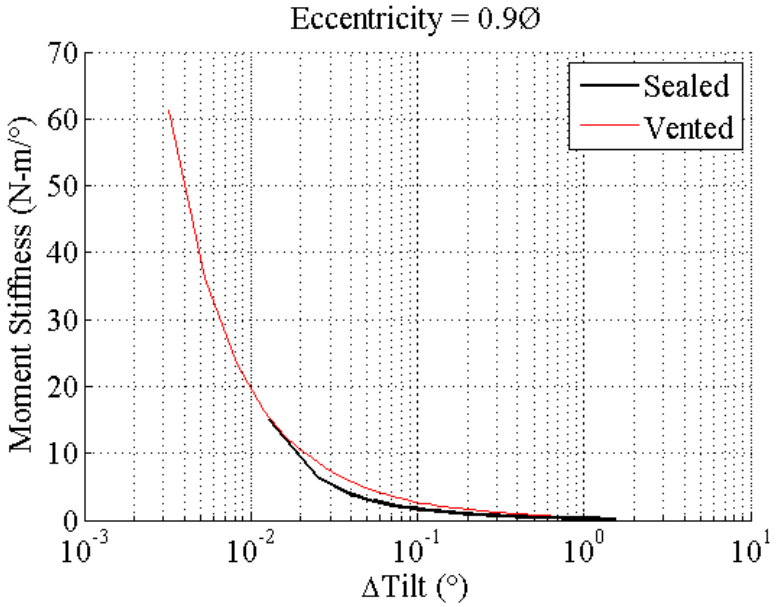

Fig. 6.9. Venting effect on rocking stiffness, load eccentricity of 0.9Ø

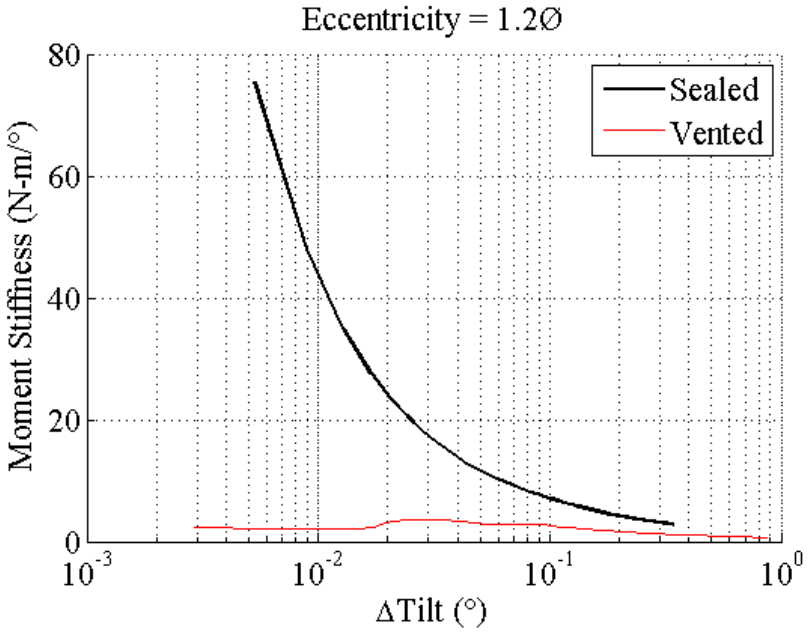

Fig. 6.10. Venting effect on rocking stiffness, load eccentricity of 1.2Ø

6.1.5 Effects of Caisson Venting on Strain Hardening

Strain hardening is defined here as the increase of force or moment with displacement or rotation at magnitudes beyond 5% normalized displacements at the soil surface. Lateral load strain hardening behavior, presented in Fig. 6.11 – 6.12, was not normalized since effective stress in the 1-g model were not typical of those in a field prototype. As with the stiffnesses the small sample size makes it difficult to make any definitive statements. However, these results indicate that venting resulted in more hardening for load eccentricity of 0.9 diameters, Piles 1 and 2, and less hardening for load eccentricity of 1.2 diameters, Piles 3 and 4.

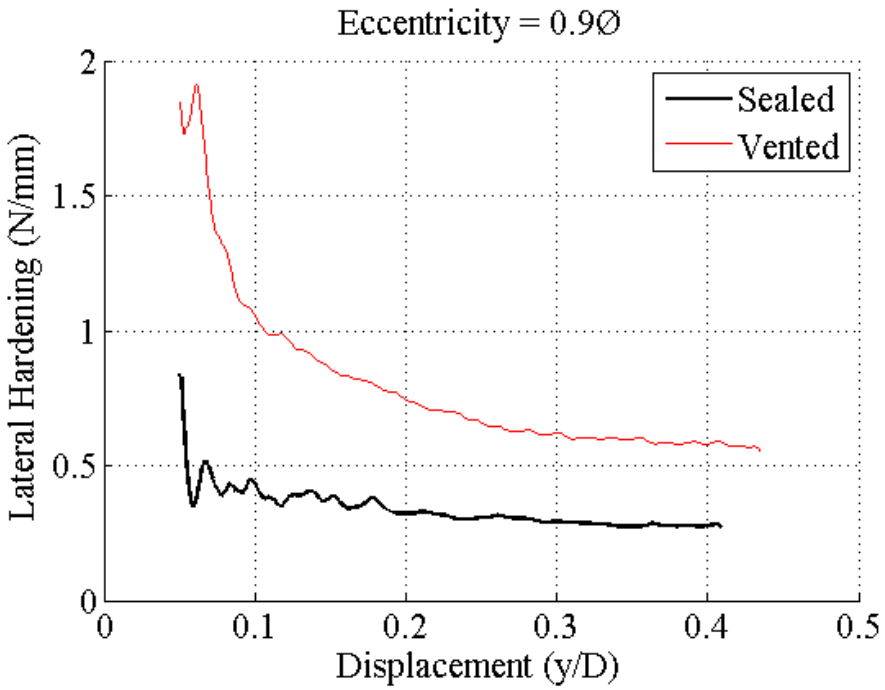

Fig. 6.11. Venting effect on lateral strain hardening, load eccentricity of 0.9Ø

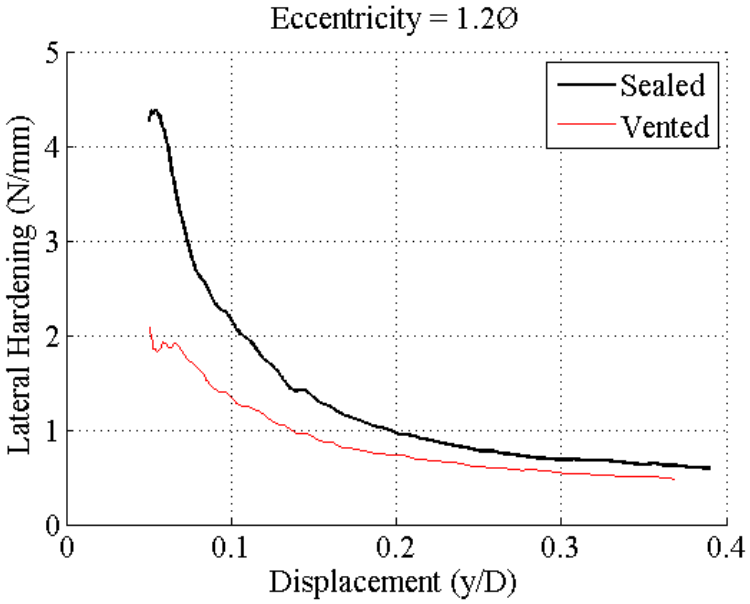

Fig. 6.12. Venting effect on lateral strain hardening, load eccentricity of 1.2Ø

Rotational strain hardening behavior, presented in Fig. 6.13 – 6.14, was not normalized since effective stress in the 1-g model were not typical of those in a field prototype. As with the lateral strain hardening the small sample size makes it difficult to make any definitive statements. However, as with lateral strain hardening results indicate that venting resulted in more hardening for load eccentricity of 0.9 diameters, Piles 1 and 2, and less hardening for load eccentricity of 1.2 diameters, Piles 3 and 4.

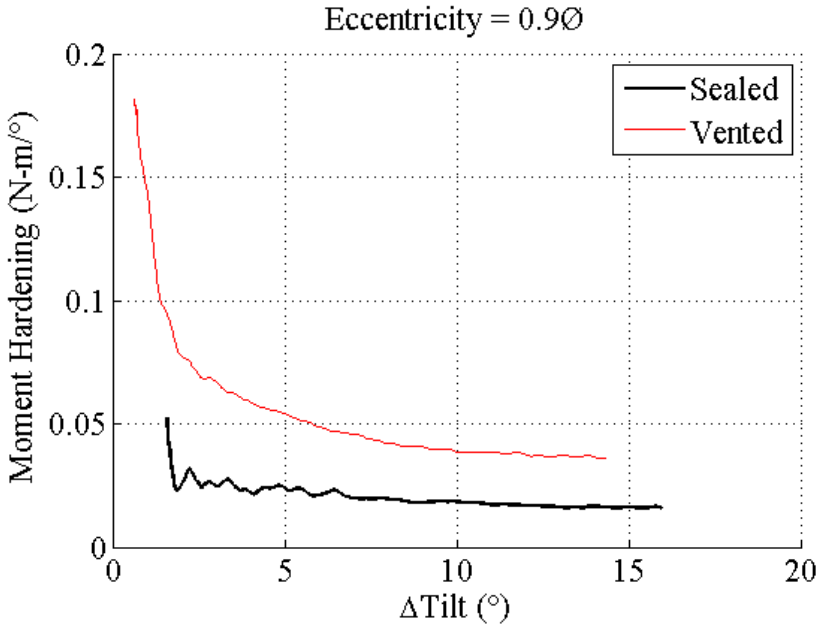

Fig. 6.13. Venting effect on moment strain hardening, load eccentricity of 0.9Ø

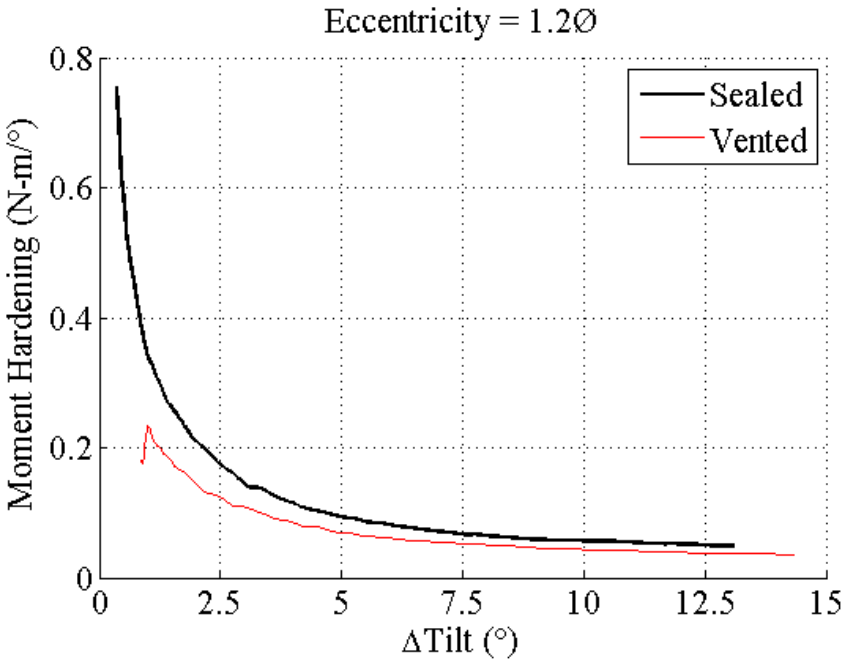

Fig. 6.14. Venting effect on moment strain hardening, load eccentricity of 1.2Ø

6.1.6 Comments on Failure Mechanisms in Regards to Caisson Venting

The behavior presented in 6.1.1 -6.1.5 is not consistent with conventionally assumed failure mechanisms for caissons. It is common to assume a rotational failure surface below or around the caisson with a constant point of rotation as in Fig. 6.15 as in Aubeny et al. (2003), Murff and Hamilton (1993), and Palix et al. (2011). This assumption of a circular or spherical failure mechanism should not be impacted by internal suction within the pile since the base is isolated by a shear plane. It should not matter whether the pile is solid or hollow, because there is no mechanism for plug deformation relative to the caisson.

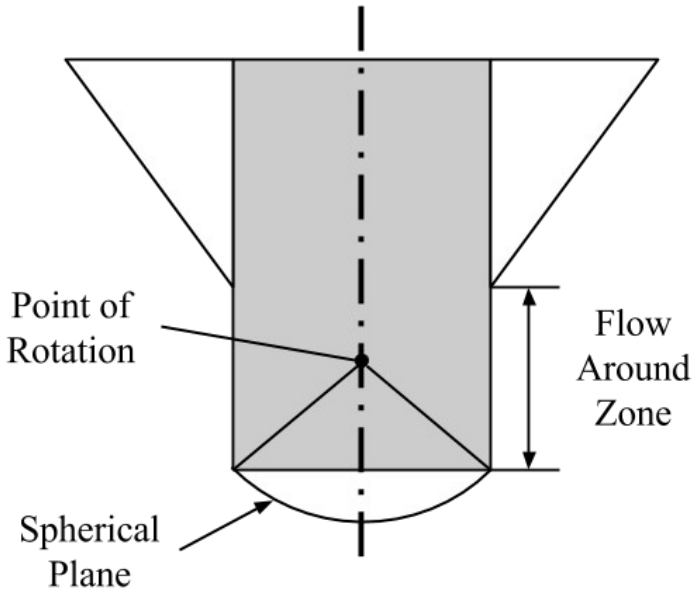

Fig. 6.15. Traditional spherical base failure mechanisms

The vented behavior does align reasonably well traditional failure mechanisms. Though depth of rotation is not constant, it only varies by two diameters and is at one diameter from the base at 5% normalized displacement. The stabilized point of rotation is then half a diameter from the base, still within the caisson. Overall this is a reasonable approximation.

The results from the sealed tests do not match traditional mechanisms. Sealing the caisson increases lateral and moment capacity by as much as 30%. The depth to center of rotation is not constant, as it varies significantly during loading, especially at small magnitudes of displacement, reaching well below 10 diameters. At a failure criterion of 5% normalized displacement for all load eccentricities the depth of rotation is still well below the caisson, 2.25-6 diameter. This indicates that sealing the caisson provides significant resistance to rotation at small magnitudes of displacement/rotation. In turn this leads the pile to translate more than expected and have a larger capacity.

Though visualization experiments can and should be conducted to examine the failure mechanisms for sealed eccentrically loaded caissons with a length to diameter aspect ratio of 2, conjecture can be made at this point. The caisson attempts to rotate when loaded eccentrically. If vented: the caisson overcomes internal skin friction and moves relative to its plug. If sealed: the caisson translates while rotating until lateral resistance is greater than the rotational resistance provided by the plug. These responses are possible if the caissons center of rotation was located between its center-line and its toe. This could occur if the downward resistance at the toe is greater than the upward resistance at the heel.

6.2 Centrifuge Modeling Experimental Results

6.2.1 Experiment Overview

Four scale model piles were also tested in the 160 g-ton geotechnical centrifuge to examine at Rensselaer Polytechnic Institute (RPI) (Elgamal et al. 1991) the effects of load eccentricity and displacement amplitude on the cyclic behavior of the caissons. The

full setup for the experiment can be found in 4 DESIGN OF CENTRIFUGE AND 1-G EXPERIMENTS, but for clarity; the gravity caissons had a length to diameter aspect ratio of two and kaolinite soil's water content varied from 62% to 66%. Each caisson was cycled under three sets of 50 one-way cycles further information can be found in the centrifuge testing matrix in Table 6.4. These experiments were followed by monotonic failure tests which are discussed by Murali (2015).

As noted in Table 6.4, each pile had a different vertical load due to self-weight from the caisson cap, stem, and sensor platform. Monopile vertical capacity was estimated as 225 Newtons. Approximately 60%-78% of vertical capacity was engaged.

Table 6.4. Centrifuge testing matrix

Phase	Pile	Load Eccentricity	Model Vertical Load	Test	Displacement Magnitude	Initial Load Direction	Cycles
#	#	Ø	Newtons	#	Ø (%)	±(X,Y,Z)	#
2	2	1.20	135	1	2.5	+X	50
				2	5	+X	50
				3	10	+X	50
3	1	2.25	155	1	2.5	+X	50
				2	5	+X	50
				3	10	+X	50
	2	1.10	175	1	2.5	+X	50
				2	5	+X	50
				3	10	+X	50
	3	3.05	150	1	2.5	+X	50
				2	5	+X	50
				3	10	+X	50

The application of the cyclic load was highly influenced by the RPI 4 Degree of Freedom (DOF) robot and the pile behavior. The maximum acceleration of the robot is 50 mm/s^2. To ensure a constant strain rate over all tests it was necessary to minimize robot velocity to 2 mm/s. This ensured that at least 95% of each motion was at a constant velocity.

Prior to making any move, the robot runs an anti-collision algorithm. The computation time to complete these calculations varied significantly as seen in microelectro-mechanical systems (MEMS) accelerometer output in Figure 6.16. Thus the load frequency and period were not constant. Target load periods (calculated from robot acceleration, velocity, and displacement magnitude) and applied load periods (total cycling time divided by number of cycles) have been provided in Table 6.5. On average the pauses caused by the robot's anti-collision algorithm added 3.95 seconds to the load period, at model scale.

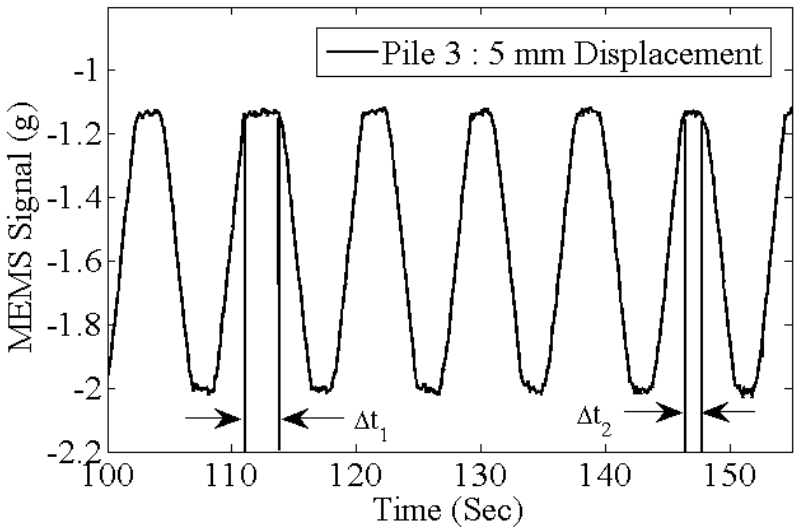

Fig. 6.16. Example of pauses between RPI 4 DOF robot motions

Table 6.5. Target versus applied load periods

Eccentricity	Test	Target Load Period	Applied Load Period
Ø	#	s	s
1.10	1	1.64	5.65
	2	2.88	6.54
	3	5.38	9.02
1.20	1	1.64	6.54
	2	2.88	7.40
	3	5.38	10.15
2.25	1	1.64	5.48
	2	2.88	6.56
	3	5.38	8.81
3.05	1	1.64	5.52
	2	2.88	6.53
	3	5.38	8.85

6.2.2 Initial Orientation of Caissons

During centrifuge spin up all three piles tilted slightly in the –X direction. There was a concern that this initial movement of the monopiles would result in the LVDT sensors going out of range during testing; so, during Phase 3 Experiment 2, Monopiles 1 and 3 were straighten, towards the +X direction, to ensure the sensors would stay in range. Both piles were allowed to sit for five minutes of model time (19 days in prototype time, N^2 for diffusion) to allow any generated excess pore pressures to dissipate. Adjusted locations (robot coordinates) and initial pile tilts from MEMS accelerometers, after adjustment, are provided in Table 6.6. It should be noted that initial orientation of the pile is difficult to ascertain because the basket angle relative to centrifuge gravity was not measured during the experiments. The largest sources in uncertainty in orientation of the basket like come from the robot changing the baskets center of gravity and applied

moment about the basket hinge, see (Beemer et al. 2016). However, given that the model was centered in the basket and the RPI robot was centered when it was over Monopile 2; it is likely error in initial tilt is at most on the order of ±1°-3°.

Table. 6.6. Initial pile orientation

Eccentricity	Pre-Spin Up Robot Location	Post-Spin Up Robot Location	Adjusted Robot Location	Adjusted Tilt MEMS
Ø	X (mm)	X (mm)	X (mm)	(°)
1.10	227	213	227	1.20
1.20	406.8	401	401	3.72
2.25	417	412	413	4.63
3.05	598	579.5	585	2.15

6.2.3 Caisson Settlement

The RPI 4 DOF robot was used to measure caisson settlement. After each test the robot was stepped in 0.1 mm increments until it fully connected with a pile stem. The measurement was taken as change in robot vertical coordinate. Settlement appears to be dependent on load eccentricity, Table 6.7, even though Phase 3 Experiment 2 Pile 1's stem was constructed from steel and weighed about 40 % more than Monopile 4's aluminum stem. It is possible that the combined lateral-vertical load resulted in plastic failure, as noted earlier 60% - 78% of vertical capacity was engaged. Given the high ratio of vertical to horizontal load any plastic deformation would include a significant vertical component.

Table 6.7. Pile settlement

	Phase 2	Phase 3		
Test	Pile 2	Pile 1	Pile 2	Pile 3
#	Caisson Model Settlement (mm)			
1	2	4	3	5
2	2	3	2	3
3	2	3	3	3
Total:	6	10	8	11
Total (Ø/*L*):	5.9%	9.8 %	7.8 %	10.8 %
Eccentricity:	1.20 Ø	2.25 Ø	1.10 Ø	3.05 Ø

6.2.4 General Observations on Caisson Cycling

A few general observations can be made from time series plots of moment at the top of the caisson, horizontal load, and rotation, Fig. 6.17. Comparisons are made for varying load eccentricity or constant displacement at height of load application. Trends were constant across displacement magnitudes, so only results from displacement magnitudes of 5% diameter are provided; results for 2.5% and 10% diameter displacement magnitudes can be found in APPENDIX A.

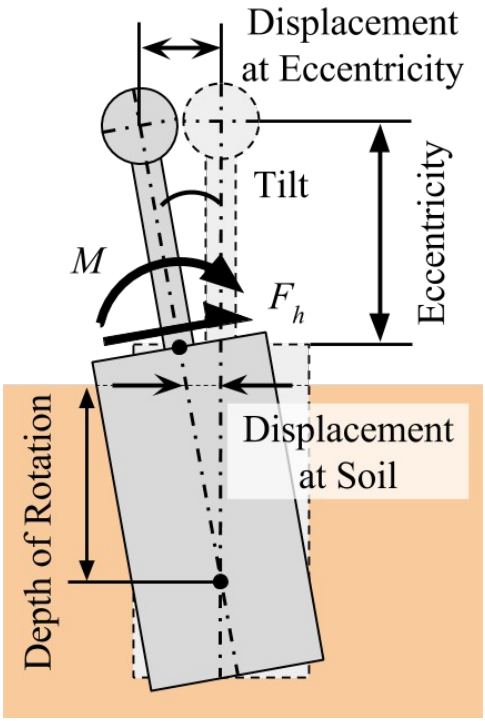

Fig. 6.17. Pile loading schematic

When loaded eccentrically reactive moment at the top of the caisson peaks at the first cycle and stabilizes quickly, Fig 6.18. Though loading is one-way, significant negative moment is measured when returning to the initial position. Reactive moment appears to max at a load eccentricity of 2.25 diameters even though Pile 2, eccentricity of 1.10 diameters, was rotated further and displaced further at the soil surface (discussed below), its moment resistance was less. This could be due to combined loading effects; that is, the combined effected of loading laterally and rotationally simultaneously resulted in a decreased rotational resistance.

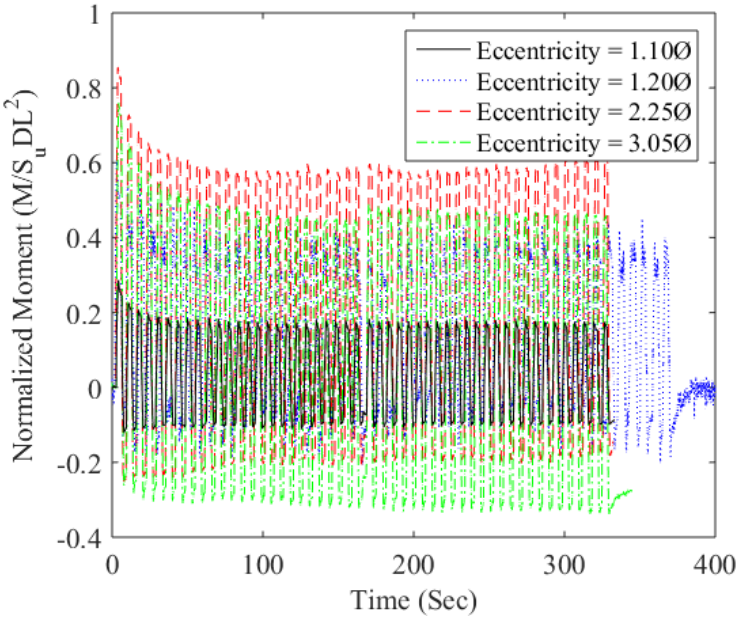

Fig. 6.18. Normalized moment 5% Ø displacement at eccentricity

As with reactive moment, peak horizontal load occurred on the first cycle and quickly stabilized, Fig. 6.19. The highest resistance to horizontal load occurred at and eccentricity of 2.25 diameters. With Phase Three Pile 2, eccentricity of 1.20 diameters or Phase 3 Pile 2, eccentricity of 1.10 diameters, which are about equal. This a function of moment resistance and moment arm.

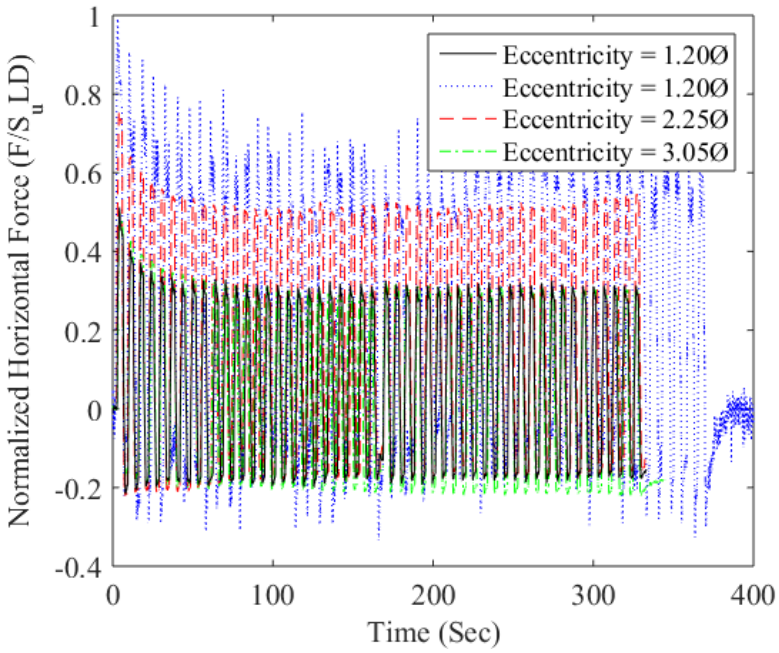

Fig. 6.19. Normalized horizontal load 5% Ø displacement at eccentricity

Caisson rotation appears extremely stable. It decreases with increasing eccentricity, Fig. 6.20. This in part is due to compliance in the pile stems. Long stems will bend instead of rotating the caissons. It is difficult to comment on how this impacts the experimental results. It is surprising, however, that Pile 1 with an eccentricity of 2.25 diameters had the largest resisting moment even though Pile 2 with an eccentricity of 1.10 diameters rotated more. A possible explanation can be seen by examining the piles depth of rotation.

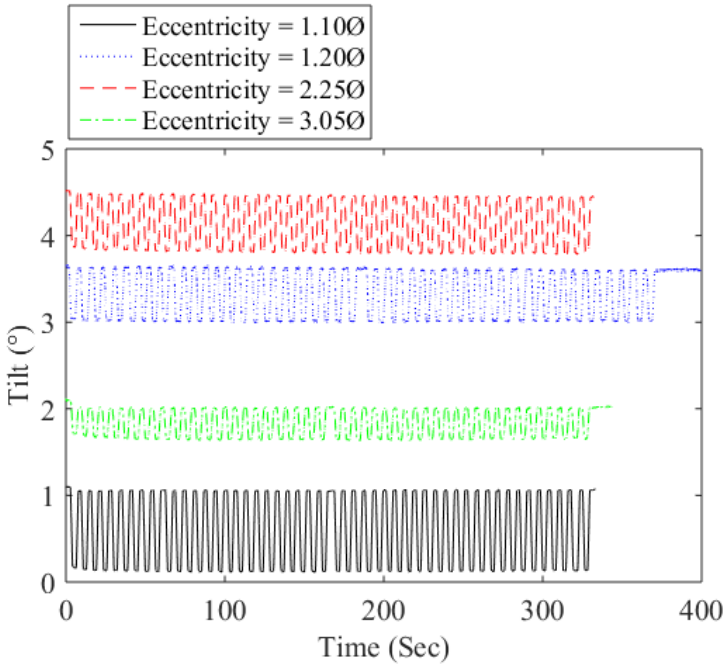

Fig. 6.20. Tilt 5% Ø displacement at eccentricity

Caisson behavior appears to be highly dependent on depth of rotation, as seen in Fig. 6.21a-6.21b. As expected with a one-way motion depth of rotation cycled between zero and a maximum. Phase 3 Pile 2, eccentricity of 1.10, had the largest depth of rotation while Pile 1, eccentricity of 2.25 diameter, had the smallest. This corresponds well with the measure reactive moment, Fig. 6.18, with the smallest depth of rotation resulting in the most resistance to moment. Large depth of rotations would result in more translation than rotation, so the two piles with the largest initial tilt Phase 3 Pile 1 and Phase 2 Pile 2 also had the smallest depth of rotation. This would suggest that depth of rotation is a function of both eccentricity and orientation.

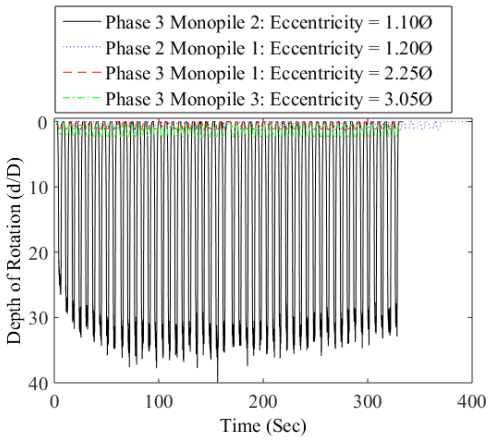

Fig. 6.21a. Depth of Rotation 5% Ø displacement at eccentricity

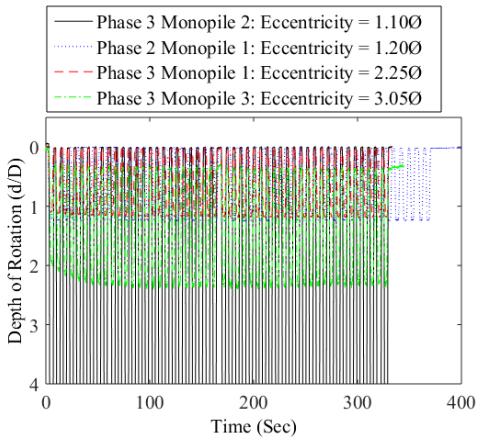

Fig. 6.21b. Depth of Rotation 5% Ø displacement at eccentricity (zoomed)

All displacement controlled loading was conducted the height of pile eccentricity, as such displacement at the soil surface was not controlled. Displacements at the soil surface were calculated from applied displacements at eccentricity and measured pile tilt. As seen in Fig. 6.22 - Fig. 6.24 all tests had differential displacements between 0.5% and 6.0% caisson diameters. Also of note is that Phase 3 Pile 1 and Pile 3 (eccentricities of 2.25 and 3.05 diameters, respectively) appear to walk slightly while cycling, Fig. 6.22. These piles also walked in different directions.

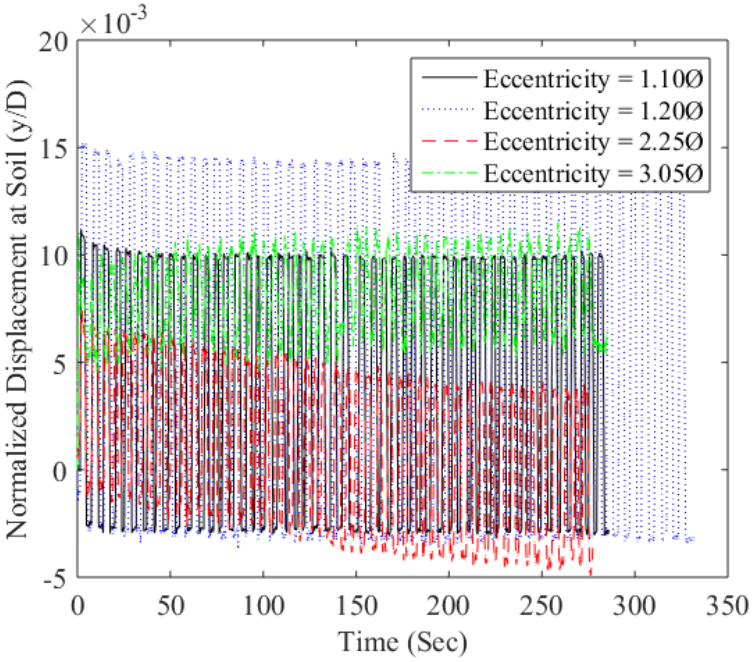

Fig. 6.22. Displacement at the soil surface 2.5% Ø displacement at eccentricity

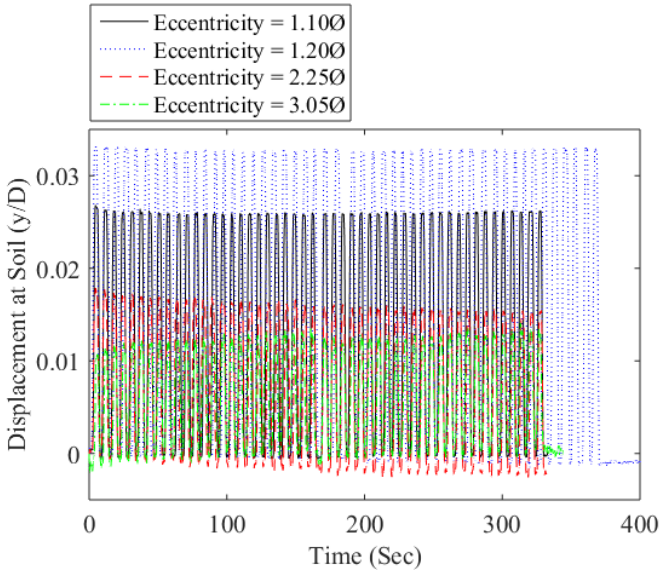

Fig. 6.23. Displacement at the soil surface 5% Ø displacement at eccentricity

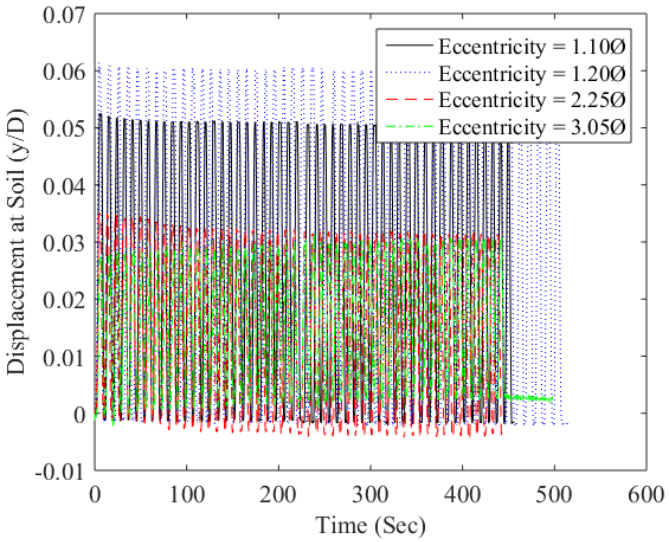

Fig. 6.24. Displacement at the soil surface 10% Ø displacement at eccentricity

6.2.5 Effect of Cyclic Displacement on Moment Resistance

Comments can also made regarding resisting moment dependent on displacement magnitude at eccentricity. Resisting moment plots for Phase 3 Experiment 2 Pile 1, Fig. 6.25, this behavior was typical between load eccentricities and plots of other eccentricities can be found in the APPENDIX A. In all cases the loads leveled out after approximately 11 cycles (given the applied load periods in Table 6.5). Steady state maximum moment (per cycle) appears to react nonlinearily to increasing displacement magnitudes. Doubling the displacement magnitudes from 2.5% of caisson diameter to 5% of diameters results in an approximate 75-80% increase in resistance while a further doubling results in only a 15-30% decreased in resistance. This result aligns well with previous assumptions that 5% normalized displacement being the criterion for serviceability limit state. That is, most of the pile's resistance is engaged at a normalized displacement of 5% of diameter. Also of note is the fact that the return moment is much larger for a displacement at eccentricity of 2.5% of diameter than 5% or 10% of

diameter. This could be the result of the initial cyclic test remoulding the soil or gapping occurring at larger displacements, but the evidence is inconclusive

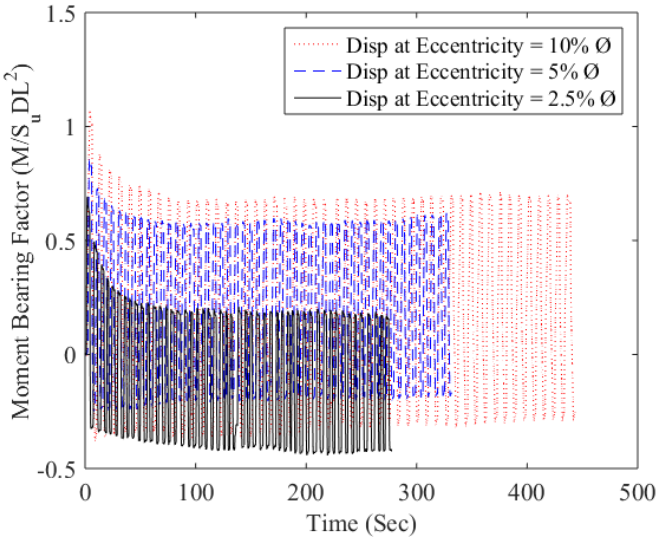

Fig. 6.25. Effect of displacement magnitude at eccentricity on reactive moment Phase 3 Experiment 2 Pile 1, eccentricity = 2.25Ø

6.2.6 Cyclic Rocking Behavior

Some general comments can be made from an example the moment-rotation behavior. Provided in Fig. 6.26 are all the moment-rotation plots for Phase Three Experiment Two Pile One. All other plots can be found in the APPENDIX A. This shows that that the piles exhibit regular behavior while cycling and stabilize quickly, after approximately 10 cycles. Though the cyclic behavior is relatively well behaved, the hysteresis loops do appear to drift slightly over time, with this drift being more prominent at smaller displacement magnitudes. This behavior could be the result of creep during the RPI 4

DOF pauses. This is most apparent in the first two cycle of 2.5% diameter displacement at eccentricity plot in Fig. 6.26.

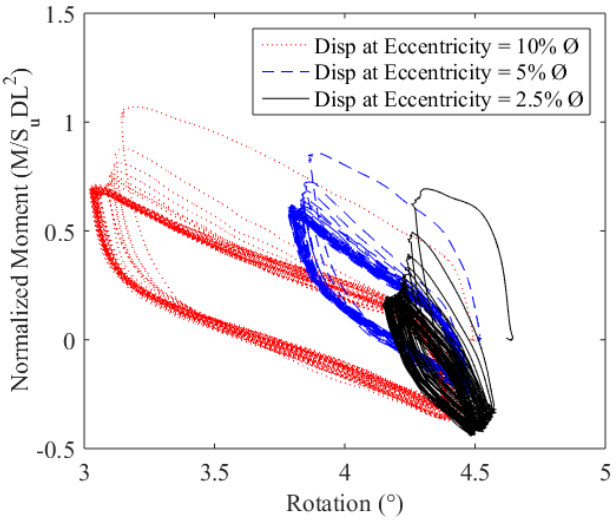

Fig. 6.26. Moment-rotation (rocking) behavior for Phase Three Experiment Two Pile One

The behavior of Pile 1 in Phase Three Experiment Two appears to be nearly linearly elastic at a displacement of 2.5% diameter and an eccentricity of 2.25 diameters after the first cycle. At higher displacements magnitudes the behavior is significantly nonlinear. Significant damping occurs during all tests and the magnitude of damping appears to increase with increasing displacement magnitude.

6.2.7 Cyclic Rocking Stiffness Behavior

Stiffness was analyzed for each half cycle with results divided into load and unload curves. A plot of global load stiffness curves from Pile 1 in Phase Three Experiment Two

is provided in Fig. 6.27a-6.28b. It can be seen that stiffness curves are relatively linear, beyond 0.05 degrees, on a log-log plot, suggesting a power law can be used to describe the behavior. Though there is trend towards lower stiffness with increasing number of cycles, it is much more apparent in the unload curves, Fig. 6.28a-6.28b, than in the load curves. This could possibly be due to the load direction; due to initial tilt of the piles during centrifuge spin up all piles were rotated towards vertical during the loading rather than away from vertical. The unload curve may represent as a more typical behavior, but is also reworked by the load cycle. Stiffness curves for all piles can be found in the APPENDIX A.

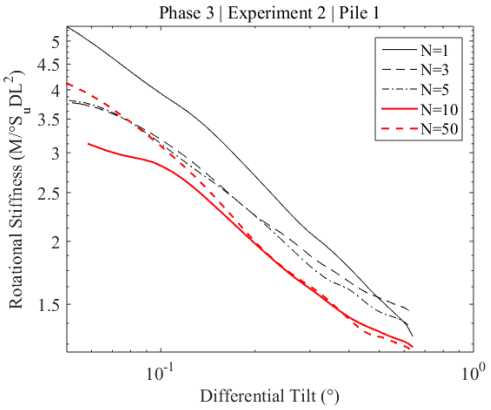

Fig. 6.27a. Stiffness load curves displacement at eccentricity = 5% Ø

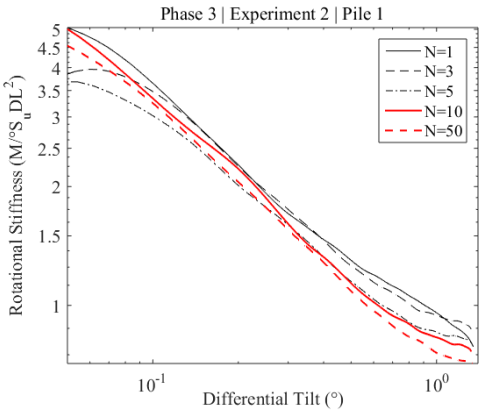

Fig. 6.27a. Stiffness load curves displacement at eccentricity = 10% Ø

In all cases, Fig. 6.27a-6.28b, stiffness appears to stabilize by the tenth cycle with the largest decrease after the first cycle. This can be seen more clearly in Fig. 6.29a-6.30b, where cycles 10-50 are a jumble of pick-up-sticks. Though the stiffness curves appear fairly linear beyond 10 cycles, their behavior does not appear consistent in terms number

of cycles. In Fig. 6.29a and 6.30a cycle 50 is stiffer than cycles 15-45. It is believed this behavior could be due to pile settlement, 6.2.3. As the pile settles, it engages stiffer soil that was consolidated by the self-weight of the pile.

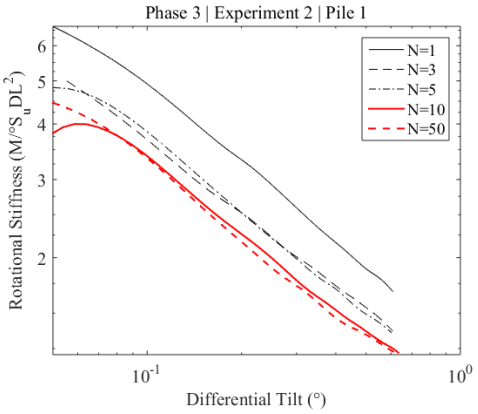

Fig. 6.28a. Stiffness unload curves displacement at eccentricity = 5% Ø

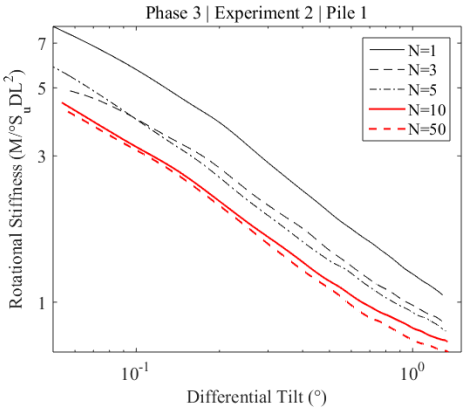

Fig. 6.28b. Stiffness unload curves displacement at eccentricity = 10% Ø

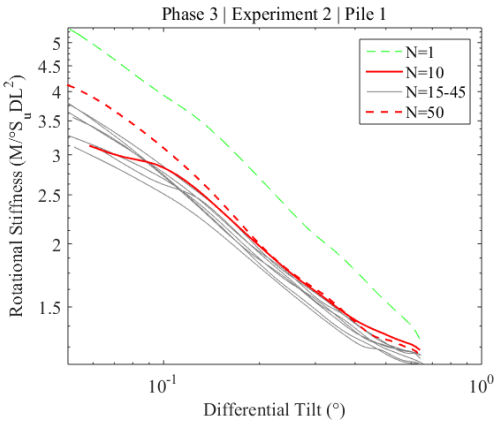

Fig. 6.29a. Stiffness load curves cycles 10-50 disp. at eccentricity = 5% Ø

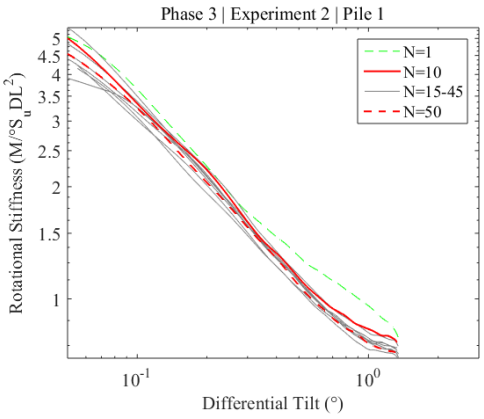

Fig. 6.29b. Stiffness load curves cycles 10-50 disp. at eccentricity = 10% Ø

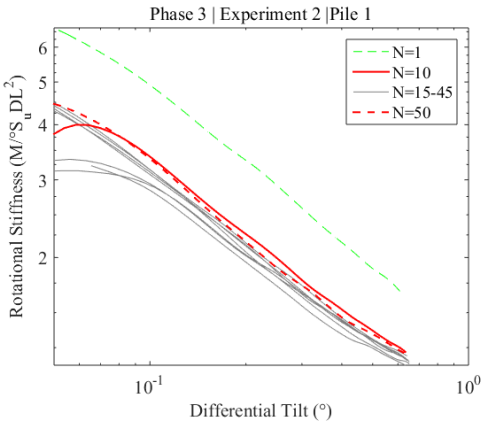

Fig. 6.30a. Stiffness unload curves cycles 10-50 disp. at eccentricity = 5% Ø

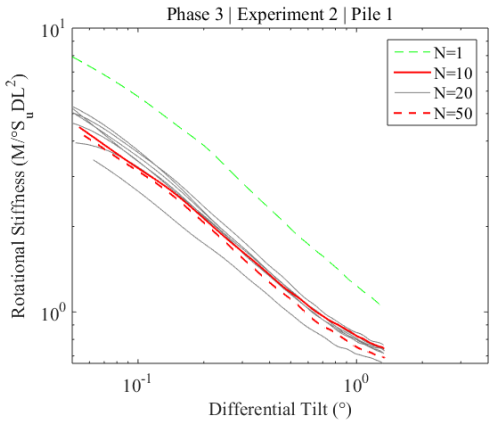

Fig. 6.30b. Stiffness unload curves cycles 10-50 disp. at eccentricity = 10% Ø

Given the relatively stable rocking behavior between 10 and 50 cycles, it is possible to fit power law curve over all cycles 10-50, as demonstrated in Fig. 6. 31. The power law parameters, to the form of Eq. (6.1) or logarithmically, Eq. (6.2). All plots of the power law fitting can be found in the APPENDIX A. When using referencing the coefficient of determination in log scale it appears the power law fitting worked well. The exceptions being for Phase 2 Experiment 2 Pile 2 and low displacement magnitudes for Phase 3 Experiment 2 Pile 3. As noted in Chapter 4 strain gages in Phase 2 did not behave well. This reduced data quality substantially. For Phase 3 Experiment 2 Pile 3 the combination of load at large eccentricity and small displacements pushed the limits of the sensors resulting in lower quality data.

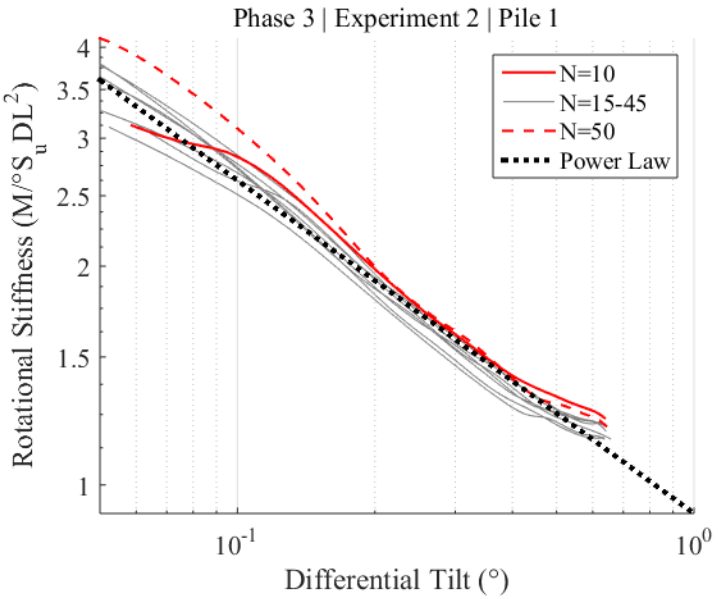

Fig. 6.31. Stiffness curve fitting process example

$$K_r = b\theta_d^m \tag{6.1}$$

$$\log(K_r) = m \cdot \log(\theta_d) + \log(b) \tag{6.2}$$

where: K_r is the steady state normalized rocking stiffness, θ_d is the differential rotation of the pile, and m and b are the power law parameters

Table 6.8. Power law fitting parameters for load rocking stiffness 10-50 cycles

Eccentricity	Displacement Magnitude	*b*	*m*	R^2 (logarithmic)	Range
∅	∅ (%)	—	—	—	°
1.10	2.5	0.307	-0.433	0.926	0.05-0.40
	5	0.249	-0.515	0.971	0.05-0.80
	10	0.218	-0.625	0.964	0.05-1.50
1.20	2.5	0.451	-0.614	0.705	0.09-0.23
	5	0.400	-0.547	0.704	0.06-0.50
	10	0.357	-0.498	0.727	0.05-1.30
2.25	2.5	1.161	-0.388	0.897	0.05-0.30
	5	0.914	-0.458	0.967	0.05-0.60
	10	0.772	-0.586	0.971	0.05-1.00
3.05	2.5	1.735	-0.387	0.606	0.05-0.10
	5	1.138	-0.504	0.8613	0.05-0.30
	10	0.874	-0.580	0.927	0.05-0.80

A summary of all power law fitting parameters are provided in Table 6.8-6.9. A number of comments can be made regarding the steady state (10-50 cycles) rocking stiffness behavior given in Tables 6.8-6.9. Further comments will be made in reference to the logarithmic scale, where *m* will be referred the rate of change of rocking stiffness with respect to differential angle and log(*b*) will be referred to as the rocking stiffness intercept. First, it should be noted that the stiffness intercept, log(*b*), reduces with each subsequent cyclic test on the same pile. This is very likely caused by conducting a number of displacement controlled cyclic test directly after one another. Hopefully, this was minimized by running small displacement magnitudes first. Regardless, this would result in softening of the soil around the pile.

Table 6.9. Power law fitting parameters for unload rocking stiffness 10-50 cycles

Eccentricity	Displacement Magnitude	*b*	*m*	R^2 (logarithmic)	Range
∅	∅ (%)	—	—	—	°
1.10	2.5	0.306	-0.376	0.882	0.05-0.40
	5	0.240	-0.521	0.980	0.05-0.80
	10	0.221	-0.634	0.981	0.05-1.50
1.20	2.5	0.746	-0.382	0.325	0.07-0.20
	5	0.607	-0.226	0.091	0.09-0.50
	10	0.426	-0.547	0.803	0.09-1.30
2.25	2.5	0.998	-0.504	0.968	0.06-0.30
	5	0.902	-0.519	0.982	0.05-0.60
	10	0.799	-0.603	0.980	0.05-1.00
3.05	2.5	0.223	-1.027	0.335	0.05-0.13
	5	0.464	-0.651	0.606	0.05-0.25
	10	0.524	-0.452	0.558	0.05-0.60

In most cases the rate of change, or slope m, of steady state rocking stiffness, K_r, increases with increasing displacement/rotation. Under small displacements rocking stiffness is less variable than under large combined displacements/rotations. In general unload curves exhibited higher rate of change indicating rocking stiffness changed more after the soil had been remolded by the initial pile loading.

6.2.8 Cyclic Rocking Damping Ratio

The steady state rocking damping ratio was difficult to determine from these experiments. First, the quality of the strain gage was low in Phase 2 Experiment 2 Pile 2, especially at small displacements/rotations. Noise in the data can be seen to clear affect the area inside of the cyclic hysteresis loops, Fig. 6.32. Second, the pauses built into the

RPI 4 DOF robot impact the shape of the hysteresis loops. Discussion on the robot pauses can be found in 6.2.1 and discussion on its impact to data interpretation can be found in 5.2.9. Specifically, creep, or possibly pore pressure dissipation, occurs during each pause. This results in either: additional tilt of the pile or decreased load on the pile. In general this increases the size of the hysteresis loop beyond what it would be if the pause had not occur. This makes the damping ratio appear much larger than it would actually be. There is no simple way to fix this issue; however, a number of loading cycles appear to have very little creep. They have been used to estimate the foundations damping ratio in Phase 3 Experiment 2 Pile 1 and Pile 2. Unfortunately, this could not be done for Pile 3 in Phase 3 Experiment 2, even its best hysteresis loops exhibited significant change during the RPI 4 DOF pauses, Fig. 6.33. Where the blank spot at 2° is where the pause occurred and can be seen to increase the area of the hysteresis loop.

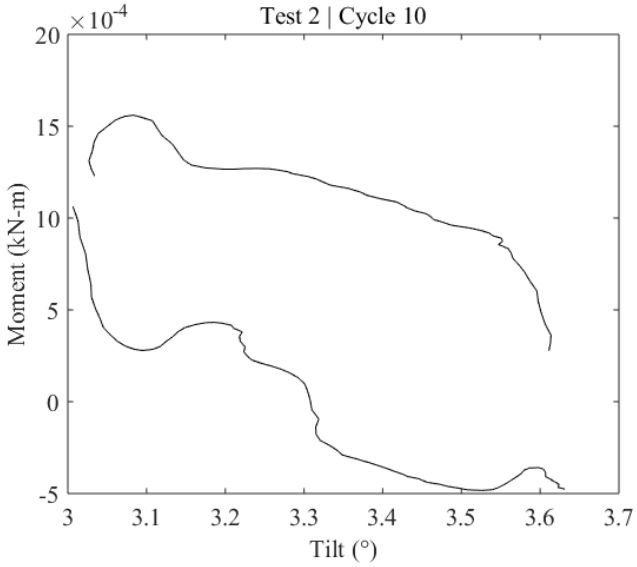

Fig. 6.32. Sample hysteresis loop from Phase 2 Experiment 2 Pile 2

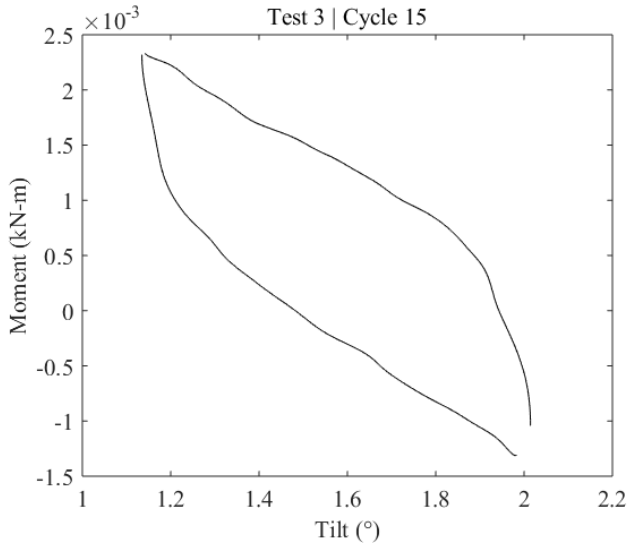

Fig. 6.33. Example of highest quality hysteresis loop from Phase 3 Experiment 2 Pile 3

Results from Phase 3 Experiment 2 Pile 1 and Pile 2, Fig 6.34a-6.34b, suggest gravity caissons with an aspect ratio of 2 have a rocking damping ratio between 0.12 and 0.22. Given the limitation of these test due to the RPI 4 DOF robot these are the best estimates that can be made at this time. There appears to be a trend for deceased damping ratio with smaller displacements/rotations. It is also possible that damping ratios are higher for increasing load eccentricity at the same displacement magnitude at eccentricity. However, the data quality is low and further testing is necessary

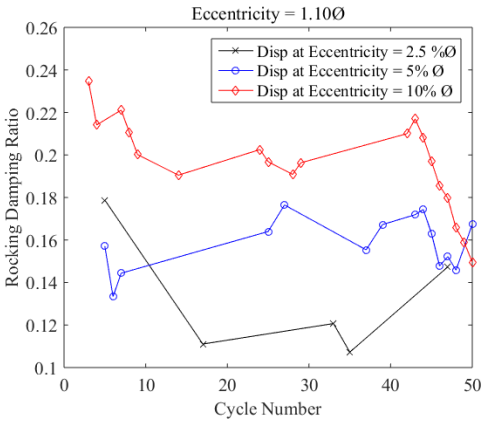

Fig. 6.34a. Damping Pile 2, Phase 3 Experiment 2

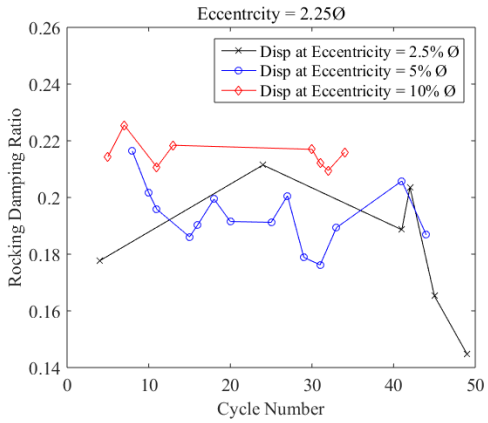

Fig. 6.34b. Damping Pile 1, Phase 3 Experiment 2

6.2.9 Pore Pressure at Caisson Mid-Depth

Pore pressures were only successfully measured near the mid-depth of two piles: Pile 2 in Phase 2 Experiment 2 and Pile 3 in Phase 3 Experiment 2. As noted in Chapter 4 and there were a number of issues with the pore pressure sensors that led to unsuccessful data collection. However, when measurements were collect they were of high quality. All pore pressure plots for the six successful tests are provided in the APPENDIX A. Samples for displacement at eccentricity of 5.0 % pile diameter are provided in Fig. 6.35a-6.35b. These show that the results from Phase 2 Experiment 2 Pile 2 were significantly impacted by the longer pause duration, Table 6.5, Compared to Phase 3 Experiment 2 Pile 3. The results from Phase 3 Experiment 2 Pile 3 should be more representative of real cyclic behavior. Fig. 6.35b clearly showed the pile was loaded under undrained conditions. As the pile cycled the pore pressure did slowly dissipate. This suggests that if the pile had been allowed to cycle for another 100 to 300 cycles it could have reached a stead state condition about hydrostatic conditions. More testing is recommended without the robot pauses and with an increased number of cycles.

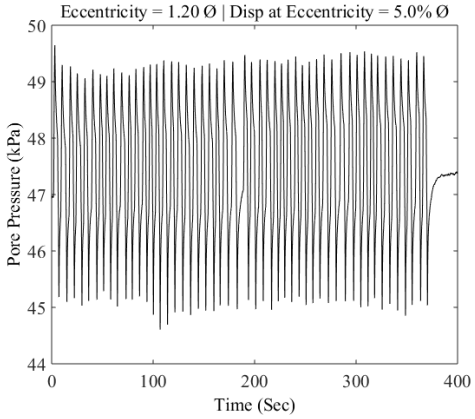

Fig. 6.35a. Measured pore pressures Phase 2 Experiment 2 Pile 2

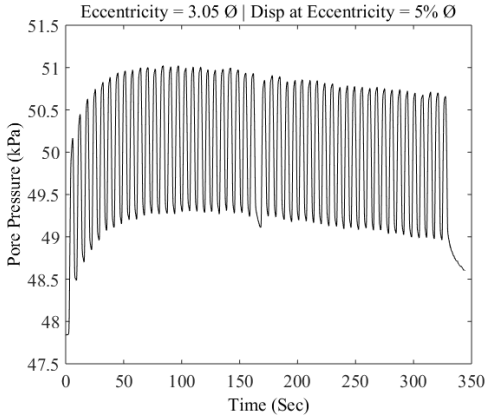

Fig. 6.35b. Measured pore pressures Phase 3 Experiment 2 Pile 3

6.2.10 Caisson Reaction Force

An estimate of the reaction force against the caisson was estimated from strain gages 1.27 cm (0.5 in) from the bottom of the caisson. Specifically, the gages located 90 degrees from the load direction. It appears that data from Pile 1 and Pile 2 in Phase 3 Experiment was of high quality. Pile 3 from Phase 3 Experiment 2 and Pile 2 from Phase 2 Experiment 2 appeared to be noisy, Fig. 6.36, additionally one or two gages from each of these piles failed. The magnitude of noise vs signal can be seen after approximately 450 seconds in Fig. 6.36. Additionally, it is believed the steps in the signal are artificial.

All plots of strain at the side of the caisson and calculated reaction force at the bottom of the caisson for Phase 3 Experiment 2 Pile 1 and Pile 2 can be found in the APPENDIX A. Test 3 for Phase 3 Experiment 2 Pile 2 is provided as an example in Fig. 6.37. Of note is the fact that the reaction force increases over time in spite of a reduction in global reactive horizontal force at the pile cap Fig. 6.19. It is likely this is due to the pile settlement, 6.2.3. Though the pile loses strength overall as the soil remoulds, its tip sinks into strong deeper soil. This impacted is even furthered due to the piles self-weight consolidating the soil.

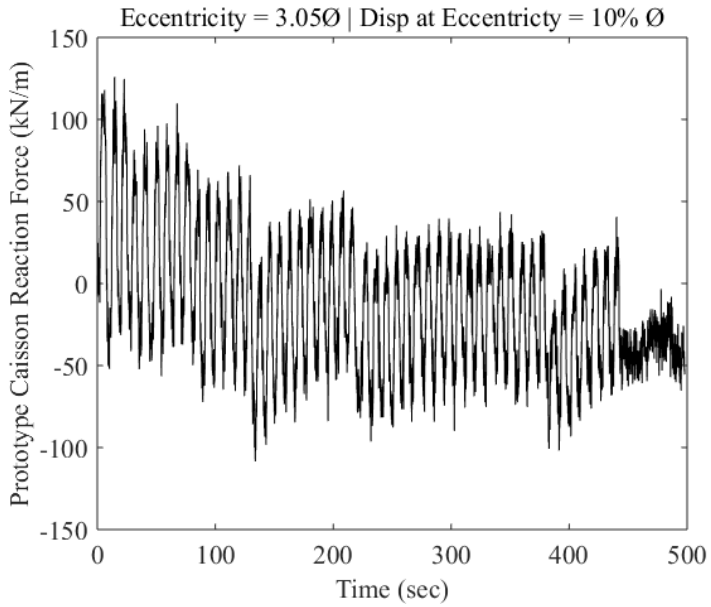

Fig. 6.36. Example of low quality data from Phase 3 Experiment 2 Pile 3

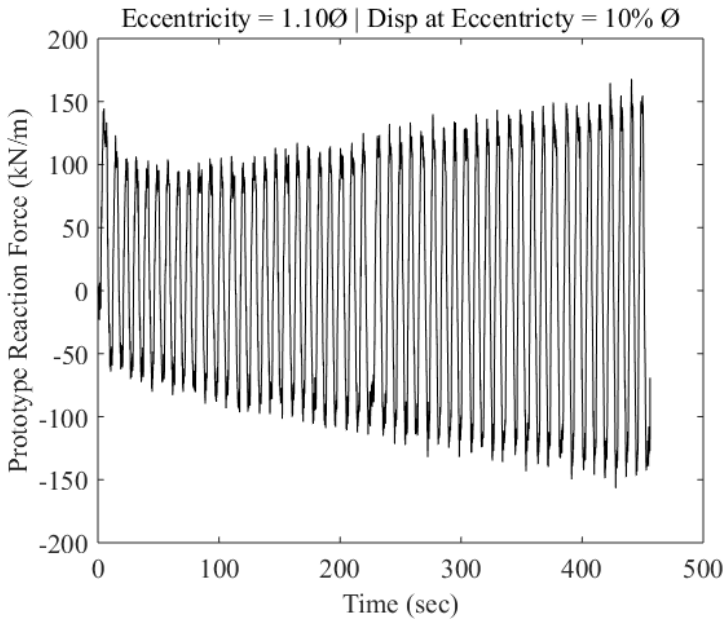

Fig. 6.37. Reaction force at caisson base Phase 3 Experiment 2 Pile 2

7 CONCLUSIONS

7.1 Overview

This dissertation covers a range of topics relevant to geotechnical centrifuge scale modeling and the behavior of squat gravity caissons. This includes a description of the two dimensional gravity field on the plane of Earth's gravity and centrifugal acceleration independent of centrifuge geometry, how to use low g single-axis microelectro-mechanical systems (MEMS) accelerometers to measure orientation within a geotechnical centrifuge model, and the rocking/rotational behavior of gravity caisson/monopiles with a length to diameter aspect ratio of two. Though the work on 2D centrifuge gravity and MEMS accelerometers is more or less complete, for the two dimensional case, the chapters on caissons provides opportunities for future work.

7.2 Centrifuge Model 2D Gravity in the Vertical Rotational Reference Frame

Presented in this paper is a methodology for determining the magnitude and direction of the 2D gravity field throughout a centrifuge model independent of centrifuge type or geometry. Instead the magnitude and orientation of a single reference vector relative to the model local coordinate system and the angular velocity of the centrifuge are used.

The mechanics of drum and beam centrifuges were also examined in terms of the new methodology. Specifically, the orientation of model local coordinates relative to the centrifuge gravity field was addressed relative to centrifuge geometry and mechanics. This investigation resulted in some interesting conclusions for a beam type centrifuge:

1. A movement of the centrifuge basket's center of gravity along its center-line could easily result in a change in basket angle, ξ. As an example, a displacement of 25% of the centrifuge radius would result in a change in basket angle, ξ, and therefore a change in the angle between centrifuge gravity and model local coordinates, β, of 0.4°, at high-g, Fig. 2.5.
2. A movement of the basket's center of gravity off of its center-line by as little as

20% width to length, d/L, (20 cm in a one meter long basket) can result in a change in angle, β, of 10°, at high-g, Fig. 2.7.

3. It was analytically confirmed, under different assumptions, that friction in the basket hinge can easily result in a change in angle, β, of 1° at high-g, Fig. 2.9, as initially reported in (Xuedoon, 1988). Additionally, the method presented in this research is generalized for any applied moment about the basket hinge, such as that applied by hoses and cables, Equation 2.33.

For a drum type centrifuge it is important to note that the angle between a reference centrifuge gravity vector and the model local coordinates, β, is dependent on the radial distance to the model, Equations 2.18 and 2.1. With the angle being theoretically 90° at the centrifuge axis and 0° at infinite radial distance.

The angle of centrifuge gravity with respect to the model local coordinates, β, can have significant impact on geotechnical models and sensors. For example, in modeling slight slopes, as related to lateral spreading and submarine landslides, having centrifuge gravity at an angle of 1° to 10° relative to vertical could be very significant. This could also be significant for measurements of rotational stiffness of foundations within the serviceability limits, offshore wind turbines have a recommended limit of 0.5° (DNV, 2007). Additionally, sensors such as MEMS accelerometers measure orientation relative to centrifuge gravity. If gravity were angled relative to a model, errors in absolute orientation would be introduced. By defining the orientation of model local coordinates with respect to centrifuge gravity, as done here, it is possible to measure and correct for orientation of centrifuge gravity with respect to a model.

7.3 Use of a MEMS Accelerometer to Measure Orientation in a Geotechnical Centrifuge

A number of conclusions can be drawn from the updated quasi-static orientation theory for single-axis MEMS accelerometers and its experimental validation.

1. Low-g single-axis MEMS accelerometers can be used to make fine measurements of orientation in a high-g environment when rotated into centrifuge gravity. In this research it was possible to measure the absolute orientation of a platform constructed at a 4° angle to the basket floor while centrifuge gravity was greater than 65 g.

2. A measurement made by a single-axis MEMS accelerometer will be significantly impacted by cross-axis acceleration, acceleration applied perpendicular to its measurement direction, Fig. 3.8-3.10. This in turn impacts measurements of orientation relative to centrifuge gravity, Table 3.9. In this research a maximum difference of 1.60º (0.85º on average) was seen when a cross-axis acceleration correction was used versus when it was neglected. Errors of this magnitude could be significant in experiments within serviceability limits or in experiments on slight slopes.

3. The cross-axis correlation factor, C_x, and intercept, b_x, should be determined with the accelerometer perpendicular to centrifuge gravity. If the calibration is conducted at an angle to centrifuge gravity, β, that angle will be incorporated into the correlation factor, C_x, Equation 3.12.

7.4 Cyclic Eccentric Loading on Squat Caissons and Piles

7.4.1 Conclusions

The initial results from the 1-g and geotechnical centrifuge experiments provide some insights into the rotational behavior of squat caisson/monopiles in soft clay:

1. Venting has a significant impact on gravity caisson monotonic rotational capacity. In undrained 1-g experiments, venting the caissons resulted in a 23%-35% drop in both lateral and moment capacity, Fig. 6.1 – 6.4 and Tables 6.2-6.3. It is believed this is due to interaction between the soil plug and the caisson. If this is true it could indicate that conventionally assumed failure mechanisms for

open ended piles cannot be readily applied to squat caissons. The difference between predicted and measured depth of rotation for sealed piles also corroborates this, Fig. 6.5-6.6.

2. Monotonically loaded squat gravity caissons show a hardening behavior at large displacements, Fig. 6.1-6.4 and Fig. 6.7–6.10. This behavior is unexpected and more study is recommended.

3. Monopiles with vertical gravity loads settle significantly under cyclic loading; as much as 10.8% of pile diameter, Table 6.7. This was directly measured and can be inferred by the measurements of strain in the base of the caisson shell, Fig. 6.37. This may be the result of combined loading causing vertical plastic deformation. It is estimated the caissons were loaded to 60%-78% of their vertical capacity. This would put them at the top of any moment-vertical load-horizontal load interaction curve. It would be reasonable, that any applied moment or horizontal load would result in plastic deformation. With such a large component of gravity load, vertical displacement would be expected.

4. Moment resistance appears highly dependent on depth of rotation. The caisson with the most moment resistance had the shallowest depth of rotation; in spite of load eccentricity, Fig. 6.18 compared to Fig. 6.21a-6.21b. It is possible that this behavior is the result of combined horizontal and moment loading. At larger depths of rotation the piles translate more (have more horizontal load) resulting in a decrease in moment resistance. Additionally, initial tilt could have an impact on depth of rotation. Increasing tilt appear to result in a decreased depth of rotation and therefore increased resistance to moment loading. This can be seen in the data were the piles with the shallowest depth of rotation had the most initial tilt, Table 6.6 and Fig. 6.21a-6.21b.

5. Monopile tilt stabilizes very quickly under displacement controlled loading, Fig. 6.20. This is in spite of measured pore pressures indicating that a cyclic, stead state, mean pore pressure had not been reached. It would have

(qualitatively) taken an extra 50 to 250 cycles to reach mean steady state.

6. Caissons appear to translate horizontally under displacement controlled loading. This is only prominent at large eccentricities and small displacements, Fig. 6.22-6.24. Though field loading is not displacement controlled, this is an interesting result that should be examined further.

7. Cyclic rocking of the caisson appears to be significantly affected by the Rensselaer Polytechnic Institute inflight Four Degree of Freedom Robot's tendency to pause every half cycle, Fig. 6.16. During each pause the caissons appeared to creep slightly, see first cycles in Fig. 6.26. This effects pile orientation and moment, especially when loaded.

8. Cyclic rocking stiffness can be modeled fairly well by a power law curve, Fig. 6.31 and Table 6.8-6.9. Pile stiffness drops significantly over the first 10 cycles, after which it fluctuates without significant change magnitude. In fact, there were a number of cases where cycle number 50 was stiffer than cycles 15-45, Fig. 6.29a-6.30b. It is believed this behavior is due to settlement. As the foundation settles it engages stiffer soil, as seen in the increased resistance its base, Fig. 6.37. This may be the typical behavior of gravity caissons as their large gravity loads could result in vertical displacements in the field.

9. It was difficult to evaluate caisson damping ratio due to the pauses in the loading protocol. Pile creep, every half cycle, changed the size of the hysteresis loop in an unpredictable manner. However, some general trends appeared. Damping ratios are likely between 10% and 20%, Fig. 6.34a-6.34b. Additionally, damping ratio decreases with smaller magnitudes of rotation/displacements and also appeared to increase with increasing load eccentricity, also Fig. 6.34a-6.34b. However, experiments without creep/pauses should be conducted to verify these results.

10. It is possible to get high quality measurements of strain in the caisson shell

during rotational loading in the centrifuge. However, it is difficult to interpret results from this data in a quantitative manner. This data may be more useful if compared to FEM models. However, general trends can be observed such as increasing or decreasing strain, Fig. 6.37.

7.4.2 Future Work

This research has identified a number of cases for future work regarding the behavior of gravity caissons/monopiles. The immense quantity of data with little to no data to compare to means future studies are necessary. Additionally, issues with loading protocols/devices also necessitates the need for further study.

1. First it is recommended that all geotechnical centrifuge testing be re-conducted with a different loading system. The robot used in these studies paused for an indeterminate amount of time each half cycle resulting in creep of the pile. This in turn effected the foundation's damping ratio and likely its stiffness. That being said the centrifuge data is still of high quality and is meaningful, as long as considerations are made for the atypical loading scheme.
2. Initial results indicate depth of rotation to be the driving factor behind rotational resistance. It would be beneficial to assess the variables that affect depth of rotation such as: load eccentricity and initial orientation of the foundation.
3. Settlement of gravity caissons could play an important role in their behavior. It would be beneficial to study the combined moment-vertical-horizontal behavior to determine if plasticity theory can predict caisson settlement.
4. Surprisingly, caisson venting has a large impact on capacity. It is recommended that the failure mechanisms of vented versus sealed caissons be study to discover why this is the case. This could be done with planar imaging experiments or 3D imaging experiments in translucent soil.
5. Caisson walking under one-way loading should be examined. Even though these

experiments were displacement controlled, it is reasonable to wonder if there is any tendency for squat gravity caissons to walk under constant one-way wind or wave loading?

REFERENCES

Acosta-Martinez, H., Gourvenec, S., and Randolph, M. F. (2011). "Centrifuge study of capacity of a skirted foundation under eccentric transient and sustained uplift." *Géotechnique*, ICE, (4), 317–328.

Al-Defae, A., and Knappett, J. (2014). "Centrifuge modeling of the seismic performance of pile-reinforced slopes." *J. Geotech. and Geoenviron. Eng.*, ASCE, 140(6), 1–13.

Allmond, J. D., Hakhamaneshi, M., Wilson, D. W., and Kutter, B. L. (2014). "Advances in measuring rotation with MEMS accelerometers." *Proc. of the 8th Int. Conf. on Phys. Model. in Geotech.*, C. Gaudin and D. White, eds., CRC Press, Perth, 353–359.

Anagnostopoulos, C., and Georgiadis, M. (1993). "Interaction of axial and lateral pile responses." *J. of Geotech. Eng.*, ASCE, 119(4), 793–798.

Andersen, K. H., and Lauritzsen, R. (1988). "Bearing capacity for foundations with cyclic loads." *J. of Geotech. Eng.*, ASCE, 114(5), 540–555.

Aubeny, C. P., Han, S. W., and Murff, J. D. (2003). "Inclined load capacity of suction caissons." *Int. J. for Numer. and Anal. Met. in Geo.*, Wiley, 27(14), 1235–1254.

Barrette, P. D., Phillips, R., Clark, J. I., Crocker, G., and Jones, S. J. (1999). "Flexural behavior of model sea ice in a centrifuge." *J. of Cold Reg. Eng.*, ASCE, 13(3), 122–138.

Beemer, R. D., Murali, M., Aubeny, C. P., and Biscontin, G. (2016). "Considerations for use of MEMS accelerometers to measure orientation in a centrifuge." *In Preparation*.

Beemer, R. D., Murali, M., Biscontin, G., and Aubeny, C. P. (2015). "Theory on measuring orientation with MEMS accelerometers in a centrifuge." *IFCEE*, ASCE, San Antonio.

Bennett, V., Abdoun, T., Shantz, T., Jang, D., and Thevanayagam, S. (2009). "Design and characterization of a compact array of MEMS accelerometers for geotechnical instrumentation." *Smart Struct. and Syst.*, Techno-Press, 5(6), 663–679.

Bhattacharya, S., Murali Krishna, A., Lombardi, D., Crewe, A., and Alexander, N. (2012). “Economic MEMS based 3-axis water proof accelerometer for dynamic geo-engineering applications.” *Soil Dyn. Earthquake Eng.*, Elsevier, 36, 111–118.

Black, J. A., Baker, N., and Ainsworth, A. (2014). “Establishing a 50 g-ton geotechnical centrifuge at the University of Sheffield.” *8th Int. Conf. on Physical Modelling in Geotechnics*, Perth, Australia, 181–186.

Blake, A. P., and O’Loughlin, C. D. (2015). “Installation of dynamically embedded plate anchors as assessed through field tests.” *Can. Geotech. J.*, NRC Research Press, 52(9), 1–13.

Byrne, B. W., and Houlsby, G. T. (2004). “Experimental Investigations of the Response of Suction Caissons to Transient Combined Loading.” *J. Geotech. and Geoenviron. Eng.*, ASCE, 130(3), 240–253.

Chow, S. H., O’Loughlin, C. D., Corti, R., Gaudin, C., and Diambra, A. (2015). “Drained cyclic capacity of plate anchors in dense sand : Experimental and theoretical observations.” *Geotechnique Letters*, ICE, 5(2), 80–85.

Clukey, E. C., Aubeny, C. P., and Murff, J. D. (2004). “Comparison of analytical and centrifuge model tests for suction caissons subjected to combined loads.” *J. of Offshore Mech. and Arct. Eng.*, ASME, 126(4), 364.

Craig, W. H. (2002). “The seven ages of centrifuge modelling.” *Workshop on Constitutive and Centrifuge Modelling*, S. Springman, ed., Balkema, Monte Verità, Ascona, Switzerland.

Craig, W. H. (2014). “Pioneers of centrifuge modelling.” *Proc. of the 8th Int. Conf. on Phys. Model. in Geotech.*, C. Gaudin and D. White, eds., CRC Press, Perth, 421–426.

Dejong, J. T., Yafrate, N., Degroot, D. J., Low, H. E., and Randolph, M. F. (2012). “Recommended practice for full-flow penetrometer testing and analysis.” *Geotech. Test. J.*, ASTM International, 33(2), 1–13.

DNV. (2007). *Offshore standard DNV-OS-J101: design of offshore wind turbine structures*. Hovik, Norway.

Elgamal, A., Dobry, R., and Van Laak, P. (1991). “Design, construction and operation of 100 g-ton centrifuge at RPI.” *Centrifuge 91*, Boulder, CO, 27–34.

Ellis, E., Cox, C., Yu, H., Ainsworth, A., and Baker, N. (2006). "A new geotechnical centrifuge at the University of Nottingham, UK." *6th Int. Conf. Phys. Model. Geotech.*, CRC Press, Hong Kong, 129–133.

Ghayoomi, M., and Wadsworth, S. (2014). "Renovation and reoperation of a geotechnical centrifuge at the University of New Hampshire." *Proc. of the 8th Int. Conf. on Phys. Model. in Geotech.*, CRC Press, Perth, 201–205.

Hamilton, J. M., Dunnavant, T. W., Murff, J. D., and Phillips, R. (1991). "Centrifuge study of laterally loaded behavior in clay." *Centrifuge 91*, Balkema, Rottterdam.

Hoffman, K., Varuso, R., and Fratta, D. (2006). "The use of low-cost MEMS accelerometers for the near-surface monitoring of geotechnical engineering systems." *GeoCongress 2006*, ASCE, Atlanta, 1–6.

Houlsby, G. T., Byrne, B. W., Huxtable, J., and Kelly, R. B. (2005). "Field trials of suction caissons in clay for offshore wind turbine foundations." *Géotechnique*, ICE, 55(4), 287–296.

Jeanjean, P. (2009). "Re-assessment of P-Y curves for soft clays from centrifuge testing and finite element modeling." *2009 Offshore Technology Conference*, Houston, 1–23.

Kim, D.-S., Kim, N.-R., Choo, Y. W., and Cho, G.-C. (2012). "A newly developed state-of-the-art geotechnical centrifuge in Korea." *KSCE Journal of Civil Engineering*, 17(1), 77–84.

Kloor, K. (2013). "Anecdotal evidence of wind Turbine syndrome: collide-a-scape." *Discover Magazine*, <http://blogs.discovermagazine.com/collideascape/?p=11003#.UXWjdbVg_AI> (Apr. 22, 2013).

Lau, B. H. (2015). "Cyclic behaviour of monopile foundations for offshore wind farms." *PhD Dissertation*, University of Cambridge, Cambridgeshire.

Madabhushi, G. (2015). *Centrifuge modeling for civil engineering*. CRC Press, Boca Rotan, FL.

Martin, C. M., and Randolph, M. F. (2006). "Upper-bound analysis of lateral pile capacity in cohesive soil." *Géotechnique*, ICE, 56(2), 141–145.

"MATLAB r2013a." (2013). The MathWorks Inc., Natick, MA.

Matlock, H. (1970). “Correlations for design of laterally loaded piles in soft clay.” *Proc. Offshore Technology Conference*, Houston, 577–588.

Mayne, P. W., Kulhawy, F. H., and Trautmann, C. H. (1995). “Laboratory modeling of laterally-loaded drilled shafts in clay.” *J. of Geotech. Eng.*, ASCE, 121(12), 827–835.

MEMSIC. (n.d.). *CXL-GP series general purpose accelerometer.* San Jose, CA.

Murali, M. (2015). “Characterization of soft clay and the respones of soil-foundation system for offshore applications.” *PhD Dissertation*, Texas A&M University.

Murff, J. D. (1996). “The geotechnical centrifuge in offshore engineering.” *1996 Offshore Technology Conference*, OTC, Houston, OTC 8265.

Murff, J. D., and Hamilton, J. M. (1993). “P-ultimate for undrained analysis of laterally loaded piles.” *J. of Geotech. Eng.*, ASCE, 119(1), 91–107.

Musial, W., and Ram, B. (2010). *Large-scale offshore wind power in the United States*. National Renewble Energy Laboratory, Oak Ridge, TN.

Neukirchner, R. J., and Nixon, J. F. (1987). “Behavior of laterally loaded piles in permafrost.” *Journal of Geotechnical Engineering*, ASCE, 113(1), 1–14.

O’Loughlin, C. D., Gaudin, C., Morton, J. P., and White, D. J. (2014). “MEMS accelerometers for measuring dynamic penetration events in geotechnical centrifuge tests.” *Int. J. of Phys. Modell. in Geotech.*, ICE, 14(2), 1–9.

Oppenheim, I. J., Garrett Jr., J. H., and Ganerial, K. J. (2000). “Potential MEMS applications in civil engineering.” *Space 2000*, ASCE, Albuquerque, 495–501.

Palix, E., Willems, T., and Kay, S. (2011). “Caisson capacity in clay : VHM resistance envelope – Part 1 : 3D FEM numerical study.” *Frontiers in Offshore Geotechnics II*, CRC Press, Perth, 753–758.

Park, D. S. (2014). “The effect of radial G-field on the centrifuge modelling.” *Proc. of the 8th Int. Conf. on Phys. Model. in Geotech.*, CRC Press, Perth, 385–390.

Phillips, R. (1995). “Centrifuge modelling: practical considerations.” *Geotechnical centrifuge technology*, R. N. Taylor, ed., Blackie Academic & Professional, Glasgow, 35–60.

Phillips, R., Clark, J. I., Paulin, M. J., Meany, R., Millan, D. E. L., and Tuff, K. (1994). "Canadian national centrifuge centre with cold regions capabilities." *Centrifuge 94*, Singapore, 57–62.

Pokrovsky, G. I., and Fyodorov, I. S. (1936). "Studies of soil pressures and deformations by means of a centrifuge." *1st Int. Conf. on Soil Mechanics and Foundation Engineering*, Harvard, Cambridge, MA, 70.

Poulos, H. G., and Davis, E. H. (1991). *Elastic Solutions for Soil and Rock Mechanics*. Centre for Geotechnical Research, University of Sydney, Sydney, Australia.

Randolph, M. F. (1981). "The response of flexible piles to lateral loading." *Geotechnique*, ICE, 31(2), 247–259.

Randolph, M. F., and Gourvenec, S. (2011). *Offshore Geotechnical Engineering*. Spon Press, New York.

Randolph, M. F., and Houlsby, G. T. (1984). "The limiting pressure on a circular pile loaded laterally in cohesive soil." *Géotechnique*, Ice Virtual Library, 34(4), 613–623.

Randolph, M. F., Jewell, R. J., Stone, K. J. L., and Brown, T. A. (1991). "Establishing a new centrifuge facility." *Centrifuge 91*, Balkema, Boulder, CO.

Saftner, D. A., Green, Russell, A., Hryciw, R. D., and Lynch, J. P. (2008). "Instrumentation for the NEESR sand aging field experiment." *GeoCongress 2008*, ASCE, New Orleans.

Schofield, A. N. (1980). "Cambridge geotechnical centrifuge operations." *Géotechnique*, ICE, 30(3), 227–268.

Schofield, A. N. (1988). "An introduction to centrifuge modelling." *Centrifuges in Soil Mechanics*, W. H. Craig, R. G. James, and A. N. Schofield, eds., Balkema, Rotterdam, 1–9.

Scott, R. F. (1977). "Model pile testing by centrifuge." *Annual Meeting Papers, Division of Production*, American Petroleum Institute, Houston.

Scott, R. F. (1983). "Centrifuge model testing at Caltech." *Int. J. of Soil Dynamics and Earthq. Eng.*, 2(4), 188–198.

Shaeffer, D. K. (2013). "MEMS inertial sensors: A tutorial overview." *IEEE Communications Magazine*, IEEE, 51(April), 100–109.

Silicon Design Inc. (2013). *Model 2012*. Kirkland, WA.

Snyder, B., and Kaiser, M. J. (2009). "A comparison of offshore wind power development in europe and the U.S.: patterns and drivers of development." *Applied Energy*, 86(10), 1845–1856.

Springman, S., Laue, J., Boyle, R., White, J., and Zweidler, A. (2001). "The ETH Zurich geotechnical drum centrifuge." *Int. J. of Phys. Model. in Geotech.*, ICE, 1(1), 59–70.

Stark, N., Kopf, A., Hanff, H., Stegmann, S., and Wilkens, R. (2009). "Geotechnical investigations of sandy seafloors using dynamic penetrometers." *OCEANS 2009, MTS/IEEE Biloxi - Marine Technology for Our Future: Global and Local Challenges*.

Stewart, D. P., Boyle, R. S., and Randolph, M. F. (1998). "Experience with a new drum centrifuge." *Proc. Int. Conf. Centrifuge*, Tokyo, 35–40.

Stratasya. (2015). "Fortus: 380mc and 450 mc." Stratasy, Eden Praire, MN.

Stringer, M., Heron, C., and Madabhushi, S. (2010). "Experience using MEMS-based accelerometers in dynamic testing." *Proc. of the 7th Int. Conf. on Phys. Model. in Geotech.*, C. Gaudin and D. White, eds., CRC Press, Perth, 389–394.

Sun, X., Huang, D., and Wu, G. (2012). "The current state of offshore wind energy technology development." *Energy*, Elsevier Ltd, 41(1), 298–312.

Taboada-Urtuzuástegui, V. M., and Dobry, R. (1998). "Centrifuge modeling of earthquake-induced lateral spreading in sand." *J. Geotech. Geoenviron. Eng.*, ASCE, 124(12), 1195–1206.

Tanaka, M. (2007). "An industrial and applied review of new MEMS devices features." *Microelectronic Engineering*, Elsevier, 84(5-8), 1341–1344.

Taylor, R. N. (1995). "Centrifuge in modelling: principles and scale effects." *Geotechnical Centrifuge Technology*, R. N. Taylor, ed., Blackie Academic & Professional, Glasgow, 19–33.

Tessari, A. (2012). "Centrifuge modeling of the effects of natural hazards on pile-founded concrete floodwalls." *PhD Dissertation*, Rensselaer Polytechnique Institute.

Tuttle, M. (1981). “Load measurement in a cylindrical column or beam using three strain gages.” *Experimental Tecniquea*, Wiley, 5(4), 19–20.

Vinogradov, V. V, Frolovsky, Y. K., and Zaytsev, a a. (2014). “The history of geotechnical centrifuge modeling in Russia.” *Proc. of the 8th Int. Conf. on Phys. Model. in Geotech.*, CRC Press, Perth, 441–444.

Watson, P. G., Randolph, M. F., and Bransby, M. F. (2000). “Combined lateral and vertical loading of caisson foundations.” *Offshore Technology Conference*, Offshore Technology Conference, Houston.

Wu, T. H. (1971). *Soil Dynamics*. Allyn and Bacon, Boston.

Xuedoon, W. (1988). “Studies on the design of large scale centrifuge for geotechnical and structural tests.” *Centrifuges in Soil Mechanics*, W. H. Craig, R. G. James, and A. N. Schofield, eds., Balkema, Rotterdam, Netherlands, 81–92.

Zhang, C., White, D., and Randolph, M. F. (2011). “Centrifuge modeling of the cyclic lateral response of a rigid pile in soft clay.” *J. Geotech. and Geoenviron. Eng.*, ASCE, 137(7), 717–729.

Zhu, B., Kong, D., Chen, R., Kong, L., and Chen, Y. (2011). “Installation and lateral loading tests of suction caissons in silt.” *Can. Geotech. J.*, NRC Research Press, 48(7), 1070–1084.

APPENDIX A

CENTRIFUGE EXPERIMENT RESULTS

A.1 Normalized Moment Plots

The following section provides all plots of normalized moment versus time. Each plot presents a single displacement magnitude at load eccentricity and demonstrates effects of load eccentricity.

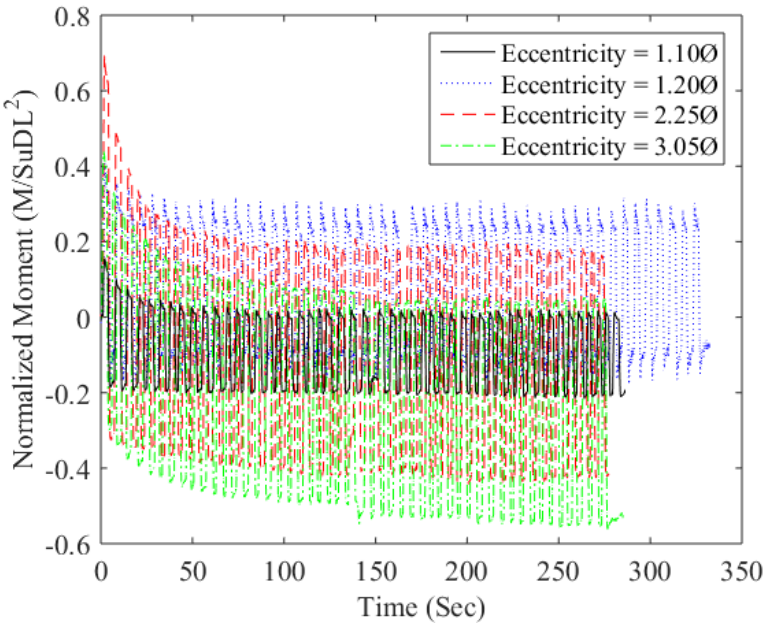

Fig. A.1. Normalized moment, displacement at eccentricity = 2.5% Ø

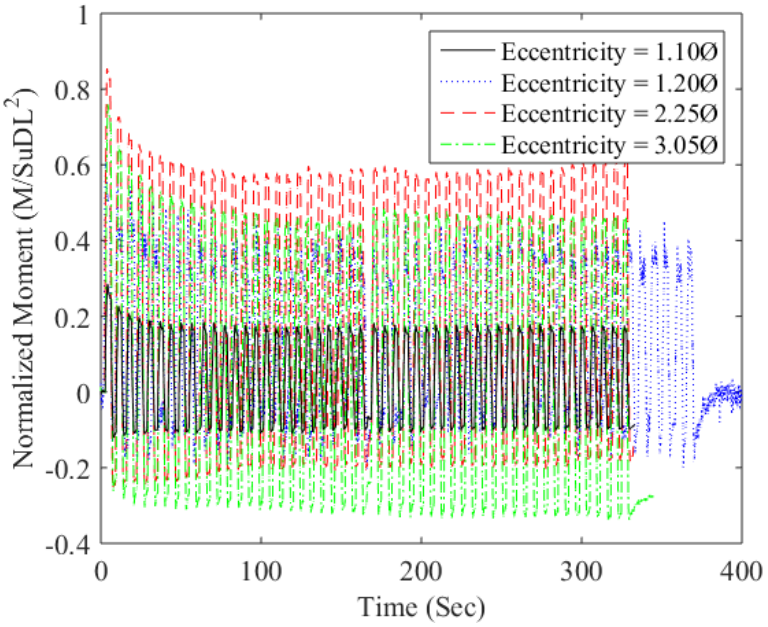

Fig. A.2. Normalized moment, displacement at eccentricity = 5.0% Ø

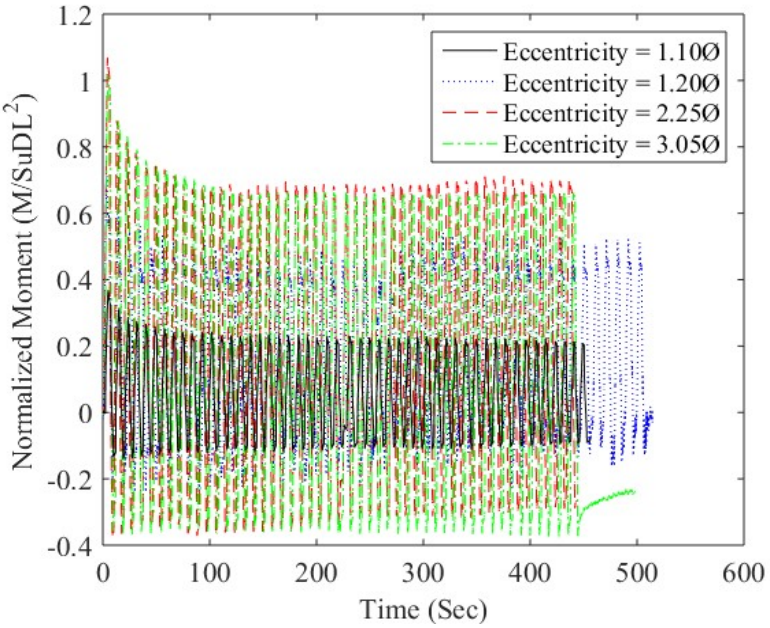

Fig. A.3. Normalized moment, displacement at eccentricity = 10% Ø

A.2 Normalized Horizontal Force Plots

The following section provides all plots of normalized horizontal force versus time. Each plot presents a single displacement magnitude at load eccentricity and demonstrates effects of load eccentricity.

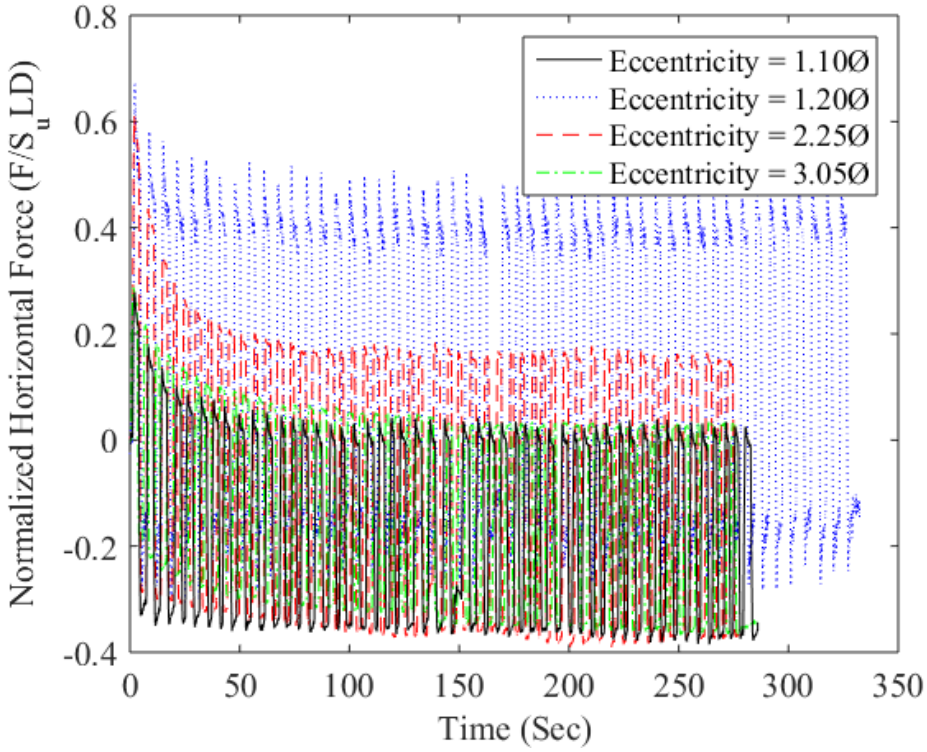

Fig. A.4. Normalized horizontal force, displacement at eccentricity = 2.5% Ø

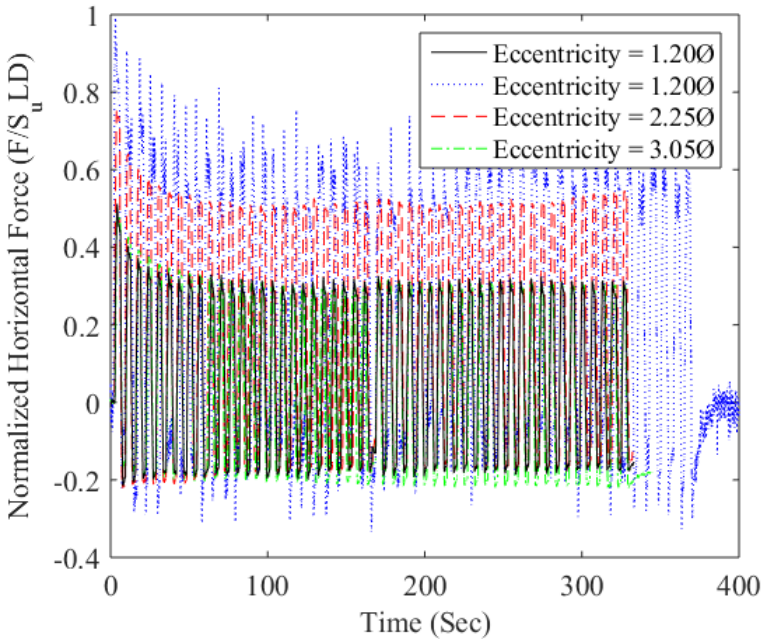

Fig. A.5. Normalized horizontal force, displacement at eccentricity = 5.0% Ø

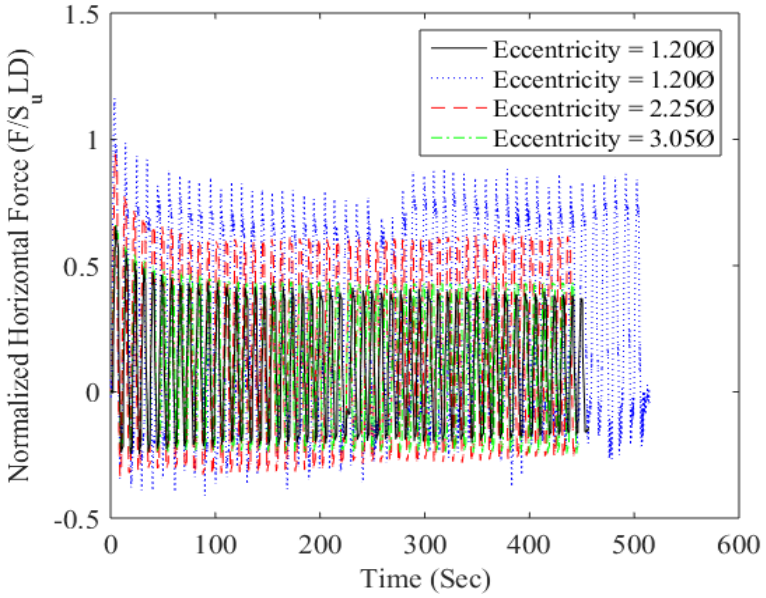

Fig. A.6. Normalized horizontal force, displacement at eccentricity = 10% Ø

A.3 Tilt Plots

The following section provides all plots of orientation relative to centrifuge gravity versus time. Each plot presents a single displacement magnitude at load eccentricity and demonstrates effects of load eccentricity.

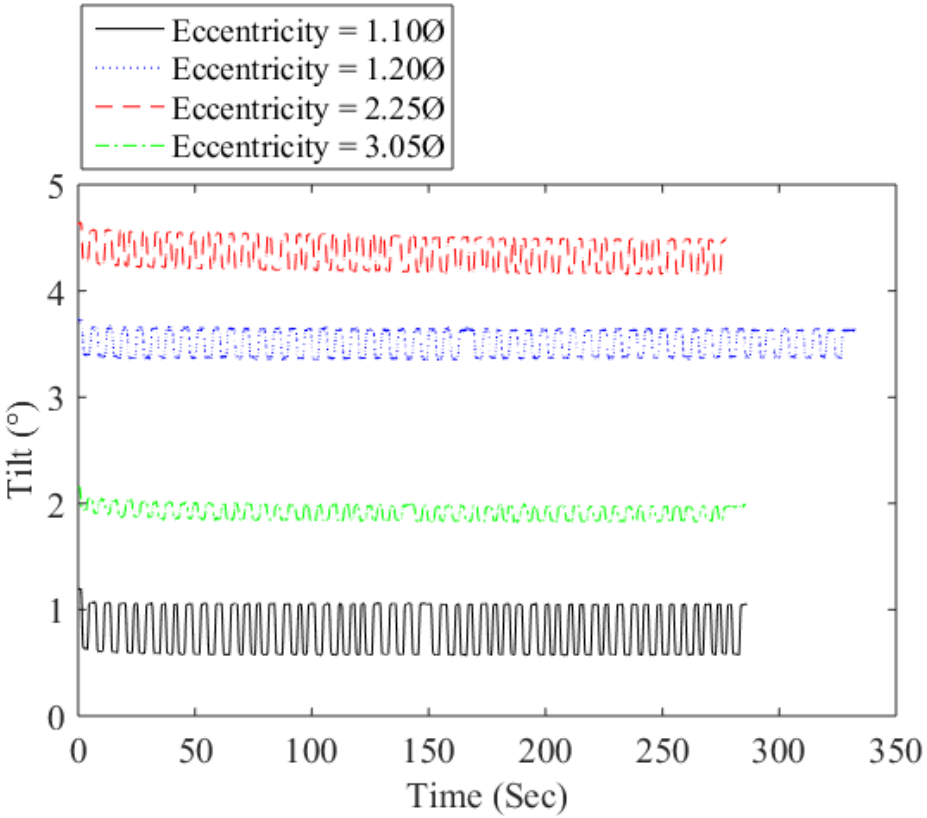

Fig. A.7. Tilt, displacement at eccentricity = 2.5%Ø

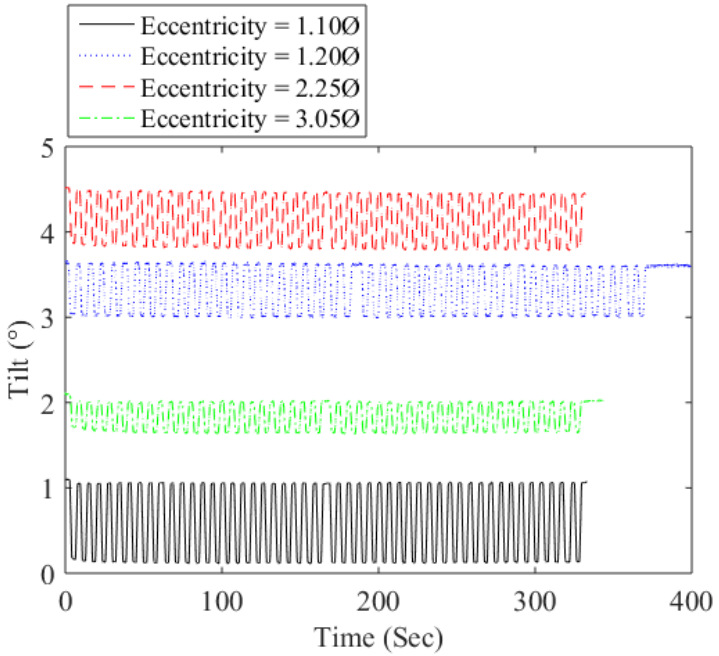

Fig. A.8. Tilt, displacement at eccentricity = 5.0% Ø

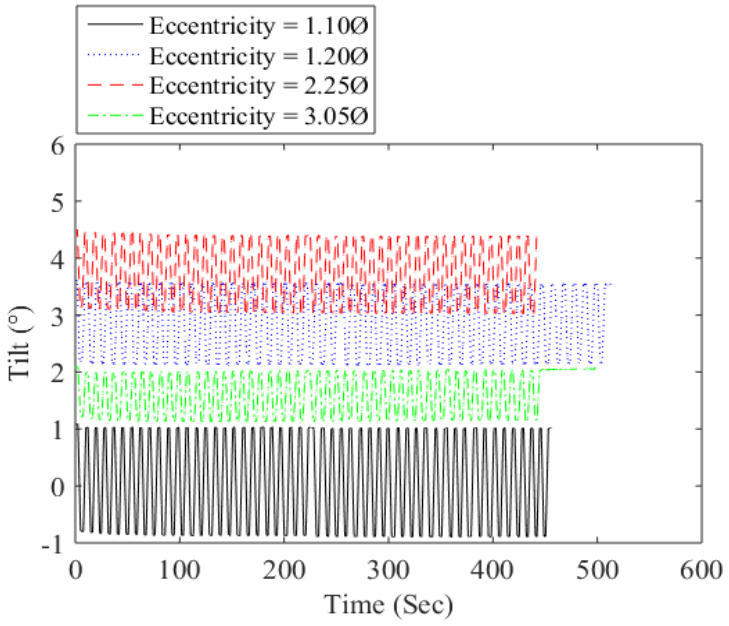

Fig. A.9. Tilt, displacement at eccentricity = 10% Ø

A.4 Depth of Rotation Plots

The following section provides all plots of monopile depth of rotation versus time. Each plot presents a single displacement magnitude at load eccentricity and demonstrates effects of load eccentricity.

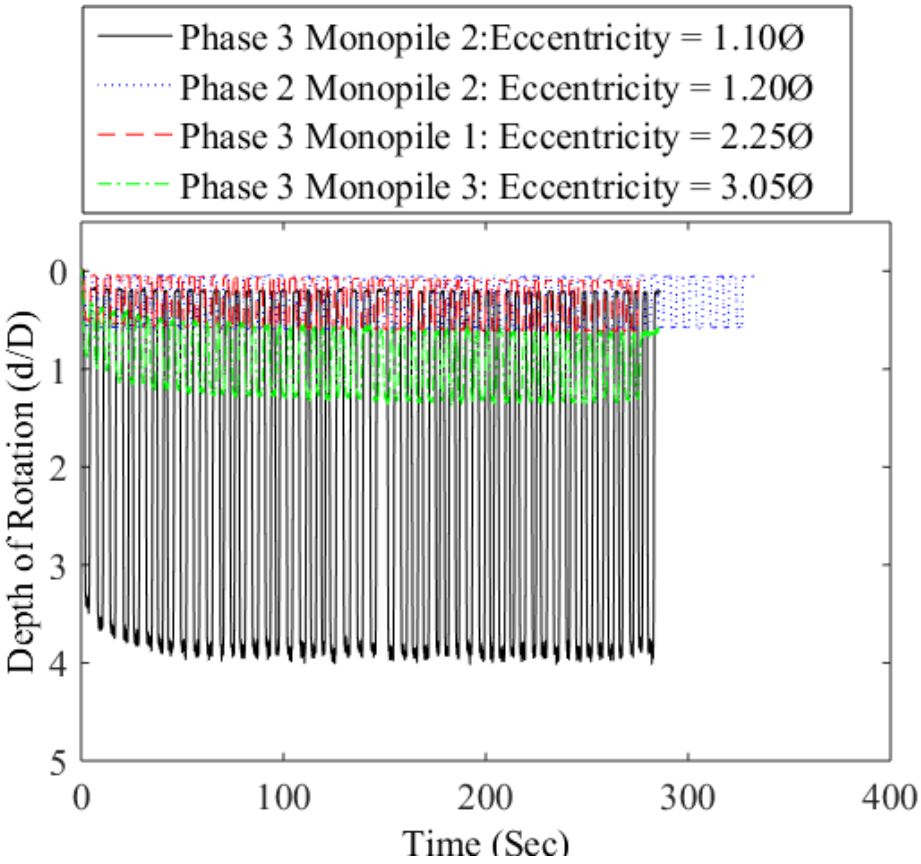

Fig. A.7. Depth of rotation, displacement at eccentricity = 2.5%Ø

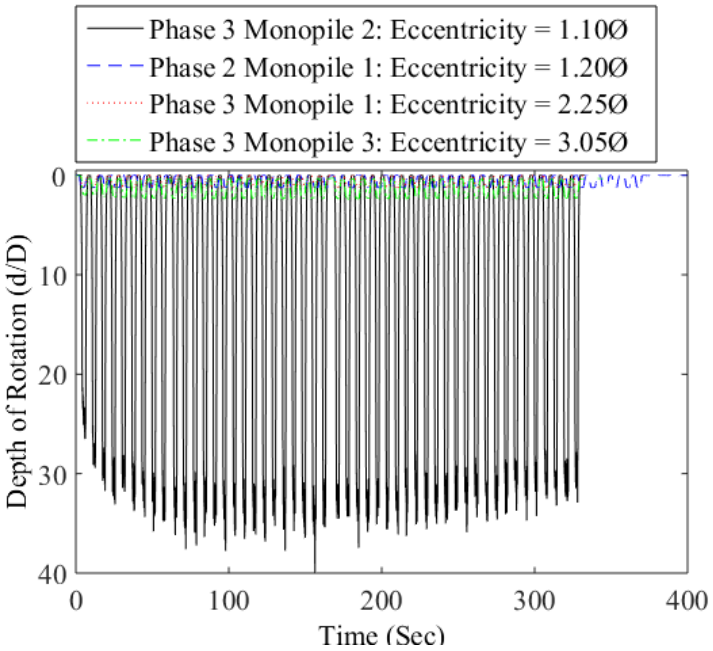

Fig. A.8. Depth of rotation, displacement at eccentricity = 5.0%Ø

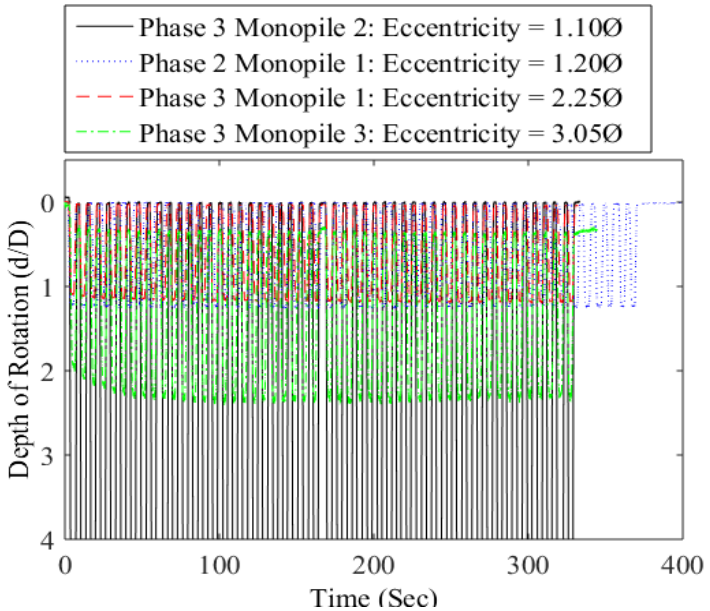

Fig. A.9. Tilt, displacement at eccentricity = 5.0% Ø (zoomed)

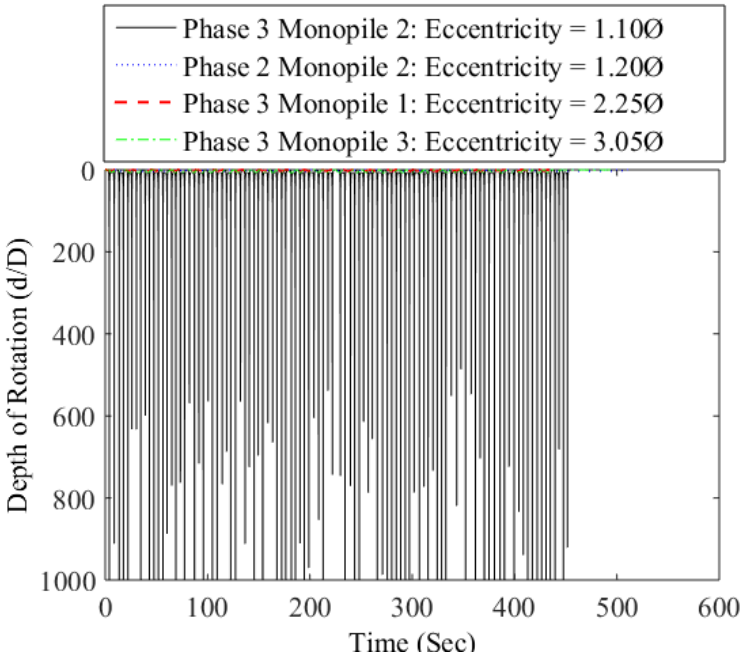

Fig. A.10. Tilt, displacement at eccentricity = 10% Ø

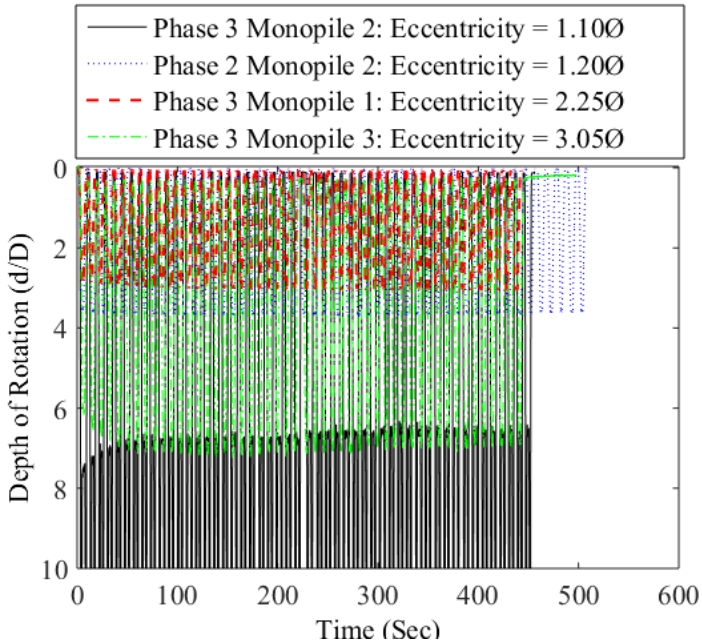

Fig. A.11. Tilt, displacement at eccentricity = 10% Ø (zoomed)

A.5 Normalized Moment Plots by Displacement Magnitude

The following section provides all plots of normalized moment versus time. Each plot presents a single load eccentricity and demonstrates effects of displacement magnitude at load eccentricity.

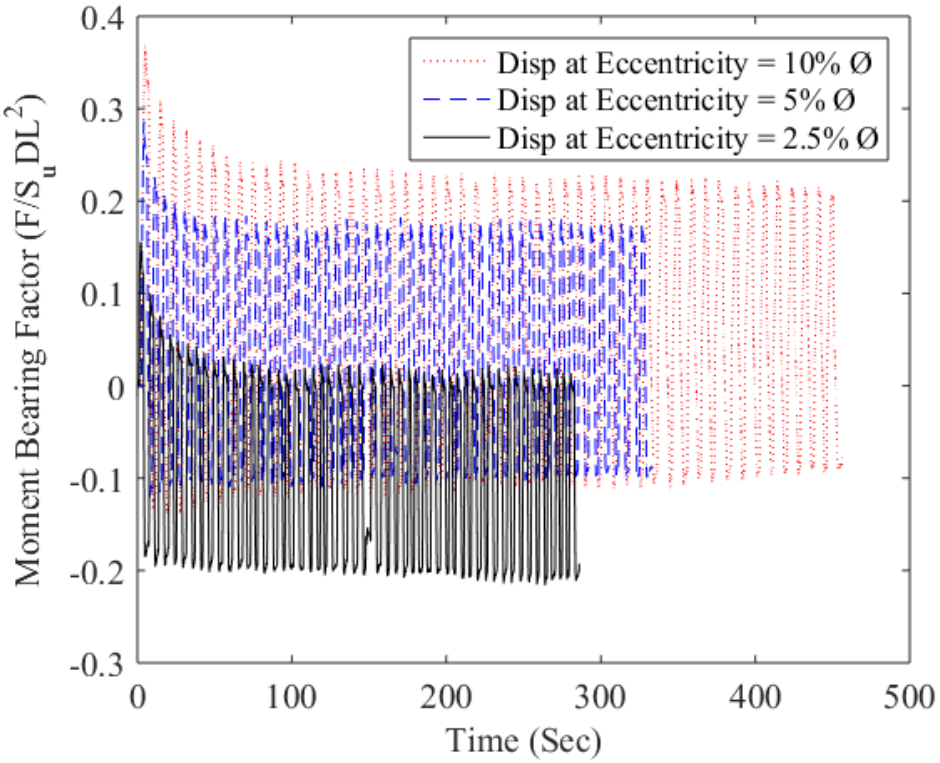

Fig. A.12. Normalized moment, Phase 3 Experiment 2 Pile 2, eccentricity = 1.10Ø

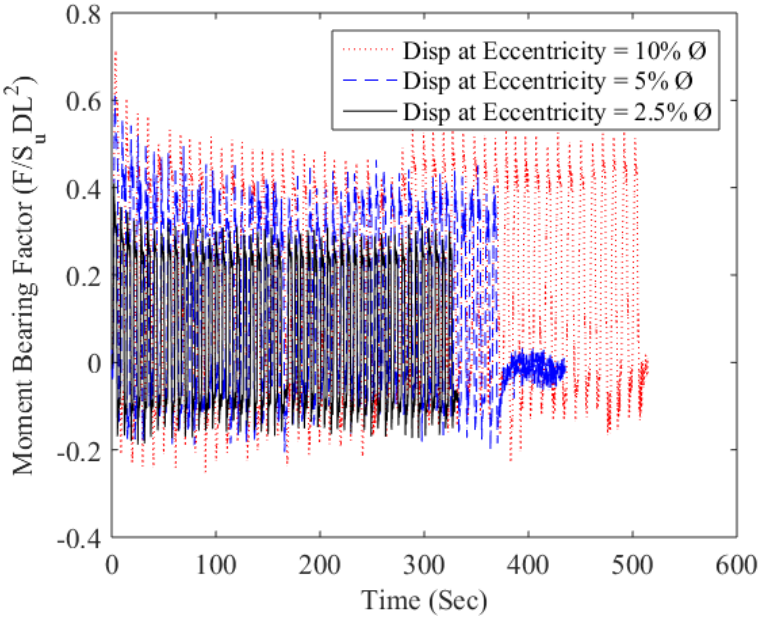

Fig. A.13. Normalized moment, Phase 2 Experiment 2 Pile 2 eccentricity = 1.20Ø

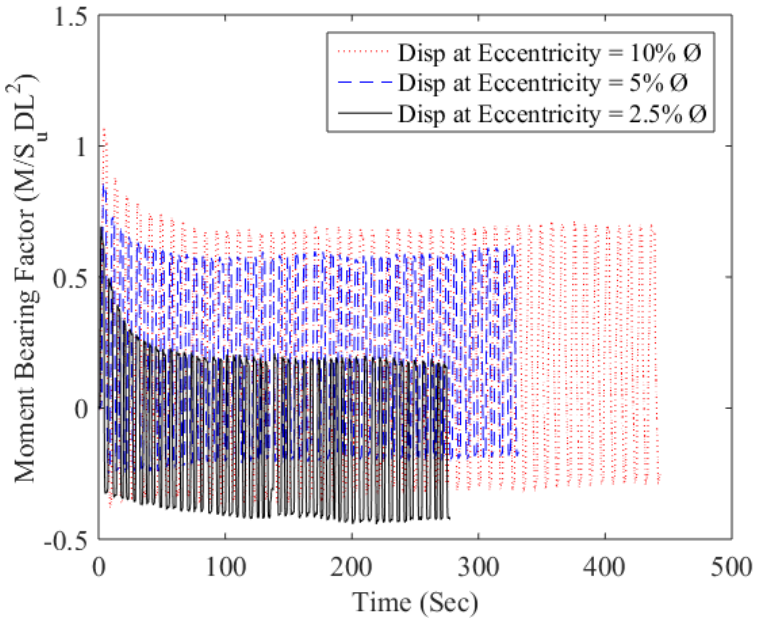

Fig. A.14. Normalized moment, Phase 3 Experiment 2 Pile 1 eccentricity = 2.25Ø

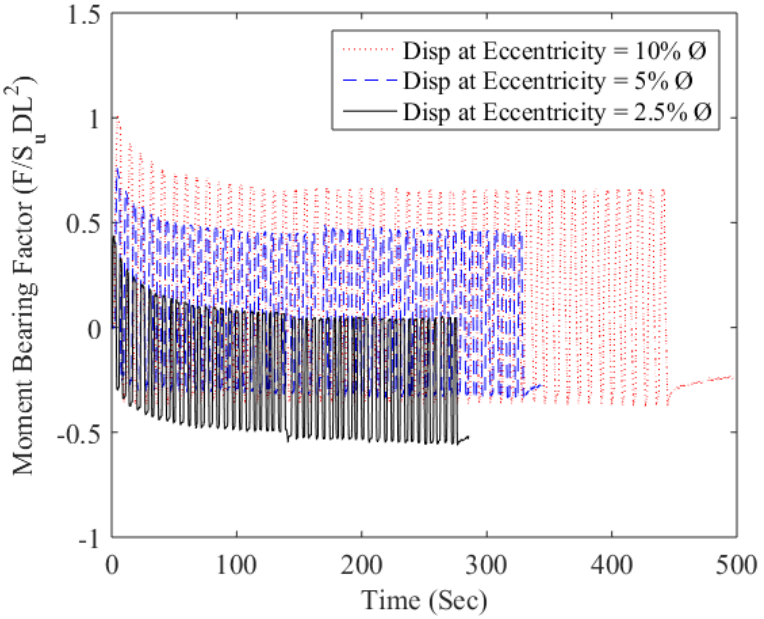

Fig. A.15. Normalized moment, Phase 3 Experiment 2 Pile 3 eccentricity = 3.05Ø

A.6 Rocking Moment-Rotation Plots

The following section provides all plots of moment-rotation plots. Each plot presents a single load eccentricity and demonstrates effects of displacement magnitude at load eccentricity. As noted in the 6 1-G and CENTRIFUGE EXPERIMENTAL RESULTS, data quality from Phase Two Experiment Two Pile Two was very low as a result it has been excluded from the plots below.

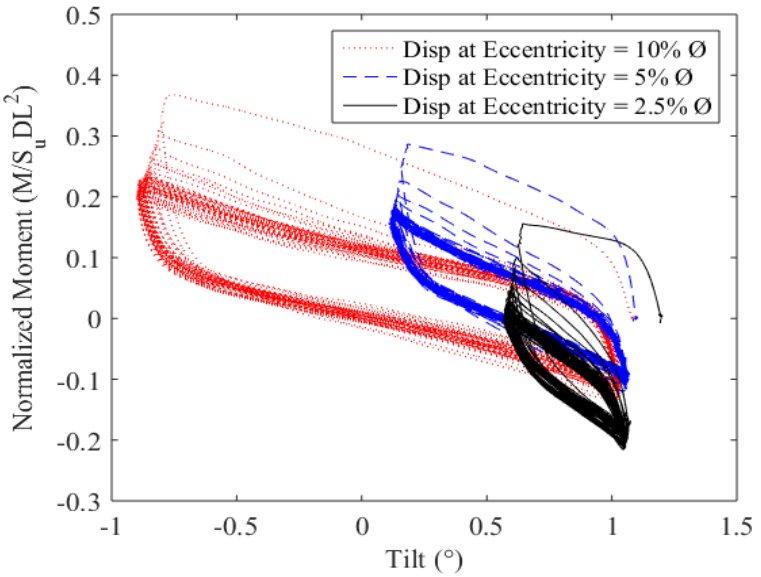

Fig. A.16. Moment-rotation, Phase 3 Experiment 2 Pile 2, eccentricity = 1.10Ø

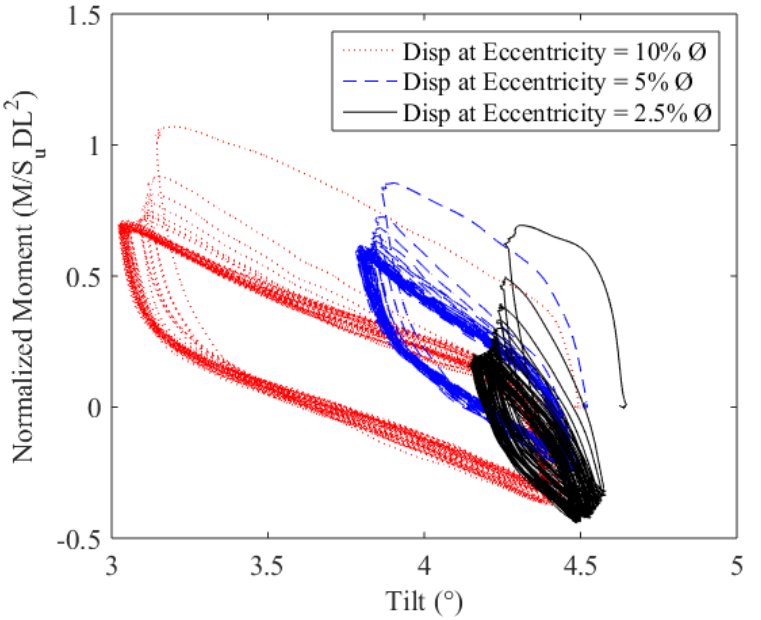

Fig. A.17. Moment-rotation, Phase 3 Experiment 2 Pile 1 eccentricity = 2.25Ø

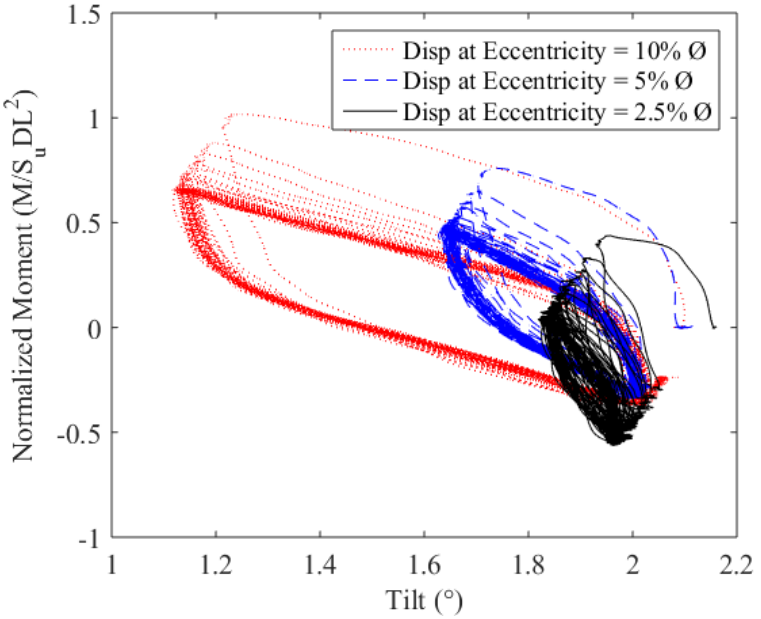

Fig. A.18. Moment-Rotation, Phase 3 Experiment 2 Pile 3 eccentricity = 3.05Ø

A.7 Load and Unload Stiffness Curves

The following section provides plots of normalized rocking/rotational stiffness versus angular magnitude. The data is presented in two ways: cycles 1-10 and cycle 50 and cycles 10-50 fitted with a power law. Given there was four piles cycled at three displacement magnitudes, that load and unload stiffness are of interest, and there are two plots for each case 48 plots of stiffness are presented below.

A.7.1 Phase 3 Experiment 2 Pile 2, Eccentricity of 1.10

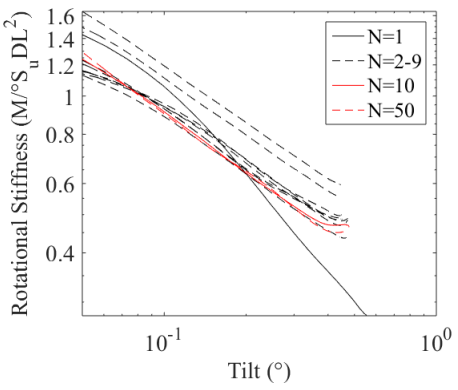

Fig. A.19a. Load stiffness curves, displacement at eccentricity = 2.5% Ø, eccentricity = 1.10Ø

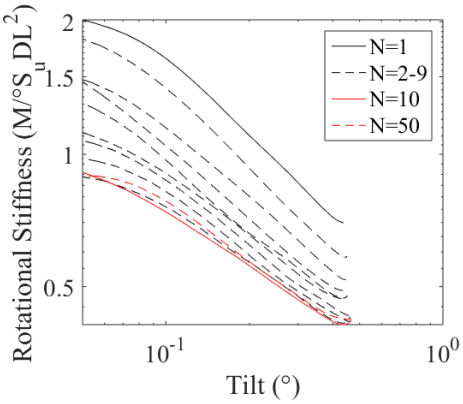

Fig. A.19b. Unload stiffness curves, displacement at eccentricity = 2.5% Ø, eccentricity = 1.10Ø

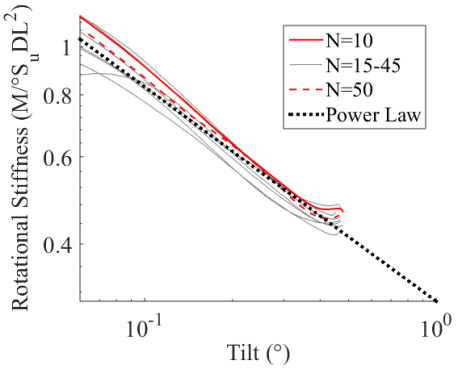

Fig. A.20a. Load stiffness curves power law fitting, displacement at eccentricity = 2.5% Ø, eccentricity = 1.10Ø

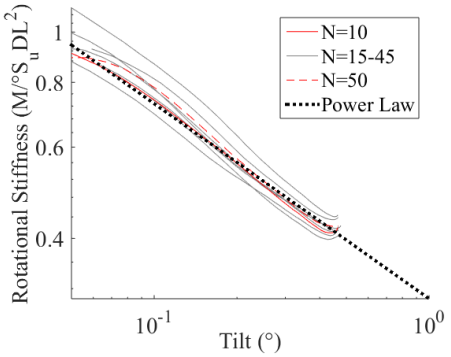

Fig. A.20b. Unload stiffness curves power law fitting, displacement at eccentricity = 2.5% Ø, eccentricity = 1.10Ø

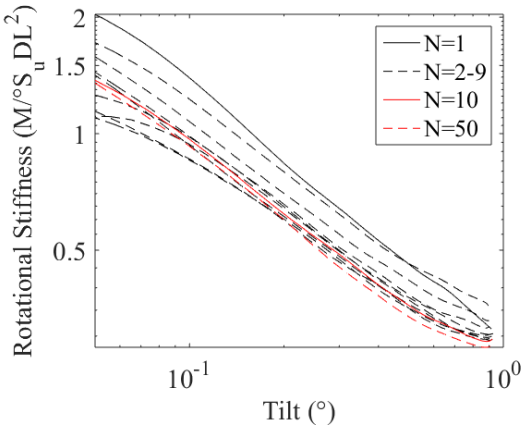

Fig. A.21a. Load stiffness curves, displacement at eccentricity = 5.0% Ø, eccentricity = 1.10Ø

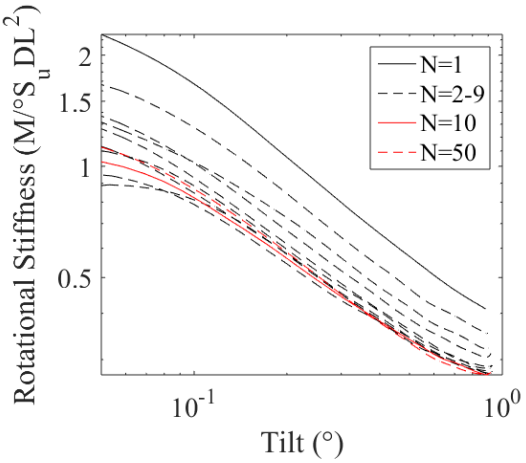

Fig. A.21b. Unload stiffness curves, displacement at eccentricity = 5.0% Ø, eccentricity = 1.10Ø

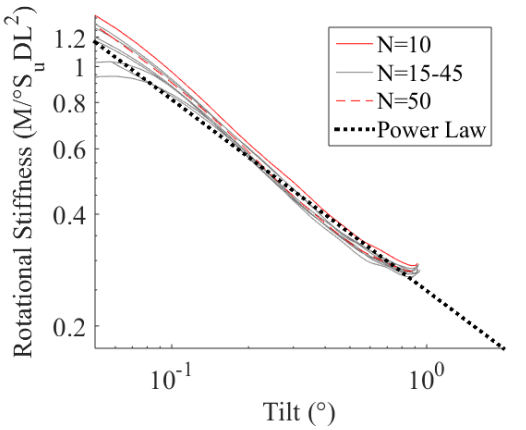

Fig. A.22a. Load stiffness curves power law fitting, displacement at eccentricity = 5.0% Ø, eccentricity = 1.10Ø

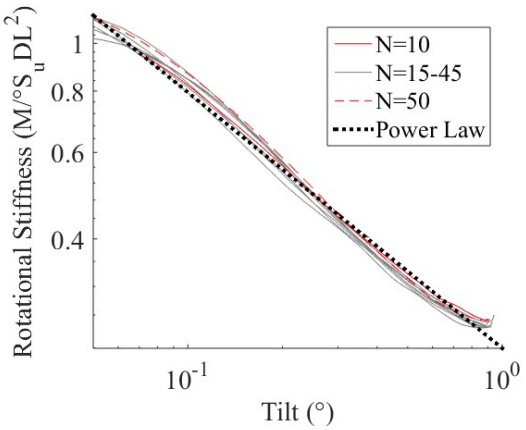

Fig. A.22b. Unload stiffness curves power law fitting, displacement at eccentricity = 5.0% Ø, eccentricity = 1.10Ø

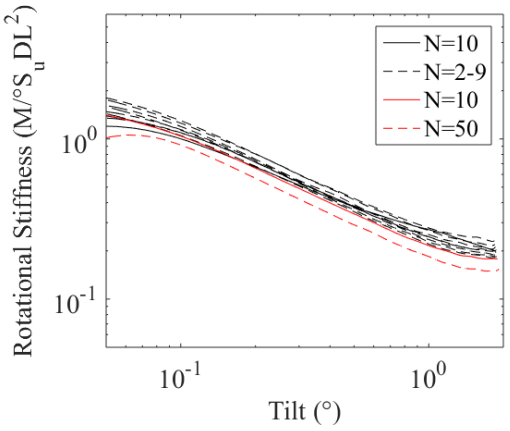

Fig. A.23a. Load stiffness curves, displacement at eccentricity = 10% Ø, eccentricity = 1.10Ø

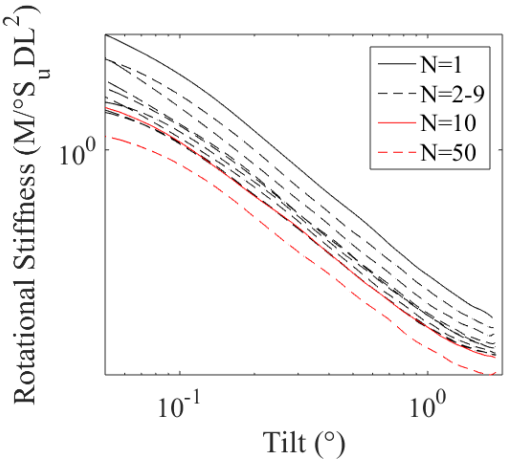

Fig. A.23b. Unload stiffness curves, displacement at eccentricity = 10% Ø, eccentricity = 1.10Ø

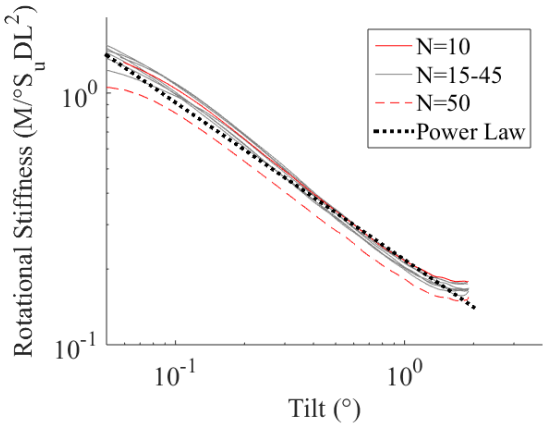

Fig. A.24a. Load stiffness curves power law fitting, displacement at eccentricity = 10% Ø, eccentricity = 1.10Ø

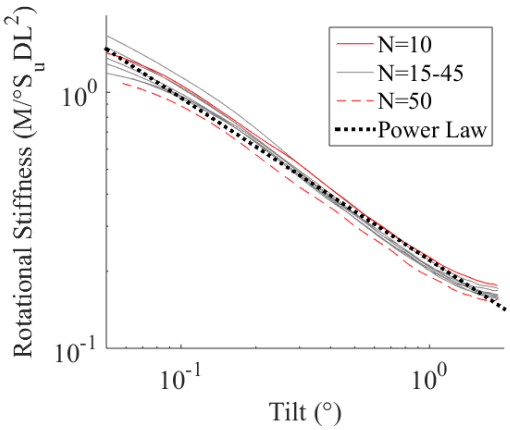

Fig. A.24b. Unload stiffness curves power law fitting, displacement at eccentricity = 10% Ø, eccentricity = 1.10Ø

A.7.2 Phase 2 Experiment 2 Pile 2, Eccentricity of 1.20

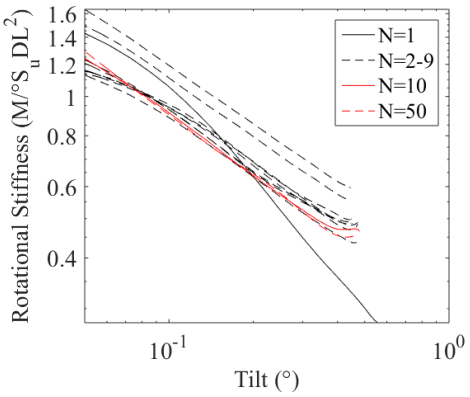

Fig. A.25a. Load stiffness curves, displacement at eccentricity = 2.5% Ø, eccentricity = 1.20Ø

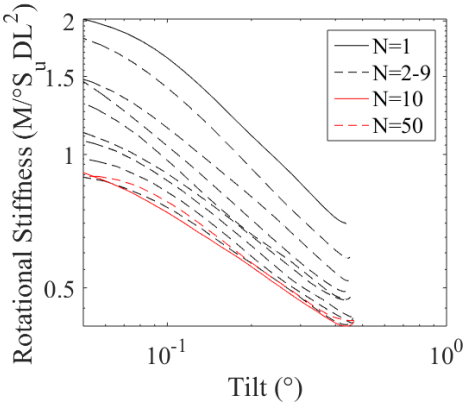

Fig. A.25b. Unload stiffness curves, displacement at eccentricity = 2.5% Ø, eccentricity = 1.20Ø

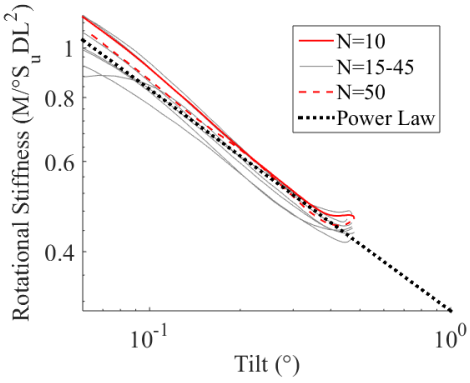

Fig. A.26a. Load stiffness curves power law fitting, displacement at eccentricity = 2.5% Ø, eccentricity = 1.20Ø

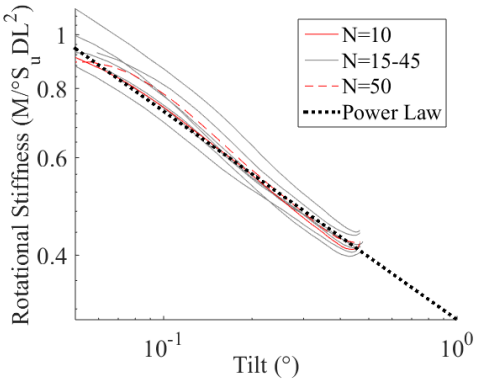

Fig. A.26b. Unload stiffness curves power law fitting, displacement at eccentricity = 2.5% Ø, eccentricity = 1.20Ø

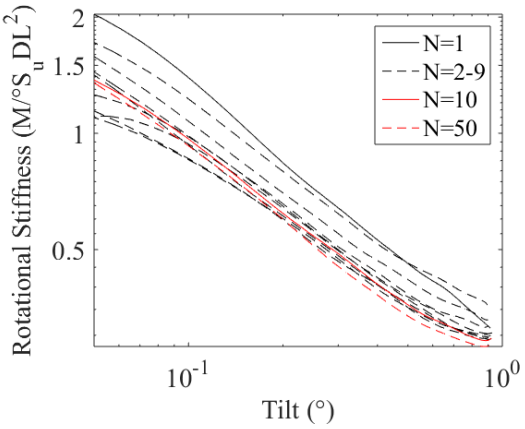

Fig. A.27a. Load stiffness curves, displacement at eccentricity = 5.0% Ø, eccentricity = 1.20Ø

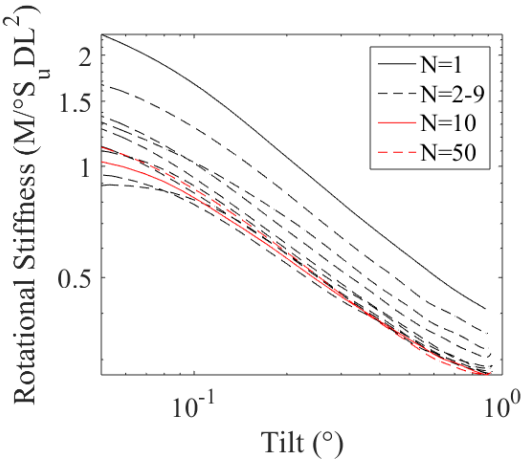

Fig. A.27b. Unload stiffness curves, displacement at eccentricity = 5.0% Ø, eccentricity = 1.20Ø

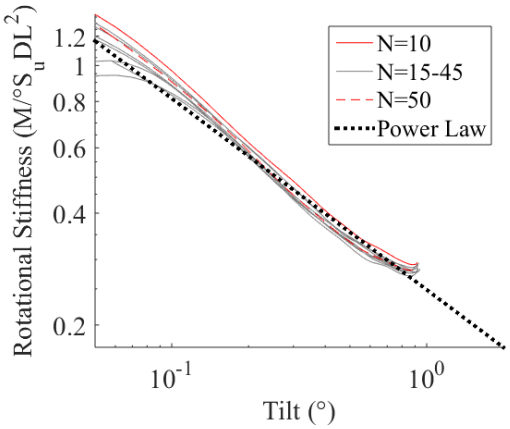

Fig. A.28a. Load stiffness curves power law fitting, displacement at eccentricity = 5.0% Ø, eccentricity = 1.20Ø

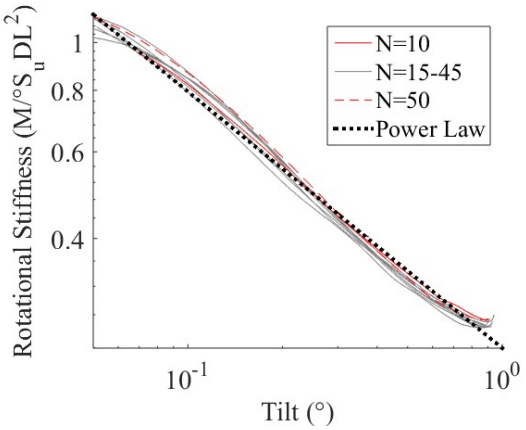

Fig. A.28b. Unload stiffness curves power law fitting, displacement at eccentricity = 5.0% Ø, eccentricity = 1.20Ø

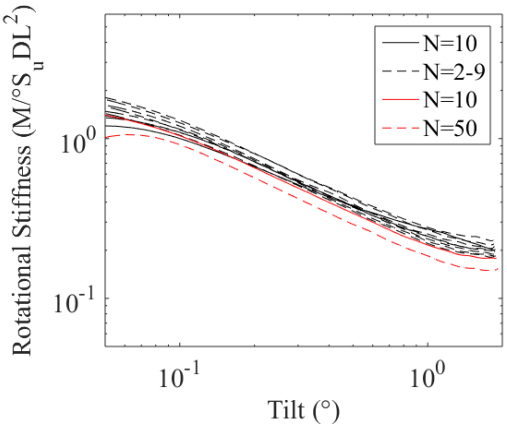

Fig. A.29a. Load stiffness curves, displacement at eccentricity = 10% Ø, eccentricity = 1.20Ø

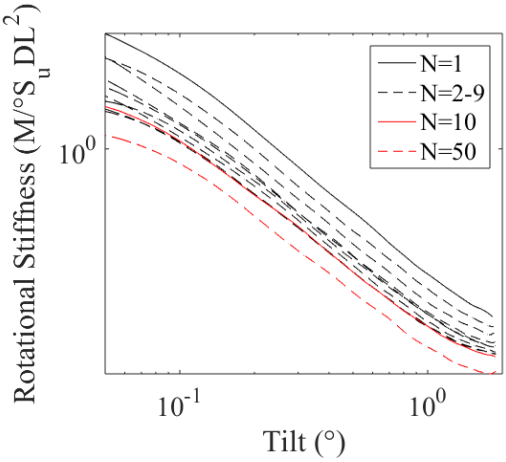

Fig. A.29b. Unload stiffness curves, displacement at eccentricity = 10% Ø, eccentricity = 1.20Ø

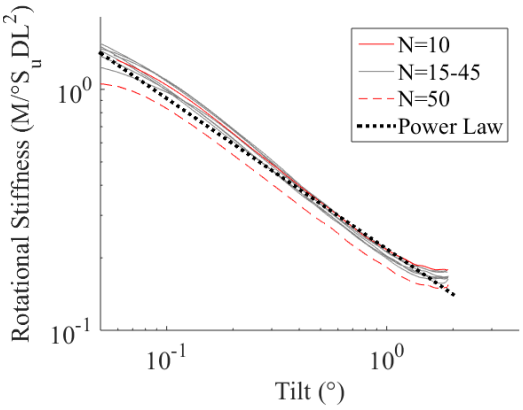

Fig. A.30a. Load stiffness curves power law fitting, displacement at eccentricity = 10% Ø, eccentricity = 1.20Ø

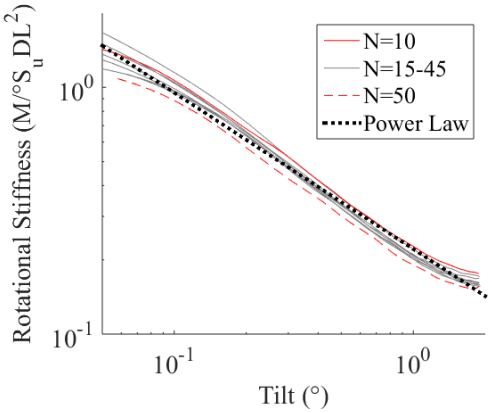

Fig. A.30b. Unload stiffness curves power law fitting, displacement at eccentricity = 10% Ø, eccentricity = 1.20Ø

A.7.3 Phase 3 Experiment 2 Pile 1, Eccentricity of 2.25

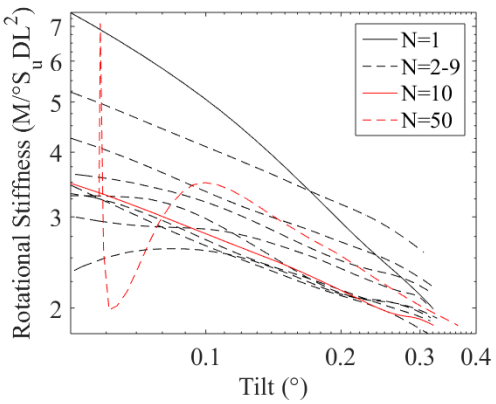

Fig. A.31a. Load stiffness curves, displacement at eccentricity = 2.5% Ø, eccentricity = 2.25Ø

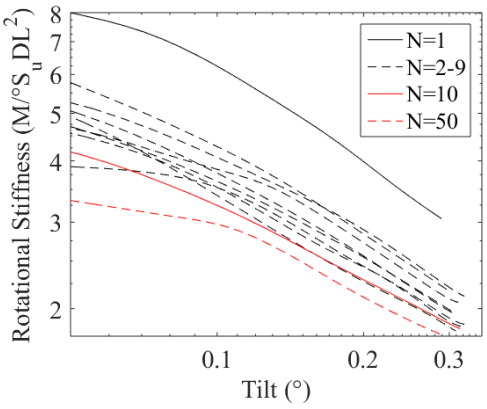

Fig. A.31b. Unload stiffness curves, displacement at eccentricity = 2.5% Ø, eccentricity = 2.25Ø

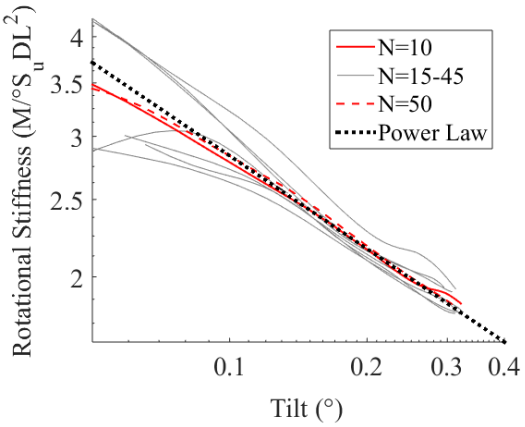

Fig. A.32a. Load stiffness curves power law fitting, displacement at eccentricity = 2.5% Ø, eccentricity = 2.25Ø

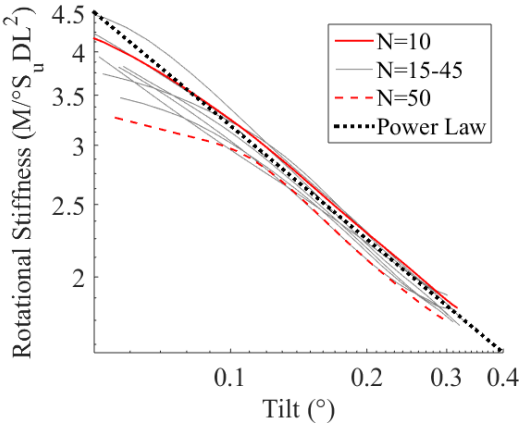

Fig. A.32b. Unload stiffness curves power law fitting, displacement at eccentricity = 2.5% Ø, eccentricity = 2.25Ø

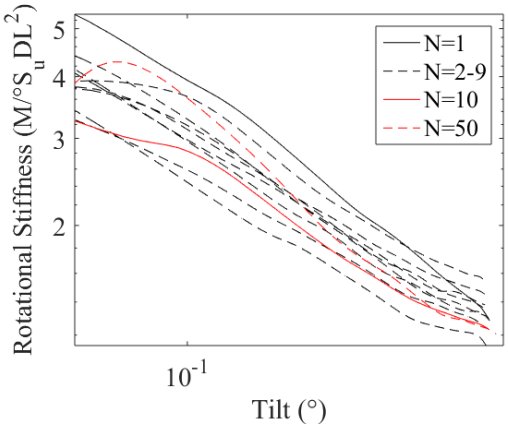

Fig. A.33a. Load stiffness curves, displacement at eccentricity = 5.0% Ø, eccentricity = 2.25Ø

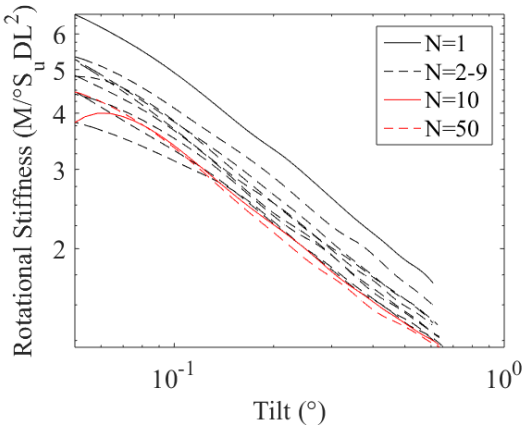

Fig. A.33b. Unload stiffness curves, displacement at eccentricity = 5.0% Ø, eccentricity = 2.25Ø

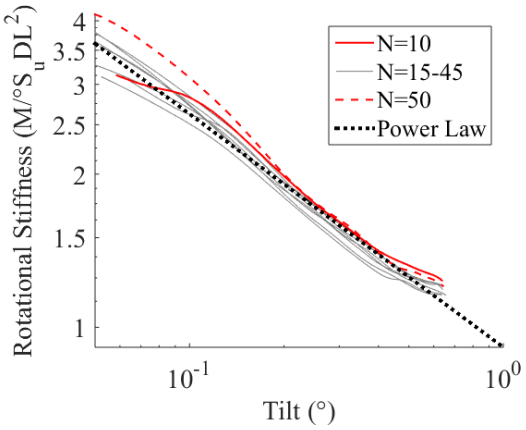

Fig. A.34a. Load stiffness curves power law fitting, displacement at eccentricity = 5.0% Ø, eccentricity = 2.25Ø

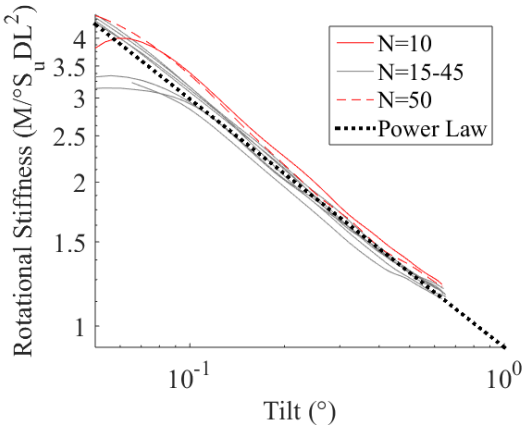

Fig. A.34b. Unload stiffness curves power law fitting, displacement at eccentricity = 5.0% Ø, eccentricity = 2.25Ø

A.7.4 Phase 3 Experiment 2 Pile 3, Eccentricity of 3.05

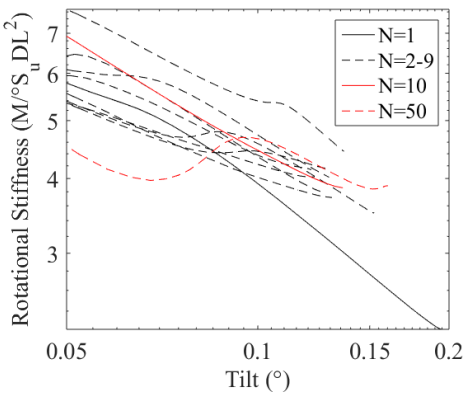

Fig. A.37a. Load stiffness curves, displacement at eccentricity = 2.5% Ø, eccentricity = 3.05Ø

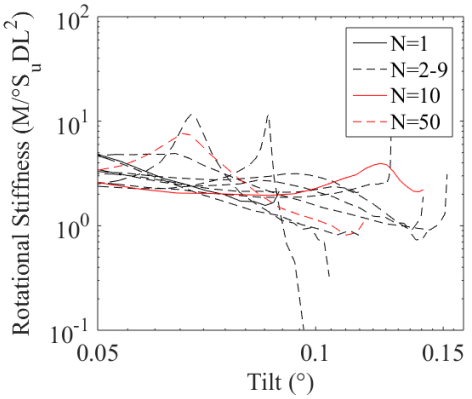

Fig. A.37b. Unload stiffness curves, displacement at eccentricity = 2.5% Ø, eccentricity = 3.05Ø

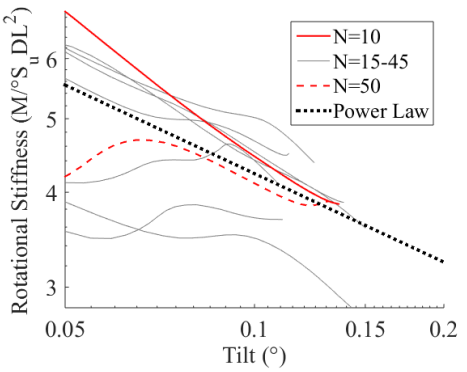

Fig. A.38a. Load stiffness curves power law fitting, displacement at eccentricity = 2.5% Ø, eccentricity = 3.05Ø

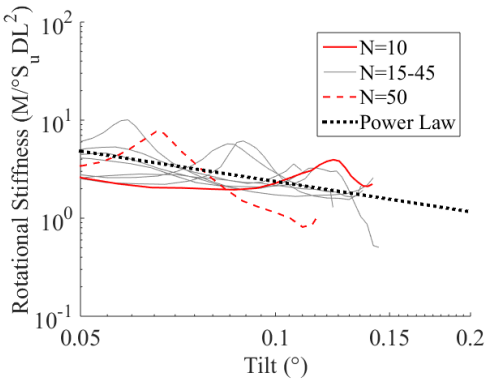

Fig. A.38b. Unload stiffness curves power law fitting, displacement at eccentricity = 2.5% Ø, eccentricity = 3.05Ø

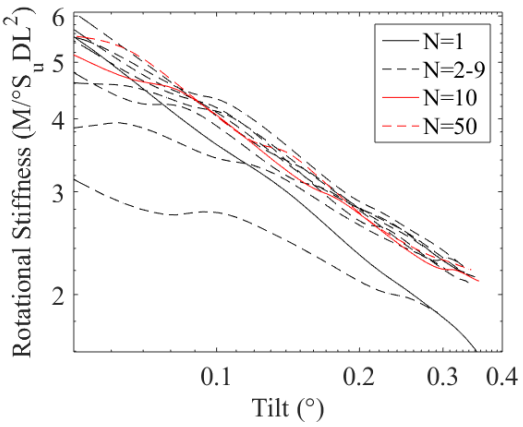

Fig. A.39a. Load stiffness curves, displacement at eccentricity = 5.0% Ø, eccentricity = 3.05Ø

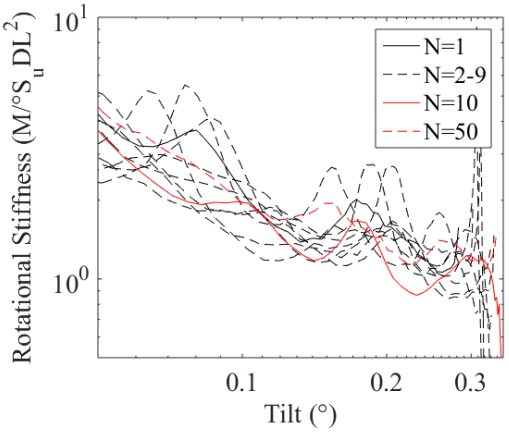

Fig. A.39b. Unload stiffness curves, displacement at eccentricity = 5.0% Ø, eccentricity = 3.05Ø

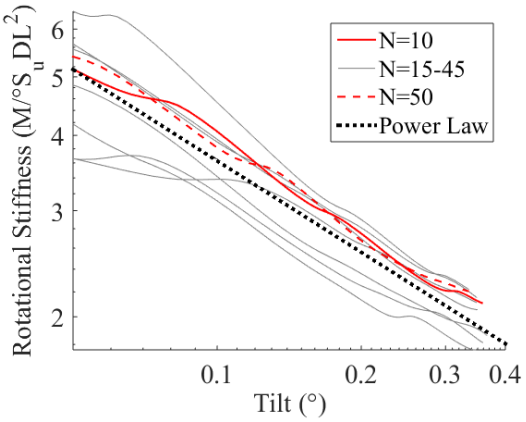

Fig. A.40a. Load stiffness curves power law fitting, displacement at eccentricity = 5.0% Ø, eccentricity = 3.05Ø

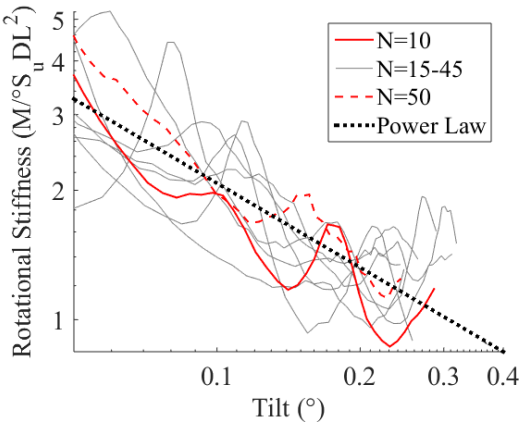

Fig. A.40b. Unload stiffness curves power law fitting, displacement at eccentricity = 5.0% Ø, eccentricity = 3.05Ø

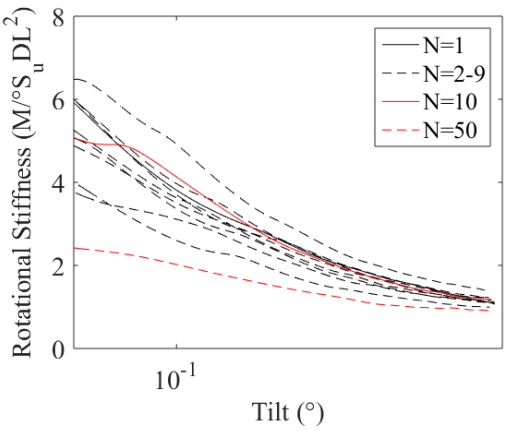

Fig. A.41a. Load stiffness curves, displacement at eccentricity = 10% Ø, eccentricity = 3.05Ø

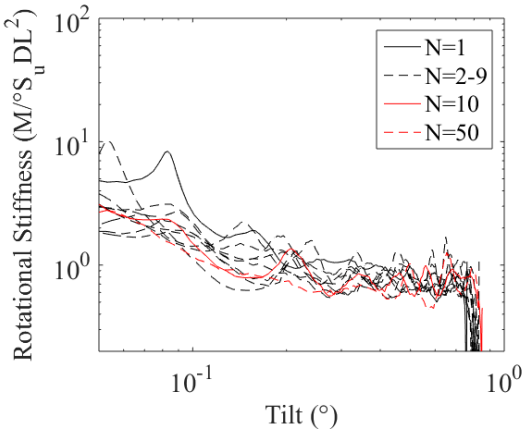

Fig. A.41b. Unload stiffness curves, displacement at eccentricity = 10% Ø, eccentricity = 3.05Ø

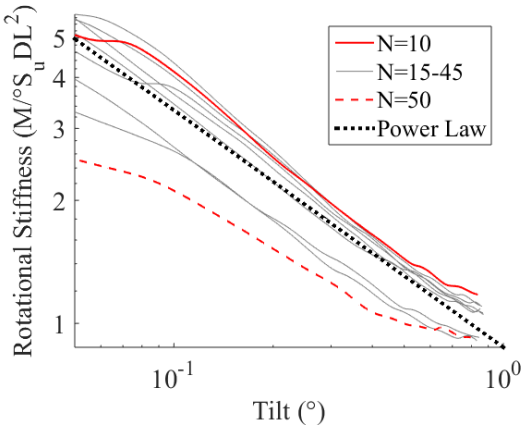

Fig. A.42a. Load stiffness curves power law fitting, displacement at eccentricity = 10% Ø, eccentricity = 3.05Ø

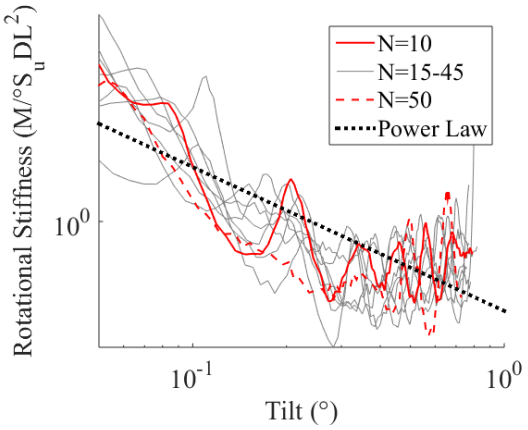

Fig. A.42b. Unload stiffness curves power law fitting, displacement at eccentricity = 10% Ø, eccentricity = 3.05Ø

A.8 Pore Pressure Plots

The following section provides all plots of pore pressure versus time.

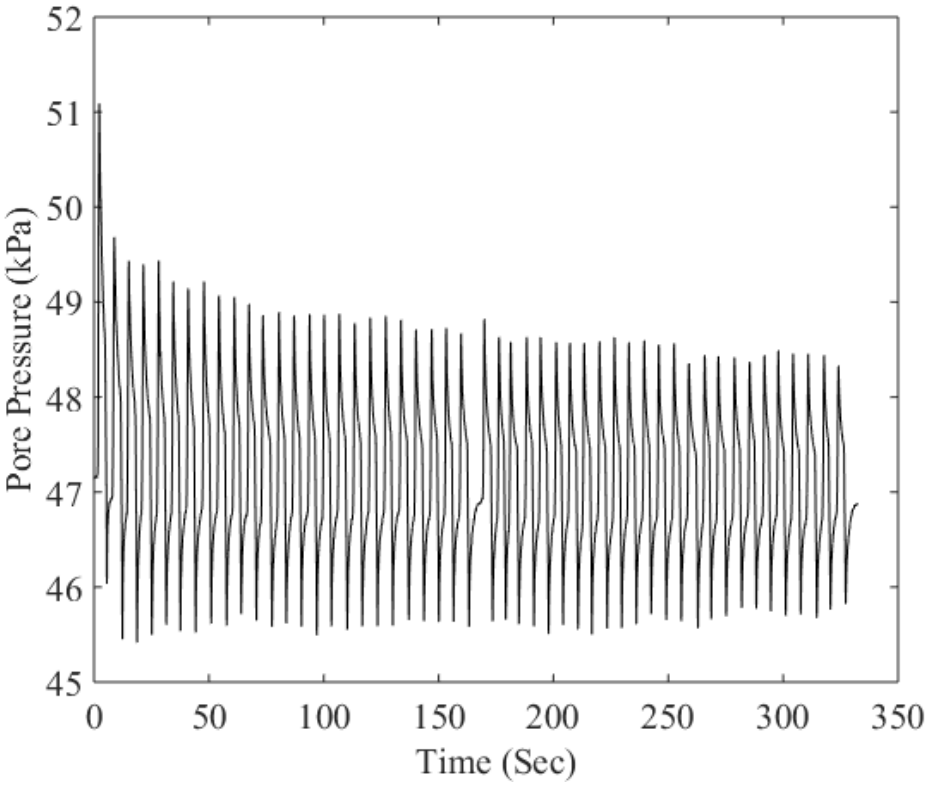

Fig. A.43. Pore pressure time series, displacement at eccentricity = 2.5% Ø, eccentricity = 1.20Ø

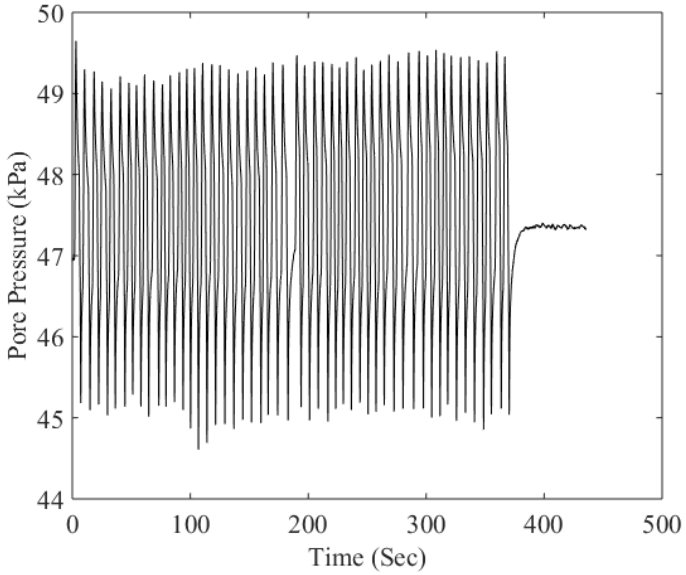

Fig. A.44. Pore pressure time series, displacement at eccentricity = 5% Ø, eccentricity = 1.20Ø

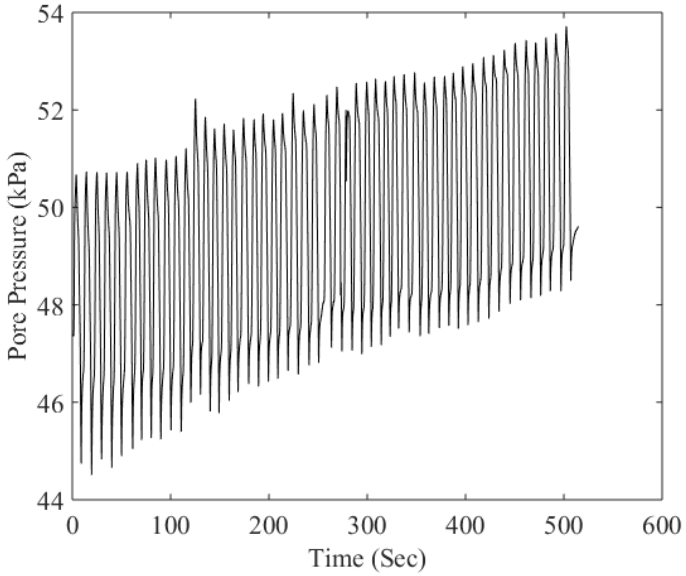

Fig. A.45. Pore pressure time series, displacement at eccentricity = 10% Ø, eccentricity = 1.20Ø

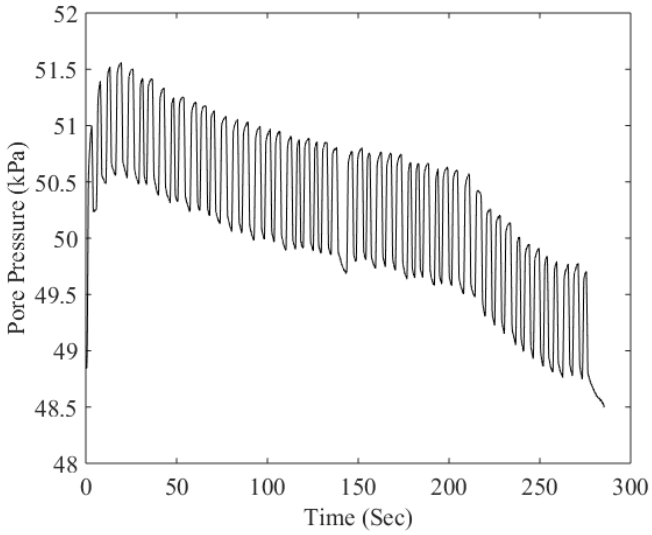

Fig. A.46. Pore pressure time series, displacement at eccentricity = 2.5% Ø, eccentricity = 3.05Ø

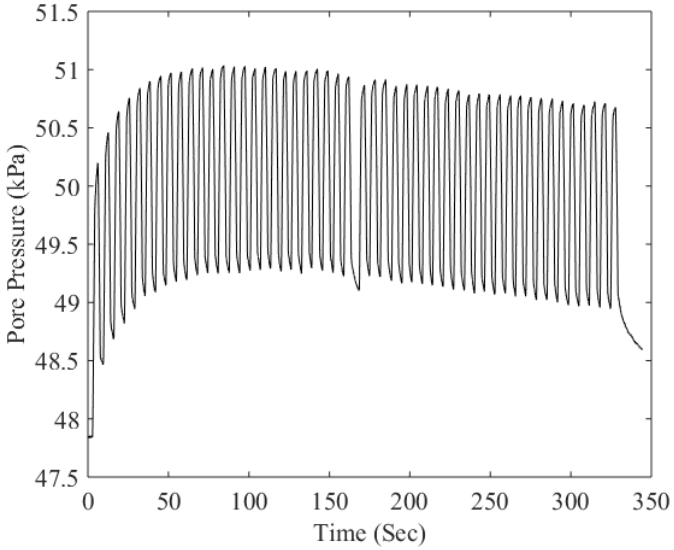

Fig. A.47. Pore pressure time series, displacement at eccentricity = 5% Ø, eccentricity = 3.05Ø

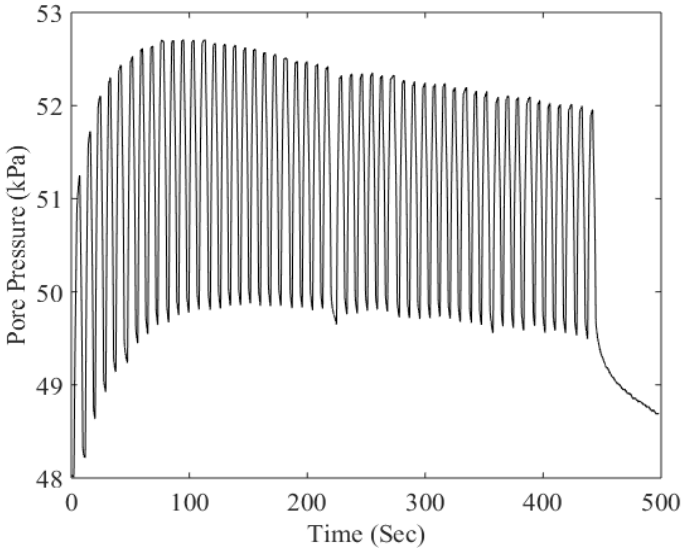

Fig. A.48. Pore pressure time series, displacement at eccentricity = 10% Ø, eccentricity = 3.05Ø

A.9 Caisson Strain and Reaction Force Plots

The following section provides all plots of caisson strain and reaction force versus time. Each plot presents a single displacement magnitude at load eccentricity and demonstrates effects of load eccentricity.

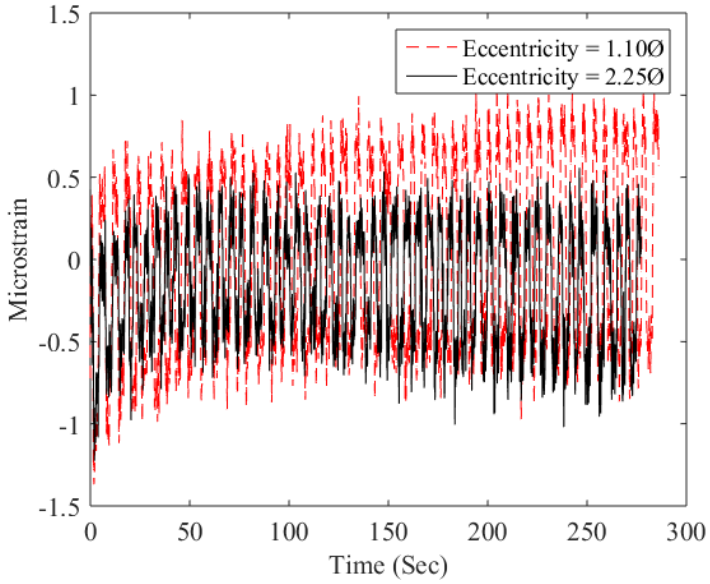

Fig. A.49. Caisson strain time series, displacement at eccentricity = 2.5% Ø

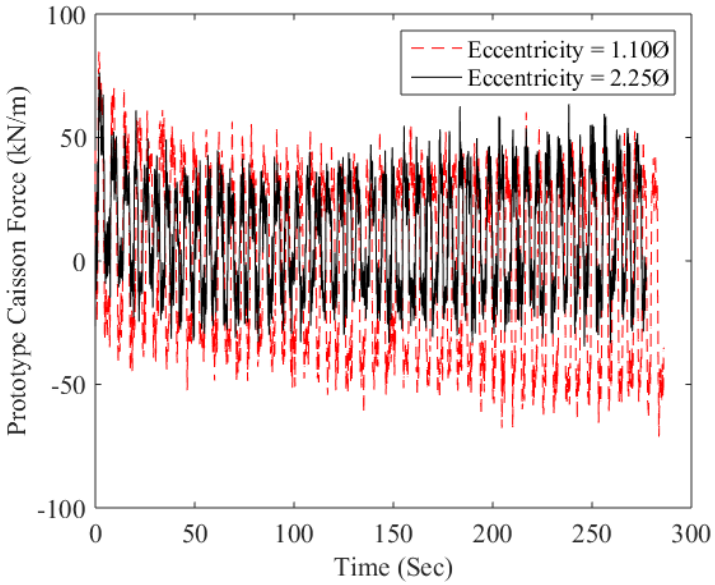

Fig. A.50. Caisson reaction force time series, displacement at eccentricity = 2.5% Ø

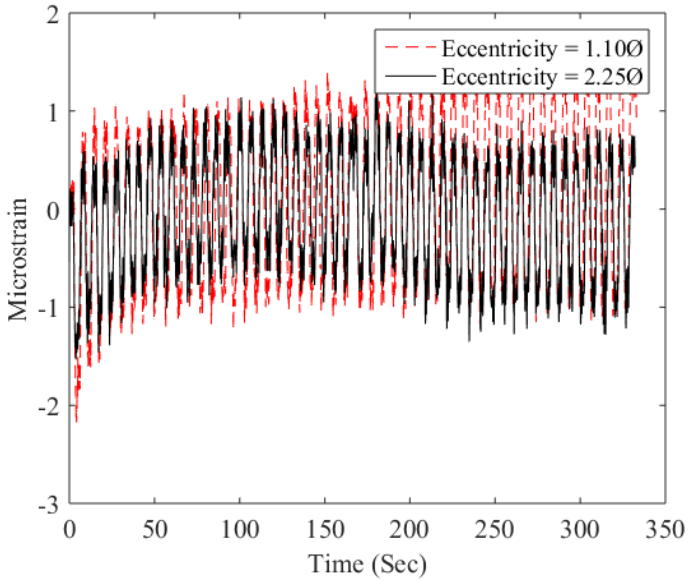

Fig. A.51. Caisson strain time series, displacement at eccentricity = 5% Ø

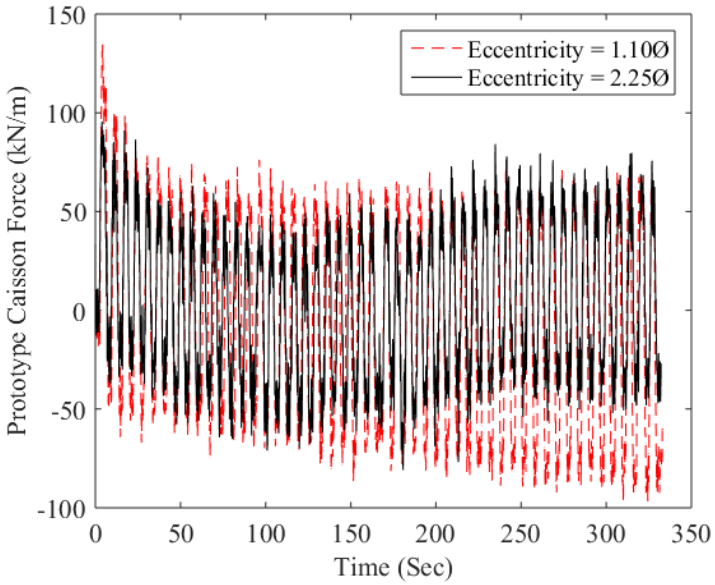

Fig. A.52. Caisson reaction force time series, displacement at eccentricity = 5% Ø

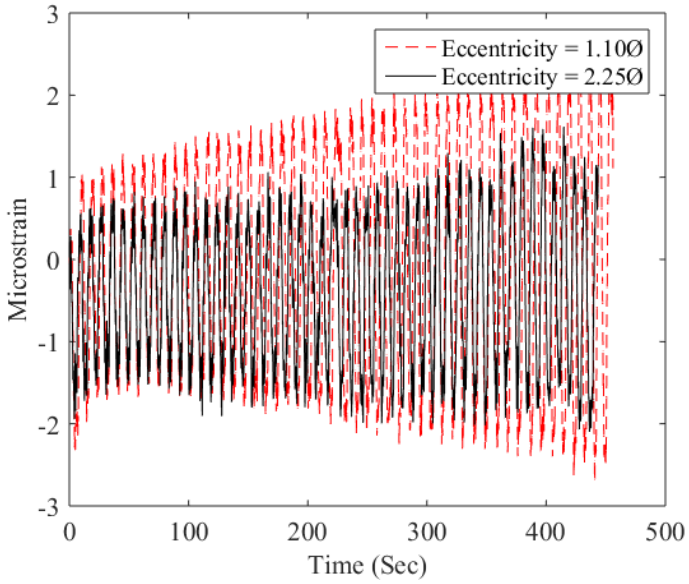

Fig. A.53. Caisson strain time series, displacement at eccentricity = 10% Ø

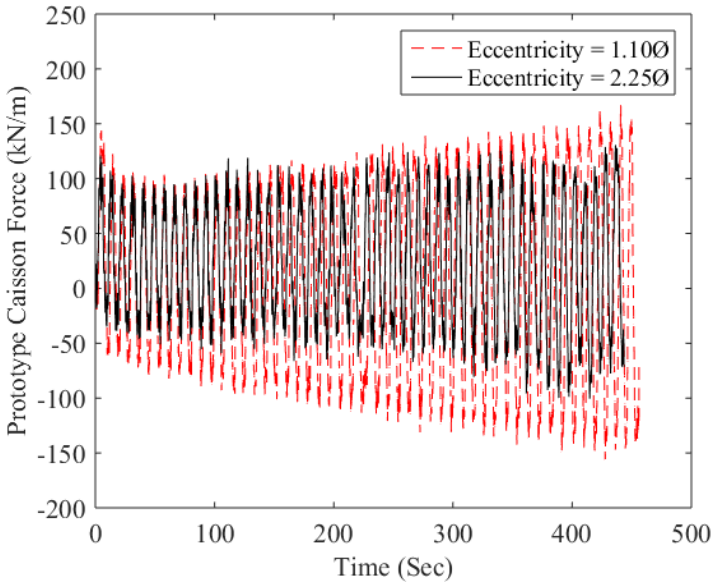

Fig. A.54. Caisson reaction force time series, displacement at eccentricity = 10% Ø

APPENDIX B

DRAWINGS

B.1 Monopile/Pile Parts

Drawings for the parts used to construct the piles in both the 1-g and geotechnical centrifuge experiments have been included as .pdf files. Drawings provided are listed below:

- Caisson, scale model of the foundation constructed from aluminum tube
    - Caisson.pdf
- 0.9Ø (1-g Experiments) or 1.10Ø (centrifuge experiments) stem. Shortest loading stem used in experiments. The slight height difference was due to strain gages attached to the stem in the centrifuge experiments. They limited the screw in depth of the stem.
    - Stem e 0_9 and e 1_10.pdf
- 1.2Ø stem, second shortest stem used in all experiments
    - Stem e 1_2.pdf
- 2.25Ø stem, second tallest stem used in the geotechnical centrifuge experiments
    - Stem e 2_25.pdf
- 3.05 stem, tallest stem used in centrifuge experiments
    - Stem e 3_05.pdf
- Ball placed on the top of the stem to prevent moment transfer from the loading systems
    - Ball.pdf

- MEMS platform, 3D printed platform to carry Microelectricalmechanical systems (MEMS) accelerometers and for securing strain gage wires. This is constructed from two parts and assembled with bolts and nuts:
    - MEMS Platform_Assembled.pdf
    - MEMS Platform_Base.pdf
    - MEMS Platform_Top.pdf

B.2 1-g Experiments

Drawings for the 1-g experiments on rotational behavior of gravity caissons have been included digitally as .pdf files. An outline of available Drawings is provide below.

- Pile 1 with a load eccentricity of 0.9Ø. Used in Test 1 (Ex-1) and Test 2
    - 1-g_Pile 1.pdf
- Pile 2 with a load eccentricity of 1.20Ø. Used in Test 3 and Test 4
    - 1-g_Pile 2.pdf
- Test 1 layout. Only a single experimental layout was include because they were identical with the exception of the pile tested
    - 1-g_Test 1.pdf

B.3 Geotechnical Centrifuge Experiments

- Phase Two Experiment Two
    - Pile 2 layout, drawing of pile assembly. Was the only pile to survive the experiment
        - Phase 2_Pile 2_Ex 2.pdf
    - Pile 2 sensors layout, location and names of all the sensors on the pile
        - Phase 2_Pile 2_Ex 2_Sensors.pdf

- Experiment layout, drawing including locations of all parts
  - Phase 2_Ex 2.pdf
- Experiment sensor layout, location and names of all the sensors on the pile
  - Phase 2_Ex 2_Sensors.pdf
- Experiment orientation, provides experiment layout relative the to local coordinate system includes an estimated orientation of gravity vectors
  - Phase 2_Ex 2_Orientation.pdf

- Phase Three Experiment Two
  - Pile 1 layout, drawing of pile assembly for the second tallest pile
    - Phase 3_Pile 1_Ex 2.pdf
  - Pile 1 sensors layout, location and names of all the sensors on the pile
    - Phase 3_Pile 1_Ex 2_Sensors.pdf
  - Pile 2 layout, drawing of pile assembly for the shortest pile
    - Phase 3_Pile 2_Ex 2.pdf
  - Pile 2 sensors layout, location and names of all the sensors on the pile
    - Phase 3_Pile 2_Ex 2_Sensors.pdf
  - Pile 3 layout, drawing of pile assembly for the tallest pile
    - Phase 3_Pile 3_Ex 2.pdf
  - Pile 3 sensors layout, location and names of all the sensors on the pile
    - Phase 3_Pile 3_Ex 2_Sensors.pdf

- Experiment layout, drawing including locations of all parts
  - Phase 3_Ex 2.pdf
- Experiment sensor layout, location and names of all the sensors on the pile
  - Phase 3_Ex 2_Sensors.pdf
- Experiment orientation, provides experiment layout relative the to local coordinate system includes an estimated orientation of gravity vectors
  - Phase 3_Ex 2_Orientation.pdf